

**HZDR-094**

# **THE STUDY AND DEVELOPMENT OF PULSED HIGH-FIELD MAGNETS FOR APPLICATION IN LASER-PLASMA PHYSICS**

Florian Kroll

Wissenschaftlich-Technische Berichte  
HZDR-094 · ISSN 2191-8708

**WISSENSCHAFTLICH-  
TECHNISCHE BERICHTE**

**hZDR**

 **HELMHOLTZ**  
ZENTRUM DRESDEN  
ROSSENDORF



Wissenschaftlich-Technische Berichte  
HZDR-094

Florian Kroll

**THE STUDY AND DEVELOPMENT  
OF PULSED HIGH-FIELD MAGNETS  
FOR APPLICATION  
IN LASER-PLASMA PHYSICS**

**HZDR**

 **HELMHOLTZ**  
| ZENTRUM DRESDEN  
| ROSSENDORF

Druckausgabe: ISSN 2191-8708

Elektronische Ausgabe: ISSN 2191-8716

Die elektronische Ausgabe erscheint unter Creative Commons License (CC BY 4.0):

<https://www.hzdr.de/publications/Publ-28306>

<urn:nbn:de:bsz:d120-qucosa2-322841>

Die vorliegende Arbeit wurde sowohl als Dissertation an der Fakultät Mathematik und Naturwissenschaften der Technischen Universität Dresden sowie als Wissenschaftlich-Technischer Bericht des Helmholtz-Zentrum Dresden – Rossendorf mit der Berichtsnummer **HZDR-094** veröffentlicht.

2018

Herausgegeben vom

Helmholtz-Zentrum Dresden - Rossendorf

Bautzner Landstraße 400

01328 Dresden

Germany



# **THE STUDY AND DEVELOPMENT OF PULSED HIGH-FIELD MAGNETS FOR APPLICATION IN LASER-PLASMA PHYSICS**

Dipl.-Phys. Florian Kroll

Geboren am: 09.10.1987 in Neuhaus am Rennweg

## **DISSERTATION**

zur Erlangung des akademischen Grades

## **DOCTOR RERUM NATURALIUM (DR. RER. NAT.)**

Betreuender Hochschullehrer

**Prof. Dr. Ulrich Schramm**

Eingereicht am: 15.12.2017

Die Dissertation wurde in der Zeit von 12/2011 bis 12/2017 am Institut für Strahlenphysik des Helmholtz-Zentrums Dresden – Rossendorf angefertigt.





## KURZFASSUNG

Die vorliegende Arbeit befasst sich mit der Entwicklung, Charakterisierung und experimentellen Erprobung gepulster Hochfeldmagnete für den Einsatz im Feld der Laser-Plasma-Physik. Die zentrale Aufgabe war es dabei, eine Technologieplattform zu schaffen, die es ermöglicht lasergetriebene Ionenquellen so zu beeinflussen, dass die erzeugten Teilchen für komplexe Anwendungsexperimente, wie zum Beispiel radiobiologische Zell- oder Tumorbestrahlungen, eingesetzt werden können.

Die lasergetriebene Ionenbeschleunigung im Regime der sogenannten Target Normal Sheath Acceleration (TNSA) bietet dabei den Vorteil, dass Ionen kinetische Energien von einigen 10 MeV auf einer nur Mikrometer langen Beschleunigungstrecke erreichen können. Dabei werden sehr kurze und intensive Teilchenpulse erzeugt, die sich durch ein breites, zu hohen Energien exponentiell abfallendes Spektrum auszeichnen und stark divergieren. Um die erzeugten Teilchen effektiv zu nutzen, ist es erforderlich in unmittelbarer Nähe zur Quelle Kontrolle über ihre Divergenz zu erlangen. Für die meisten Anwendungen ist es zudem vorteilhaft, die Energiebandbreite zu senken. In dieser Arbeit wird gezeigt, dass mittels der entwickelten gepulsten Hochfeldmagnete, sogenannter Solenoide (Zylinderspulen), divergente lasergetriebene Ionenstrahlen effektiv eingefangen, transportiert und fokussiert werden können. Dabei ist dank der Chromatizität der magnetischen Linse auch eine Energieauswahl möglich.

Es wurden drei an unterschiedliche Anwendungszwecke angepasste Solenoidprototypen und zugehörige Pulsstromgeneratoren entwickelt. Die Magnete erzeugen Felder von mehreren 10 T. Die Pulslängen liegen im Bereich einer Millisekunde und können als quasi-statisch für die auf ps- bis ns-Skala ablaufenden Laser-Plasma-Wechselwirkungen angesehen werden. Die hohen Felder und der Verzicht auf feldformende Magnetkerne, machen sie besonders kompakt und leicht.

Die beschriebenen Experimente konzentrieren sich auf einen gepulsten Solenoidmagneten zum Einfang divergenter laserbeschleunigter Ionen. Sie wurden am 6 MV Tandetron-Beschleuniger sowie am Laserbeschleuniger Draco des Helmholtz-Zentrums Dresden – Rossendorf und am PHELIX-Laser des GSI Helmholtzzentrums für Schwerionenforschung, Darmstadt durchgeführt. Es wird gezeigt, dass die entwickelte Technologieplattform Wegbereiter für eine Vielzahl praktischer Anwendungen der Laserteilchenbeschleunigung sein kann. Es werden Studien vorgestellt, die demonstrieren, dass lasergetriebene Ionenstrahlen effektiv in konventionelle Beschleunigerstrukturen injiziert und anschließend manipuliert werden können. Weiterhin werden erste praktische Untersuchungen zu medizinischen Strahlführungssystemen präsentiert. So ermöglichen die vorgestellten Magnete das Potenzial der oft diskutierten laserbasierten Ionenstrahltherapie von Tumorerkrankungen zu untersuchen und bemessen. Die Magnettechnologie bringt uns der Realisierung dieser ambitionierten Idee einen Schritt näher, denn sie bahnt sowohl den Weg für kompakten und effizienten Strahltransport zum Patienten als auch zu der in der Phase translationaler Forschung essentiellen Charakterisierung der radiobiologischen Eigenschaften der neuartigen Strahlungsquelle. Hierzu wurden im Rahmen der präsentierten Forschungsarbeit weltweit erste Bestrahlungsexperimente volumetrischer Tumoren im Mausmodell mittels laserbeschleunigter Protonen vorbereitet, ihre Machbarkeit untersucht und bereits erreichte radiobiologische Anforderungen sowie noch zu überwindende Hindernisse identifiziert.

## ABSTRACT

The thesis at hand addresses design, characterization and experimental testing of pulsed high-field magnets for utilization in the field of laser-plasma physics. The central task was to establish a technology platform that allows to manipulate laser-driven ion sources in a way that the accelerated ions can be used in complex application studies, e.g. radiobiological cell or tumor irradiation.

Laser-driven ion acceleration in the regime of target normal sheath acceleration (TNSA) offers the unique opportunity to accelerate particles to kinetic energies of few 10 MeV on the micrometer scale. The generated bunches are short, intense, show broad exponentially decaying energy spectra and high divergence. In order to efficiently use the generated particles, it is crucial to gain control over their divergence directly after their production. For most applications it additionally is favorable to reduce the energy spread of the beam. This work shows that the developed pulsed high-field magnets, so-called solenoids (cylindrical magnets), can efficiently capture, transport and focus laser-accelerated protons. The chromaticity of the magnetic lens thereby provides for energy selection.

Three prototype solenoids, adapted to fit different application scenarios, and associated current pulse drivers have been developed. The magnets generate fields of several 10 T. Pulse durations are of the order of one millisecond and thus the fields can be considered as quasi-static for laser-plasma interaction processes taking place on the ps- to ns-scale. Their high field strength in combination with abandoning magnetic cores make the solenoids compact and light-weight.

The presented experiments focus on a solenoid magnet designed for the capture of divergent laser-driven ion beams. They have been carried out at the 6 MV tandetron accelerator and the laser acceleration source Draco of Helmholtz-Zentrum Dresden – Rossendorf as well as at the PHELIX laser of GSI Helmholtzzentrum für Schwerionenforschung, Darmstadt. The results show that the developed technology platform breaks ground for a variety of practical applications of laser ion acceleration. It is shown that laser-driven ion beams can be efficiently injected into conventional accelerator structures to allow for phase space modulation. Furthermore, first practical studies on medical beam guidance systems are presented. Hence, the developed magnets allow to investigate feasibility and potential of the frequently proposed laser-based ion beam therapy of tumor diseases. The pulsed high-field magnets bring us one step closer to the realization of this ambitious endeavor, as they pave the way for compact and efficient beam guidance toward the patient but also, in the phase of translational research, allow to study the radiobiological properties of the novel particle source. In this context, worldwide first irradiation studies with laser-accelerated protons on volumetric tumors in the mouse model have been prepared and their feasibility studied, identifying already met radiobiological criteria and hurdles yet to overcome.

# PUBLICATIONS BY THE AUTHOR

## List of Publications by the Author

- F Kroll, J Pawelke, and L Karsch. „Preliminary investigations on the determination of three-dimensional dose distributions using scintillator blocks and optical tomography“. In: *Medical Physics* 40.8 (2013), p. 082104.  
DOI: 10.1118/1.4813898.
- B Albertazzi, J Béard, A Ciardi, T Vinci, J Albrecht, J Billette, T Burris-Mog, SN Chen, DD Silva, S Dittrich, T Herrmannsdörfer, B Hirardin, F Kroll, M Nakatsutsumi, S Nitsche, C Riconda, L Romagnagni, HP Schlenvoigt, S Simond, E Veuillot, TE Cowan, O Portugall, H Pépin, and J Fuchs. „Production of large volume, strongly magnetized laser-produced plasmas by use of pulsed external magnetic fields“. In: *Review of Scientific Instruments* 84.4 (2013), p. 043505.  
DOI: 10.1063/1.4795551.
- B Albertazzi, A Ciardi, M Nakatsutsumi, T Vinci, J Beard, R Bonito, J Billette, M Borghesi, Z Burkley, SN Chen, TE Cowan, T Herrmannsdorfer, DP Higginson, F Kroll, SA Pikuz, K Naughton, L Romagnani, C Riconda, G Revet, R Riquier, HP Schlenvoigt, IY Skobelev, AY Faenov, A Soloviev, M Huarte-Espinosa, A Frank, O Portugall, H Pepin, and J Fuchs. „Laboratory formation of a scaled protostellar jet by coaligned poloidal magnetic field“. In: *Science* 346.6207 (2014), pp. 325–328.  
DOI: 10.1126/science.1259694.
- S Busold, D Schumacher, O Deppert, C Brabetz, S Frydrych, F Kroll, M Joost, H Al-Omari, A Blažević, B Zielbauer, I Hofmann, V Bagnoud, TE Cowan, and M Roth. „Focusing and transport of high-intensity multi-MeV proton bunches from a compact laser-driven source“. In: *Physical Review Special Topics - Accelerators and Beams* 16.10 (2013).  
DOI: 10.1103/physrevstab.16.101302.
- S Busold, D Schumacher, O Deppert, C Brabetz, F Kroll, A Blažević, V Bagnoud, and M Roth. „Commissioning of a compact laser-based proton beam line for high intensity bunches around 10 MeV“. In: *Physical Review Special Topics - Accelerators and Beams* 17.3 (2014).  
DOI: 10.1103/physrevstab.17.031302.

- S Busold, A Almomani, V Bagnoud, W Barth, S Bedacht, A Blažević, O Boine-Frankenheim, C Brabetz, T Burris-Mog, T Cowan, O Deppert, M Droba, H Eickhoff, U Eisenbarth, K Harres, G Hoffmeister, I Hofmann, O Jaeckel, R Jaeger, M Joost, S Kraft, F Kroll, M Kaluza, O Kester, Z Lecz, T Merz, F Nürnberg, H Al-Omari, A Orzhekhovskaya, G Paulus, J Polz, U Ratzinger, M Roth, G Schaumann, P Schmidt, U Schramm, G Schreiber, D Schumacher, T Stoehlker, A Tauschwitz, W Vinzenz, F Wagner, S Yaramyshev, and B Zielbauer. „Shaping laser accelerated ions for future applications – The LIGHT collaboration“. In: *Nuclear Instruments and Methods in Physics Research Section A: Accelerators, Spectrometers, Detectors and Associated Equipment* 740 (2014), pp. 94–98.  
DOI: 10.1016/j.nima.2013.10.025.
- S Busold, D Schumacher, C Brabetz, D Jahn, F Kroll, O Deppert, U Schramm, TE Cowan, A Blažević, V Bagnoud, and M Roth. „Towards highest peak intensities for ultra-short MeV-range ion bunches“. In: *Scientific Reports* 5.1 (2015).  
DOI: 10.1038/srep12459.
- U Masood, M Bussmann, TE Cowan, W Enghardt, L Karsch, F Kroll, U Schramm, and J Pawelke. „A compact solution for ion beam therapy with laser accelerated protons“. In: *Applied Physics B* 117.1 (2014), pp. 41–52.  
DOI: 10.1007/s00340-014-5796-z.
- E Brambrink, S Baton, M Koenig, R Yurchak, N Bidaut, B Albertazzi, JE Cross, G Gregori, A Rigby, E Falize, A Pelka, F Kroll, S Pikuz, Y Sakawa, N Ozaki, C Kuranz, M Manuel, C Li, P Tzeferacos, and D Lamb. „Short-pulse laser-driven x-ray radiography“. In: *High Power Laser Science and Engineering* 4 (2016).  
DOI: 10.1017/hpl.2016.31.
- U Masood, TE Cowan, W Enghardt, KM Hofmann, L Karsch, F Kroll, U Schramm, JJ Wilkens, and J Pawelke. „A light-weight compact proton gantry design with a novel dose delivery system for broad-energetic laser-accelerated beams“. In: *Physics in Medicine & Biology* 62.13 (2017), pp. 5531–5555.  
DOI: 10.1088/1361-6560/aa7124.
- U Schramm, M Bussmann, A Irman, M Siebold, K Zeil, D Albach, C Bernert, S Bock, F Brack, J Branco, J Couperus, T Cowan, A Debus, C Eisenmann, M Garten, R Gebhardt, S Grams, U Helbig, A Huebl, T Kluge, A Köhler, J Krämer, S Kraft, F Kroll, M Kuntzsch, U Lehnert, M Loeser, J Metzkes, P Michel, L Obst, R Pausch, M Rehwald, R Sauerbrey, H Schlenvoigt, K Steiniger, and O Zarini. „First results with the novel petawatt laser acceleration facility in Dresden“. In: *Journal of Physics: Conference Series* 874 (2017), p. 012028.  
DOI: 10.1088/1742-6596/874/1/012028.

### The Author also Contributed to Following Inventions

- M Schürer, L Karsch, J Pawelke, J Zschetsche, and F Kroll. *Elektromagnet zur Führung von Teilchenstrahlen zur Strahlentherapie*. Patent No. DE 10 2015 200 213 A1. 2016.
- U Masood, L Karsch, J Pawelke, and F Kroll. *Einrichtung zum Abrastern mit aufgeweiteten Teilchenstrahlen*. Patent App. No. DE 10 2016 225 798.6. 2017.

# CONTENTS

|   |           |
|---|-----------|
| Kurzfassung   | 3         |
| Abstract  | 4         |
| Publications by the Author  | 5         |
| <b>1 Introduction</b>   | <b>9</b>  |
| 1.1 Motivation . . . . .  | 9         |
| 1.2 Thesis Outline . . . . .  | 13        |
| <b>2 Target Normal Sheath Acceleration</b>                                      | <b>15</b> |
| 2.1 Introduction to the TNSA Mechanism . . . . .                                | 15        |
| 2.2 TNSA Proton Sources in the Context of the Thesis . . . . .                  | 17        |
| 2.3 Conclusion . . . . .  | 21        |
| <b>3 High-field Magnet Technology for Laser-driven Plasma Physics</b>           | <b>23</b> |
| 3.1 Fundamentals of High-field Magnets and Beam Optics . . . . .                | 23        |
| 3.1.1 Types of High-field Magnets . . . . .                                     | 23        |
| 3.1.2 Introduction to the Solenoid Lens . . . . .                               | 24        |
| 3.1.3 Comparison of Focusing Optics for Laser-driven Ion Beams . . . . .        | 28        |
| 3.1.4 Pulsed High-field Magnets – Properties, Design and Construction . . . . . | 31        |
| 3.1.5 Current Pulse Generation . . . . .  | 35        |
| 3.2 Developed Pulsed High-field Magnets . . . . .                               | 37        |
| 3.2.1 Capturing Solenoid . . . . .  | 39        |
| 3.2.2 40-T-Solenoid . . . . .   | 42        |
| 3.2.3 Split-pair Solenoid . . . . .   | 46        |
| 3.3 Developed Portable Current Pulse Generators . . . . .                       | 50        |
| 3.3.1 Pulse Generator PG3 . . . . .   | 50        |
| 3.3.2 Pulse Generator PG4 . . . . .   | 53        |
| 3.3.3 Pulse Generator PG5 . . . . .   | 56        |
| <b>4 Experimental Characterization of the Capturing Solenoid</b>                | <b>59</b> |
| 4.1 Characterization at Tandetron . . . . .                                     | 59        |
| 4.1.1 Introduction . . . . .  | 59        |

## Contents

|          |  |            |
|----------|--|------------|
| 4.1.2    | Experimental Setup . . . . .   | 59         |
| 4.1.3    | Results . . . . .  | 60         |
| 4.2      | Characterization at Draco . . . . .  | 62         |
| 4.2.1    | Introduction . . . . .   | 62         |
| 4.2.2    | Experimental Setup . . . . .   | 62         |
| 4.2.3    | Results . . . . .  | 64         |
| <b>5</b> | <b>Application Studies Using the Capturing Solenoid</b>                              | <b>79</b>  |
| 5.1      | The LIGHT Beamline . . . . .   | 79         |
| 5.1.1    | Introduction . . . . .   | 79         |
| 5.1.2    | Towards Highest Proton Beam Intensities . . . . .                                    | 80         |
| 5.1.3    | Towards Application of Heavy Ion Beams . . . . .                                     | 83         |
| 5.1.4    | Conclusion . . . . .   | 85         |
| 5.2      | Functional Test of a First Pulsed Medical Beamline . . . . .                         | 86         |
| 5.2.1    | Introduction . . . . .   | 86         |
| 5.2.2    | Experimental Setup . . . . .   | 86         |
| 5.2.3    | Results . . . . .  | 88         |
| 5.2.4    | Conclusion . . . . .   | 92         |
| 5.3      | Preparation of Volumetric Tumor Irradiation with Laser-accelerated Protons . . . . . | 93         |
| 5.3.1    | Introduction . . . . .   | 93         |
| 5.3.2    | Results . . . . .  | 95         |
| 5.3.3    | Conclusion . . . . .   | 104        |
| <b>6</b> | <b>Summary and Outlook</b>   | <b>107</b> |
| <b>A</b> | <b>Laser Systems</b>   | <b>111</b> |
| <b>B</b> | <b>Derivation of the Solenoid Field</b>  | <b>113</b> |
| <b>C</b> | <b>Particle Beam Diagnostics</b>   | <b>115</b> |
| C.1      | Radiochromic Films . . . . .   | 115        |
| C.2      | Scintillators . . . . .  | 116        |
| C.3      | Thomson Parabola Spectrometer . . . . .  | 117        |
| C.4      | The Pepper-Pot Method . . . . .  | 118        |
| <b>D</b> | <b>Distances at the Draco Beamline</b>   | <b>121</b> |
| <b>E</b> | <b>Raw Data</b>  | <b>123</b> |
|          | <b>References</b>  | <b>127</b> |

# 1 INTRODUCTION

## 1.1 MOTIVATION

"Scientific discovery and scientific knowledge have been achieved only by those who have gone in pursuit of them without any practical purpose whatsoever in view [1]." This notion by Max Planck can be found in *The New Science* first published in 1959. Surely, the statement holds true for a multitude of revolutionary scientific discoveries; nonetheless, Planck diminishes the target-oriented and purposeful research that shapes our modern society. Planck writes further, "Heinrich Hertz, for instance, never dreamt that his discoveries would have been developed by Marconi and finally evolved into a system of wireless telegraphy. And Roentgen could never have called up a vision of the immense range of beneficial purpose to which the X-rays are applied today," thereby not only praising the importance of fundamental research but also indicating that scientific breakthrough also requires additional research and visionary thinking to carve out practical purpose and benefit for mankind. This type of research has been writing a success story over decades, especially but not solely in the field of medicine, where it is named translational research [2]. Magnetic resonance imaging, computer tomography, endoscopy and (Doppler) ultrasound are just a few examples where conjoint target-oriented interdisciplinary work has transferred fundamental scientific discoveries into versatile tools for physicians around the world.

An exceptionally fascinating example is the use of radioactivity and radiation for medical diagnostics and treatment. After the discovery of X-rays by Röntgen in 1895, radioactivity by Becquerel in 1896 and Radium by the Curies in 1898, within barely a decade radiological societies formed, scientific journals were established and X-ray imaging and radiotherapy developed [3]. In the following decades the technologies advanced and health care benefits grew. In 1946 American physicist Robert Wilson was the first to recognize the potential of protons as alternative to X-rays in radiotherapy. Protons show an inverse depth dose profile when passing through matter. At shallow depths the dose is considerably lower than at the end of the particle trajectory, where, after the so-called Bragg peak, a steep dose fall-off follows. Wilson's idea was to make use of the proton inherent interaction characteristics to improve the dose distribution delivered to the tumor in radiotherapy. The inverted dose profile allows for sparing healthy tissue in front of the tumor and the steep distal edge helps to prevent irradiation of organs at risk. The generation of protons with sufficiently high kinetic energy, i.e. above 200 MeV for reaching deep seated tumors, then and now requires highest technological efforts. Wilson's proposal led to a first treatment in 1958 at Lawrence Berkeley

## 1.1 Motivation

National Laboratory using the proton cyclotron developed under the lead of Lawrence in the 30's [4]. Later on, cancer treatment using heavier ions, such as helium but especially carbon, was established.

Modern proton or in general ion beam therapy (IBT) machines, consisting of particle source, accelerator and beam transport, make special demands on building construction and infrastructure [5, 6]. They require large-scale facilities and are still costly. As a result, their size and cost limit the wide-spread of the novel treatment technique. To date (last update: November 2017), there are only 66 radiotherapy facilities world-wide that offer proton irradiation and additional 11 centers equipped for carbon ion therapy [7] – a minuscule number in comparison to X-ray therapy.

The advantageous physical properties of proton and heavy ion beams carry the great potential to improve treatment outcome for specific tumor entities and a considerable number of radiotherapy patients. All the potential pros and cons of proton and carbon ion therapy cannot be discussed here; the interested reader may be referred to the literature [8–12]. IBT is still undergoing research and possible benefits are not yet fully demonstrated nor quantified. Finding proof for significant beneficial qualities is a cumbersome but necessary task that requires extensive radiological long-term studies at numerous IBT centers around the world. Both clinical as well as technological advances are necessary to reduce cost and size, to justify further erection of such centers and to finally end the struggle for quantifying the efficacy of proton and ion beam therapy. However, the low number of operational IBT facilities limits the necessary scientific and technological innovation, resulting in a vicious circle intricate to overcome.

In a field where so many professions convene, a goal-oriented translational research approach might be the only driver of the innovation process. Interdisciplinarity is key. Because, how should a physicist or engineer improve a technology if he does not understand its clinical limitations? He relies on an active information exchange with clinicians. Therefore, it is absolutely necessary to pursue the goal of finding and providing the perfect treatment modalities for the patient within a strong multidisciplinary collaboration. Of course, the target-oriented translational research is by no means a guarantor for success. It also needs to be critically discussed as in Baumann et al. [2] because one needs to remember, that the road to a groundbreaking scientific discovery can be as bumpy as the road to its utilization. There can be setbacks and show-stoppers, but also novel and unpredicted discoveries wait along the way. So, if Planck's statement should teach us one thing, then that research is never futile.

Within the German joint research project onCOOPtics<sup>1</sup>, a multidisciplinary team of physicists, medical physicists, radiobiologists, technicians and engineers with close connection to clinical research and infrastructure is pursuing the goal to make ion beam therapy compact and more affordable by conducting translational research that builds on a great scientific discovery - Laser-driven ion acceleration: High-power lasers are able to trigger plasma processes that enable acceleration of ion bunches with unique properties. As an example, the Titanium-Sapphire dual beam laser Draco of Helmholtz-Zentrum Dresden – Rossendorf (HZDR) is constructed to generate 30 fs short light pulses of 800 nm central wavelength and 3 to 30 J pulse energy, thus reaching the PW (i.e.  $10^{15}$  W) power level. Focused onto thin foils to micrometer spot sizes, relativistic intensities in excess of  $10^{21}$  W cm<sup>-2</sup> are reached that trigger ion acceleration processes. The generated accelerating field gradients are up to six orders

---

<sup>1</sup>onCOOPtics is formed by the collaboration partners Helmholtz-Zentrum Dresden – Rossendorf (HZDR) and two Centers for Innovation Competence, OncoRay, Dresden and ultra optics, Jena

of magnitude higher than in conventional accelerators, i.e.  $\text{TV m}^{-1}$  in comparison to  $\text{MV m}^{-1}$ . Multi-MeV ion acceleration becomes possible on a  $\mu\text{m}$  scale [13, 14]. Protons (originating from hydrocarbon layers on the target surface) are accelerated in highest number ( $10^{11}$  to  $10^{13}$ ). The ps long bunches exhibit large divergence angles (approx.  $20^\circ$  half angle) and a broad, exponentially decaying energy spectrum with cut-off at high energies [15].

The discovery of laser-driven ion acceleration gave rise to the idea of IBT by means of these novel particle sources instead of a conventional source coupled to an accelerator like a cyclotron (most common for protons) or synchrotron (for carbon ions). Thereby, the acceleration length can be reduced by orders of magnitude. Anyhow, complexity, size and cost of an IBT facility are not only predetermined by the accelerator, also the beam transport towards the patient, radiation shielding and in general building construction are equally important to consider for optimization. Therefore, the onCOOPTics collaboration is working on a holistic concept for a laser-driven ion beam facility and performs leading multidisciplinary research that ranges from laser development [16–18] and fundamental investigation of laser acceleration [19–21] over detector development and dosimetry [22–25] to radiobiology [26–32] and medical beam transport [33, 34]. With respect to the over-all size and complexity of IBT facilities, the proposed concept offers the following potential improvements besides the laser-driven source: First, a laser beam can be transported without magnetic beam guidance elements and without large scale radiation shielding. Thus, by generating the ionizing radiation that is used for the treatment in close vicinity to the patient, magnetic transfer lines and radiation shielding between accelerator and treatment bunker become obsolete. Of course, one laser could be provided to several treatment rooms via optical transfer lines. Second, the most sophisticated IBT systems employ rotational devices, so-called gantries, to guide the particles towards the patient and shape the irradiation field. The rotatability of the gantry grants physician and medical physicist control over the irradiation direction and full flexibility for the cancer treatment. Typical proton gantries reach diameters of approximately 10 m and weigh about 100 t.<sup>2</sup> Nevertheless, maintaining sub-millimeter positioning accuracy is crucial. All these facts demonstrate how large and costly gantry systems for IBT can be.

Under the proposition of making use of the pulsed nature of the laser-driven source, it is possible to combine the pulsed source with equally pulsed high-field magnets as particle beam optics. For short times in the range of ms these magnets can reach fields at least one order of magnitude higher than conventional electro- or permanent magnets. The size of a gantry system employing high-field magnets could be reduced by a factor of 2–3 compared to conventional gantry systems [33], as higher fields allow for efficient particle transport with smaller bending radii and shorter particle drift spaces. Furthermore, abandoning iron yokes makes the system not only compact, but also considerably lighter. A concept study of such a compact gantry system is depicted in fig. 1.1.

The concept goes even further. It aims to make use of broad parts of the energy spectrum of the laser-driven proton source for conformal dose delivery. In this manner, the generated particles are used more efficiently and treatment times would remain short. Based on this idea, novel dose delivery schemes as well as treatment planning systems are under investigation [34].

To give a balanced picture, it may be noted that conventional IBT technology is still a rapidly evolving field. Increasing demand and commercial competition stimulate research and devel-

---

<sup>2</sup>Currently there is only one gantry system for carbon ions at the Heidelberg Ion-Beam Therapy Center (HIT). HIT describes the gantry as follows: "The gantry at HIT is a gigantic steel construction. It is 25 meters long, 13 meters in diameter and weighs 670 tons, of which 600 tons can be rotated with submillimeter precision [35]."

## 1.1 Motivation

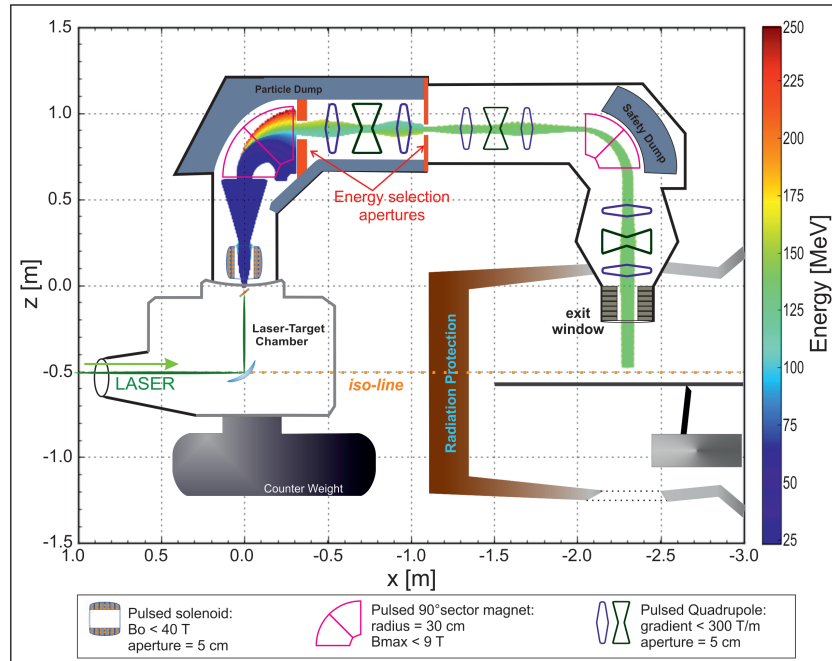


Figure 1.1: Sketch of a gantry concept developed for guiding laser-accelerated protons by means of pulsed high-field magnets. The gantry can circle the patient (right side). The rotation axis is given by the iso-line. The color-coded particle trajectories originate from beam tracing simulation. For a more detailed discussion see Masood et al. [33].

opment and make IBT facilities more compact, affordable and attractive even for smaller clinics. Today, many vendors, e.g. Varian, Mevion, Ion Beam Application (IBA) or Protom, offer turn-key IBT systems. Superconducting technology is reducing the size of accelerators. Even first super-conducting gantry systems for proton and heavy ion therapy are under preparation [36, 37]. A notably critical, yet not fully objective discussion on laser acceleration in the context of current advances in IBT technology can be found in Linz and Alonso [38].

In this regard, it is of highest importance for the scientific community not to praise laser acceleration as the "redeemer of radiotherapy" before the feasibility of a laser-driven IBT solution has been demonstrated and its potential fully evaluated. The presented work can be seen a steppingstone towards the quantification of this potential or the potential for any other application that requires a high amount of control over the beam. Essential components for gaining control can be pulsed high-field magnets tailored for utilization in the field of laser-plasma physics.

In the framework of this thesis, three pulsed high-field magnet prototypes and dedicated pulsed power current sources were developed, characterized and employed in multiple experimental campaigns. The versatile, scalable technology platform that was built up is centered around pulsed solenoids. These cylindrical magnets carry the potential to become the crucial link between discovery and application of laser-driven ion sources as they are able to efficiently capture, transport and focus their highly divergent beams. They prevent particle loss and allow for gaining control over important beam properties, such as beam divergence, energy spread and energy distribution while still maintaining compact measures due to their

high field amplitude. A pulsed high-field solenoid is therefore considered to be a well-suited first beam transport element in a medical gantry for laser-driven ion beams. The magnets designed and used in this work are forerunners when it comes to "taming" a laser-driven ion source, yet a full-scale gantry requires at least two further magnet types (cf. fig. 1.1), namely dipole bending magnets and quadrupoles. The work briefly touches their challenging development and application while the focus remains on the solenoids.

In comparison to previous studies employing pulsed high-field solenoids for beam transport, i.e. Harres et al. [39], Harres [40], Burris-Mog et al. [41], Burris-Mog [42], Busold et al. [43–46], and Busold [47],<sup>3</sup> this thesis is the first work that also treats practical research on high-field beam transport for medical (gantry development) and radiobiological (in vivo tumor irradiation) purposes. The work at hand provides further significant technological and scientific improvements: The developed magnets and pulse generators allow for the production of fields at least twofold higher than previously applied. Hence, they allow for higher capture efficiencies and can focus (or collimate) particles that are more energetic. The scalability of the entire technology platform towards even higher field strengths has been investigated and was deemed possible. The described magnets are safer and more compact due to an improved housing concept. The beam optical characterizations both at conventional and laser-driven proton sources go further as previously investigated and include new approaches such as the pepper-pot method. The work of Busold et al. [43–46] and Busold [47], that focuses on injecting laser-driven proton beams into a conventional accelerator structure for phase space manipulation, has been continued. Improvements with regard to the utilizable beam flux as well as the number of utilizable ion species could be achieved. These advances are complemented by completely new scientific studies and technological approaches. Two novel magnet prototypes enable a multitude of fundamental and application studies aside from translational medical research. They allow to experimentally investigate astrophysical processes in the laboratory and manipulate laser-driven particle sources with highest fields directly at target position. The following outline summarizes the multifaceted magnet development and experiments conducted within the scope of this thesis.

## 1.2 THESIS OUTLINE

The following chapter, chapter 2, gives a brief introduction to the principle mechanisms of target normal sheath acceleration (TNSA). The properties of ion beams originating from relativistic laser-target interactions are discussed and exemplary source parameters are given for the laser accelerators used in this work.

In chapter 3 follows an elaborate discussion on magnet technology that can provide control over the laser-driven source. It is shown that pulsed high-field magnets, and in particular pulsed solenoids, are the most suitable type of high-field magnet for this purpose. An explanation on how a solenoid acts as a charged particle lens follows. Pros and cons of their beam optical properties are critically discussed and concluded by a comparison of different approaches to capture and control laser-accelerated ions. After an introduction to the technological basics of pulsed high-field magnets and current sources, the developed solenoid prototypes and pulsed power drivers are presented. Their specific properties are put into

---

<sup>3</sup>With the exception of Harres et al. [39] and Harres [40], who used a coil from a disassembled Faraday rotator, all previous studies employ pulsed high-field solenoids similar in construction to the one studied in this work and fabricated by the high-field laboratory of HZDR.

## 1.2 Thesis Outline

context with state-of-the-art technology employed in high-field laboratories, highlighting differences and adaptations.

Chapter 4 focuses on the experimental characterization of a pulsed high-field solenoid. It begins with a description of a beam transport study carried out using proton beams from a conventional tandemron accelerator. Then the same magnet has been employed at the laser accelerator Draco. Beam transport properties are derived and discussed in the context of the reference experiments at the tandemron.

Finally, the thesis is concluded by chapter 5 on application of the characterized pulsed magnet. Besides the clear focus of this thesis on translational medical research, a small excursion to more fundamental accelerator research and development marks the beginning of the chapter and highlights the versatility of the developed technology. Subsequently, beam transport studies with a first pulsed high-field beamline for future medical application are discussed. The chapter ends with the presentation of experimental findings that assess the feasibility of a world-wide first radiobiological study with laser-driven proton beams on an in vivo tumor model employing up to two pulsed solenoids.

The experimental findings are summarized in chapter 6 and complemented by an outlook on technological and experimental advancements to be sought in the future.

## 2 TARGET NORMAL SHEATH ACCELERATION

### 2.1 INTRODUCTION TO THE TNSA MECHANISM

The most extensively studied laser-based acceleration mechanism is Target Normal Sheath Acceleration (TNSA) [15, 48].<sup>1</sup> A complete explanation of the relativistic laser-target interaction processes as well as resulting complex plasma dynamics is beyond the scope of this study. The TNSA process shall therefore be introduced only briefly and in a figurative manner. The interested reader may be referred to books, such as Gibbon [50], Mulser and Bauer [51], and Macchi [52], or review articles like Mora [53], Perego et al. [54], and Daido, Nishiuchi, and Pirozhkov [55]. The process is depicted schematically in fig. 2.1 and shall be explained in the following in accordance to the given literature.

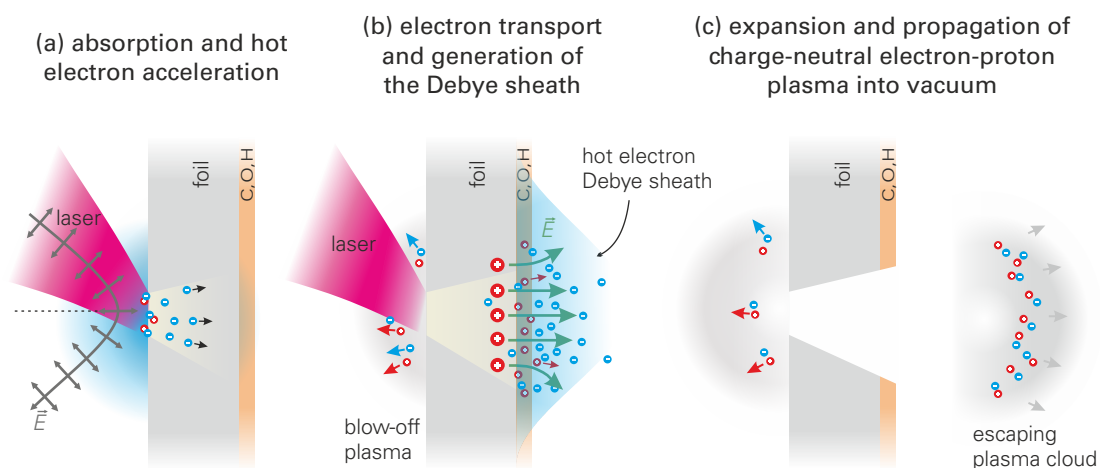


Figure 2.1: Sketch of ion acceleration via Target Normal Sheath Acceleration (TNSA), electrons are depicted in blue, (positive) ions in red. For explanation see text.

<sup>1</sup>Other acceleration mechanisms under investigation are for example Radiation Pressure Acceleration (RPA), the Break Out Afterburner (BOA), Hole Boring (HB) or Shock Acceleration, see Borghesi [49] and references therein.

**Absorption and hot electron acceleration (cf. fig. 2.1(a)):** TNSA relies on high-power short-pulse lasers focused onto  $\mu\text{m}$ -thin solid targets, commonly metal foils. The lasers, e.g. Draco of HZDR (see appendix A), are operated at peak powers ranging from several 10 TW to PW, i.e.  $10^{15}$  W, and pulse lengths of few 10 to several 100 fs. When focused down to a  $\mu\text{m}$  spot size typical laser accelerators reach intensities of  $10^{18}$  to  $10^{21}$   $\text{Wcm}^{-2}$ . The ionization threshold of the target is of the order of  $10^{12}$  to  $10^{13}$   $\text{Wcm}^{-2}$ . In fact, this threshold is typically already exceeded before the main laser pulse arrives, e.g. by pre-pulses or amplified spontaneous emission generated in the laser chain. The main laser pulse (in most cases impinging p-polarized and under an angle) therefore interacts with the already ionized target front side, i.e. the so-called pre-plasma. The laser can only propagate in the underdense region of the plasma, where the electron plasma frequency  $\omega_P$  is smaller than the laser frequency  $\omega_L$ . Reaching the critical density  $n_c$ , where  $\omega_P = \omega_L$ , the laser can only evanescently penetrate further and is reflected. The direct acceleration of the inert target ions in the laser field cannot be achieved by current lasers. Instead the ion acceleration is result of secondary accelerating fields generated by hot electrons. The laser energy is partially transferred to the plasma electrons in a process called electron heating. They are accelerated to mean kinetic energies  $k_B T_e$  of few MeV. Here  $k_B$  denotes the Boltzmann constant and  $T_e$  the electron temperature. In dependence of pre-plasma conditions (density gradient) different energy absorption mechanisms give rise to a net-energy gain, predominantly resonance absorption, Brunel heating and  $\vec{j} \times \vec{B}$  heating (see literature given above). Electrons start to penetrate the target material.

**Electron transport and generation of the Debye sheath (cf. fig. 2.1(b)):** As the accelerated electrons travel through the target material they ionize the bulk but are shielded due to the presence of the cold target electrons. Upon leaving the foil at its rear surface, the shielding effect vanishes and they are attracted by the positive charge of the target ions. As consequence, the electrons begin to oscillate back and forth through the target.<sup>2</sup> This behavior leads to the formation of a quasi-static hot electron sheath at target front and back with an average extension of one Debye length

$$\lambda_D = \sqrt{\frac{\epsilon_0 k_B T_e}{n_e e^2}}. \quad (2.1)$$

Here  $n_e$  denotes the hot electron density and  $\epsilon_0$  the vacuum permittivity. In plasma physics, the Debye length  $\lambda_D$  is a characteristic distance over which a discrete charge is screened by the plasma (here in the  $\mu\text{m}$ -range). The charge separation leads to the formation of a strong electric field of the order of  $\text{TV m}^{-1}$  that can field ionize atoms at the target surfaces.

**Expansion and propagation of charge-neutral electron-proton plasma into vacuum (cf. fig. 2.1(c)):** Target ions and ions originating from the contaminant layer that is present on the target surfaces under typical vacuum conditions ( $10^{-5}$  to  $10^{-6}$  mbar) are accelerated by the quasi-static field of the electron sheath. Protons (originating from named hydrocarbon contaminant layers) are accelerated most efficiently due to their high charge to mass ratio. The acceleration performance for heavier ions like carbon, oxygen or the target material (titanium, aluminum, gold, etc.) is limited as the protons screen the electric fields. The protons

<sup>2</sup>In fact, recirculating electrons can again interact with the laser field on the target front side if the laser pulse is still acting on the target when the electrons arrive.

expand together with the electrons as a charge-neutral plasma cloud in target normal direction with kinetic energies of up to several 10 MeV. For ultra-short laser pulses, i.e. laser pulse lengths in the range of 30 fs, that impinge obliquely on the target a prominent non-target-normal emission of energetic protons favoring the laser-forward direction has been observed (cf. fig. 2.2) [14]. The number of protons measured at the target rear is in the range of  $10^{11}$  to  $10^{13}$  and thus unprecedented by conventional accelerator technology. The bunches are temporally very short, in the range of ps. They show large divergence angles (approx.  $20^\circ$  half angle), yet are generated with ultra-low emittance. Finally, they exhibit a broad, exponentially decaying energy spectrum with cut-off at high energies [13–15, 48, 56].

The cut-off energy is a very important measure for the performance of a laser accelerator. The laser acceleration community strives for ever-new record ion energies, in order to open up novel possibilities for application and fundamental research. The highest proton energy recorded in a laser acceleration experiment to date (December 2017) is 85 MeV by Wagner et al. [57] using the PHELIX laser at GSI Helmholtzzentrum für Schwerionenforschung, Darmstadt. To understand and actively manipulate the conversion from laser energy to particle energy is thereby the greatest challenge in the field. The influencing parameters are numerous, theoretical and experimental investigations therefore very complex. In the following list, some important factors that influence the acceleration performance are named. The interested reader may be referred to the literature cited above for in-depth discussion.

- **Target parameters influencing TNSA are:** thickness, material composition (density, conductivity, ionization threshold, etc.), lateral dimension, geometry, surface structure, etc.
- **Laser parameters influencing TNSA are:** energy and focal spot size (i.e. intensity) on target, beam profile, wavelength, pulse length, temporal contrast, polarization, spatial chirp, etc.

## 2.2 TNSA PROTON SOURCES IN THE CONTEXT OF THE THESIS

After the general explanation above, this section specifically addresses the TNSA-based proton sources that were used throughout this thesis. Three different laser systems were applied in the presented study: Draco TW, Draco PW of Helmholtz-Zentrum Dresden – Rossendorf (HZDR) and PHELIX (Z6) of GSI Helmholtzzentrum für Schwerionenforschung, Darmstadt (see appendix A for a summary of important properties and parameters of the laser systems). The following description on source characterization focuses on Draco PW. Differences with respect to the other sources are given where necessary.

During the course of this thesis' work, the Ti:sapphire laser system Draco of HZDR underwent an upgrade and was transformed from a single-beam facility operating at 150 TW to a dual-beam facility able to simultaneously provide a 150 TW (Draco TW) as well as a 1 PW (Draco PW) beam for experimentation [58]. Scaling models predict that an increase in laser power  $P_L$  is followed by an increase in maximum kinetic energy  $E_{\max}$  of the TNSA protons [59–62]. The scaling of the maximum proton energy with laser power can be roughly described by  $E_{\max} \propto \sqrt{P_L}$ , yet for ultra-short pulse lasers, i.e. lasers with pulse lengths of few 10 fs such as Draco, the scaling becomes linear, i.e.  $E_{\max} \propto P_L$  [13]. These scaling predictions are the reason why laser facilities around the world are erected and upgraded (see for example [63–65]), as the efforts to break new scientific ground promote laser development

## 2.2 TNSA Proton Sources in the Context of the Thesis

and vice versa. The exploration of novel, more powerful laser architectures is at an all-time high, both in commercial as well as scientific research and development.

As important part of this thesis, first commissioning experiments on the upgraded Draco laser system have been performed. The experiments have been conducted with slightly reduced laser power on target,  $P_L \approx 600$  TW.

At the example of these experiment at Draco PW, it shall be briefly explained how the parameters of a laser-driven proton source have been determined and monitored throughout the work of this thesis. More detailed discussions follow in section 4.2.1.

Inside of the evacuated target chamber ( $10^{-5}$  to  $10^{-6}$  mbar) the Draco PW beam is focused by means of an off-axis parabolic mirror onto a metallic foil target (mostly titanium, Ti) of  $\mu\text{m}$  thickness. Protons are accelerated and emitted from the target rear side in normal direction. The properties of the generated pulsed proton beam (or bunch) are measured by online and offline diagnostics systems at different positions downstream of the laser target (also see fig. 4.3). Typical detector systems in the field of laser-driven ion acceleration include radiochromic films (RCF) for retrospective analyses of proton number, energy and beam profile (cf. appendix C.1); scintillation detectors giving immediate information on beam profile and/or energy (cf. appendix C.2) and the Thomson parabola spectrometer (TPS), an online tool for determining proton spectra and cut-off energies (cf. appendix C.3). In general, these diagnostics cannot be used simultaneously. The online diagnostics are typically used to optimize and monitor the laser acceleration performance on a regular basis, while the radiochromic film stacks allow for precise absolute evaluation of beam parameters after completion of the experiment. Figure 2.2 summarizes the findings of the commissioning experiments and shows that the RCF data can be used to determine angular distribution and energy spectrum of the laser-accelerated proton bunches. The Thomson parabola spectrometer is especially useful for regular verification of the proton cut-off energy.

The key plot, fig. 2.2(a) in the lower left, compares cut-off energies of generated proton spectra (measured via RCF stacks) with a theoretical proton scaling prediction in accordance to Kluge et al. [66]. From the plot we see that the increased laser power of Draco PW yields significantly higher maximum proton energies (green squares) in comparison to Draco TW (blue squares). In fact, proton energies above 40 MeV have been recorded. The scaling prediction is well reproduced by the previously obtained data at Draco TW. On the other hand, Draco PW data points remain below the expectation. This behavior was attributed to the preliminary laser-conditions in the commissioning phase. Improvements, especially on temporal contrast and compression, are ongoing as the team is eager to close the gap.

The scaling plot also illustrates energy ranges associated with certain radiobiological or radiological applications of (laser-driven) proton beams. The lower area (5 to 20 MeV, depicted in red) marks the energy range where in vitro cell irradiation studies can be performed (cf. [26, 27, 67–69]). Above 20 MeV in vivo studies in small animal models become feasible (yellow). Kinetic energies in excess of 200 MeV mark the threshold for application of proton beams for deep seated tumor treatment in men (green). It can be seen that the increase in proton energy, owing to the Draco PW beam, opens up new experimental opportunities for laser-based radiobiology studies, as it breaks the barrier for small animal experiments. These studies are necessary to quantify the radiobiological effectiveness of the high dose-rate beams originating from laser acceleration sources. As such, they are a crucial step along the translational research track. In conclusion, the successfully performed laser upgrade and commissioning experiment were prerequisites for a key part of this work, i.e. the preparatory studies for a controlled in vivo tumor irradiation with laser-driven protons.

Figure 2.2 characterizes the typical Draco PW proton source further. Figure 2.2(b) shows

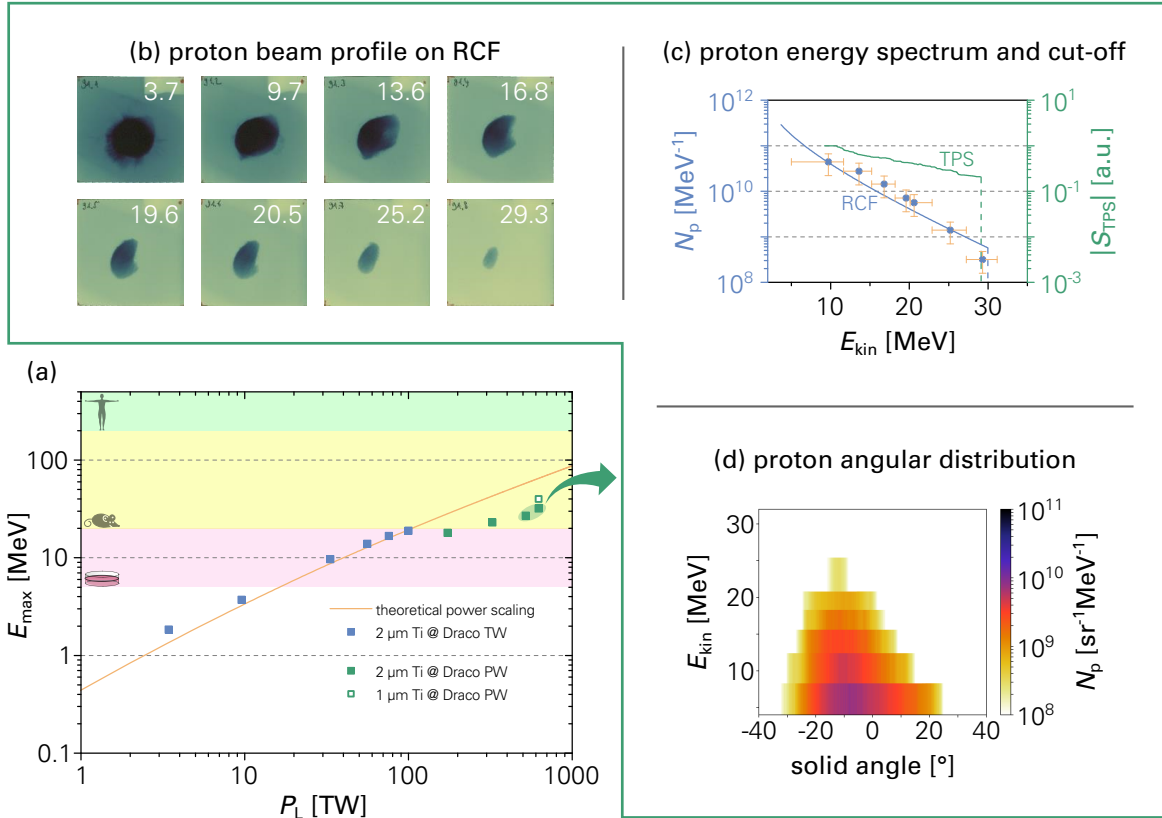


Figure 2.2: TNSA source parameters and power scaling at the Draco laser facility, see text for further details: (a) Comparison of theoretical power scaling with maximum proton energies  $E_{\max}$  measured at Draco TW/PW; energy ranges associated with radiobiological/radiological applications pictographically illustrated. (b,c,d) Proton source parameters for a typical 600 TW Draco laser pulse (see arrow). (b) Radiochromic film (RCF) stack; corresponding Bragg peak energies (in MeV) given in white; 2  $\mu\text{m}$  Ti target with 1  $\mu\text{m}$  photoresist rear side coating (acting as proton donor). (c) Proton spectrum ( $N_p$  is proton number) obtained from RCF stack depicted in (b) and compared to normalized signal  $|S_{\text{TPS}}|$  from Thomson parabola spectrometer (TPS); differences in curve slope explained in text. (d) Angular proton distribution as function of the kinetic energy  $E_{\text{kin}}$ ; extracted from RCF stack; 2  $\mu\text{m}$  pure Ti target, laser impinging under  $45^\circ$ .

## 2.2 TNSA Proton Sources in the Context of the Thesis

an RCF stack that images the homogeneous two-dimensional lateral beam profile of the TNSA bunch. The RCF data was used to extract the reference energy spectrum (blue curve) depicted in fig. 2.2(c). A fit of the deconvoluted discrete RCF data (blue circles) according to the formula

$$\frac{dN_p}{dE_{\text{kin}}} = \frac{N_0}{E_{\text{kin}}} e^{-\frac{E_{\text{kin}}}{k_B T_e}}, \quad (2.2)$$

with proton number  $N_p$  and kinetic energy  $E_{\text{kin}}$  and fit parameters  $N_0$  and  $k_B T_e$ , yielded the shown curve. Fit parameters and typical cut-off energies for the presented spectrum as well as for representative spectra of Draco TW and PHELIX have been determined to

$$\text{Draco PW:} \quad N_0 = 1.9 \cdot 10^{12} \quad k_B T_e = 6.4 \text{ MeV} \quad E_{\text{max}} \approx 30 \text{ MeV} \quad (2.3)$$

$$\text{Draco TW:} \quad N_0 = 2.3 \cdot 10^{11} \quad k_B T_e = 3.1 \text{ MeV} \quad E_{\text{max}} \approx 15 \text{ MeV} \quad (2.4)$$

$$\text{PHELIX:} \quad N_0 = 10^{11} \quad k_B T_e = 4 \text{ MeV} \quad E_{\text{max}} \approx 28 \text{ MeV} \quad (2.5)$$

The corresponding spectra are only exemplary and may change over the course of an experimental campaign or even on a shot-to-shot basis. They have been evaluated to serve as conservative estimate of particle numbers at given energy intervals as will be explained in later chapters. In all experiments at the Draco laser, the energy spectrum and especially the cut-off energy of the spectrum is regularly monitored by Thomson parabola spectrometer measurements (see green curve in fig. 2.2(c)).

The consecutively measured proton energy spectra from RCF and TPS exhibit different shapes, yet the agreement with respect to the cut-off energy has been proven to be very reliable. The TPS data shows higher particle numbers towards the cut-off. On the one hand, this may be attributed to the interaction properties between the broad-energetic proton bunch and the TPS particle detector, a micro-channel plate. On the other hand, the TPS measures only a small fraction of protons in the center of the generated particle distribution, namely a solid angles of the order of few  $100 \mu\text{sr}$ . In TNSA the emission of more energetic particles is peaked in forward direction, thus the number of protons at the high end of the spectrum is proportionately increased, while lower energy protons are emitted with a broader divergence. This behavior is reflected by fig. 2.2(d), showing a typical angular distribution of a TNSA proton bunch. Clearly visible is the upper mentioned enhanced emission in laser forward direction for ultra-short pulse lasers (cf. [14]). The non-normal emission can be counterbalanced by rotating the target a few degrees.<sup>3</sup>

Following the above description, it becomes clear that the performance of any beam transport system applied to a laser acceleration source is strongly affected by changing source parameters. As the energy spectrum changes, so does the angular distribution of the particles. Hence, the acceptance or transport efficiency of the beam transport system is altered. In order to allow for comparing experimental data obtained under different experiment conditions, i.e. at different laser acceleration facilities, across different experimental campaigns or just at different times of day, it is essential to regularly monitor the source characteristics.

In this thesis, the presented data will therefore always include detailed descriptions on laser, target and ion source parameters. Some parameters, such as the cut-off energy of the spectrum, cannot be measured on-shot without impairing the main study. In this case, con-

<sup>3</sup> The principle characteristics of angular proton beam distribution are the same for Draco TW and PHELIX with the exception that the non-normal emission is not present for the PHELIX-driven source, see Busold [47].

servative estimates are given which have been derived from measurements shortly before and/or after the main experiment.

## 2.3 CONCLUSION

In conclusion, due to the small acceleration length as well as the unmatched properties of laser-accelerated ion beams, i.e. highest flux and shortest bunch lengths, a variety of applications has been proposed over the last years for these novel particle sources [55]. The constant pursuit of reaching higher ion energies is enabled by on-going laser development and gained knowledge about the complex laser-target interaction mechanisms. Potential applications that are currently investigated range from fast ignition in inertial confinement fusion [70], warm dense matter research [71] and radiography of transient phenomena [72, 73] to isotope production [74], compact neutron sources [75, 76] and, the formerly introduced, laser-driven ion beam therapy of cancer.

Most named applications can only be realized when the uniquely high intensity of the laser-driven bunches is preserved and simultaneously control over their angular divergence and energy distribution is gained. The following chapter describes the technological development of pulsed high-field solenoid magnets and associated pulsed power equipment that poses as missing link between the fundamental laser acceleration processes and their application, as they provide for named control while preserving beam intensity.



# 3 HIGH-FIELD MAGNET TECHNOLOGY FOR LASER-DRIVEN PLASMA PHYSICS

This chapter focuses on the description of the technological platform that has been established within the framework of this thesis. After an introduction to basic principles of pulsed magnet development and operation as well as current pulse generation follows an elaborate discussion on magnet prototypes and pulse generators. In this context, it will be shown how the magnet prototypes and corresponding pulse generators were specifically designed, manufactured and tested to meet the demands of a variety of plasma physical experiment scenarios, i.e. capture and transport of laser-accelerated ion beams, TNSA experiments in external magnetic fields and manipulation of plasma flows to study astrophysical phenomena.

## 3.1 FUNDAMENTALS OF HIGH-FIELD MAGNETS AND BEAM OPTICS

### 3.1.1 TYPES OF HIGH-FIELD MAGNETS

The physical properties of permanent magnets and the saturation of core materials, e.g. iron, limit their achievable field strengths to values typically lower than 2 T. In order to systematically study electronic properties of super-, semi- and metallic conductors higher field strengths are required. Over decades, high-field laboratories, such as the Dresden High Magnetic Field Laboratory (HLD) at Helmholtz-Zentrum Dresden – Rossendorf (HZDR), have developed magnet technology to reach ever increasing field strengths to make new scientific discoveries possible. There are four principle types of magnets that are operated by high-field laboratories around the world:

First, DC air-core electromagnets, made from normal conducting materials and powered by enormous generators. They can provide static fields of several 10 T [77]. Thermal dissipation requires continuous cooling. Typically, these magnets are so-called Bitter magnets consisting of stacked perforated conductor disks separated by thin paper-like insulation. The coolant flows through the perforation holes of the aligned disks. DC Bitter magnets make high demands on power-supply and cooling infrastructure.

Second, DC superconducting magnets also allow for static field generation up to about 20 T [78]. They are wire wound and embedded in a cryogenic vessel typically cooled to liquid

### 3.1 Fundamentals of High-field Magnets and Beam Optics

helium temperature. To prevent quenching, changes in magnetic field amplitude need to be performed slowly.

The third type of magnet is the destructive pulsed high-field magnet. They can be wire wound or milled from a solid conductor block. In the simplest case a single winding can be used. A pulsed source drives currents up to the MA-level through the magnet. Even a single turn magnet can thereby easily reach fields of several 100 T but is destroyed (ripped apart, evaporated or transformed into plasma) during the pulse [79]. The examined sample usually is also damaged or destroyed. Therefore, the analyses of the sample properties need to be performed during the magnet pulse. Experimentalists have gone so far, they placed explosives around a magnetic coil to compress the magnetic flux inside the coil when both magnet and explosion are triggered simultaneously. This so-called explosion-driven flux compression can provide kT-fields [80].

The fourth and last type of magnet is the non-destructive pulsed high-field magnet. This magnets is typically wire wound and of cylindrical shape, a so-called solenoid. The race for reaching the highest non-destructive fields is a constant driver for technological and scientific innovation. At the moment the highest non-destructive fields can be generated by the Dresden High Magnetic Field Laboratory at HZDR, Dresden, Germany and the National Magnetic Field Laboratory, Tallahassee, USA with 94.2 T and 100 T respectively [81, 82]. The electromagnets are typically powered by capacitor-based current pulse generators with MW peak power but very low average power since the magnets are operated at low pulse repetition rates ( $\approx 1 \text{ h}^{-1}$ ). The magnets are often placed in a Dewar vessel and cooled to liquid nitrogen temperature before the current pulse. During a single pulse they are heated up to room temperature or above.

The adoption of the upper mentioned magnet technologies to manipulate laser-driven plasma or particle sources is especially promising for the last type of magnet, as will be shown below. The pulsed nature of the plasma or particle source is well matched. Down-scaled magnets can be operated at higher-repetition rates ( $\approx 1 \text{ min}^{-1}$ ) even without active cooling. On the other hand, demanding power supply and cooling infrastructures, restricted field variation rates and destructive properties limit the applicability of the first three technologies. In the following two sections, the question, whether a non-destructive high-field magnet can be a useful device for charged particle transport, will be answered. Therefore, it will be discussed how solenoid fields can act as lens for charged particle beams. Thereafter, the high-field solenoid lens is critically compared to other state-of-the art technologies for beam capture.

#### 3.1.2 INTRODUCTION TO THE SOLENOID LENS

The focusing of charged particle beams traversing a solenoid magnet is typically treated in textbooks by applying Busch's theorem [83] of the conservation of canonical angular momentum in the solenoid's field. In comparison to the formal derivation, for example in Reiser [84], a graphically descriptive approach by Kumar [85] is presented in an adapted form in the following to explain the basic principles of solenoidal focusing.

The symmetry of a solenoid allows to describe its field by a radial component  $B_r(r, z)$  and an axial component  $B_z(r, z)$ . The derivation of the magnetic field of a solenoid surrounded by air or vacuum, i.e. relative permeability  $\mu_r = 1$ , can be found in appendix B. For the axial

component one finds the series representation

$$B_z(r, z) = \sum_{n=0}^{\infty} \frac{(-1)^n}{(n!)^2} B^{(2n)} \left( \frac{r}{2} \right)^{2n} = B(z) - \frac{r^2}{4} B''(z) + \dots \quad (3.1)$$

and

$$B_r(r, z) = \sum_{n=1}^{\infty} \frac{(-1)^n}{n!(n-1)!} B^{(2n-1)} \left( \frac{r}{2} \right)^{2n-1} = -\frac{r}{2} B'(z) + \frac{r^3}{16} B'''(z) + \dots, \quad (3.2)$$

for the radial component. Here, the prime denotes the partial derivative with respect to  $z$ . Inside the solenoid the magnetic field is dominated by axial components. On the outside, but in close vicinity, radially directed field components of the so-called fringe fields are present.

Now, for the sake of simplicity, consider a parallel beam of protons traveling in  $z$ -direction, with proton rest mass  $m_p$ , particle charge  $q = e$  and velocity  $v_z$ . The associated setup and coordinate system are depicted in fig. 3.1. They enter the solenoid with a radial distance  $r$  to the magnet axis;  $r$  be small in comparison to the solenoid radius, i.e.  $r \ll r_{\text{solenoid}}$ . Applying this paraxial approximation, eqs. (3.1) and (3.2) can be linearized with respect to  $r$ . The simplified field components become

$$B_z(z) = B(z), \quad (3.3)$$

$$B_r(r, z) = -\frac{r}{2} B'(z). \quad (3.4)$$

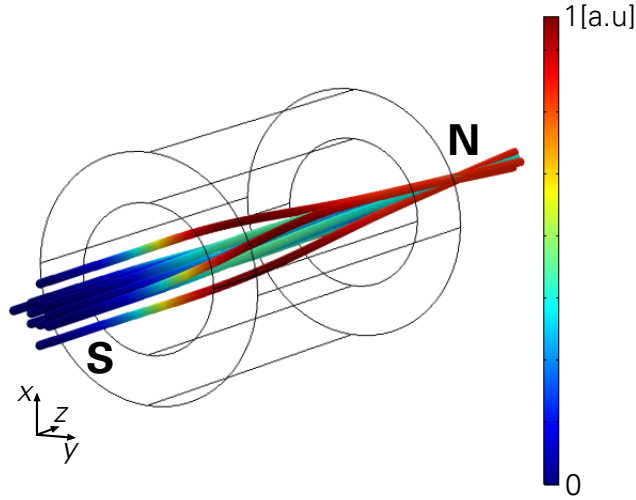


Figure 3.1: Proton trajectories of a parallel beam of twelve test particles traversing a solenoid field, extracted from a field and particle tracing simulation. N and S indicate north and south pole of the solenoid. The radial velocity component  $v_r$  that a particle gains during passage is color coded. As can be seen, particles entering the solenoid at a larger off-axis distance gain higher radial velocity.

We assume further that for a solenoid of length  $s$  the field inside, i.e. for  $0 < z < s$ , is constant and has no radial component,

$$B_z(z) = B_0 [H(z) - H(z - s)], \quad (3.5)$$

### 3.1 Fundamentals of High-field Magnets and Beam Optics

with the Heaviside step function  $H(z) = 1$  for  $z > 0$  and  $H(z) = 0$  else. Thus, on the outside the field  $B_z$  drops to zero. For the radial component follows

$$B_r(z) = -\frac{r}{2}B_0 [\delta(z) - \delta(z - s)], \quad (3.6)$$

with the Dirac delta function  $\delta$ , approximating the solenoid fringe fields. When a proton, coming from the field free region, enters the solenoid at a radial distance  $r_0 \neq 0$ , it experiences a kick by the Lorentz-force and thereby gains the transverse velocity

$$v_{\perp} = r_0 \frac{eB_0}{2\gamma m_p}, \quad (3.7)$$

with  $\gamma$  being the Lorentz-factor.<sup>1</sup> Inside the solenoid, the transverse velocity component interacts with the axial field and forces the particle on a helical trajectory as illustrated by fig. 3.1. The radius is equal to the cyclotron radius  $r_c = \gamma m_p v_{\perp} / eB_0$ . A comparison with eq. (3.7) gives  $r_c = r_0/2$ , thus the radius of a single particle's helical trajectory is half of its initial radial displacement. In conclusion, all particle trajectories have an intersection with the solenoid axis. The protons move with the cyclotron frequency  $\omega_c = eB_0/\gamma m_p$  around their individual helix axes but circle the solenoid axis with the Larmour frequency  $\omega_L = eB_0/2\gamma m_p$ . The difference is graphically explained in fig. 3.2, where the projection of two test particle trajectories onto the x-y-plane is shown.

The preceding explanations have shown that a the presented proton beam undergoes periodic focusing in the uniform field region of the solenoid. The evolution of the radial and azimuthal coordinate of a particle traveling inside the solenoid (cf. particle B in fig. 3.2) is given by

$$r(z) = r_0 \cos\left(\frac{\omega_L z}{v_z}\right), \quad (3.8)$$

$$\theta(z) = \theta_0 + \frac{\omega_L z}{v_z}, \quad (3.9)$$

with  $\theta_0$  as initial angle when entering the solenoid and  $z/v_z = t$ . In the presented work, the multiple focusing inside the solenoid cannot be observed, since the protons are typically very energetic and the solenoid is of limited length and field. Thus, the focal spot is usually generated downstream of the solenoid and the protons pass the fringe field region in the back of the magnet. As can be seen from fig. 3.2, the transverse velocity  $v_{\perp}$  can be decomposed into a radial ( $v_r$ ) and azimuthal ( $v_{\theta}$ ) component. The question is now, what happens to  $v_r$  and  $v_{\theta}$  when the particles interact with  $B_r$  again. The velocity components can be derived from eqs. (3.8) and (3.9) to

$$v_r(z) = -r\omega_L \tan\left(\frac{\omega_L z}{v_z}\right), \quad (3.10)$$

$$v_{\theta}(z) = r\omega_L. \quad (3.11)$$

Note, that  $r$  also is a function of  $z$ .<sup>2</sup> Depending on solenoid length  $s$ , field strength and particle velocity, the protons generally exit the uniform field region with a different radial

<sup>1</sup>Following the energy conservation law, the rise of a transverse velocity component  $v_{\perp}$  goes along with a decreasing longitudinal velocity  $v_z$ . In the paraxial approximation, however, the decrease is negligibly small.

<sup>2</sup>The derivation of eq. (3.11) immediately follows from the definition of the tangential velocity; eq. (3.10) can be found by forming the time derivative of eq. (3.8) ( $\frac{dr(z)}{dt} = \frac{dr(z)}{dz} \frac{dz(t)}{dt}$ ) followed by an expansion with  $r$  and substitution of  $r$  in the denominator by eq. (3.8).

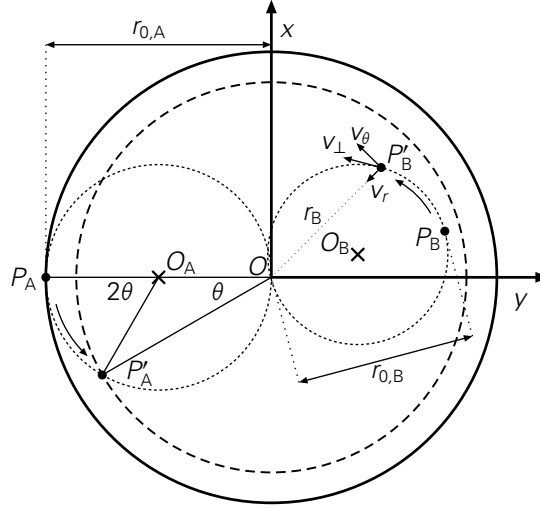


Figure 3.2: Schematic explanation of the movement of two proton test particles inside a solenoid (B-field into the drawing plane, adapted from Kumar [85]). Test proton A enters the solenoid at  $P_A$  with largest radial displacement  $r_{0,A}$ . The solid line therefore represents the edge of the incoming proton distribution. As proton A travels through the solenoid field, it moves towards  $P'_A$ , reducing the size of the beam periphery to the dashed line's dimension. With respect to  $O_A$  the particle sweeps an angle of  $2\theta$ ; however, with respect to  $O$  only an angle  $\theta$ . Therefore, the Larmour frequency is half the cyclotron frequency. For comparison, a second proton with  $r_{0,B} < r_{0,A}$  is depicted. For proton B the decomposition of the transverse velocity in radial ( $v_r$ ) and azimuthal ( $v_\theta$ ) components is indicated.

displacement  $r(z=s) = r_1 \neq r_0$ . The azimuthal velocity at the exit is  $v_\theta(z=s) = r_1\omega_L$ . In analogy to eq. (3.7) the particles experience a change in velocity given by  $\Delta v_\theta = -r_1\omega_L$ , canceling the azimuthal velocity component. The radial velocity remains unchanged:

$$v_r = -r_1\omega_L \tan\left(\frac{\omega_L s}{v_z}\right). \quad (3.12)$$

The particles travel along a straight path downstream of the solenoid. Note that particles with larger radial distance  $r_1$  gain higher radial velocities (cf. fig. 3.1) enabling the focusing of a laterally broad incoming particle beam.

In the so-called thin lens approximation, i.e.  $s \ll v_z/\omega_L$ , simplifications can be made to eq. (3.12): For the tangent the small angle approximation gives  $\tan(\omega_L s v_z^{-1}) \rightarrow \omega_L s v_z^{-1}$  and  $r_0 \approx r_1 \approx r$  for  $0 < z < s$ . Equation (3.12) becomes

$$v_r = -r \frac{e^2}{4\gamma^2 m_p^2 v_z} B_0^2 s. \quad (3.13)$$

Herefrom, the slope of the particle trajectory behind the thin solenoid can be derived by

$$\frac{dr}{dz} \frac{dz}{dt} = -r \frac{e^2}{4\gamma^2 m_p^2 v_z} B_0^2 s \quad \Rightarrow \quad \frac{dr}{dz} = -r \frac{e^2}{4\gamma^2 m_p^2 v_z^2} B_0^2 s. \quad (3.14)$$

### 3.1 Fundamentals of High-field Magnets and Beam Optics

In conclusion, the focal length  $f$  is given by

$$\frac{1}{f} = \frac{e^2}{4\gamma^2 m_p^2 v_z^2} B_0^2 s. \quad (3.15)$$

Equation (3.15) can be generalized by introducing an arbitrary spatial variation in the B-field along the z-direction. The text book formula for the focal length of a thin solenoid follows:

$$\frac{1}{f} = \frac{e^2}{4\gamma^2 m_p^2 v_z^2} \int B_0^2 dz. \quad (3.16)$$

It may be noted that in a real laser acceleration experiment that employs a solenoid magnet for particle capture one or more assumptions of the upper approach can be violated. The thin lens approximation does not hold true for low energy protons as will be seen later on. Furthermore, to allow for high capture efficiencies, the solenoid bore is typically used to almost full extend. The outermost protons therefore cannot be considered to be fully in accordance with the paraxial approximation. A real solenoid also differs from the idealized field distributions in eqs. (3.1) and (3.2) as given in section 3.1.4. Winding geometries (pitch, transition between winding layers, imperfections in rotation symmetry) are different to the ideal current loop and can therefore introduce field perturbations. The latter two scenarios can be named geometrical aberrations. Solenoids also exhibit so-called chromatic aberrations, i.e. their focal strength is not independent of the incoming particles' energies (or momenta) as can be seen from eq. (3.16). The chromaticity of solenoidal focusing can be used to perform a rough energy selection when the incoming beam has a broad energy spectrum (cf. TNSA ion source) and an aperture is applied at the focus position of the desired energy.

Figure 3.3 shows proton trajectories extracted from simulations with the General Particle Tracer (GPT) software by Pulsar Physics [86], which illustrate the chromatic focusing of a solenoid magnet and the aberration introduced by non-paraxial particles. Last, small distances between solenoid and particle source (i.e. laser target) can increase the transport efficiency but lead to a non-negligible field strength at the particle origin. The result is, that the azimuthal velocity components are not fully canceled on the back of the solenoid. This gives rise to emittance growth (Busch emittance) as will be discussed later on.

In conclusion a solenoid magnet can provide control over beam divergence. Its chromatic focusing can be used to cut out parts of an incoming exponential spectrum of TNSA protons or ions. Thereby, the energy selection is not that sharp so that the transmitted particle numbers remain high. The next section gives a comparison to other approaches for focusing laser-driven beams.

#### 3.1.3 COMPARISON OF FOCUSING OPTICS FOR LASER-DRIVEN ION BEAMS

When studying the literature, a variety of methods for controlling laser-driven particle sources can be found. The principle concepts are based on permanent magnetic quadrupoles (PMQ), pulsed and seldom superconducting solenoids, plasma based lenses or specially shaped laser targets. When particle loss is tolerable, a combination of magnetic chicanes, apertures and slits can produce high quality beams [87–89]. But since most application profit from high beam intensities and the remarkably high flux is one of the most important qualities of laser acceleration sources, only the more efficient approaches that try to capture the divergent beam and conserve the flux will be critically discussed in the following.

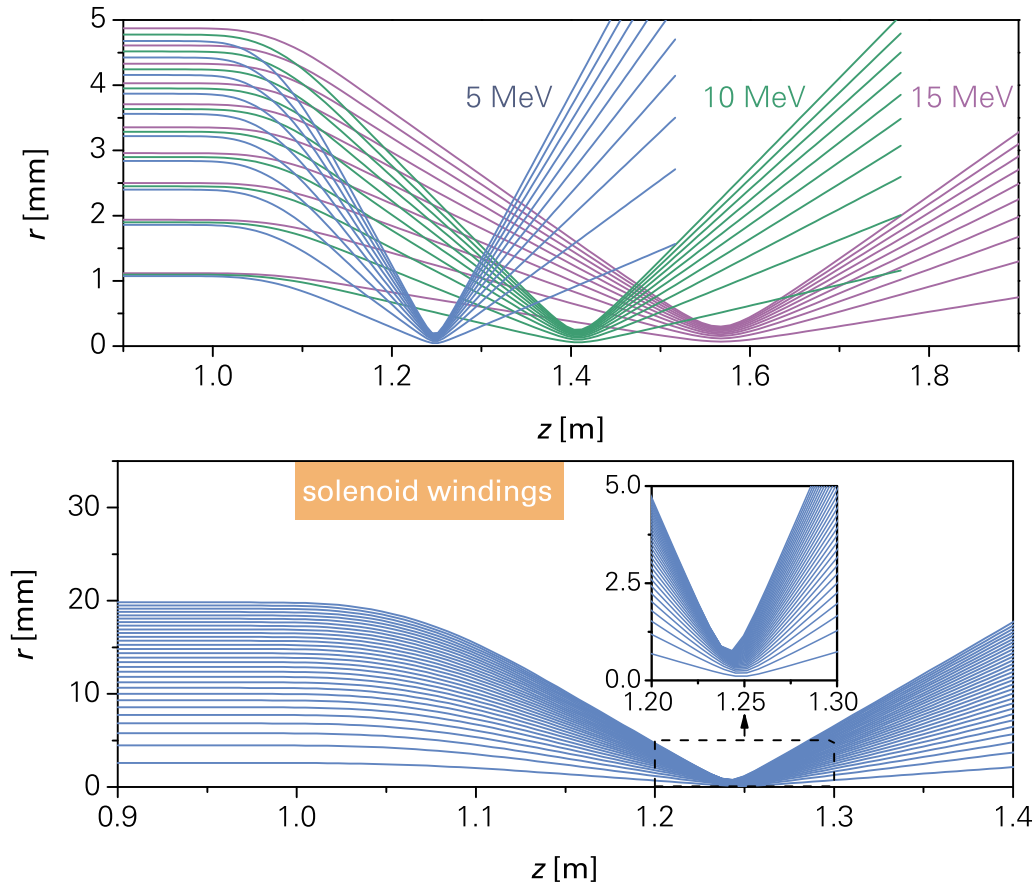


Figure 3.3: Visualization of two GPT particle tracing simulations. The magnet is composed of 120 current loops (5 kA) arranged in four layers over a length of 15 cm. The upper plot illustrates the chromatic focusing of the solenoid lens for three parallel proton beams of 5 MeV, 10 MeV and 15 MeV. The lower shows 5 MeV proton data, now for a wider (40 mm diameter) incoming beam. The outer particles of the broad beam experience higher fields in close vicinity to the solenoid windings (orange). Therefore, they are focused closer to the solenoid exit. This so-called spherical aberration, which occurs due to the realistic field distribution and violating the paraxial approximation, increases the lateral focal spot size from sub-mm to mm.

### 3.1 Fundamentals of High-field Magnets and Beam Optics

Quadrupole magnets have been used in many experimental studies at laser accelerators [44, 90–92]. Three advantages over a pulsed solenoid electromagnet are attributed to PMQs. The first is, they are easy to use because they do not require a power source, are comparably small and can be employed and motorized under vacuum conditions without difficulty. The second advantage is that they do not limit the laser shot repetition rate, whereas a pulsed high-field magnet relies on repetition rate optimized power supplies and suffers from ohmic heating. Finally, the third claimed advantage is that PMQs scale better towards higher particle energies. Revisiting eqs. (3.15) and (3.16) one finds for the focal length of a thin solenoid the relation

$$f_{\text{solenoid}} = \frac{4}{s_s} \left( \frac{p}{qB_0} \right)^2, \quad (3.17)$$

where  $p = \gamma mv$  denotes the particle momentum,  $q$  the particle charge,  $s_s$  the solenoid length and  $B_0$  the magnetic field strength. In comparison, a single quadrupole magnet can only focus a charged particle beam with respect to one transverse direction, e.g. horizontally, and acts defocusing in the perpendicular transverse, i.e. vertical, direction. For a single PMQ according to Reiser [84] the focal length can be expressed as

$$f_{\text{PMQ}} = \frac{r}{s_q} \frac{p}{qB_0}, \quad (3.18)$$

with aperture radius  $r$  and length  $s_q$  of the magnet. A second quadrupole rotated by  $90^\circ$  is necessary to focus the beam both horizontally and vertically. The setup is then called quadrupole doublet. If the two quadrupoles are identical the over-all focal length of the doublet is given by

$$F_{\text{doublet}} = \frac{f_{\text{PMQ}}^2}{D} = \frac{r^2}{Ds_q^2} \left( \frac{p}{qB_0} \right)^2, \quad (3.19)$$

with  $D$  being the distance between the two PMQs. Considering identical field strengths and particle properties, the focal length terms can now be compared as follows:

$$\frac{f_{\text{solenoid}}}{F_{\text{doublet}}} = \frac{4Ds_q^2}{r^2s_s}. \quad (3.20)$$

Equation (3.20) is used in the literature to demonstrate that for typical small aperture quadrupoles ( $r \ll s_q$ ) and comparable setup dimensions ( $D \approx s_s$ ) the focal length of the doublet is considerably shorter than for a solenoid [84, 93]. Therefore, PMQs are supposed to be better suited for focusing energetic charged particle beams in most cases. On the other hand, laser-accelerated beams exhibit unique properties that demand for rethinking on this general statement. The large beam divergence (typically  $20^\circ$  half angle [48]) limits the acceptance and transport efficiency of a small aperture quadrupole, whereas pulsed high-field solenoids can be manufactured with considerably larger aperture while still maintaining maximum field strengths one order of magnitude higher than PMQs. Increasing the aperture of a quadrupole goes along with a decrease in field gradient due to the limited maximum pole tip field (approximately 1.6 T for NdFeB magnets). The transport efficiency of a quadrupole doublet is further decreased by the defocusing of the first magnet in one direction. Finally, to change the focal length or to focus a different part of the broad incoming energy spectrum at a certain position, the doublet can only be tuned by changing the distance between both PMQs (cf. eq. (3.19)) since  $B_0$  is fixed. This makes the acceptance of the magnet system energy dependent. On the contrary, a pulsed solenoid can be tuned by changing the coil current and thereby the magnetic field amplitude on a pulse-to-pulse basis, leaving acceptance

and geometry unchanged. A last disadvantage of permanent magnets in general is that they can be demagnetized when exposed to high radiation doses [94, 95]. It remains to be seen if permanent magnets tolerate the harsh laser acceleration environment and the associated high dose rates. Demagnetization might limit the applicability for rep-rated operation.

In conclusion, both magnet systems are valuable tools to gain control over laser-driven beams. Pros and cons have to be considered for a given scientific purpose or application approach. We are convinced that, in order to facilitate a compact medical beamline, a stable transport system based on pulse high-field magnets that relies on a like-wise pulsed solenoid as first capturing element is the most efficient way to enable laser-driven proton or heavy ion beam therapy for future cancer treatments and therefore has to be studied.

The other named approaches like laser-driven beam optics or special target designs have already been demonstrated and provide for superior beam qualities in comparison to flat foil targets without focusing lenses [96–99]. Nevertheless, they can suffer from the same technologically inherent fluctuations as laser acceleration itself and produce unwanted debris. Both the laser target and beam optics have to be specially prepared. For high rep rate applications, such as laser-driven ion beam therapy, complex target geometries and beam optics that have to be replaced after every single shot and that might leave severe amounts of debris in the target chamber cannot be considered.

Repeatedly pulsed gas-filled discharge capillaries as used for laser-driven electron acceleration (cf. Karsch et al. [100] and Tilborg et al. [101]) and their generated field could also be used to guide a laser-accelerated proton beam – an interesting approach that still has to be demonstrated. Same holds for the so-called Gabor lens [102]. This space charge lens uses a confined electron plasma to focus a traversing ion beam. The feasibility for application in laser acceleration still has to be shown and the transport properties need to be quantified.

### 3.1.4 PULSED HIGH-FIELD MAGNETS – PROPERTIES, DESIGN AND CONSTRUCTION

It has been explained how valuable the non-destructive pulsed high-field solenoid is for focusing highly divergent charged particle beams. In the following paragraphs the reader will be introduced to its most important properties and construction principles.

Pulsed high-field magnets, no matter what they are used for, are usually of cylindrical shape and rotationally symmetric with respect to their axis. With few exceptions, these magnets can either be described as cylindrical or as a combination of cylindrical coils, thus solenoids. The most important property of such a magnet is the magnetic field distribution, as shape and amplitude of the  $B$ -field determine whether the pursued influence on an experimental measurement can be achieved or not.

It has been shown in eqs. (3.1) and (3.2) that the solenoid field can be described by a radial component  $B_r(r, z)$  and an axial component  $B_z(r, z)$ . The field components are functions of the radial coordinate  $r$  and the on-axis field  $B(z)$  and its derivatives. For a thin-walled solenoid electromagnet of finite length  $s$ , mean radius  $r_m$  and  $N$  windings, the on-axis field can be expressed by the formula

$$B(z) = \frac{\mu_0 Ni}{2s} \left( \frac{z - z_1}{\sqrt{(z - z_1)^2 + r_m^2}} - \frac{z - z_2}{\sqrt{(z - z_2)^2 + r_m^2}} \right), \quad (3.21)$$

where  $z_1$  and  $z_2$  denote the positions of the solenoid entrance and exit ( $z_2 > z_1 \Rightarrow z_2 - z_1 = s$ ), coil current  $i$  and vacuum permeability  $\mu_0$ .

### 3.1 Fundamentals of High-field Magnets and Beam Optics

In general, wire-wound pulsed high-field solenoids cannot be described by the upper formula, since they typically employ multiple winding layers and are therefore not considered to be thin-walled. To derive the formula for a finite cylindrical solenoid with rectangular cross section, eq. (3.21) has to be integrated over a range of radii, i.e. from inner radius  $r_i$  to outer radius  $r_o$ . The result of the integration is

$$B(z) = \frac{\mu_0 Ni}{2s(r_o - r_i)} \left( (z - z_1) \ln \frac{\sqrt{r_o^2 + (z - z_1)^2} + r_o}{\sqrt{r_i^2 + (z - z_1)^2} + r_i} - (z - z_2) \ln \frac{\sqrt{r_o^2 + (z - z_2)^2} + r_o}{\sqrt{r_i^2 + (z - z_2)^2} + r_i} \right). \quad (3.22)$$

Finally, eq. (3.22) can be simplified for the case of  $z = \frac{z_2 + z_1}{2}$ , giving the magnetic field  $B_0$  in the center of the solenoid

$$B_0 = \frac{\mu_0 Ni}{2(r_o - r_i)} \ln \frac{\sqrt{r_o^2 + \left(\frac{s}{2}\right)^2} + r_o}{\sqrt{r_i^2 + \left(\frac{s}{2}\right)^2} + r_i}. \quad (3.23)$$

It may be noted that the central field of a cylindrical magnet is in general also the maximum on-axis field, i.e.  $B_0 = B_{z,\max}$ .<sup>3</sup> When magnetic field values are given without further specification in the following, they describe the central field of the magnet.

The central field  $B_0$ , as discussed, is an essential parameter for magnet design and application. Yet, with the aim of manipulating laser-driven particle or plasma sources, it is also important to consider the given experimental conditions and geometrical constraints. The experiment geometry is defined by the laser setup as well as laser, particle and plasma diagnostics. It restricts the space that can be taken up by the magnet. The experimental conditions dictate further magnet properties. For example, experiments at the Draco laser acceleration source are performed under high vacuum (HV, typically  $10^{-6}$  mbar); therefore, the magnet needs to be constructed from vacuum compatible materials and needs to perform under HV conditions. Further constrictions might be: remote controlled motorization, reflectivity, temperature, fringe field length or electromagnetic compatibility (EMC). These constrictive considerations give the most valuable input for the magnet design process.

Bearing all constrictions in mind, the next step is to figure out whether and, if so, how a magnetic field of adequate shape and amplitude, for achieving a desired effect, can be created. A first crucial consideration concerns the energy that is required to generate the magnetic field. The magnetic energy  $E_{\text{mag}}$  can be derived from the volume to which the magnetic field extends and its amplitude,

$$E_{\text{mag}} = \oint_V \rho_m d\vec{r} = \oint_V \frac{B^2}{2\mu_0} d\vec{r}, \quad (3.24)$$

where  $\rho_m$  denotes the magnetic energy density and  $\mu_0$  the vacuum permeability. The required energy needs to be provided by the current source. Limited resources of electrical energy have to be taken into account.

In electrical engineering it is a more common approach to use the (self) inductance<sup>4</sup>  $L$  as a

<sup>3</sup>Pulsed high-field magnets employing inhomogeneous current density distributions can violate that rule. One example will be presented in section 3.2.3 where a split-pair solenoid is discussed that deviates from the ideal Helmholtz coil geometry and has two off-center field maxima.

<sup>4</sup>The self inductance of a conductor geometry is defined by the formula  $u(t) = L di/dt$  with voltage  $u$  and current  $i$  of named conductor.

measure of the energy of a conductor geometry that carries the current  $i$ . It holds that

$$E_{\text{mag}} = \frac{1}{2} Li^2. \quad (3.25)$$

When the winding geometry is being designed, the repeated inductance calculation allows to keep the energy requirements in view. For practical reasons the following formulas, taken from Wheeler [103] and transferred to metric units, provide reasonable estimates. For a thin-walled solenoid of finite length  $s$ , mean radius  $r_m$  and  $N$  windings, Wheeler found

$$L \approx \frac{0.39 r_m^2 N^2}{9 r_m + 10 s} \text{ in } \mu\text{H}, \quad (3.26)$$

for spatial measures in cm. Equation (3.26) can be simplified to

$$L \approx \frac{0.39 r_m^2 N^2}{10 s} \text{ in } \mu\text{H}, \quad (3.27)$$

for very long solenoids ( $s \gg r_m$ ). Finally, consider a magnet that is short but radially thick, i.e. a multi-layer solenoid with inner and outer winding radii  $r_i$  and  $r_o$ . The associated Wheeler formula is

$$L \approx \frac{0.31 r_m^2 N^2}{6 r_m + 9 s + 10 t} \text{ in } \mu\text{H}, \quad (3.28)$$

where  $r_m = (r_i + r_o)/2$  is the mean winding radius and  $t = r_o - r_i$  denotes the radial thickness of the rectangular cross section of the cylindrical magnet. Again, all spatial measures in cm. In case of more complex geometries the handbook of Grover [104] and the inductance calculation formulas and tables therein have proven to be very useful.

If the energy provided by the current pulse generator is sufficient to power the coil, the next design steps would be to calculate the mechanical as well as thermal properties of the coil. The forces and stresses induced in the magnet during the current pulse define how strongly the solenoid needs to be reinforced. The following simplified example illustrates the stresses present in pulsed high-field magnets and why special exigencies are required for their development:

Consider a cylindrical magnet made of copper. The magnet is supposed to generate a field of  $B = 10$  T in its center. The magnetic pressure inside the solenoid is defined by

$$P_{\text{mag}} = \frac{B^2}{2\mu_0} \approx 40 \text{ MPa} \quad (3.29)$$

and identical to the magnetic energy density (cf. eq. (3.24)). The copper windings shall have a radial thickness of  $t = 1$  cm and a mean radius of  $r_m = 10$  cm.

We now want to calculate the so-called hoop stress  $\sigma_\theta$ , which is stress resulting from a force exerted circumferentially, i.e. perpendicular to the solenoid's axial and radial directions. For thin-walled pressure vessels, such as the example solenoid, one finds for the hoop stress

$$\sigma_\theta = \frac{r_m}{t} P_{\text{mag}} \approx 200 \text{ MPa}. \quad (3.30)$$

The upper formula is sometimes referred to as pipe formula. The hoop stress can now be compared to the yield strength and the ultimate tensile strength of copper. The yield strength of soft copper is approximately 70 MPa, the ultimate tensile strength is 220 to 230 MPa. Therefore, the coil would not yet rip apart but would experience strong plastic deformation.

### 3.1 Fundamentals of High-field Magnets and Beam Optics

The example demonstrates how high mechanical stresses can become already at moderate field strengths. The aim for field strengths well in excess of 10 T calls for stronger winding materials and reinforcements introduced into the high-field magnet construction. All mechanical reinforcement measures need to be in accordance with the electrical and thermal properties of the magnet. A good compromise of strong electrical insulation and high heat conductivity needs to be sought when designing a magnet since pulse generation involves high voltages, typically up to 24 kV, and results in a high heat input that needs to be dissipated.

The calculation of coil heating and heat dissipation is very complex considering that the coils consist of a multitude of different materials in complex geometry. If necessary computational methods or elaborate thermal network modeling can be applied. A very conservative estimation can be made if the mass  $m_{\text{Cu}}$  of all copper windings of the solenoid is known. A fraction of the pulse energy is dissipated by the ohmic resistance of the coil. This energy fraction  $Q$  can be calculated by

$$Q = R \int_0^{t_{\text{pulse}}} i^2(t) dt \quad (3.31)$$

where  $R$  is the coil resistance and  $i(t)$  the coil current. It may be noted that the fast current rise times in pulsed high-field magnets increase the acting resistance due to the skin effect. As the current changes abruptly, the current density becomes larger near the surface of the conductor therefore the full wire cross section cannot be used effectively.

For the first half-wave of a sinusoidal current pulse of period  $T$  and amplitude  $i_{\text{max}}$  eq. (3.31) can be written as

$$Q = R \int_0^{T/2} i_{\text{max}}^2 \sin^2 \left( 2\pi \frac{t}{T} \right) dt \quad (3.32)$$

$$= R i_{\text{max}}^2 \frac{T}{4} \quad (3.33)$$

$$= R i_{\text{max}}^2 t_{\text{rise}}, \quad (3.34)$$

where the quarter period has been expressed by the rise time  $t_{\text{rise}}$  of the current pulse.

The temperature jump  $\Delta T$  can then be approximated by using the heat capacity formula

$$C = \frac{Q}{\Delta T} \quad (3.35)$$

Under the assumption of small temperature changes (bear in mind that the heat capacity is temperature dependent) one can approximate the temperature increase of the copper windings by

$$\Delta T = \frac{Q}{c_{\text{Cu}} m_{\text{Cu}}}, \quad (3.36)$$

with the specific heat capacity of copper  $c_{\text{Cu}}$  at room temperature.

All theoretical considerations of  $B$ -field generation, heating as well as mechanical forces and stresses are far beyond the scope of this introduction and may be found in the literature, e.g. in Kratz and Wyder [105]. The analytical calculation of magnet properties during

the design process is highly complex due to the high number of entwined magnetic, thermal and mechanical parameters and their transient evolution. Typically the design process involves either simplified models or simulations using the finite element method (FEM). FEM programs, such as Comsol [106], allow for coupled calculations beginning from the current pulse generating circuit network, over magnetic field generation, to heating and mechanical deformation of solenoid magnets in 3D or 2D-axisymmetric simulation frameworks. In this study, Comsol was routinely applied for magnetic field prediction and structural mechanics evaluation. Current pulse generation has been simulated with the more suitable software OrCAD PSpice [107].

Above, basic principles of magnet design and fabrication have been presented and should suffice to give the reader a feeling on important properties and orders of magnitude. If necessary more detailed theoretical analyses will follow in the sections dealing with the conception of the magnet prototypes used throughout this thesis. This section is concluded by the description of an exemplary manufacturing process of a pulsed high-field magnet for a laser-plasma experiment.

The result of the coil design process usually is a compromise between the different coil properties, e.g. field strength, mechanical strength, power consumption, etc. If the magnet design is acceptable under consideration of all boundary conditions and constraints, the pulsed high-field magnet can be manufactured. The fabrication process is built on machinery, know-how and experience of high-field laboratories. The solenoid magnets presented in this thesis have all been manufactured by HLD. The first step is to make the coil body, usually a cylindrical tube with a strong flange at one end. Typical materials are fiber reinforced plastics (FRP) like G10. Then the actual coil winding begins. The wire material should be a strong copper alloy ( $\sigma_{ts} > 500 \text{ MPa}$ ), insulated ideally with overlapping Kapton tape (dielectric strength =  $303 \text{ kV mm}^{-1}$ ). The wire cross section is supposed to be rectangular, increasing the filling factor, i.e. the ratio of current carrying conductor to the entire coil cross section, and providing for more evenly distributed stresses. While the wire is wound around the coil body, it is kept under constant tension, checked for insulation defects and braided with strong fibers like glass, carbon and Zylon. The process is illustrated by fig. 3.4. Immersed in epoxy resin, the braiding forms a compound and provides for additional structural strength and insulation space between the windings. When a single layer of windings is finished, a reinforcement layer of Zylon fibers ( $\sigma_{ts} = 5.8 \text{ GPa}$ ) imbued with epoxy (the compound ultimate tensile strength is still of the order of  $3 \text{ GPa}$ ) is applied [105]. The thickness of the reinforcement layer can be tailored to the mechanical stresses calculated for the magnet. Between the layers, Teflon tape can be applied to allow the layers to separate during the pulse, i.e. the outer layers cannot pull on the inner layers. The transition between layers is sometimes eased by introducing transition pieces made of FRP. In this manner, the magnet is wound layer by layer. Fiber and resin compositions can be chosen to provide for higher heat conductivity or for the ability to machine the outer reinforcement layer. After the finished winding process the second end flange is bolted together with the flange on the opposite site of the coil body applying axial pressure on the windings. The magnet can be operated when the epoxy has hardened. Baking the coil speeds up this process.

#### 3.1.5 CURRENT PULSE GENERATION

For generating highest magnetic fields in non-destructive electromagnets, high-field laboratories around the world rely on capacitor-based current pulse generation. To drive currents of up to several 100 kA through the magnet, large, high-voltage capacitor banks are required.

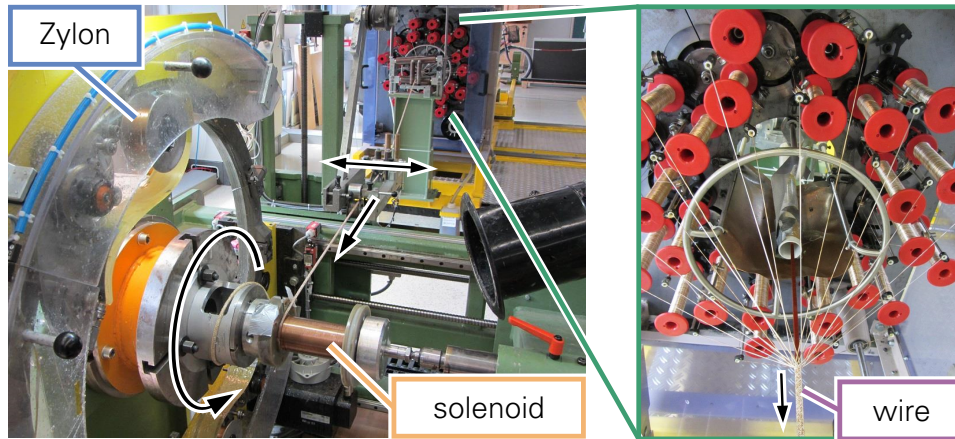


Figure 3.4: Photographs of HLD's winding machine during a production run of the capturing solenoid (see section 3.2.1). The left picture shows the most important parts of the winding machine with mounted solenoid magnet. As the machine rotates around the solenoid axis, the wire is pulled forward (indicated by arrows) while it is braided with the reinforcing fibers. As the manufacturing process proceeds, the wire guide (double arrow) moves the wire to the right. When the layer is finished Zylon reinforcement is applied. The winding of the next layer continues from right to left now, the guidance moves in the opposite direction. The braiding is continuously performed by the red rotating spindles shown in the right picture.

The installations typically fill halls and provide multiple magnet cells with pulsed-power due to their modular setup. Figure 3.5(a) gives an impression on one of the two capacitor banks of the Dresden High Magnetic Field Laboratory (HLD) at HZDR (for properties see caption). For the application of pulsed high-field magnets in plasma science it is neither practical nor required to make use of a large-scale facility like HLD. Therefore, capacitor-based portable pulse generators (PG) have been developed within the framework of this thesis, with properties tailored to meet the demands of the magnets used for experimentation. The well known technology of the high-field laboratories was adopted and, if necessary, adapted for more practical applicability.

The function principle of PG and magnet is that of a resonant circuit. The PG's capacitance  $C$  is first charged, then discharged via a high-voltage switch into the high-field electromagnet. The inductance  $L$  of the magnet results in the formation of a resonant circuit of angular frequency  $\omega_0 = 1/\sqrt{LC}$ . The electrical energy stored in a capacitor charged to voltage  $u_C$ ,

$$E_{\text{el}} = \frac{1}{2} C u_C^2, \quad (3.37)$$

is thereby converted into magnetic energy of the pulsed magnet's establishing field. The magnetic energy is characterized by the magnet's inductance  $L$  and the flowing current  $i_L$  according to

$$E_{\text{mag}} = \frac{1}{2} L i_L^2. \quad (3.38)$$

Neglecting ohmic losses and parasitic inductances or capacitances, equalizing eqs. (3.37) and (3.38) gives handy formulas to estimate the current flow through a magnet of known

inductance or, vice versa, to calculate the required peak capacitor voltage  $u_{C,\max}$  to reach a desired current amplitude  $i_{L,\max}$  and field value:

$$i_{L,\max} \approx \sqrt{\frac{C}{L}} u_{C,\max}, \quad (3.39)$$

$$u_{C,\max} \approx \sqrt{\frac{L}{C}} i_{L,\max}. \quad (3.40)$$

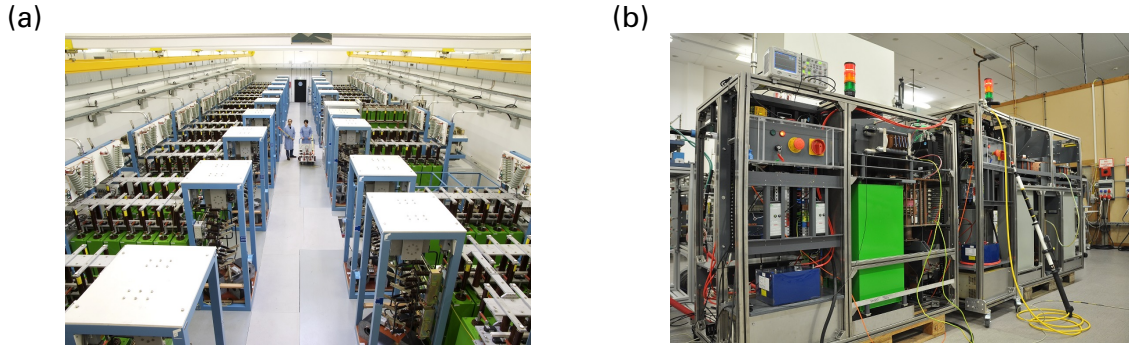


Figure 3.5: Comparison of the Dresden High Magnetic Field Laboratory (HLD) capacitor bank (a) and two portable pulse generators (b) developed within the scope of this thesis. The HLD capacitor bank stores up to 50 MJ electrical energy at 24 kV and can deliver current pulses as high as 600 kA.

In a realistic resonant circuit, ohmic resistances of magnet, PG components, transmission lines, etc. damp the otherwise sinusoidal current flow:

$$i_L(t) = \frac{U_C}{\omega_e L} \cdot e^{-\delta t} \cdot \sin \omega_e t \quad (3.41)$$

with  $\delta = R/2L$  and  $\omega_e = \sqrt{\omega_0^2 - \delta^2}$ ,  $R$  being the sum of all acting resistances. The dominant resistance in the circuit is the resistance of the magnet of the order of 10 to 100 m $\Omega$ , giving a moderate damping. The lasting current and voltage oscillation result in two unwanted conditions: First, almost the entire energy of the system is thermally dissipated via the pulsed magnet; second, the capacitor needs to tolerate a high voltage reversal. Usually, pulsed-power capacitors rely on technologies that allow for voltage reversal of the order of only a few 10% of their max specified charge voltage. Capacitors with > 90% voltage reversal rapidly grow in terms of price and volume per Farad. To enable the use of the efficient and affordable capacitors mentioned firstly, a so-called crowbar diode circuit can be used. The HV diode is connected in parallel to the capacitor and equipped with a series resistor. The diode becomes conducting when the polarity of the capacitor changes. The resistance is chosen to limit the capacitor voltage reversal to the tolerable level. The pulse generators developed during the work of this thesis all employ this technology. Figure 3.6 explains the principle functionally in more detail.

## 3.2 DEVELOPED PULSED HIGH-FIELD MAGNETS

In the following sections the pulsed high-field magnets developed within the framework of this thesis will be introduced. The focus will lie on three solenoid magnets for different fields

### 3.2 Developed Pulsed High-field Magnets

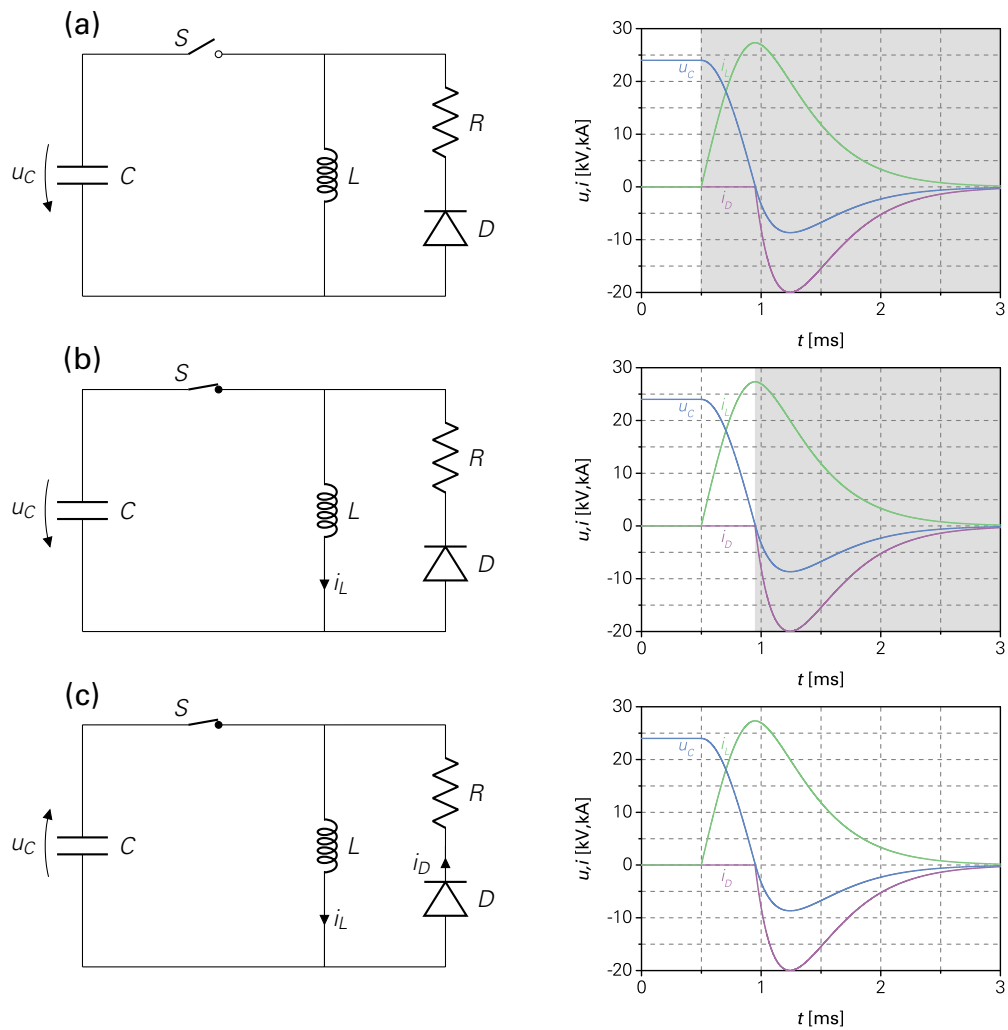


Figure 3.6: Functional principle of capacitor based pulse generator with crowbar diode. Left: simplified circuit diagram. Right: corresponding temporal evolution of voltages and currents from SPICE simulation (parameters geared to realistic PG and magnet properties). (a) Capacitor  $C$  is charged, HV switch  $S$  is still open, no current flow. (b) After 0.5 ms switch  $S$  is closed, current flow through the pulsed magnet of inductance  $L$  is established (resonant circuit),  $i_L$  rises and reaches maximum when capacitor voltage drops to  $u_C = 0$  V. The electrical energy  $E_{el}$ , initially stored in the capacitance, is fully transformed into magnetic energy  $E_{mag}$ . The HV diode  $D$  operated in reverse direction, therefore not conducting. (c) At approximately 0.9 ms the capacitor voltage is reversed,  $D$  is now forward biased and conducting. The energy in the system is dissipated in resistor  $R$  of the crowbar circuit.

of application, highlighting the versatility of the strong technology platform that has been built.

### 3.2.1 CAPTURING SOLENOID

This section introduces the solenoid magnet that has been used most extensively for experiments presented in this thesis, the capturing solenoid. The name has been chosen because the magnet is specifically designed to capture large fractions of the highly divergent laser-accelerated ion beams with the goal to provide them for irradiation experiments. Thereby, application scenarios include, amongst others, the controlled irradiation of cancer cells for radiobiological studies, high-flux irradiation of samples from material science, proton radiography as well as potentially isochoric heating with heavy ions. The solenoid is the key component for gaining control over the laser-driven beam while still maintaining highest particle numbers. It was manufactured on the basis of a previous design developed by Burris-Mog [42]. Similar designs of the presented solenoid have been used for transportation studies of laser-accelerated proton beams before and during this thesis work. The magnet has been proven to generate collimated or focused beams with mean energies up to 10 MeV and transport efficiencies in excess of 30 % [41, 43–45].

The solenoid design features 112 evenly distributed windings in four layers. The magnet was manufactured using a strong copper alloy (Wieland K88) wire of  $4.3 \times 2.8 \text{ mm}^2$  cross section. The wire is wound on a cylindrical FRP coil body with 54 mm outer diameter. Every layer is backed by at least 1.5 mm Zylon reinforcement. With a length of 15 cm, an outer winding diameter of 10 cm and a mass of less than 10 kg, the capturing solenoid magnet is exceptionally small, lightweight, practical and energy efficient. It was designed with a bore of 48 mm, larger than most pulsed magnets developed by high-field laboratories. The large bore size was chosen specifically for the capture of divergent laser-accelerated ions in order to facilitate high transport efficiencies.

The fiber reinforced plastic as well as the Zylon-epoxy composite that strengthen the magnet cannot be considered vacuum compatible, since their outgassing can cause debris on laser optics. Even when this risk is tolerated, locally the outgassing can result in a severe reduction of the break down voltage, in accordance to Paschen's law, putting the magnet and surrounding equipment in danger. That is why the presented pulsed magnet is installed in a sealed stainless steel housing connected to the air volume outside of the target vacuum chamber via bellows. The steel is non-magnetic and its low conductivity prevents strong induced eddy currents. Figure 3.7 depicts the application scenario schematically and shows the construction of magnet and housing in comparison to an older design used throughout the work of Busold et al. [43–45] and Busold [47]. The new design was deliberately tailored for size and weight reduction to increase the applicability of the solenoid and simplify motorization. The 50 % weight and 45 % volume reduction result in compact installation dimension, approximately  $25 \times 25 \times 25 \text{ cm}^3$ , and a setup mass below 20 kg. The lightweight assembly allows for using an affordable hexapod positioning system to precisely align the solenoid with respect to the laser target. The housing reduces the aperture size slightly to 40.5 mm.

The magnet was modeled using the Comsol multiphysics simulation software. The magnetic field distribution of the solenoid geometry, approximated by a composition of closed wire loops, is depicted in fig. 3.8 for a static current of 23.4 kA, i.e. the maximum current achievable at the moment. The simulation results reproduce prior on-axis field measurements by Busold [47] exceptionally well. These measurements as well as the presented simulation describe the ratio of the maximum solenoid current  $i_{\text{max}}$  to the peak on-axis field

### 3.2 Developed Pulsed High-field Magnets

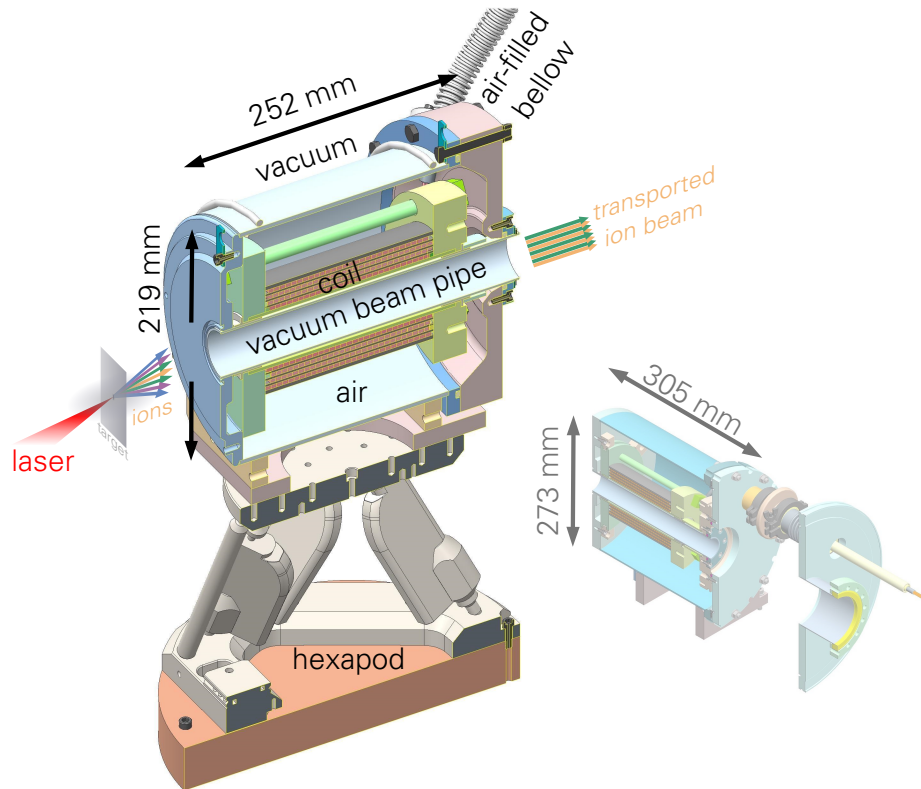


Figure 3.7: Cutaway view of the capturing solenoid with stainless steel housing and typical application scenario, important design features and components marked. The laser-driven ion beam is depicted and the broad energy distribution illustrated by the manifold colored arrows. The particles are transported through the beam pipe as the chromaticity of the solenoids provides for a rough energy selection. The right side shows the bulky previous design (not to scale) that needed to be revised to enable experiments at the Draco laser accelerator.

$B_{z,\max}$  as follows:

$$\frac{B_{z,\max}}{i_{\max}} \approx 0.84 \text{ T kA}^{-1} \quad (3.42)$$

For the simulated maximum current of 23.4 kA eq. (3.42) yields a maximum on-axis field strength of

$$B_{z,\max} \approx 19.7 \text{ T} \quad (3.43)$$

The presented Comsol field distribution can be used for particle tracing simulations either using Comsol itself or, for more sophisticated simulations, the field can be exported and introduced to the General Particle Tracer (GPT). It may be noted that GPT is also able to calculate magnetic field distributions from current loops as has been done for the generation of fig. 3.3. The simulation model will be presented in later sections were a thorough comparison with experimental particle transport data follows.

From the magnetic field distribution Comsol can calculate the solenoid inductance by integrating over the magnetic energy density in accordance to eq. (3.24) and by applying

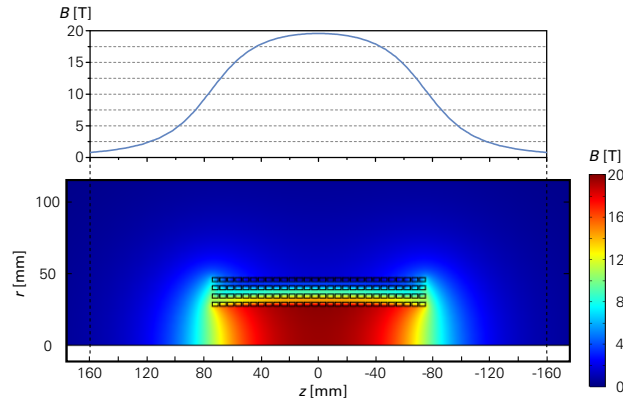


Figure 3.8: Color coded magnetic field distribution from a 2D axisymmetric Comsol simulation. The symmetry axis is on the bottom of the plot. Rectangles indicate the positions of the closed wire loops (wire current 23.4 kA). The upper plot shows the on-axis field of the corresponding simulation.

eq. (3.25). It yields a solenoid inductance of  $300 \mu\text{H}$ . The output was compared to inductance calculations using eq. (3.28) ( $r_m \approx 3.7 \text{ cm}$ ,  $s = 15 \text{ cm}$  and  $t \approx 2 \text{ cm}$ ) as well as the formulas and tables given in Grover [104]. The calculated values show a deviation of less than 1 % in comparison to the simulation, thus for the presented cylindrical geometry the textbook approaches are well suited for inductance calculations. The inductance was additionally measured by means of a LCR meter while the magnet was installed in the housing. At a 600 Hz test frequency the inductance was measured to be  $L_{\text{sol}} \approx 270 \mu\text{H}$  and the resistance  $R_{\text{sol}} \approx 150 \text{ m}\Omega$ . The inductance is reduced due to eddy currents induced in the steel housing. These eddy currents can also limit the maximum achievable field strength. A reduction of up to 5 % can occur for typical pulse rise times of approximately 380 to 420  $\mu\text{s}$ . This reduction needs to be accounted for in simulation and experimental analysis.

Finally, the mechanical and thermal limitations of the magnet will be discussed. The magnet is designed for highest mechanical stability, reliability and long life time. Stress simulations suggest that the magnet can be operated safely up to 35 T maximum on-axis field strength with future pulse generators. Such high field values are typically required for medical beam transport systems for laser-driven ion beams [33].

The heating of the magnet can be conservatively approximated by the approach discussed in section 3.1.4. Considering a typical pulse rise time of  $t_{\text{rise}} = 420 \mu\text{s}$  and a peak current of  $i_{\text{max}} = 23.4 \text{ kA}$  the heat input can be calculated in accordance to eq. (3.34). It holds that

$$Q = R_{\text{sol}} i_{\text{max}}^2 t_{\text{rise}} = 34.5 \text{ kJ}. \quad (3.44)$$

The temperature of the wire (cf. eq. (3.36)) is abruptly increased by

$$\Delta T = 30 \text{ K}. \quad (3.45)$$

The wire mass was calculated to be approximately 3 kg. The specific heat capacity of copper at room temperature, i.e.  $0.381 \text{ kJ kg}^{-1} \text{ K}^{-1}$ , has been used for the determination.

The heat is then transferred to the material contacting the wire. The temperature rise of the whole magnet, including reinforcement and flanges, is therefore limited to approximately 10 K per full energy pulse. The capturing solenoid should therefore not be operated with

### 3.2 Developed Pulsed High-field Magnets

repetition rates in excess of one full-energy pulse per minute for few minutes. For a reduced pulse energy higher repetition rates ( $\propto i_{\max}^{-2}$ ) can be achieved. The magnet temperature may be monitored by means of temperature sensors or resistance measurements (only wire temperature). A temperature above 60 °C is to be avoided to prevent the epoxy from softening.

#### 3.2.2 40-T-SOLENOID

The second magnet presented in this thesis employs a more compact design than the capturing solenoid, yet enables particle transport experiments at highest fields in excess of 40 T with present pulse generator technology, optionally with the TNSA source inside the magnetic field. Figure 3.9 shows a cutaway view of the magnet construction and illustrates the application scheme for TNSA in an external field.

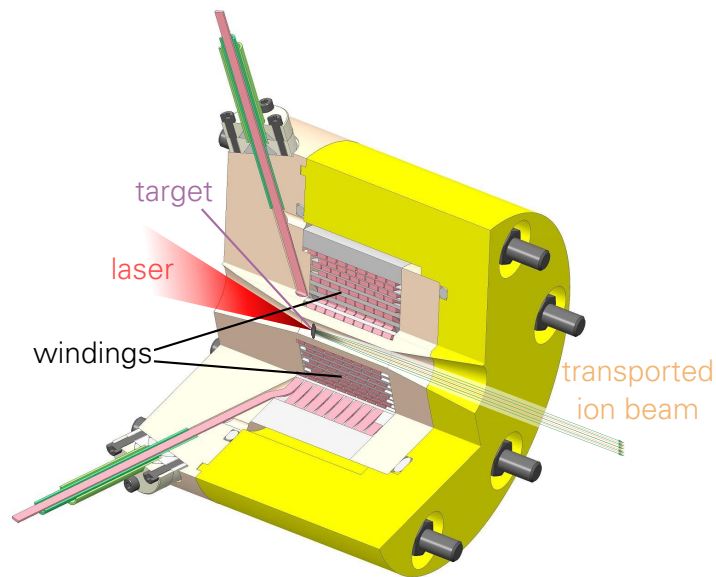


Figure 3.9: Cutaway view of the 40-T-solenoid and typical application scenario for a TNSA ion source inside an external magnetic field. The body as well as the housing are made of PEEK plastic. The bore is shaped conically to prevent clipping of the laser. The applied sealing technique is comparable to the split-pair solenoid (see following section 3.2.3). The wires are guided inside flexible plastic tubes accordingly.

The magnet is a simple cylindrical solenoid with 72 windings in 8 layers over a winding length of 48 mm. The wire material is an exceptionally strong Cu-Ag-alloy equipped with Kapton insulation. The cross section was chosen to be  $4 \times 2 \text{ mm}^2$ . The geometry results in an inductance of approximately 120  $\mu\text{H}$ . The magnet combines the strong mechanical strength of the capturing solenoid with a compact housing technology. The thick PEEK shell defines the size of the magnet and was chosen as a safety feature that protects the surrounding in case of a coil failure. The 40-T-solenoid has a length of 138 mm and a diameter of 175 mm. The conical bore has a minimum open aperture in the center of the magnet of 10 mm. Future designs might be manufactured with a more compact shell and a larger bore.

In order to explore the technological feasibility of even higher fields for the application

in laser-plasma physics, thorough mechanical analyses allow for reliable prediction on the maximum field strength structurally achievable. Using the Comsol FEM software the most thorough structural mechanics analysis has been performed for the presented magnet. The energy requirement of the magnet has been assessed and for the described geometry of 72 windings a winding current of 30 kA has been found as achievable for present pulse generator technology, yet still enabling an on-axis field in excess of 40 T. The corresponding field map has been calculated by Comsol in a 2D axisymmetric simulation. To keep the simulation small, the mirror symmetry with respect to the magnet's midplane was used and appropriate boundary conditions applied. Thereby, the properties of the whole magnet can be assessed by only modeling a quarter of the windings and reinforcement. The results of the field calculation are presented in the top section of fig. 3.10. For 30 kA coil current a maximum on-axis field in excess of 42 T is predicted.

The box in fig. 3.10 summarizes the structural mechanics simulations by showing the von Mises stress distribution of the 40-T-solenoid.<sup>5</sup> To gain reliable results on the structural strength of the magnet, several sophisticated modeling steps were followed. At first the modeling of the Zylon reinforcement will be discussed. Zylon is a so-called orthotropic material. In contrast to isotropic materials, these fibers exhibit different mechanical properties in dependence of the load direction. The fiber is exceptionally tear-resistant but only for forces exerted along the fiber. For the Zylon resin composite the following material properties have been used for the mechanical simulation in accordance to the literature [108, 109]:

$$\begin{array}{llll}
 E_r = 10 \text{ GPa} & \nu_r = 0.005 & & \\
 E_\varphi = 230 \text{ GPa} & \nu_\varphi = 0.35 & G_{r/\varphi/z} = 12 \text{ GPa} & \rho = 1560 \text{ kg m}^{-3} \\
 E_z = 10 \text{ GPa} & \nu_z = 0.6 & & 
 \end{array}$$

Here,  $E_{r/\varphi/z}$  denote Young's modulus,  $\nu_{r/\varphi/z}$  Poisson's ratio and  $G_{r/\varphi/z}$  the shear modulus with respect to the spatial direction in cylindrical coordinates;  $\rho$  is the density of the composite. The linear elastic, isotropic wire properties were chosen to be  $E = 140 \text{ GPa}$ ,  $\nu = 0.35$  and  $\rho = 8700 \text{ kg m}^{-3}$  and modeled to start yielding at 0.5 GPa. That means that the wire material starts flowing at stresses in excess of 0.5 GPa increasing the forces that need to be taken up by the reinforcement. As can be seen from the bottom right of fig. 3.10, for the first six layers of the magnet the yield criterion is met as the stress saturates at 0.5 GPa.

As discussed in section 3.1.4, Teflon tape can be applied to allow the layers to separate during the pulse, meaning that the outer layers cannot pull on the inner layers. The simulation has been carried out to mimic both cases, with and without Teflon. Figure 3.10 shows, that if a separation of the layers is allowed a more homogenous stress distribution throughout the reinforcement layers is obtained, whereas the result for a magnet without Teflon shows maximum load on the first reinforcement layer. For both cases the stresses are well below the UTS of the reinforcing composite, which is approximately 3 GPa, yet to achieve the more homogenous stress distribution, Teflon tape has been introduced to the first prototype. Functional test are ongoing.

In order to be able to use a compact magnet design with small bore and still facilitate high capture efficiencies for ion beam transport studies, the particle source has to be right in front or even inside the solenoid. This changes the behavior of the particle trajectories behind the

<sup>5</sup>The von Mises stress is a scalar stress value that can be computed from the stress tensor. A material starts yielding when the von Mises stress reaches the yield strength of named material.

### 3.2 Developed Pulsed High-field Magnets

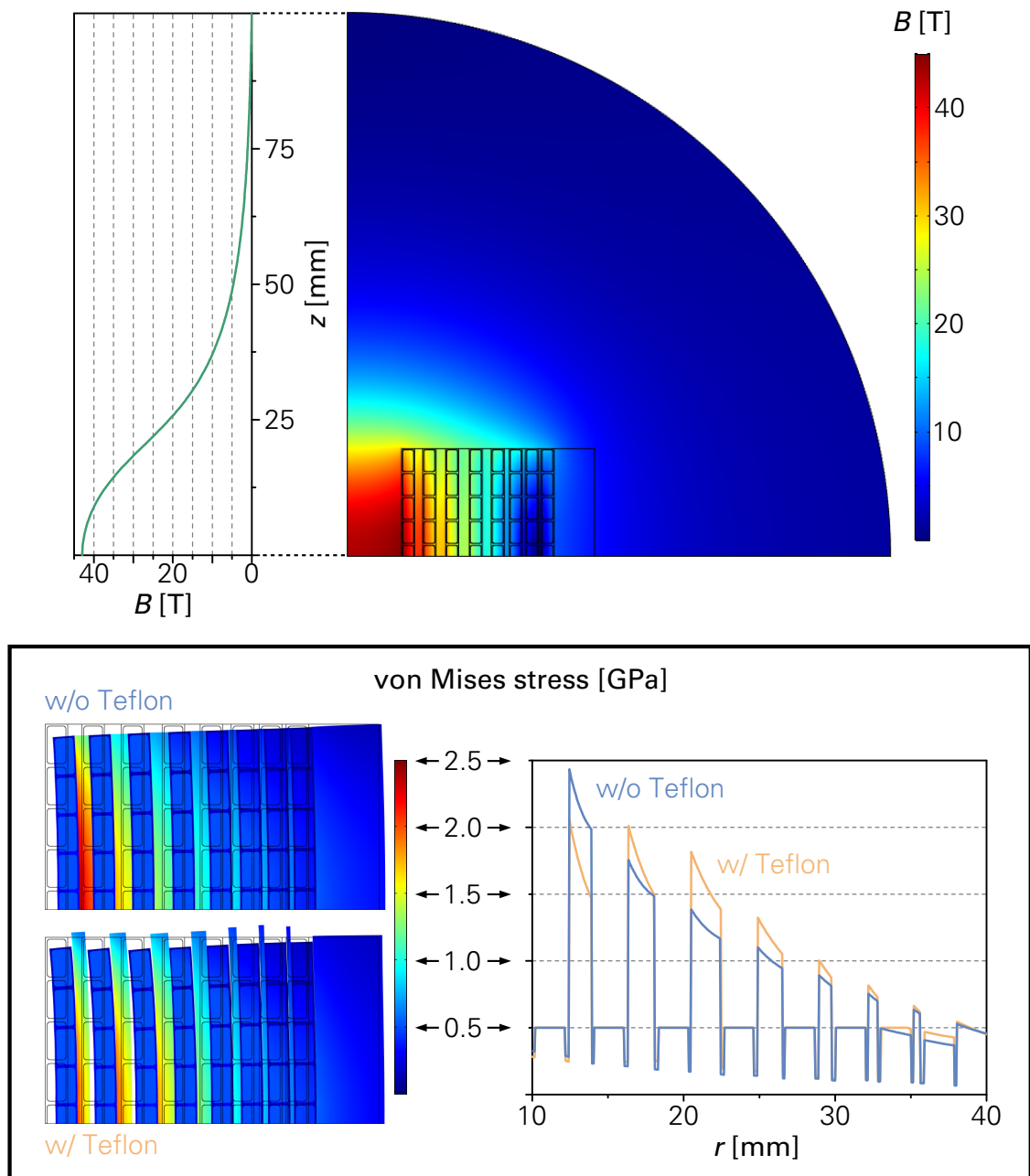


Figure 3.10: Top: Color-coded field map and line out of corresponding on-axis field for the 40-T-solenoid at 30 kA winding current. The small rectangles depict the wire loops, backed by Zylon reinforcement layers of different thicknesses. Axial and mirror symmetry of the cylindrical magnet have been used to keep the simulation small. Box: Von Mises stress distributions for a coil equipped with Teflon, i.e. layers are allowed to separate, and without Teflon. The midplane stress plot shows more equally distributed peak stress on the reinforcement for the coil modeled with separation (w/ Teflon). Both results are uncritical with respect to the UTS of the Zylon reinforcement compound of the order of 3 GPa. The deformation depicted on the left is tenfold exaggerated for demonstrative purposes.

magnet. Ideally the source is far in front of the coil, and the ions start rotating when passing the magnetic fringe field while entering the solenoid. This movement is canceled out at the other side of the solenoid when the particles leave the field again as shown in section 3.1.2. In case of a laser target very close to or inside of the magnet, the ions are not generated in a field free region, thus they do not pass the first fringe field region to full extent. As already presented in the previous section 3.2.3, charged particles ( $n$ ) generated with a certain divergence and radial displacement  $r_{0,n}$  inside a solenoid show helical trajectories of radii  $r_{c,n}$ <sup>6</sup>, whose centers are at distances  $\Delta r_n = r_{0,n} \pm r_{c,n}$  from the solenoid axis ( $\pm$  depending on the chirality of the helical trajectory). In section 3.1.2 it has been shown that for particles on helical trajectories intersecting the solenoid axis, the azimuthal velocity components cancel when the particles leave through the second fringe field region. More detailed theoretical analyses, based on the concept of canonical angular momentum conservation [84], show that this scenario, with  $\Delta r_n = r_{c,n}$ , is the only case where the particles leave the magnet with only the desired radial velocity components, without azimuthal shares. For the presented setup, only ions originating from the axis of the solenoid in general fulfill this criterion. Therefore, off-axis particles usually leave the magnet with nonzero azimuthal momenta and thereby increase the emittance of the beam and limit the ability to focus the beam.

Anyhow, due to the small dimensions of the laser-driven particle source (several 10  $\mu\text{m}$  diameter) the emittance growth might be tolerated when, in return, the capture efficiency is increased. GPT particle tracing simulations have been carried out to compare the transport performance of the 40-T-solenoid with the capturing solenoid. The proton source was tailored to resemble a typical TNSA proton distribution generated by Draco TW, with the following parameters: Number of simulated protons  $N_{p,\text{sim}} = 45,000$ , exponentially decaying energy spectrum in the range of  $E_{\text{kin}} = 3$  to 14 MeV and maximum proton half-angle divergence of  $\theta_{\text{max}} = 12.4$  to  $9.1^\circ$  (lower values for high energies). The source was placed on-axis at the position of the first winding of the simulated 40-T-solenoid or 8 cm in front of the capturing solenoid's first winding (typical experiment condition). The protons were transported over a total distance of 1 m, where an aperture of 1 cm diameter was used to filter out stray particles.<sup>7</sup> The maximum on-axis field for the 40-T-solenoid was chosen to be 42 T in accordance to the Comsol simulation. The field amplitude at target position was approximately 30 T (cf. fig. 3.10). The mean transported particle energy was 11.4 MeV. The field of the capturing solenoid was tuned to transport the same mean energy efficiently through the aperture. A field value of approximately 8.5 T resulted.

The simulations show that the 40-T-solenoid can provide for transport efficiencies close to 100 % for particle energies around 11 MeV. In comparison, the transport efficiency of the capturing solenoid was determined to be  $< 50$  %. Furthermore, the particles transported via miniature solenoid show excellent beam properties in terms of emittance and divergence at focal position (cf. fig. 3.11).

As can be seen from fig. 3.11, the particle bunch transported by the 40-T-magnet exhibits a very low  $x'$  for all energy components, whereas the capturing solenoid, with its large aperture, is generating larger divergence angles at aperture position. The beam envelope stays smaller by a factor of four in the first case. The high transport efficiency and the well defined beam make the 40-T-solenoid an excellent candidate for beam transport experiments, such as injection into conventional accelerator structures or direct (radiobiological) irradiation

<sup>6</sup>The only exception are particles generated with momenta solely in z-direction, thus parallel to the magnetic field lines.

<sup>7</sup>In reality this aperture might be the entrance of an accelerator cavity, a beam pipe or a pinhole absorber for energy selection or lateral beam shaping.

### 3.2 Developed Pulsed High-field Magnets

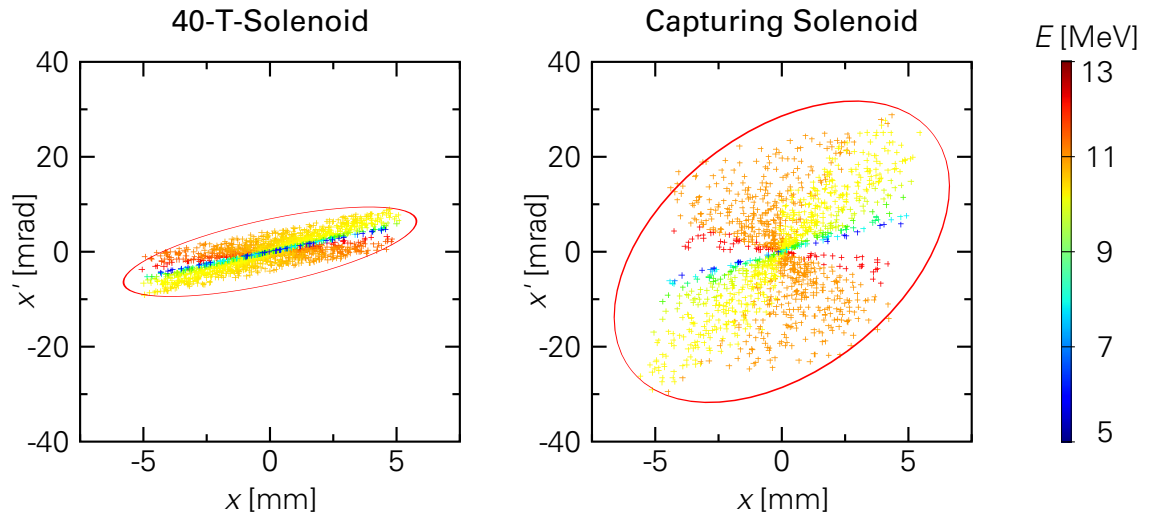


Figure 3.11: Phase space plot at aperture position (10 mm diameter, 1 m downstream of source) for a TNSA particle source inside the 40-T-solenoid (left, at first winding position) and 80 mm in front of the capturing solenoid (right). Red ellipses illustrating the emittance.

experiments, e.g. irradiation of two-dimensional in vitro cell cultures or volumetric tumors in small animal models.

Finally, it has never been experimentally studied how a TNSA ion source acts under the influence of a strong external magnetic field. Therefore, the developed magnet could be a first step towards a new type of studies: Target normal sheath acceleration in an external magnetic field. First important insights on the effect of strong magnetic fields interacting with the TNSA plasma might be acquired. Preliminary particle-in-cell simulations show that the effect of an external 40 T field on the acceleration performance is rather low. Nevertheless, studying interaction of the magnetic field not only with the generated ions but also with the electrons of the pre- and/or main plasma could help understanding the complex plasma dynamics of laser acceleration – with the presented solenoid as forerunner.

#### 3.2.3 SPLIT-PAIR SOLENOID

The third magnet developed during this work strongly differs from the previously presented solenoids. It has been designed for laser-driven laboratory astrophysics experiments at the LULI2000 laser system at École Polytechnique in Palaiseau, France. The principle application concept is illustrated by fig. 3.12 and can be explained as follows: Instead of using a single solenoid the coil is split in two halves ideally in Helmholtz coil configuration. In the magnetic field region between the coil halves, a laser-driven plasma or particle source can be probed by methods, such as shadowgraphy, streaked or gated optical imaging, pyrometric measurements and (X-ray) radiography owing to the separation of the coils [110, 111]. The application of the coil is thereby certainly not limited to laboratory astrophysics.

The purpose of the high-energy density laboratory astrophysics experiment was to study radiation hydrodynamic processes coupled with an external magnetic field as present in binary star systems known as magnetic cataclysmic variables. Cataclysmic variables consist of

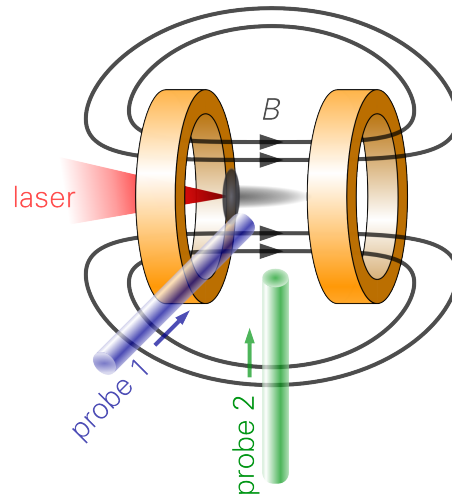


Figure 3.12: Schematic of the split-pair solenoid (orange) and its application: The coil gap allows for optical access to the laser-driven plasma or particle source. Probe beams can image the plasma outflow and measure plasma properties inside the tunable  $B$ -field.

a white dwarf primary star and a mass transferring secondary star, often named donor [112]. When the magnetic field of the white dwarf is high enough, i.e.  $B > 10 \text{ MG} = 1 \text{ kT}$ , matter coming from the donor is accreted through a collimated column and impacts the white dwarf atmosphere. To improve the modeling and understanding of accretion phenomena occurring in these highly magnetized white dwarfs, also known as polar stars, the POLAR project has been founded [113, 114]. Within the project, astronomical observations are compared to theoretical, numerical and experimental studies, leading to the challenge to generate plasma conditions in an experiment that are similar to the conditions at astrophysical scale.

Up to now, experiments used a tube in order to collimate the plasma flow which was generated by a strong shock from a long pulse, i.e. ns, laser [115]. The result is a multiplicity of unwanted effects such as wall shocks or tube explosion. To avoid these issues, it was proposed to use a pulsed high-field solenoid to generate a confining external  $B$ -field parallel to the plasma flow, thus mimicking the astrophysical scenario. The radial plasma confinement can be explained in analogy to the solenoidal focusing discussed in section 3.1.2. Although, the plasma does not pass the fringe fields, the initial outward directed radial velocity gives rise to an azimuthal velocity that similarly forces the plasma electrons and ions on helical trajectories. In order to study the coupling of radiative processes in the supersonic plasma flow with magnetic effects, it is necessary to have optical access to the interaction area. A split-pair solenoid prototype has been manufactured to facilitate a first proof-of-principle experiment.

The experimental setup can be described as follows: The frequency doubled NANO2000 beam (1.5 ns pulse length, 400 J pulse energy at 530 nm wavelength) is focused onto the target (400  $\mu\text{m}$  focus diameter FWHM). The target, a small 25  $\mu\text{m}$  thin polystyrene disc with a 6  $\mu\text{m}$  tin coating layer, is placed on axis but slightly shifted towards the incoming laser beam, thus not centrally located between the coil halves. The laser triggers a super-sonic plasma outflow that can be imaged by means of optical and X-ray diagnostics. The optical di-

### 3.2 Developed Pulsed High-field Magnets

agnostics, e.g. shadowgraphy by a short pulse laser, were, in analogy to probe 1 in fig. 3.12, arranged in the horizontal direction. The X-ray radiography was installed in a bottom-up geometry in accordance to probe 2 in fig. 3.12. The X-rays were generated by means of the short pulse laser PICO2000 (1 ps pulse length, up to 25 J pulse energy at 530 nm wavelength). The PICO2000 beam was focused on a 25  $\mu\text{m}$  vanadium wire acting as X-ray backlighter. The X-rays probing the plasma are detected by a 100  $\times$  100 mm<sup>2</sup> image plate (IP) [116]. The IP was placed 588 mm away from the X-ray source, resulting in a magnification factor of 25. A detailed description of this diagnostic can be found in Brambrink et al. [117].

The diagnostics could be delayed with respect to the interaction moment of the main driver beam (NANO2000). In this way, the temporal evolution of the plasma expansion can be imaged. Figure 3.13 compares two X-ray radiographs taken at a 60 ns delay between PICO2000 and NANO2000 beam, one without external magnetic field and the other with a confining 10 T field, the maximum field strength achievable in the proof-of-principle experiment.

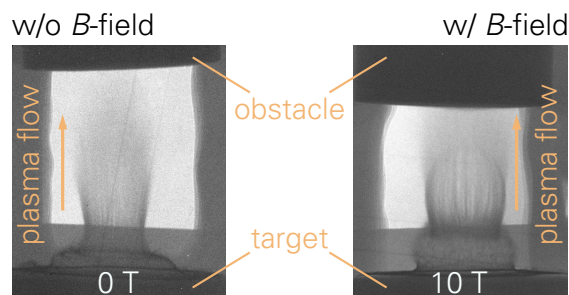


Figure 3.13: X-ray radiographs of the plasma outflow 60 ns after the laser target interaction. The left side shows the plasma plume without external magnetic field. The right side depicts the plasma under identical conditions but with external  $B$ -field of 10 T present. The radial confinement of the plasma outflow is already visible for this moderate field strength. The obstacle was made of aluminum and installed 3 mm (left) and 2.7 mm (right) downstream of the target to mimic the impact of the astrophysical plasma on the white dwarf atmosphere.

On the left, the plasma outflow without external magnetic field is depicted; the right side shows the corresponding radiograph when the split-pair solenoid is pulsed. The moderate magnetic field confines the plasma outflow, in fact, after longer propagation under influence of the field, i.e. in fig. 3.13 on the upper end of the plasma plume, an inward flow towards the magnet axis can be distinguished. Therefore, the principle application idea has been proven valid. Anyhow, to ensure the scalability to the astrophysical scale, it is desirable to generate even higher fields in excess of 15 T. Therefore, for follow-up experiments the coil design has been revised accompanied by changes of the experiment setup. The result of the revision process as well as important design features of original and improved design are depicted in fig. 3.14.

In general, a coil design as depicted in fig. 3.12, with complete unobstructed access to the interaction area, is very challenging. The coil halves exert strong attracting forces that need to be taken up by a support structure in between. The design process yielded a setup with two consecutively wound coil halves on a PEEK plastic body, giving the ideal compromise between mechanical strength, vacuum compatibility and electrical insulation. In the coil gap two bores perpendicular to the coil axis give access to the interaction area. These bores

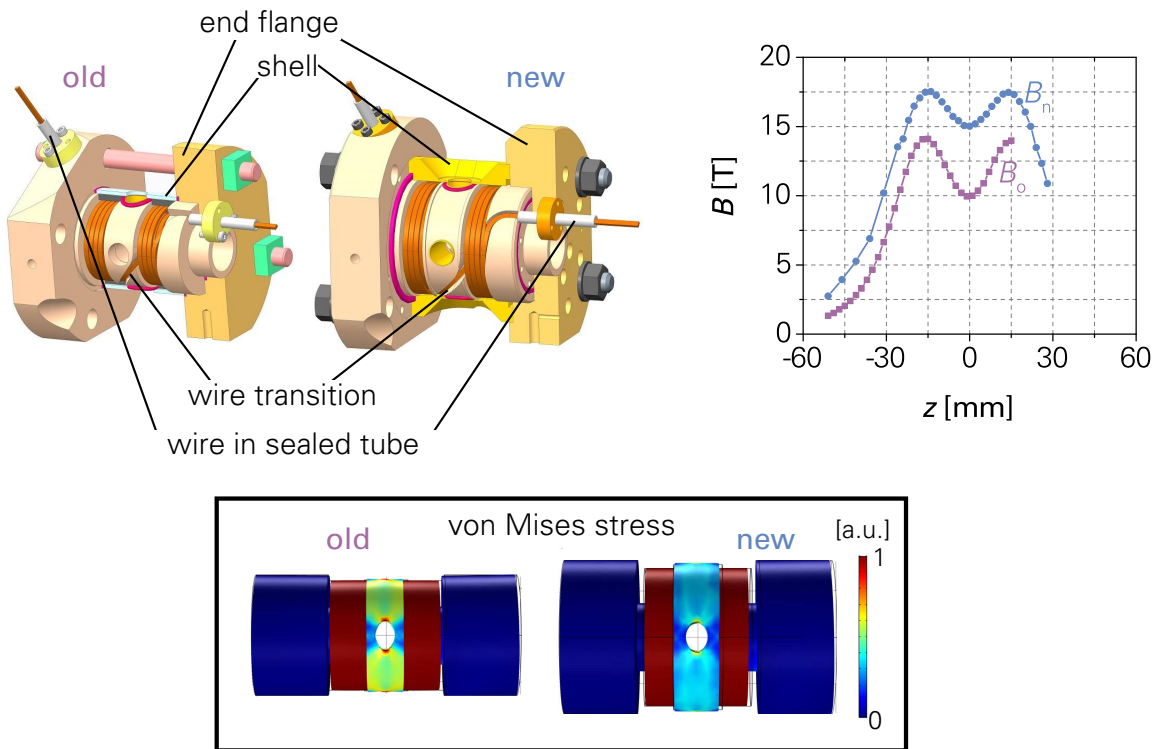


Figure 3.14: Left: Construction models of the first prototype (old) of the split-pair magnet and its latest iteration (new). The transition of the wire from first to second half is indicated. The coil windings are sealed (exemplary sealing rings depicted in pink) with respect to the exterior vacuum, the wires are guided in tubes out of the vacuum chamber. The diagnostic bores perpendicular to the coil axis allow for optical access to the laser target interaction area. Right: The corresponding (DC)  $B$ -field Hall probe measurements for old and new design, scaled to the maximum field allowed for operation. Box: Von Mises stress distributions on the material separating the coil halves. The stress is drastically reduced for the new coil (deformation tenfold exaggerated for demonstrative purposes).

weaken the gap material but are essential for the application purpose. For the first prototype magnet the material separating the coil halves was crushed when the field exceeded 12 to 13 T.<sup>8</sup> As a result, the amount of supporting material has been increased axially and radially for the revised split-pair solenoid. To account for the larger axial separation the number of windings has been increased. The first design is based on a winding scheme with four wires in three layers per coil half; the new design employs three wires in five layers. The wires are resin insulated soft copper with  $2 \times 1 \text{ mm}^2$  cross section.

As can be seen from the field measurements in fig. 3.14, the experiment geometry made it necessary to deviate from the ideal Helmholtz coil geometry, thus resulting in a local field minimum in the gap. For the first design the gap field amounts to 71 % of the maximum, for the new design, respectively, 86 % are measured. Both magnet constructions employ a compact sealed PEEK housing for operation under high vacuum conditions for the same reasons as explained in section 3.2.1. The housing adds up only marginal to the magnet size

<sup>8</sup>The operation at 10 T gap field therefore comprises a certain safety margin.

### 3.3 Developed Portable Current Pulse Generators

and mainly consists of the shell. The wires are guided inside of flexible plastic tubing to the outside of the vacuum chamber. The shell has been strengthened for the revised magnet solenoid and can be bolted to the coil flanges for force closure. The size is thereby only slightly increased. Both split-pair magnets are 101 mm long; the old design has a radial flange diameter of 110 mm, whereas the new magnet is slightly larger with 118 mm. It may be noted, that due to its small dimensions and the low number of winding the heat-up of the coil during a single pulse only allows for single shot operation with cool down periods of several 10 min. The LCR meter measurements of the split-pair solenoid yielded an inductance of 9.5  $\mu\text{H}$  and a resistance of 20  $\text{m}\Omega$  at a test frequency of 2 kHz.

The novel design successfully reduces the stress on the gap material as can be seen from the von Mises stress plot in fig. 3.14. It has been experimentally proven to be safe for operation up to the desired gap field of 15 T. Hence, it allows for first magnet-assisted laboratory studies on polar star accretion phenomena actually comparable to the astrophysical scenario. Follow-up experiments at LULI are ongoing.

As already mentioned in the beginning of this chapter, the split-pair solenoid allows also for a variety of other application. For example, the perpendicular bores can and already have been used to deflect an incoming particle beam in the dipole gap field, as will be presented elsewhere. The previously presented concept of a TNSA particle source inside of an external magnetic field can also benefit from the developed coil design as the bores simplify target adjustment and give access for various probe beams to characterize plasma and pre-plasma conditions.

## 3.3 DEVELOPED PORTABLE CURRENT PULSE GENERATORS

This section deals with the pulse generator technology that has been developed during the work for this thesis. Three portable pulse generators have been designed for the experiments presented in this thesis and future experiments. Two are in routine operation, one is currently under construction. The pulse generators are referred to as portable, but are in no case hand-held or carry-on devices. The large high-power, high-voltage components result in a typical floor space requirement of two to three square meters for a single pulse generator. In spite of their size and weight (usually several hundred kilograms) they are not limited to stationary operation. In fact, the pulse generators have been transported multiple times between different research facilities in Dresden and Darmstadt. Transport preparation and on-site setup can be performed within few hours.

### 3.3.1 PULSE GENERATOR PG3

The first pulse generator that has been developed within the scope of this thesis is the third in the development history of the Institute of Radiation Physics at HZDR. Therefore, it is named PG3 in the following. In the first place, PG3 was built to enable pulsed high-field magnet experiments at the HZDR laser accelerator Draco, since the pulse generators of the first and second generation were permanently transferred to collaborating labs<sup>9</sup>. The pulse generator design and commissioning process was accompanied by technological scalability studies. PG3 composition was tailored to meet the demands of larger coils (> 100  $\mu\text{H}$ ) such as the

---

<sup>9</sup>PG1 was developed for fundamental plasma physics experiments at the LULI laser lab in Palaiseau, France. PG2 is used for beam transport experiments at the PHELIX laser at GSI Darmstadt, Germany

capturing solenoid or the 40-T-solenoid. A full circuit diagram including detailed explanations can be found in fig. 3.15.

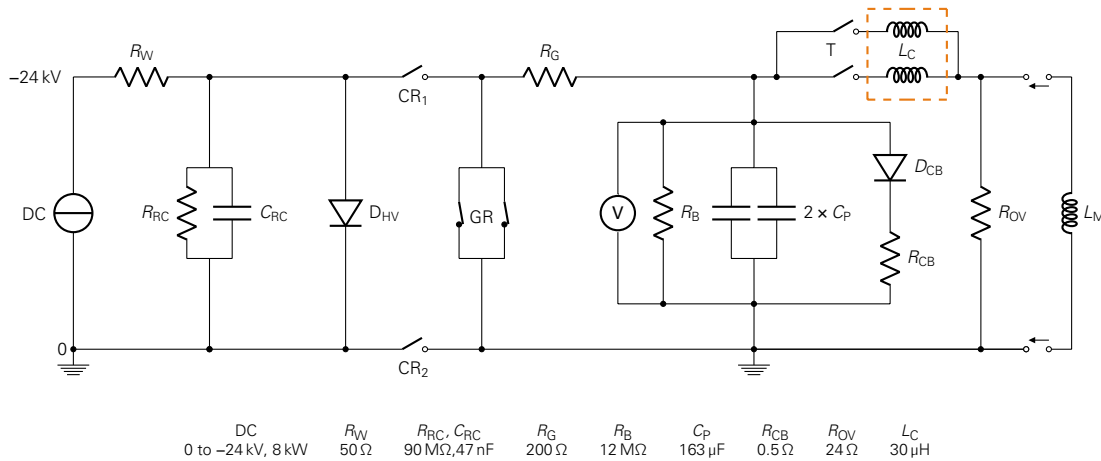


Figure 3.15: Circuit diagram of PG3: The constant DC source is used to charge the pulsed power capacitors  $C_P$ , the source requires a basic load consisting of a wire resistor  $R_W$  and RC-circuit ( $R_{RC}, C_{RC}$ ),  $D_{HV}$  protects the source from reverse currents, the normally open (NO) charging relays  $CR_{1,2}$  separate charging unit from pulsed power branch before the current pulse is triggered. The normally closed (NC) grounding relays  $GR$  are opened during charging and pulse. They close after the current pulse or, in case of pulse abort, discharge the capacitors over the grid resistor  $R_G$ . The voltage divider  $V$  is used to record the temporal evolution of the capacitor voltage. In case of a severe malfunctioning that forbids approaching the PG, the bleeder resistor  $R_B$  slowly drains the capacitors to the point when a safe approach can be made ( $t_{drain} \approx 1$  d). The crowbar diode circuit,  $D_{CB}$  and  $R_{CB}$ , has been explained previously. Rightmost, the connection of a high-field electromagnet  $L_M$  is illustrated. Resistor  $R_{OV}$  protects PG and magnet from over-voltage when the thyristors  $T$  are triggered. The dashed orange box indicates choke inductances  $L_C$  that were temporarily installed for functional testing. Important parameters given below.

The pulse generator employs two 163  $\mu$ F capacitors connected in parallel. They can be charged up to a maximum voltage of -24 kV resulting in a stored energy of 94 kJ. The capacitors limit the maximum repetition rate of PG3. Whereas, the 8 kW charger can in principle charge the capacitors within 12 seconds<sup>10</sup>, the capacitors are specified with a maximum pulse repetition rate of 0.5  $\text{min}^{-1}$ . For non-full-energy pulses, pulse repetition rates of up to 3  $\text{min}^{-1}$  have been successfully demonstrated with PG3.

A very important technical improvement was made during the development of PG3. In previous studies by Burris-Mog [42], seemingly inexplicable coil failures occurred due to over-voltages in excess of 24 kV. Thorough analysis led to the assumption that the coaxial cable that connects PG and magnet is causing the over-voltage due to poorly matched impedance values. The results are cable reflections and dangerously high voltages in the beginning of the capacitor discharge becoming more severe for longer cables lengths. By introducing

<sup>10</sup>Measurements have shown that the charging time for a 24 kV pulse is slightly prolonged to 14 s in comparison to the theoretical optimum.

### 3.3 Developed Portable Current Pulse Generators

the high-voltage resistor  $R_{OV}$  (cf. fig. 3.15) potential over-voltages can be efficiently damped without losing the flexibility of using different cable lengths and load inductances/magnets.

In PG3 as well as in all other pulse generators presented in this work, every input and output signal is registered, processed and transferred by a FPGA-based real-time controller with analog and digital input and output modules. Control/return signals are transmitted via fiber optic cables to ensure galvanic isolation. The signals are processed by LabView software running on standard computer hardware.

With regard to future pulse generator designs, the development of PG3 went along with technological scalability studies towards higher stored electrical energies and thereby potentially higher fields. The idea of a scalable pulse generator platform based on the technology of PG3 is the following: To reach higher field strengths the number of parallel operated capacitors can be increased, e.g. from one to four. Thereby, the energy transferred to the pulsed magnet is increased proportionally and has to be carried by the switch. To prevent an overload of a single switch, switches need to be operated in parallel analog to the capacitors. Thereby, the exemplary case of a fourfold energy gain (by equipping a one capacitor pulse generator with three additional capacitors) is accompanied by the installation of three further switches. A successful demonstration of this approach would enable extensive scalability. Unfortunately, the studies conducted on PG3 have shown that the chosen switch technology is not applicable for such an easily scalable pulse generator platform. The reasons will be explained in the following:

PG3, employing two capacitors, was equipped with two switches as well. The chosen switches are thyratrons, gas-filled tubes that are commonly used as fast high-power switches or rectifiers. A thyatron becomes conducting when an arc discharge between anode and cathode is triggered by the intermediate control grid electrode. The installed thyratrons are hydrogen-filled and can conduct very high currents ( $I \leq 200$  kA). They are robust, inexpensive and allow for highest current rise times of the order of  $10^{12} \text{ A s}^{-1}$  thus enabling short current pulse lengths. Their low jitter  $\leq 3$  ns motivated the attempt to operate multiple switches in parallel. They are specified with a maximum peak energy transfer per pulse of 40 kJ. Thus, a full energy current pulse (94 kJ) results in a slight overload of two parallel thyratrons. That, however, was identified to be not severe for first functional testing.

The intrinsic trigger delay of a thyatron can be changed by adjusting the heater voltage of the hydrogen reservoir and thereby the temperature of the filling gas. By carefully tuning the heater voltage the parallel operation could be successfully demonstrated with both thyratrons conducting almost equal shares of the coil current. Anyhow, especially for comparatively low voltages  $\leq 10$  kV the parallel operation was determined to be very unstable. Typically, only one of the thyratrons was carrying the total current alternating unpredictably between the two thyratrons from pulse to pulse. As one thyatron starts to conduct current the voltage across the second immediately drops and the discharge cannot be triggered due to the low potential difference between anode and cathode. The switch that sparked first is therefore carrying the full current and stressed by the high transported energy. To prevent the rapid voltage drop at the late igniting thyatron, choke coils of  $30 \mu\text{H}$  inductance have been temporarily introduced (see dashed orange box in fig. 3.15). Figure 3.16 shows the corresponding current distributions in both switches for a full energy pulse with capturing solenoid as inductive load and installed choke coils. The switching process became more reliable but over-voltages at the outside of the thyratrons, due to the attenuated current rise, resulted in arcing. As final approach the parallel connection of the capacitors was broken up and each capacitor was equipped with its own thyatron before closing the parallel loop again. This circuit setup lead to strong current flows between the two capacitors making the

generation of a well defined current pulse impossible.

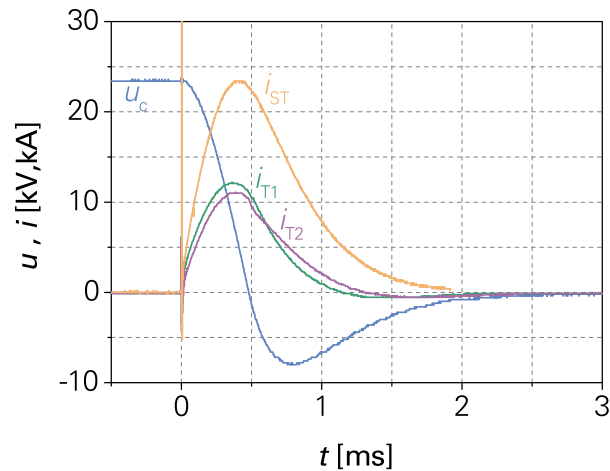


Figure 3.16: Measured thyatron currents  $i_{T1}$  and  $i_{T2}$  for a  $u_c(t=0) = 24$  kV full energy pulse employing choke coils to prevent rapid voltage drop at the late thyratrons. In comparison the current  $i_{ST}$  for single thyatron operation without choke is depicted. The spike at the beginning of the current rise is noise from the thyatron switching process.

In conclusion the parallel operation of thyratrons to gain scalability in the presented portable pulse generator is not advisable since the switching behavior is unpredictable. Thus, alternative approaches should be considered for future developments. One approach is outlined in section 3.3.3. For practical reasons and after consulting the manufacturer of the thyatron it was decided to operate PG3 always just with one thyatron. The choke coils were removed after the presented measurements.

According to eq. (3.37) a thyatron overload occurs for capacitor charge voltages in excess of 16 kV. The number of current pulses in excess of 16 kV in an experiment is usually low, full energy pulses (cf. orange curve in fig. 3.15) are very rare, thus the thyatron is only infrequently stressed by transported energies beyond specification. The manufacturer assumes that the life span of the switch is reduced in the presented operation scenario. So far the thyatron has successfully completed several thousand current pulses, thereof the number of pulses potentially stressing the thyatron was of the order of 100. A thyatron failure was never observed. If a thyatron failure occurs in the future, the second thyatron that is still installed but not triggered, can be made ready for operation within minutes.

### 3.3.2 PULSE GENERATOR PG4

The pulse generator of the fourth generation has been developed to enable experiments with highest currents for low inductance magnets, e.g. the split-pair solenoid. PG4 is the first pulse generator with a modular setup. It employs a more robust type of capacitor that can be discharged faster and to full voltage reversal. On the other hand, the capacitors are more expensive and feature a lower energy density. Protective measures, such as safety chokes, have been introduced. The development will be discussed in the following:

For applications where repetition rate is not a concern, small coils of only a few ten wind-

### 3.3 Developed Portable Current Pulse Generators

ings, like the split-pair solenoid, can be used to generate high magnetic fields. The lack of windings needs to be counterbalanced by higher current fluxes. Low inductance values of the order of  $10 \mu\text{H}$  result in very short current rise times that can damage capacitors, switches and other components. Feeding small inductance magnets with the above described PG3 is possible but limited by the specifications of the capacitors<sup>11</sup>. To get rid of these limitations, PG4 was designed in analogy to PG1 that has been used for laboratory astrophysics experiments, including the upper mentioned, at the LULI laser lab in France [110, 111]. The circuit diagram is depicted in fig. 3.17. All components were chosen to enable the operation of magnets in the range of 1 to  $50 \mu\text{H}$  while tolerating highest currents and fast voltage and current changes.<sup>12</sup> Thus the capacitors can be operated at a maximum repetitive voltage change of  $du/dt = 1010 \text{ V}\mu\text{s}^{-1}$  and tolerate a maximum voltage reversal of 95 %. A damping crowbar diode circuit is installed but can be removed if necessary. The thyatron (identical to PG3) allows for current rise times of  $di/dt = 3000 \text{ kA}\mu\text{s}^{-1}$ . PG4 originally is built up by four  $16 \text{ kV}$  capacitors of  $50 \mu\text{H}$  each. At the moment it is upgraded to house additional two capacitors, increasing the total capacitance from 200 to  $300 \mu\text{H}$  and the maximum stored electrical energy from 25.6 to  $38.4 \text{ kJ}$ . Thus, even after the upgrade the installed thyatron is not stressed beyond energy transport limits.

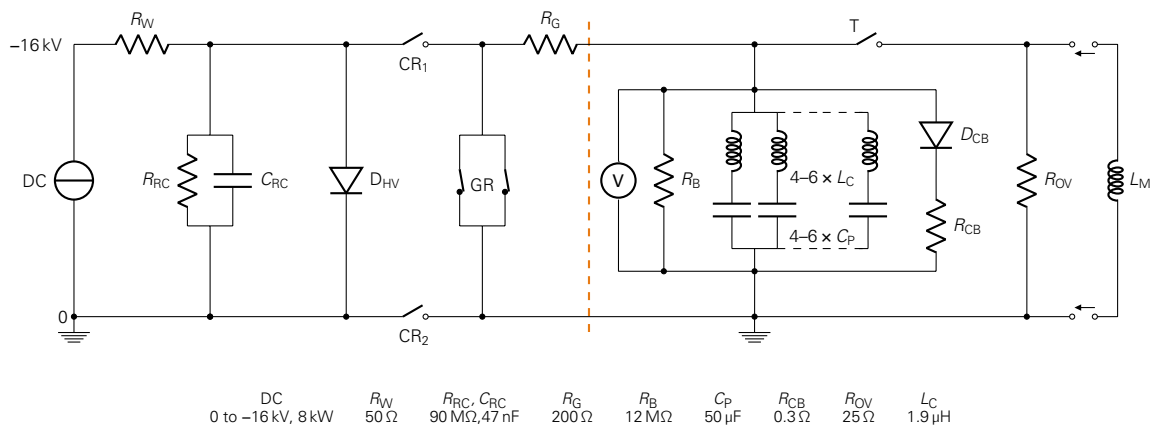


Figure 3.17: Circuit diagram of PG4: Naming and functional principle as described in fig. 3.15. The orange dashed line indicates that charging unit (left) and pulsed power branch can be separated. Important parameters given below.

Besides the capacitors with high voltage reversal and high  $du/dt$ , two novelties are associated with PG4. The fourth generation pulse generator is the first with a modular setup. Since the charging and control hardware can be designed independently of the actual high-power, high-voltage branch of the pulse generator, it was decided to develop a unit housing the DC charger and all the generally required control and safety hardware. This unit can be used easily with all types of pulse generators simply by altering the software running on the FPGA controller. Thus, in case of damage, the charging unit of one pulse generator can be replaced by the corresponding unit of another. The overall flexibility of the PG technology has been drastically increased. Maintenance is simplified and downtimes can be prevented.

The second novelty is a safety feature that is supposed to protect the capacitors of PG4. The pulse generator is equipped with up to six capacitors. The probability of failure for the

<sup>11</sup>Especially the limited action integral  $\int i^2 dt \leq 1.5 \cdot 10^5 \text{ A}^2 \text{ s}^{-1}$  is easily exceeded for low-inductance loads.

<sup>12</sup>Higher inductance values typically are not problematic. PG4 can therefore also be used to power the capturing solenoid or other high inductance magnets.

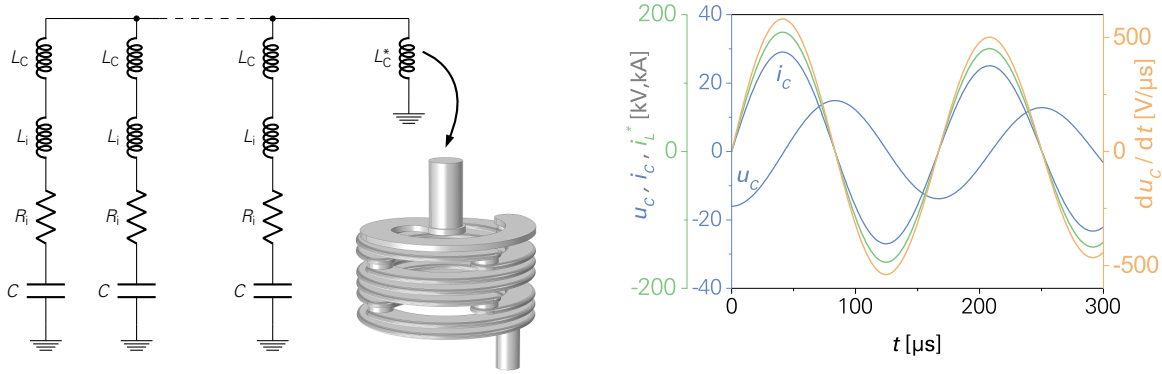


Figure 3.18: Capacitor protection choke coils of PG4: The left shows the simulated circuit and the design of a single choke coil. One of the six capacitors is supposed to be damaged in a way that its internal inductance  $L_i$ , internal resistance  $R_i$  and capacitance  $C$  are zero and only the choke coil inductance  $L_C$  remains (right side of the circuit diagram). The other five capacitors feed into the short circuit. The simulation input parameters are:  $u_C(t=0) = -16$  kV,  $C = 50$   $\mu$ F,  $L_i = 0.8$   $\mu$ H,  $R_i = 25$  mH and  $L_C = 1.9$   $\mu$ H. As can be seen from the simulation result on the right, the maximum repetitive voltage change of  $du_C/dt = 1010$   $V \mu s^{-1}$  is not reached (orange). The peak pulse current of a single capacitor is noncritical ( $i_C < 30$  kA).

capacitors is still very low but if a single capacitor should be damaged or destroyed during a pulse, all remaining capacitors feed into this defect. The thereby shorted capacitors are exposed to the risk of being equally damaged or destroyed. A defect of a single capacitor can therefore trigger a chain reaction that destroys the entire capacitor bank. To prevent that from happening, every single capacitor is supplied with a series choke inductance, see fig. 3.17, limiting current and current rise times to a tolerable level. The inductance of a single choke coil was chosen to be 1.9  $\mu$ H. Figure 3.18 shows circuit simulation results and compares the outcome with critical component parameters. The simulations demonstrate that the chokes keep the capacitor current well below the limit of 50.5 kA and the voltage change under  $1010$   $V \mu s^{-1}$ . The choke coil  $L_C^*$  of the damaged capacitor (see right side of circuit diagram in fig. 3.18) has to carry the sum of all capacitor currents. The coils were therefore designed for highest mechanical strength. The design process was accompanied by Comsol stress simulations.

Considering the introduced choke inductances, in combination with internal resistances and inductances of bus bars and cable connections, it is possible to assess the risk for damaging the PG when a pulsed high-field magnet fails and its inductance and resistance abruptly drops to zero. In such a case, the components of PG4 are still operated within their specifications. This makes PG4 the ideal source for powering novel, untested coil prototypes, since it is the pulse generator least likely to be damaged by a failing coil. Figure 3.19 shows the measured coil current and capacitor voltage of the first performed full energy pulse provided by PG4 in its commissioning phase, the load being a robust 80  $\mu$ H test coil.

The theoretical maximum of the repetition rate of pulse generator PG4 is 0.2 Hz. However, especially the heat input for small coils limits the repetition rate in dependence on coil

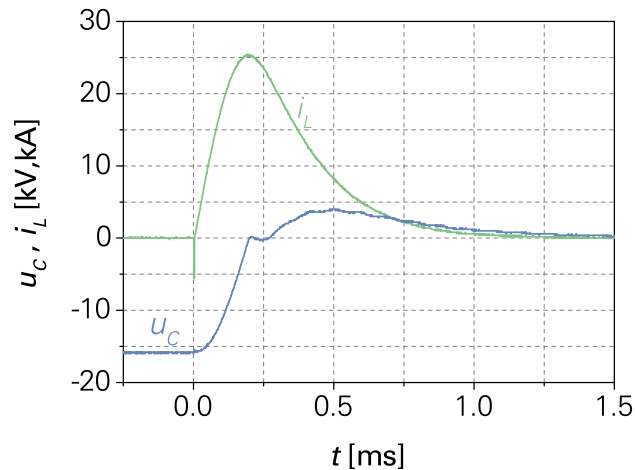


Figure 3.19: First full energy pulse measurements on PG4: The plot shows coil current, measured by means of a Rogowski coil, as well as capacitor voltage, measured by voltage divider. The discontinuous behavior of the capacitor voltage at zero crossing is caused by the introduced choke coils but uncritical.

parameters.

#### 3.3.3 PULSE GENERATOR PG5

In this section the functional principles of the technologically most advanced pulse generator, PG5, will be discussed. During the preparation of this thesis, the construction of PG5 has begun. What will be presented in the following is the elaborated concept for the pulse generator.

In section 3.3.1 it has been shown that thyratrons only allow for limited scalability in terms of transported energy per pulse. The pulse generator of the fifth generation has therefore been designed for operation with a better scalable switching technology adopted from the Dresden High Magnetic Field Laboratory (HLD). Instead of relying on gaseous switches like the thyatron, HLD solely employs solid-state semiconductor switches, so-called thyristors. A thyristor is a semi-conductor switch that is controlled by a gate structure analog to the thyatron.<sup>13</sup> The disc shaped switches are typically built up in a stacked configuration. The stacking allows for blocking even higher inverse voltages. PG5 will operate with one stack of five thyristor discs of type T1503N from Infineon Technologies Bipolar GmbH & Co. KG. [118]. The thyristors are triggered by intense UV laser light pulses transported via optical waveguides. In comparison to a thyatron, the presented switch is more expensive by a factor of ten but provides for the highest reliability.

PG5 combines conceptual ideas of PG3 and PG4. In terms of electrical properties, PG5 is basically identical to PG3 as can be seen from the circuit diagram in fig. 3.20. The fifth generation pulse generator employs the same capacitors ( $2 \times 163 \mu\text{F}$ ), thus can also store 94 kJ electrical energy and has the same repetition rate limitations. The modular setup of PG4 was kept for PG5.

The experience of HLD with thyristor switches has shown that the switches are destroyed immediately when the specified maximum current rise of  $(di/dt)_{\text{max}} = 300 \text{ A}\mu\text{s}^{-1}$  is ex-

<sup>13</sup>In fact, the name thyristor has been blended from thyatron and transistor.

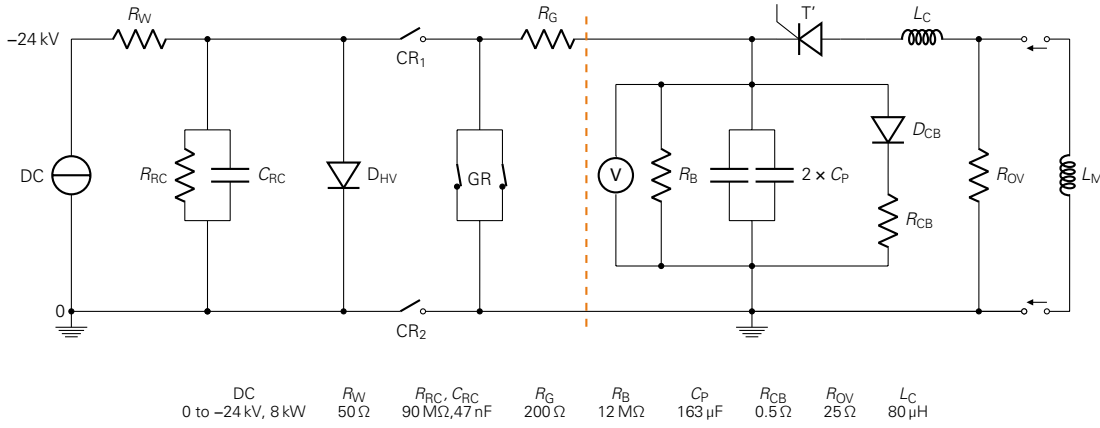


Figure 3.20: Circuit diagram of PG5: Naming and functional principle as described in fig. 3.15, the switch  $T'$  is here a thyristor instead of a thyratron. As with PG4, PG5 features a modular setup with separable charging and pulsed power units (orange dashed line). Important design parameters given below.

ceeded. As already mentioned in the previous section, the failure of a pulsed magnet typically goes along with its resistance and inductance dropping to zero thus resulting in a dramatic increase of  $di/dt$ . Considering the high cost of semiconductor switches, additional safety measures that protect the thyristor switch in case of a coil failure are indispensable.

As noted in section 3.3.2, the current rise can be limited by introducing an additional inductance, connected in series with the main pulsed coil, to the circuit. In case of a failing pulsed magnet, solely the choke is responsible for the limitation. In the fault case, the choke inductance  $L_C$  is carrying the current  $i_C = i_{C,max} \sin \omega t$ .<sup>14</sup> The maximum current rise can be calculated from the derivative of the sinusoidal current. It follows

$$\left( \frac{di_C}{dt} \right)_{\max} = \omega i_{C,max}, \quad (3.46)$$

with the constraint that the calculated maximum rate of current rise is within the thyristor specification, namely

$$\left( \frac{di_C}{dt} \right)_{\max} \leq \left( \frac{di_T}{dt} \right)_{\max} = 300 \text{ A } \mu\text{s}^{-1}. \quad (3.47)$$

With eq. (3.39) on page 37 the peak current can be expressed by

$$\left( \frac{di_T}{dt} \right)_{\max} \geq \omega u_{\max} \sqrt{\frac{C}{L_C}}, \quad (3.48)$$

with total capacity  $C$  of the pulse generator, maximum charge voltage  $u_{\max}$  and choke inductance  $L_C$ . Frequency  $\omega$  can be expressed as  $\omega = \left( \sqrt{L_C C} \right)^{-1}$ . Equation (3.47) becomes

$$\left( \frac{di_T}{dt} \right)_{\max} \geq \frac{u_{\max}}{\sqrt{L_C C}} \sqrt{\frac{C}{L_C}} = \frac{u_{\max}}{L_C}. \quad (3.49)$$

<sup>14</sup>The influence of the crowbar circuit can be neglected for the calculation of the choke properties.

### 3.3 Developed Portable Current Pulse Generators

At last, for the choke inductance follows

$$L_C \geq u_{\max} \left( \frac{di_T}{dt} \right)_{\max}^{-1} = \frac{24 \text{ kV}}{300 \text{ A } \mu\text{s}^{-1}} = 80 \text{ } \mu\text{H}. \quad (3.50)$$

The discharge frequency is calculated to be  $f = \omega/(2\pi) = 986 \text{ Hz}$  and the maximum current is  $i_{\max} = 48.4 \text{ kA}$ . The critical current value of  $58 \text{ kA}$  for the presented thyristor is thereby not exceeded. Therefore, it can be concluded that a  $80 \text{ } \mu\text{H}$  inductance effectively protects the thyristor stack in case of a magnet failure. The presented results are summed up by the SPICE simulation (including crowbar circuit) presented in fig. 3.21.

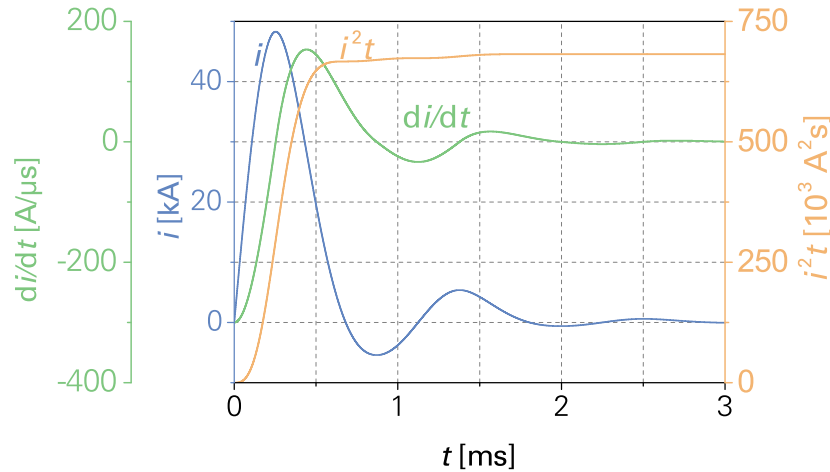


Figure 3.21: Simulation results on thyatron protection choke of PG5: The simulation was set up assuming the protective choke coil as sole inductance in the circuit as consequence of a failed high-field magnet. Shown is the thyristor current  $i$  and corresponding current rise  $di/dt$  as well as  $i^2 t$ -value in accordance to the action integral formula  $\int i^2 dt$ . As can be seen, the limits,  $(di/dt)_{\max} = 300 \text{ A } \mu\text{s}^{-1}$  and  $(i^2 t)_{\max} = 16820 \cdot 10^3 \text{ A}^2 \text{ s}$ , of the thyatron switch are not exceeded in case of a failing pulsed magnet and the switch is successfully protected by the choke.  $58 \text{ kA}$  max current

The portable pulse generators PG3 and PG4 developed and used throughout this work opened up multiple new experimental capabilities for the laser particle acceleration division of HZDR's radiation physics institute and collaborators. The significant advancements in comparison to the previous pulse generator technology run from the support of a wide range of pulsed high-field magnets and enhanced stored energy (for higher fields) to modularity and improved safety features. The development of PG5 adds user-defined scalability of the provided energy to that list and is thus essential for projects that rely on even higher fields or larger magnets such as medical beam transport (cf. [33]).

# 4 EXPERIMENTAL CHARACTERIZATION OF THE CAPTURING SOLENOID

## 4.1 CHARACTERIZATION AT TANDETRON

### 4.1.1 INTRODUCTION

Studying beam optical properties of a magnet prototype like the capturing solenoid is a task favorable to perform at a stable, well-characterized and easily tunable particle source. Thus, instead of using a laser-driven source prone to fluctuations, first characterization experiments have been conducted at HZDR's 6 MV tandetron accelerator using conventionally accelerated, well-characterized and specifically prepared proton beams. The explanations in this chapter will be kept brief, considering that the main focus of the experiment laid on gaining hands-on experience with the magnet system and proving the concept.

### 4.1.2 EXPERIMENTAL SETUP

The capturing solenoid was first characterized at HZDR's ion beam center (IBC) using the 6 MV tandetron accelerator providing 10 MeV protons.<sup>1</sup> In the presented experiment the kinetic energy of the proton beam, i.e. 10 MeV, was chosen as ideal compromise between particle energy and accelerator stability. Since a tandetron is a cw accelerator, adaptations were necessary to enable measurements with a pulsed magnet. The pulsed operation of the tandetron beam was realized using an electrostatic steerer in the low energy region of the accelerator. Connected to a fast high voltage amplifier and pulse generator, it is possible to deflect the beam into the beam pipe and on demand inject short pulses into the accelerator. The pulse structure is only limited by the employed pulse generator hardware. A repetition rate of 1 kHz and a minimum pulse duration of about 500 ns was successfully demonstrated. For even shorter durations a complex convolution of beam profile and pulse duration occurs.

The mean proton current of the tandetron accelerator is limited by radiation safety issues

---

<sup>1</sup>A tandetron accelerator provides a static electric potential, e.g. 6 MV, that allows for accelerating ions twice. To enable the twofold acceleration, the charge state of the ions has to be changed when passing the field free region. Typically, negative ions are accelerated towards the positive high-voltage terminal, then electrons are stripped and the generated positive ions are repelled by the terminal gaining further energy. A 6 MV machine can therefore accelerate protons (transition  $H^- \rightarrow H^+$ ) up to kinetic energies of 12 MeV.

## 4.1 Characterization at Tandetron

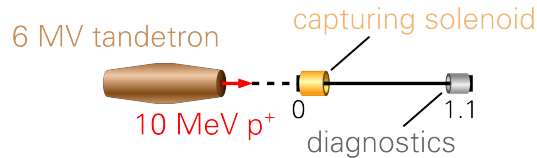


Figure 4.1: Schematic of the experimental setup for the first functional test of the capturing solenoid at HZDR's tandetron accelerator. Distance measures given in meters. The diagnostics chamber at the end of the beamline could be equipped with scintillator and radiochromic film detectors.

to  $1 \mu\text{A}$  or less (energy dependent). For pulsed operation, it is possible to get a peak current as high as  $40 \mu\text{A}$ . The lateral size of the parallel beam was adjusted from mm to cm.

The pulsed high-field magnet was connected to the tandetron accelerator's evacuated beam pipe. The capturing solenoid was operated without housing, but equipped with an extra beam pipe (inner diameter 35 mm) made from polyurethane (PU) plastic. The solenoid was mounted on a movable platform that allowed for precise positioning with respect to the axis of the incoming proton beam. The beam was detected by means of radiochromic film (RCF, cf. appendix C.1) or scintillator (cf. appendix C.2) inside a diagnostic chamber at the end of the beamline roughly 1 m downstream of the solenoid. The setup is depicted in fig. 4.1.

### 4.1.3 RESULTS

The capturing solenoid was successfully employed at HZDR's tandetron accelerator and could generate well confined focal spots. The laterally broadened (25 mm, parallel) monoenergetic proton bunch ( $2 \mu\text{s}$ ) was focused by the pulsed magnet to a 0.8 mm FWHM spot size 1.1 m downstream of the solenoid entrance (see right side of fig. 4.2(c)). For that matter, a peak on-axis field of 2.7 T was generated.

Before this minimum focal spot size could be recorded, the proton bunch (typically few  $\mu\text{s}$  long) was timed with respect to the maximum of the solenoid magnetic field. Then, a sophisticated alignment procedure of the pulsed magnet took place. In a non-ideal solenoid, geometrical and magnetic axes generally do not align. Therefore, alignment shots are required to compensate for discrepancies. Assisted by the scintillation detector's online information, the solenoid was gradually shifted and tilted until an optimal position was found. The optimum was defined as follows: An aperture plate (3 mm hole diameter) was introduced to the tandetron beam, splitting it up into five separate beamlets (cf. background of fig. 4.2(a)). The central beamlet defined the axis of the beamline. The solenoid was then supposed to generate focal spots on this axis, both for long and short focal distances. Figure 4.2(a) shows an RCF irradiated both with the unfocused and focused beam of the tandetron. The lateral offset introduced to the focal spot is approximately 1 mm. Considering the long transport distance of 1.1 m, the quality of the alignment was deemed sufficient.

After the successful alignment of the solenoid, the optimization of the focal spot size was examined to generate well-confined beams of high flux. Therefore, same aperture plate proved to be very useful. Figure 4.2(b) shows that, if the solenoid field strength is set too low, the particles are still converging towards the focus at the position of the RCF.<sup>2</sup> The high resolution of the RCF as well as the exceptionally good imaging quality of the capturing

<sup>2</sup>Same holds true for a field strength that is too high, except that the particles are already diverging after moving through the focus.

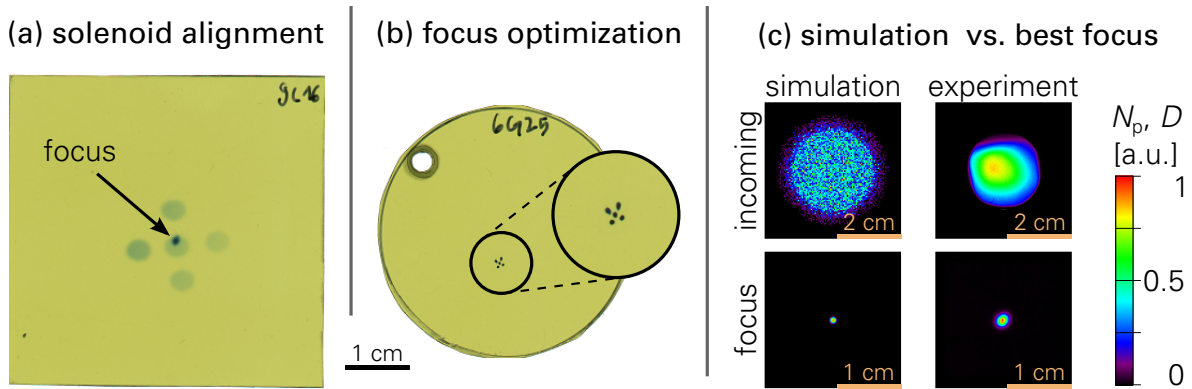


Figure 4.2: (a) RCF comparing the focal spot position to the beam axis (defined by central beamlet), obtained via consecutive irradiation of the film w/ and w/o solenoid field. (b) RCF showing separate beamlets in close proximity to the focal spot position, inset zooms in on the area of interest (1 cm diameter). (c) Comparison between simulation (proton number  $N_p$  color coded) and experiment (RCF dose  $D$  color coded) on solenoidal focusing at tandetron accelerator. See text for details.

solenoid in this scenario, allow for distinguishing the separate beamlets. The solenoid field was then gradually increased by tuning the charging voltage of the pulse generator (PG3) to the point where the separation of the beamlets vanished (2.7 T, 3.27 kA). The focal spot image in fig. 4.2 was recorded under these optimized conditions.

Finally, the experiments gave first valuable input for setting up the particle tracing model of the capturing solenoid using the software General Particle Trace (GPT) by Pulsar Physics.<sup>3</sup> The GPT particle tracing model approximates the 112 helical windings of the capturing solenoid by 112 current loops spaced to mimic the winding distribution of the solenoid in accordance to construction drawing and fabrication notes. The experiment parameters, i.e. proton energy (10 MeV), geometry (detector plane at 1.1 m) were implemented into the GPT simulation. The incoming proton beam was approximated by the distribution shown in fig. 4.2(c) and was considered to be perfectly parallel. To generate the focal spot at the identical position in simulation, the simulated winding current had to be reduced by 2 %, decreasing the simulated magnetic field strength accordingly. Figure 4.2(c) compares solenoid input and output RCF dose plots with the simulation result. It can be seen that the size of the focal spot recorded in experiment, 0.8 mm FWHM, is roughly two times larger than the tracing output.

The presented small deviations between simulation and experiment are not considered to be severe. In fact, they may be promoted by following factors: First, the tandetron beam is not perfectly parallel, yet the divergence is below  $1^\circ$  solid angle. Second, the beam defining aperture of the tandetron may introduces scattered particles to the beam. Hence, the simulation determines the focusing performance of an idealized solenoid made from current loops under ideal experiment conditions. Thus, the result represents the theoretical optimum on

<sup>3</sup>Pulsar Physics describes GPT on their website as follows: "GPT is based on full 3D particle tracking techniques, providing a solid basis for the study of 3D and non-linear effects of charged particles dynamics in electromagnetic fields. All built-in beam line components and external 2D/3D field-maps can be arbitrarily positioned and oriented to simulate a complicated setup-up and study the effects of misalignments. An embedded fifth order Runge-Kutta driver with adaptive stepsize control ensures accuracy while computation time is kept to a minimum. GPT provides various 2D and 3D space-charge models, including a sophisticated 3D particle-mesh method [86]."

solenoid focusing for the considered magnet geometry. The capturing solenoid exhibits a focal spot quality remarkably close to this optimum. The promising results encouraged further characterization studies performed at the laser accelerator Draco as described in the next section.

## 4.2 CHARACTERIZATION AT DRACO

### 4.2.1 INTRODUCTION

After the principle functionality of the solenoid has been proven at the well-known beam of HZDR's tandemron accelerator, the next major task of this thesis was to establish and characterize a high-field beam transport system at the Draco laser acceleration source. The system has to provide for high capture efficiency, beam optical quality and tunability to facilitate the generation of well-controlled laser-accelerated ion bunches. The laser-driven beams need to be shaped in a way to enable their application for irradiation of radiobiological samples, like cells or tumors, for feasibility studies on medical beam transport as well as fundamental research. Therefore, over the years 2012–2014, when the Draco laser system was upgraded to the PW, i.e.  $10^{15}$  W, level (see appendix A), necessary pulsed power components were developed, manufactured and installed, forming a linear beamline based on the capturing solenoid. The established setup is depicted in fig. 4.3 and will be explained in the following paragraphs.

### 4.2.2 EXPERIMENTAL SETUP

The beamline was built up at the PW target area of the ion acceleration laboratory of Draco. The capturing solenoid (solenoid 1) was installed in the target chamber. The downsized housing (cf. fig. 3.7) allowed for remote-controlled motorization of the magnet. The remote positioning, based on hexapod technology, is used to compensate misalignment of the solenoid.<sup>4</sup>

The Draco laser drives a TNSA proton source based on  $\mu\text{m}$ -thin titanium foil targets. The particle source properties (cf. section 2.2) can be measured by RCF stack (in front of solenoid 1) and Thomson parabola spectrometer (TPS). The TPS is installed farthest downstream of the laser target at the end of the beamline. The laser-driven proton bunch is captured by solenoid 1 and transported downstream. The tunable magnet can thereby generate a focus of desired mean energy at a position of choice, e.g. one of the many detector positions.

Online detectors based on scintillator films or blocks (as discussed in appendix C.2) allowed to gain immediate information on the focal spot position, size, shape and intensity. According to the scintillator data the beamline performance can be monitored and, if necessary, optimized: The penetration depth of a focused proton beam impinging on a scintillator block (cf. fig. C.2, depth profiling) was used to roughly measure the energy of the transported particles and tune the magnet field strength accordingly. Solenoid alignment was performed by comparing the focal spot position with the reference beam axis for two different distances between target and solenoid focus (cf. fig. C.2, lateral profiling).

---

<sup>4</sup>Again, in a non-ideal solenoid the magnetic axis is likely to deviate from the geometrical axis. Alignment settings known from reference accelerator studies (cf. section 4.1) may be transferred to the setup at the laser accelerator. Nevertheless, it is typically still required to perform alignment shots with laser-driven particles to compensate for small discrepancies.

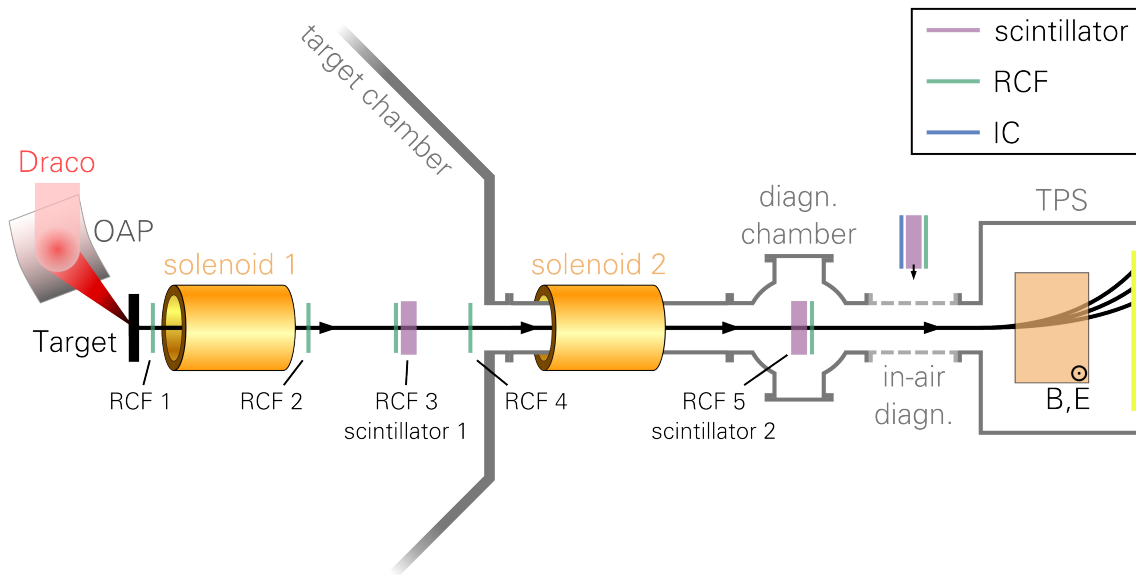


Figure 4.3: Sketch of experimental setup established at the Draco laser acceleration source (proportions not to scale). From left to right: Draco impinges on a foil target under an angle of  $45^\circ$ . Protons are accelerated in target normal direction and transported by the first capturing solenoid downstream towards diagnostic chamber, in-air diagnostics or Thomson parabola spectrometer (TPS). Optionally, the second solenoid (installed at a later time) can assist the beam transport. The proton beam can be measured by scintillator or RCF at multiple positions along the beamline (see inset). An ionization chamber (IC) can be applied in the transition area between vacuum and air for online dosimetry. For distances see table D.1.

Subsequent to the online optimization, energy resolved measurements with RCF stacks were performed. Inside the target chamber RCF wheels have been installed. These remotely operated devices enable the irradiation of multiple RCF stacks without venting the target chamber. They hold up to 15 stacks attached to a rotatable plate. Like the wings of a windmill, the RCFs can be rotated and placed on the beam axis for measurements. The diagnostic chamber is too small for such an assembly. Here, a motorized linear stage allows for multiple irradiation of an RCF stack (landscape format) as it is moved perpendicular to the beamline axis. In addition, the diagnostic chamber can be vented separately for quickly replacing RCFs. The exchange procedure can be performed in approximately 10 min.

The different positions of scintillator and RCF detectors are marked in fig. 4.3. Important distances are summarized by table D.1 in appendix D.

Although the beamline installation was performed in the PW target area, the experiments on solenoid characterization in 2015 were carried out using the 150 TW Draco beam. At that time, the PW beam was not yet operational. In 2016, the experimental capabilities of the pulsed high-field beamline were expanded when the PW beam became available and a second, identical solenoid (solenoid 2 in fig. 4.3) was set up outside of the target chamber to assist the beam transport. The installation of solenoid 2 necessitated some setup changes. Accordingly, some positions of detectors and other distances changed, as can be read from table D.1. For the results presented below, the distances of the single solenoid setup apply.

## 4.2 Characterization at Draco

Solenoid 2 is not encased by a housing, instead a ceramic beampipe (inner diameter 42 mm) was led through the magnet bore.<sup>5</sup> Additionally, for future irradiation studies, the beamline capabilities were expanded by enabling the installation of a thin (125  $\mu\text{m}$ ) Kapton window at the end of the diagnostic chamber. Thereby, irradiation experiments and beam diagnosis can also be performed in-air from now on. An optional transmission ionization chamber (IC) can be applied for online dosimetry (cf. Richter et al. [22]).

### 4.2.3 RESULTS

#### VERIFICATION OF THE SIMULATION MODEL AND TRANSMISSION STUDY

After successful alignment of the hexapod mounted solenoid, using the scintillator detectors along the beamline, the characterization studies could be performed. The initial step was to verify the GPT simulation model of the solenoid magnet that has been established during the experimental campaign at the tandemron accelerator. For this purpose the measurement depicted in fig. 4.4 was performed, where an RCF stack in front of the capturing solenoid detects half the incoming beam but lets the other half pass to be transported through and manipulated by the pulsed magnet.

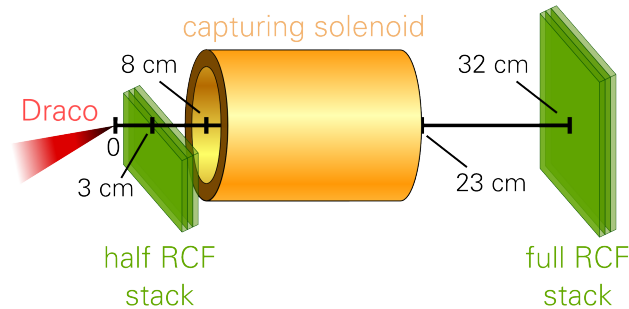


Figure 4.4: Sketch of transmission experiment setup at Draco. A (half) RCF stack of  $2.5 \times 5 \text{ cm}^2$  lateral measures was used to block half of the beam in front of the solenoid. A (full)  $5 \times 5 \text{ cm}^2$  stack downstream detected the proton beam profiles and doses after passing the solenoid.

As described in section 3.1.2, charged particles follow helical trajectories inside a solenoid magnet. Therefore, an incoming beam of semicircular lateral shape (as generated by introducing the half film stack in front of solenoid 1) is imaged by a solenoid lens as a demagnified (particles propagating towards focus) or magnified (overfocused particles already strongly diverged) semicircular distribution that experienced a rotation with respect to the beam axis. The rotation angle was used to benchmark the simulation model. Figure 4.5 compares measured and simulated proton beam data and shows the good agreement between experiment and GPT model. The simulation reproduces the rotation of the semicircular proton beam (cf. fig. 4.4) and the size of the distribution. Differences are due to field imperfections in the real solenoid and due to the broad energy imprint on the films as well as film saturation at high doses, e.g. for the focused 7.3 MeV protons on the right.

<sup>5</sup>The setup of the tandemron beamline served as a model for the installation of solenoid 2 at Draco. The ceramic beampipe was chosen due to more strict vacuum guidelines at Draco.

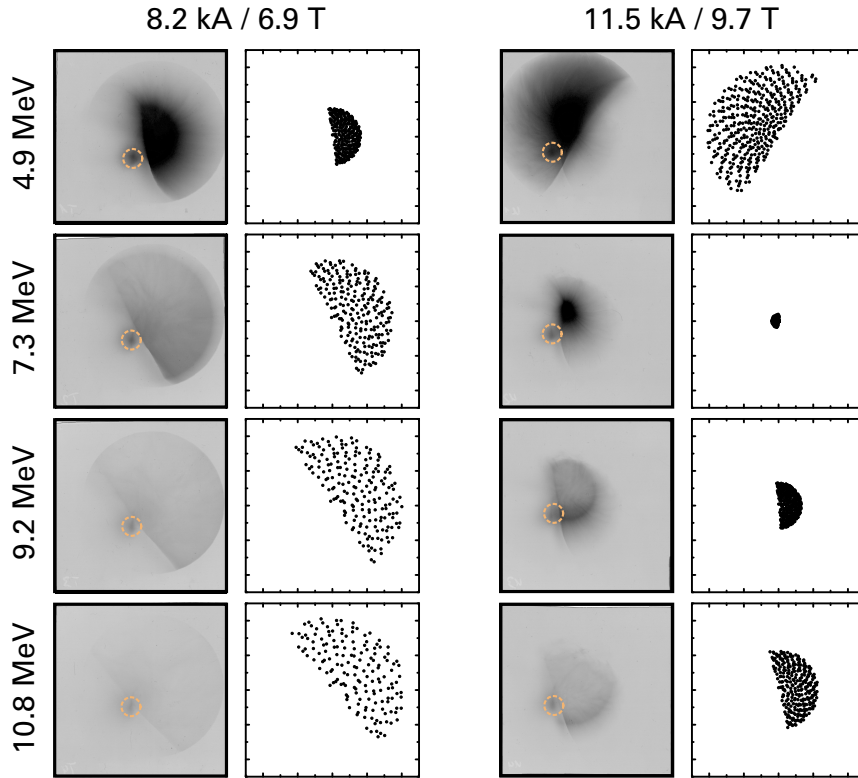


Figure 4.5: Comparison of particle beam transport experiment and simulation: For two magnetic field strengths (top), corresponding to a far (left) and near (right) focus setting, the RCF (red color channel) is presented in the left column, the simulation output is presented on the right. The energy values given on the left side of the figure indicate the Bragg peak energy corresponding to the presented RCF stack layer and were used to generate the simulation plot. Keep in mind that the RCF show a superposition of energy depositions of a multitude of proton energies equal and above the presented Bragg peak energy. The orange circles mark dose originating from electrons contributing to the laser acceleration process. Shot parameters: Draco TW,  $\approx 4$  J on  $2 \mu\text{m}$  Ti target,  $E_{\text{max}} \approx 14$  MeV.

Besides the successful verification of the simulation model, the data presented in fig. 4.5 can also be used to determine the transmission efficiency for the given setup geometry (cf. table D.1, single solenoid) and typical source parameters (cf. eq. (2.4)). The input and output dose ratios corresponding to the presented Bragg peak energies were calculated and used to determine the transport efficiencies summarized in table 4.1.

Clearly, a higher field allows for an increased transport efficiency. For protons of 10.8 MeV energy, a transport efficiency of up to 30 % was determined. This result is in very good agreement with previous studies at the PHELIX laser system using an identical solenoid, where a transmission of 34 % has been recorded for 9.8 MeV protons [43]. Comparing measurements at matching solenoid field strengths yields that the transmission efficiency for protons of lower kinetic energy rises, despite of the increase in initial proton divergence (cf. fig. 2.2).

The presented result allows for estimating the total number of protons focused by the capturing solenoid. The reference source spectrum can be integrated over a 1 MeV broad

## 4.2 Characterization at Draco

| Proton energy                 | 4.9 MeV | 7.3 MeV | 9.2 MeV | 10.8 MeV |
|-------------------------------|---------|---------|---------|----------|
| Transport efficiency at 6.9 T | 25 %    | 23 %    | 14 % *  | < 10 % * |
| Transport efficiency at 9.7 T | 47 %    | 36 %    | 31 %    | 30 %     |

Table 4.1: Proton beam transport efficiencies extracted from the RCF data in fig. 4.5. \*Proton beam still diverging after solenoid passage.

energy bin around 10 MeV. From eqs. (2.2) and (2.4) follows

$$N_{10\pm 0.5\text{MeV}} = \int_{9.5\text{MeV}}^{10.5\text{MeV}} \frac{N_0}{E_{\text{kin}}} \cdot e^{-\frac{E_{\text{kin}}}{k_B T_e}} dE_{\text{kin}} = 9 \cdot 10^8, \quad (4.1)$$

thus giving almost  $10^9$  particles for transport and application in this energy range. Consider the determined 30 % transport efficiency, it follows that for the given energy range typically  $2.7 \cdot 10^8$  particles can be captured and focused by the magnet.

The measured transmission efficiencies were successfully reproduced by the GPT simulation model when the proton source was realistically modeled in agreement with RCF data. Later on, the simulation has been expanded to provide for a simple hands-on method to estimate particle transport efficiency in dependency of proton source parameters, i.e. angular and energy distribution. The simulation results are summarized by the plot in fig. 4.6.

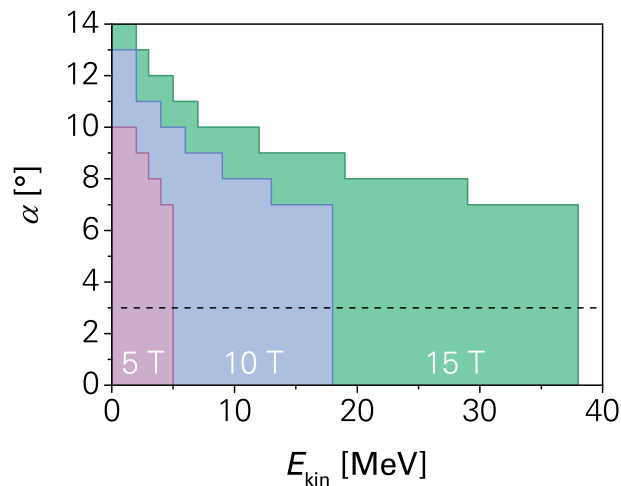


Figure 4.6: GPT simulation results on the solenoid acceptance angle  $\alpha$ , i.e. the maximum proton half-angle divergence the capturing solenoid is able to transmit losslessly (focused or collimated). The acceptance  $\alpha$  is plotted for different kinetic energies  $E_{\text{kin}}$  (1 MeV steps) and three solenoid field strengths. Applicable for proton beams up to 38 MeV and distances of approximately 8 cm between target and capturing solenoid entrance, i.e. first winding. The dashed line illustrates the geometrical limit for lossless transmission through the solenoid at  $B = 0$ , i.e.  $\alpha_{\text{geom}} \leq 3^\circ$ .

Figure 4.6 shows the acceptance angle  $\alpha$  for three solenoid field strengths as function of the proton energy. The acceptance  $\alpha$  is the maximum half-angle divergence that the solenoid

can transport without particle loss. Protons with larger divergence are lost inside the solenoid beampipe. Transportation in this context means not only that the protons leave the solenoid lossless but are also focused or collimated by the magnetic field. The plot is supposed to be used as follows:

The envelop divergence of a laser-driven beam, as presented in section 2.2, is a function of the energy. Protons at the high-energy end of the spectrum exhibit smaller divergence angles than particles of lower kinetic energy. Therefore, for a laser-driven proton source, either characterized by measurement or arbitrarily assumed for predictive purposes, the envelop divergence and energy spectrum may be used to estimate how many particles at energy of interest can be captured and provided to an experiment by the solenoid. As an example, an experienced experimentalist can quickly determine the maximum divergence of protons at energy of interest, corresponding to a certain RCF stack layer. The radius of the RCF dose imprint divided by the target to RCF distance gives  $\tan \theta_{\max}$ , with  $\theta_{\max}$  being the maximum divergence angle of the considered protons. Assuming a uniform angular distribution for these protons, the transmission efficiency  $T$  can be approximated by calculating the relation

$$T \approx \left( \frac{\tan \alpha}{\tan \theta_{\max}} \right)^2 \approx \left( \frac{\alpha}{\theta_{\max}} \right)^2, \quad (4.2)$$

with suitable  $\alpha$  estimated from fig. 4.6. The last approximation step introduces a relative error below 10 % for typical values of  $\alpha$  and  $\theta_{\max}$ .

As another example, consider the angular distribution given in fig. 2.2(d). One sees that for particle energies around 25 MeV the half-angle divergence is well below  $8^\circ$  (measured 4 to  $5^\circ$ ). Thus, for these source parameters, fig. 4.6 predicts a lossless transport of 25 MeV protons at 15 T field strength.

By means of the presented method, the experimentalist is able to make quick semi-quantitatively predictions on transmission efficiencies, particle numbers or absorbed dose values at focus position. It eliminates the necessity to fully analyze the RCF stack data and feeding the derived source parameters in an elaborate tracing simulation as long as small deviations are tolerable.

## FOCAL SPOT QUALITY

In order to continue the solenoid characterization and demonstrate its tunability, the next performed measurement was the generation of proton beam foci approximately 1.6 m downstream of the laser-target and thus far away from the harsh laser acceleration environment. Since the solenoid is a chromatic focusing device, only parts of the broad spectrum can be focused at nominal position.<sup>6</sup>

Figure 4.7 compares dose pictures, recorded by means of radiochromic film (EBT3), that image the focal spot shape for three different solenoid field strengths (5.5 T, 7.0 T and 8.7 T) corresponding to different transported central bunch energies (approximately 4.9 MeV, 7.3 MeV and 10.8 MeV). The (left) dose distribution was generated by protons of approximately 10 MeV central bunch energy and is thus comparable to the tandetron data in fig. 4.2(c).

The data in fig. 4.7 deviates from the theoretical prediction for an ideal solenoid or a solenoid modeled from coaxial current loops. The shown focal spots were compared among

<sup>6</sup>The proton energy spectrum at focus position for far focal distances  $> 1$  m is typically Gaussian and exhibits FWHM energy bandwidths of the order of few 10 % (cf. [43]).

## 4.2 Characterization at Draco

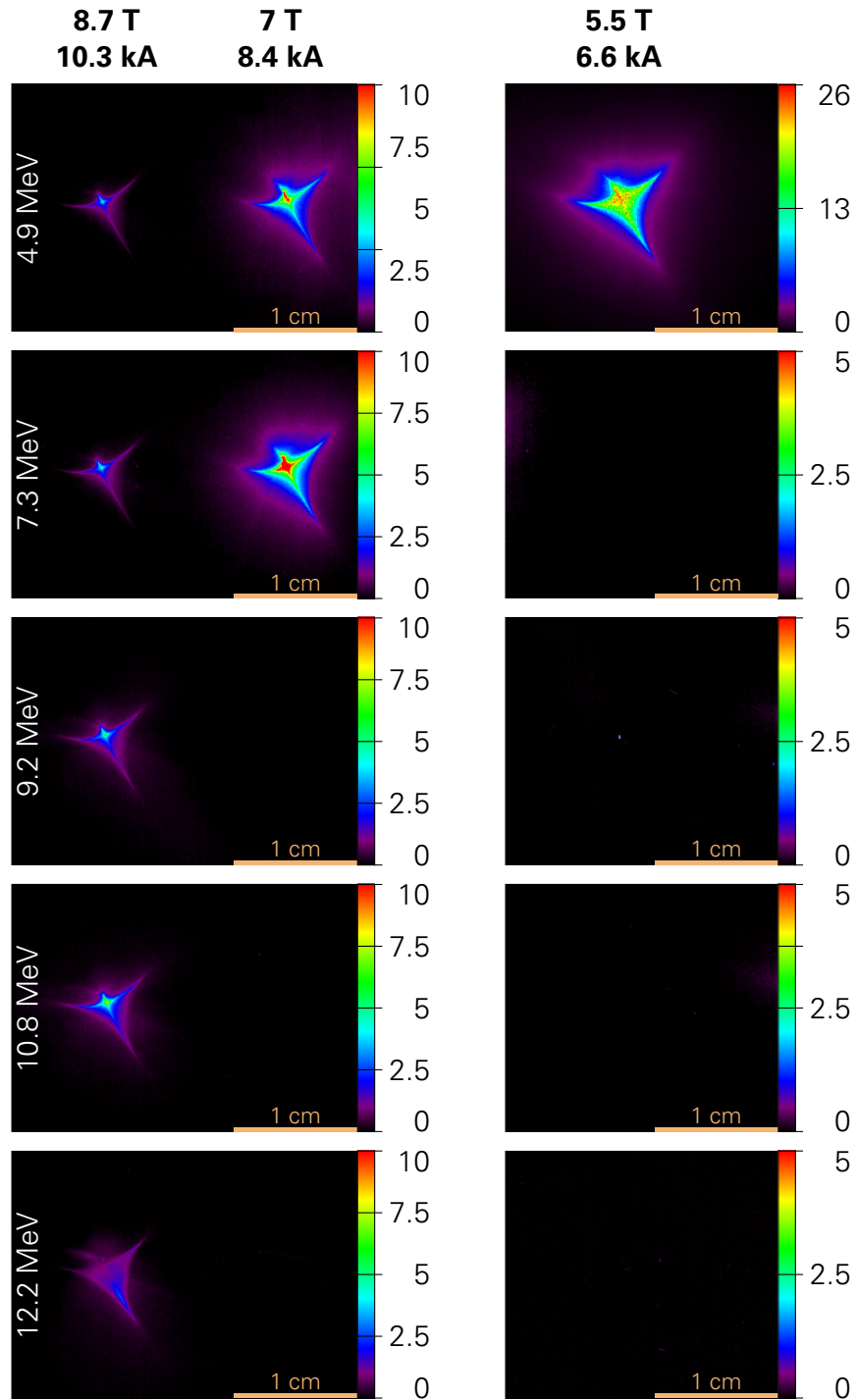


Figure 4.7: Comparison of dose distributions (color coded in Gy, different scales, beam's eye view) induced by focused proton bunches generated 1.6 m downstream of the laser target (RCF 5). The depicted RCF size is  $5 \times 2$  cm (cf. fig. E.1 under appendix E). Given energy values correspond to the kinetic energies of protons with Bragg peak at film layer position. Shot parameters: Draco TW,  $\approx 4$  J on  $2 \mu\text{m}$  Ti target,  $E_{\text{max}} \approx 14.5$  MeV.

themselves and to theoretical, simulation and previously presented tandetron reference results. The following general findings are concluded:

In analogy to classical optics, the generated focal spot can be considered as image of the particle source. The experiment geometry corresponds to an object distance (particle source to solenoid center) of 160 mm and an image distance (solenoid center to RCF) of 1437 mm. The ratio of image to object distance gives the magnification of the optical system. A ninefold increase in size can be predicted for an ideal scenario. From the measured data it can be seen that, in comparison to the previously presented data from the tandetron accelerator, the focus is strongly distorted and cross- or diamond-shaped. The visible focal spot size is almost  $1 \times 1 \text{ cm}^2$ . The magnification derived from the classical optics picture can neither explain the shape nor the size of this focal spot, as a corresponding source size of above 1 mm is unrealistic. Spherical aberrations have been taken into account for predicting more realistic focal spot sizes (cf. fig. 3.3 and fig. 4.8, left), yet in accordance to these considerations still circular focal spots of only few mm diameter have to be anticipated. The measured spot sizes can therefore not be reproduced by these simple methods.

Analyzing the data further, one finds that the highest doses lie in a small area with FWHM dimensions of  $1 \times 1 \text{ mm}^2$  (measured along the two axes of the dose distribution on film 4, 10.8 MeV). The data also shows that size and shape of the dose imprints are independent of the focused energy. They remained stable over the course of the entire experimental campaign. The high-energy focus on the left of fig. 4.7 shows an increasing dose up to the fourth RCF stack layer. This increase is a reflection of the proton inherent inverse depth dose profile known as Bragg peak.<sup>7</sup>

In summary, the capturing solenoid is able to generate focal spots meters away from the laser-target interaction position in a well-controlled, tunable way. Above  $10^8$  protons in the kinetic energy window of  $10 \pm 0.5 \text{ MeV}$  may be provided for irradiation experiments or other application studies. To the moment, the focal spot is shaped like a cross or diamond with a high dose area in the middle. The proton confinement to this  $1 \times 1 \text{ mm}^2$  area is not ideal, thus improvements on focal spot quality should be sought in future studies. In order to do so, it is crucial to first understand what causes the distorted focal spot shape. The following paragraphs explain how such shapes can be generated by a solenoid magnet.

## SOLENOID ASTIGMATISM

In section 4.1 it has been shown that the capturing solenoid is able to generate mm-small circular focal spots as long as the beam is almost parallel. The strong divergence of a laser-driven proton beam, however, leads to the formation of the distorted focal spot shape. The classical ray optical analog to this behavior is astigmatism. An optical system is astigmatic when rays propagating in two planes perpendicular to each other have different focal lengths. The result is a line focus with respect to one plane, e.g. horizontal, at a certain position and another line focus, now in the vertical direction, at a different position. In-between both focal spot positions a cross-shaped far field pattern may occur. In electron microscopy, solenoid astigmatism is a known issue limiting the resolution [119].

The key to the explanation on how a wire wound solenoid becomes astigmatic lies within its winding geometry. In simulation, a solenoid is typically modeled by coaxial current loops (applied in this study) or by a current sheet confined to a cylinder surface. Yet, the real winding

<sup>7</sup>The depth dose distribution of a proton beam transported via the capturing solenoid will be presented in section 5.3.

## 4.2 Characterization at Draco

distribution is a multilayer helix. The capturing solenoid, as mechanically stressed pulsed high-field magnet, consists of a rather low number of windings and layers in comparison to conventional, DC solenoids. Thus, the pitch of the helical windings is significantly larger and can lead to a violation of the otherwise radially symmetric field distribution inside the solenoid. The perturbing field components of the innermost winding layer can partially be compensated by the following layer that is wound with opposite pitch. Still, a complete cancellation cannot be achieved without further ado, since the pitch is reduced due to the increased radius of the outer windings. In an adapted simulation model that is still based on current loops, the winding pitch was incorporated by giving the individual current loops a tilt with respect to the  $z$ -axis, i.e. the particle propagation direction, equally in  $x$ - and  $y$ -direction. The tilt angles  $\alpha$  were determined from the real winding pitches of the four layers (L1–4) of the capturing solenoid to

$$\alpha_{L1} = 7.1^\circ, \quad \alpha_{L2} = -6.0^\circ, \quad \alpha_{L3} = 5.1^\circ, \quad \alpha_{L4} = -4.5^\circ. \quad (4.3)$$

The simulation has been performed for 10,000 protons of 10.8 MeV kinetic energy. Analog to fig. 4.7, a screen is placed 1.6 m downstream of the proton source that records the position of the transported protons. The proton density (in protons per pixel,  $200 \times 200$  pixel corresponding to a  $2 \times 2 \text{ cm}^2$  area) is plotted in fig. 4.8. The distribution is drawn to allow for direct comparison with fig. 4.7.

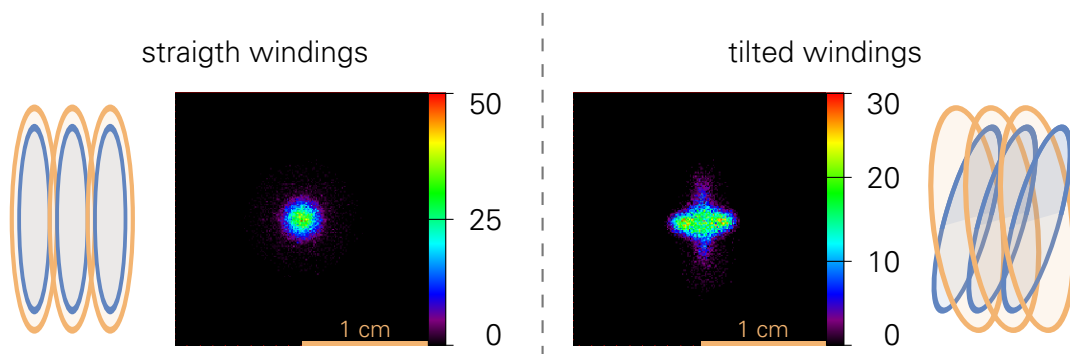


Figure 4.8: GPT tracing result for focusing 10,000 protons (10.8 MeV, divergence tailored to meet laser acceleration conditions) at 1.6 m distance to source. Simulated were straight and tilted coil windings (schematically illustrated for two winding layers). The frame shows the proton density distribution in protons per pixel in a  $2 \times 2 \text{ cm}^2$  area (color coded, different scales, beam's eye view). For comparison with the experimental data see fig. 4.7.

It can be seen from fig. 4.8 that the simulation with tilted windings differs from the more ideal simulation based on straight current loops. The latter shows the predicted Gaussian focal spot shape, whereas the simulation result on the right reproduces the diamond shape that has been observed experimentally. The focal spot size is significantly enlarged and compares well with the RCF data in fig. 4.7.

In order to quantify the effect of the tilted windings, additional GPT simulations have been performed. Instead of including the winding tilt, the solenoid field was overlain by a quadrupole field of identical length, i.e. 15 cm.<sup>8</sup> The quadrupole field gradient (in  $\text{T m}^{-1}$ ) was

<sup>8</sup>The built in quadrupole model of GPT was used. It simulates a quadrupole lens without fringe fields.

then stepwise increased until reproducing the previous simulation and experimental data. The results are summarized in fig. 4.9.

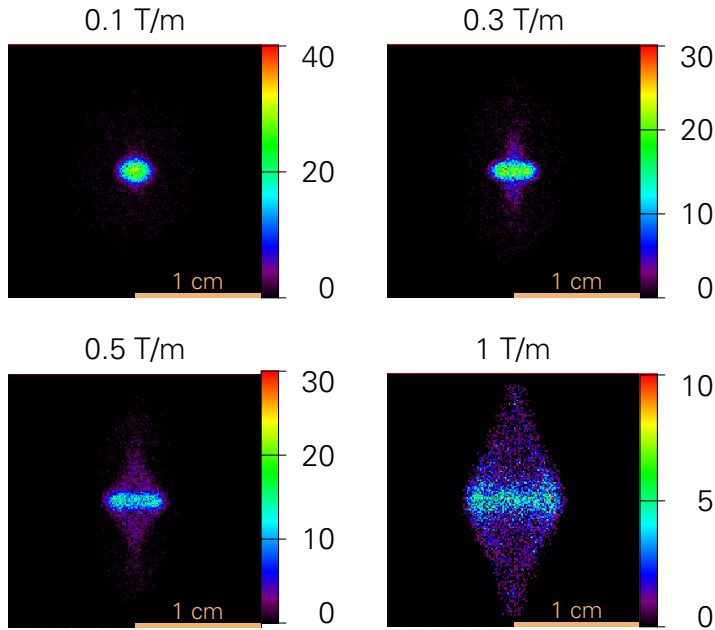


Figure 4.9: GPT tracing result for focusing 10,000 protons (10.8 MeV, divergence tailored to meet laser acceleration conditions) at 1.6 m distance to source. Simulated was a solenoid with straight coil windings overlain by a quadrupole field of different field gradients. The frame shows the proton density distribution in protons per pixel in a  $2 \times 2 \text{ cm}^2$  area (color coded, different scales, beam's eye view). For comparison see figs. 4.7 and 4.8.

As conclusion can be drawn that a quadrupole field of approximately  $0.5 \text{ T m}^{-1}$  that extends over the entire winding length of the solenoid can cause a similar focal spot as observed in experiment. The assumption of a quadrupole field as perturbing field component mainly comes from symmetry considerations. Although, another parallel to electron microscopes can be drawn that also backs the assumption. To cancel the solenoid astigmatism in these machines, devices called stigmators are used. A stigmator is basically a single, weak quadrupole magnet that follows the astigmatic lens [119] and counterbalances the unwanted effects. The stigmator concept is very interesting and might be investigated in the future to minimize the aberrations of the capturing solenoid.

In summary, the presented simulations reproduce the measured focal spot adequately well. But still, some differences are recognizable. For example, the simulated proton distribution is more symmetric (shaped like a plus sign, not like a cross) and the inner structure is not as sharp in the simulations. Further studies might shed light on this behavior and are foreseen for the future. It may be possible that collective dynamics of the plasma particle or the interaction of the magnetic field with the particle source also affect the proton beam transport.

Nevertheless, the simulations prove that the measured focal spot shape and size can be (at least partially) attributed to the winding geometry of the capturing solenoid in interplay with the strong divergence of the incoming proton beam. Thus, the capturing solenoid suffers from astigmatism.

### IMPROVEMENTS ON FOCAL SPOT QUALITY

For improving the focal spot, i.e. making it smaller, more homogenous and circular, and to prove that the divergence of the laser-accelerated protons influences the focal spot shape, further measurements were performed. Considerations in analogy to classical optics predict that the focal spots become smaller when generated in closer vicinity to the solenoid.<sup>9</sup> Thus, by increasing the field strength and consequently decreasing the focal distance, the proton confinement at focus should be considerably improved.

Figure 4.10 shows on its left that, when the solenoid field is increased to 9.1 T, the investigated protons of 10.8 MeV kinetic energy are focused approximately 1 m closer to the solenoid, i.e. at a distance of 515 mm to the laser target.<sup>10</sup> The focal spot size is significantly smaller, but still shows a similar shape as observed before. The focal spot area visible on the RCF is approximately  $5 \times 5 \text{ mm}^2$  and thus a factor of four smaller than for long distance focusing. The high dose area has a similar FWHM size as previously measured ( $1 \times 1 \text{ mm}^2$ ), yet confines a 20-fold higher proton number in this area (compare dose values in fig. 4.7 and fig. 4.10) also partially owing to the increased capture efficiencies at higher field strength (cf. table 4.1). Hence, for reaching higher beam intensities or higher absorbed dose values in a small mm-sized area, key is to generate the focus close to the solenoid. The drawback of this modality is that higher field strengths are required and thus a higher thermal load or long term magnet life time reduction result. Furthermore, in close proximity to the laser-target interaction unwanted radiation background ( $\gamma$ -rays or electrons) may prevent controlled irradiation experiments with focused proton beams. Finally, a majority of irradiation samples cannot be placed in vacuum. Thus, irradiation has to be performed in-air. Exiting the target chamber, however, e.g. via a thin Kapton window, requires long focal distances.

The right side of fig. 4.10 depicts that a nearly circular focal spot can be generated, when an aperture is placed in front of the capturing solenoid. It has been installed on the RCF wheel in front of solenoid 1 (RCF 1, 30 mm to target). The aperture has a size of 3 mm in diameter. It limits the divergence of the incoming proton beam to below  $3^\circ$  half-angle. Thereby, eliminating the astigmatic effect to almost full extend. The drawback, of course, is that the otherwise captured particles are stopped in the aperture material and cannot contribute to beam intensity or dose (note the different dose scales in fig. 4.10). The presented measurements, in combination with the previously obtained tandetron data, are a clear demonstration that the TNSA intrinsic broad angular spread of the protons is translated into a strong astigmatism by the non-ideal solenoid windings. One goal of this thesis is to prepare laser-driven sources for application. In this context, the severity of the astigmatism can be reduced by decreasing the focal length or by limiting the incoming beam divergence under the drawbacks of increased solenoid thermal and mechanical load, higher radiation background or decreased transport efficiency.

For long term improvement, the solenoid design has to be revised. A smaller winding pitch could decrease the astigmatism and is easily achieved by using wires of smaller cross section. Deliberately increasing the winding pitch in the second and fourth layer, could cancel out perturbing field components of the stronger pitched first and third layer. Both methods result in severe alteration of mechanical, electrical and thermal properties of the magnet. Therefore, thorough analyses need to be performed before a new magnet concept is considered. This new concept is beyond the scope of this thesis but should be studied in future work.

<sup>9</sup>In the classical optics picture this corresponds to an increase in refractive power. The result is an decreasing magnification of the imaging system.

<sup>10</sup>That corresponds to a reduction of the optical magnification by a factor of four in the classical picture.

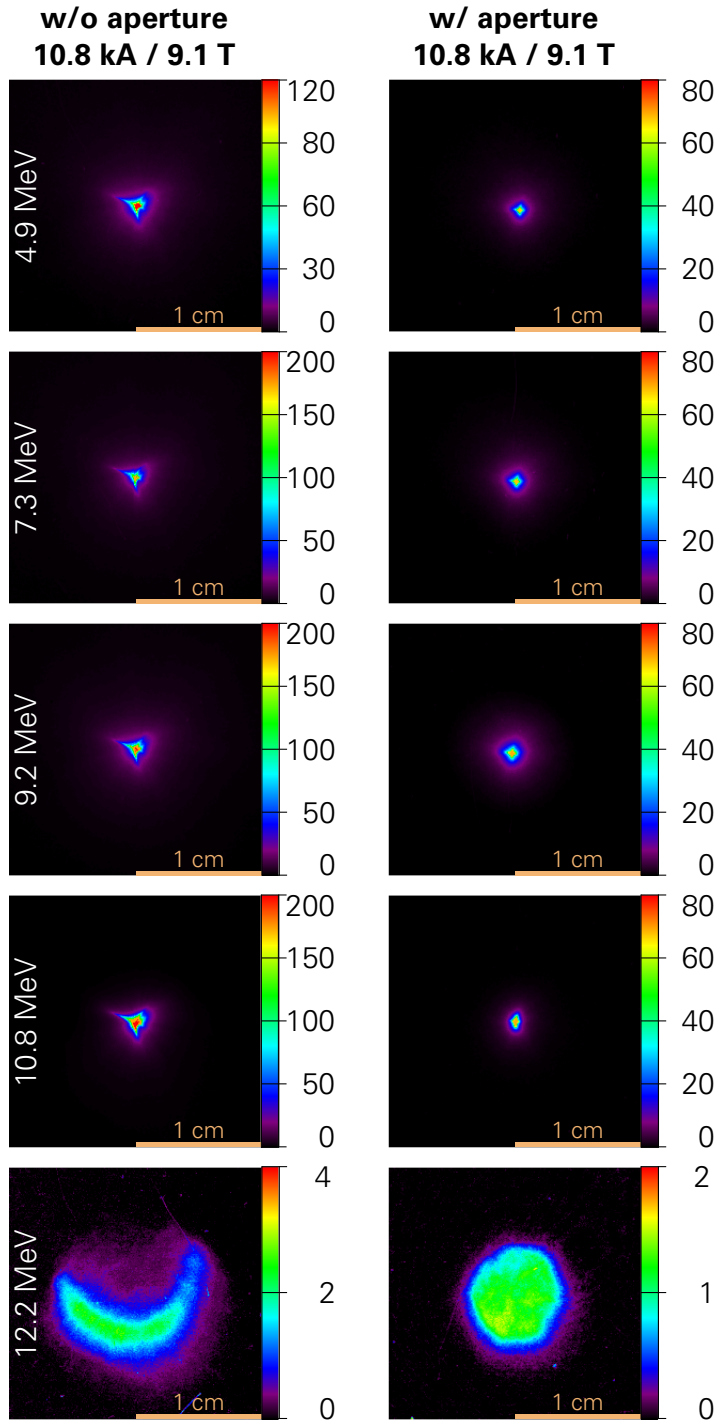


Figure 4.10: Comparison of dose distributions (color coded in Gy, different scales, beam's eye view) induced by a focused proton beam generated 0.5 m downstream of the laser target (RCF 3). The depicted RCF size is  $2 \times 2 \text{ cm}^2$  (cf. fig. E.2 under appendix E). Given energy values correspond to the kinetic energies of protons with Bragg peak at film layer position. Shot parameters: Draco TW,  $\approx 4 \text{ J}$  on  $2 \mu\text{m}$  Ti target,  $E_{\text{max}} \approx 14.5 \text{ MeV}$ .

## PEPPER-POT MEASUREMENTS

To conclude the section on solenoid characterization, pepper-pot (PP) measurements will be presented in the following (for a description of the pepper-pot method see appendix C.4). The pepper-pot was installed behind solenoid 1 inside of the Draco target chamber (RCF 3). The particles that pass through the pepper-pot apertures were detected by means of energy resolving RCF stacks (EBT3) 20 cm downstream of the PP (RCF 4). Due to the small size of the PP apertures (100  $\mu\text{m}$ ), the dose depleted in the RCFs is very low. Therefore, several consecutive laser-accelerated proton bunches have been recorded to increase the visibility on the RCFs. For the measurement without pulsed magnetic field 15 laser shots were integrated. The remarkably stable performance of the capturing solenoid made it possible to likewise perform RCF irradiation with multiple proton bunches. The increase in proton number due to the capturing effect of the solenoid allowed for reducing the number of shots to 10.

The experimental data is presented in fig. 4.11. The left side shows the magnified image of the PP aperture pattern when the solenoid was not operated.<sup>11</sup>

An upper limit on source emittance for the laser-driven protons was derived from the RCF data by Simon Weih<sup>12</sup> of TU Darmstadt:  $\epsilon_x \leq 1.1 \text{ mm} \cdot \text{mrad}$  and  $\epsilon_y \leq 1.3 \text{ mm} \cdot \text{mrad}$  ( $\epsilon_x \epsilon_y = \epsilon_x \epsilon_y \leq 1.43 \text{ mm}^2 \cdot \text{mrad}^2$ ).

These values represent a conservative measure on TNSA source emittance. They cannot reach the findings of Cowan et al. [56], as PP and setup geometry limit the resolution of the applied method. Still, the pepper-pot has been proven to be a valuable research tool for the field of laser acceleration as described below.

Appendix C.4 discusses that PP measurements with pulsed magnetic field can be used to assess the emittance blow-up introduced by the solenoid and potential aberrations or field imperfections. The expected signature of the RCF films can be described as follows: In the first RCF, all particles with sufficient energy to reach the film (here  $E_{\text{kin}} \geq 3.7 \text{ MeV}$ ) deposit energy and darken the film. In an ideal situation every single hole of the PP would be represented by a streak on the RCF pointing towards the beam axis with low energies closer to the center and high energies radially farther off (see also the reference signal in fig. C.5). This, of course, directly corresponds to the shorter focal length for low-energy particles and their higher gain of radial velocity when exiting the solenoid (cf. section 3.1.2). For the following films in the stack, the traces become shorter as the low-energy particles cannot reach deeper stack layers.

The theoretical expectation is reproduced well by the experimental data on the right side of fig. 4.11: We see straight streaks pointing towards a common center. For the first film the thick traces originate from low-energy protons that were focused in front of the RCF stack detector and as a result are already diverging. On closer inspection, small deviations regarding the intersection points of the traces were found. The deviations are a result of the formerly discussed astigmatism. Apart from this, the solenoid does not introduce severe displacements with respect the aperture pattern (see rightmost picture in fig. 4.11) of the PP. The emittance blow-up inflicted on the beam by the capturing solenoid was determined to be at least a factor of 3.8.

The presented measurement method can also assist the solenoid alignment procedure. A misalignment, like a small tilt or shift of the solenoid, results in a net dipole field component that acts on the passing proton beam. The effects can be recognized in the PP signatures. A

<sup>11</sup>The image is magnified due to the divergence of the protons that originate from a quasi point source.

<sup>12</sup>Simon Weih is part of the LIGHT collaboration. The LIGHT collaboration will be introduced in section 5.1.

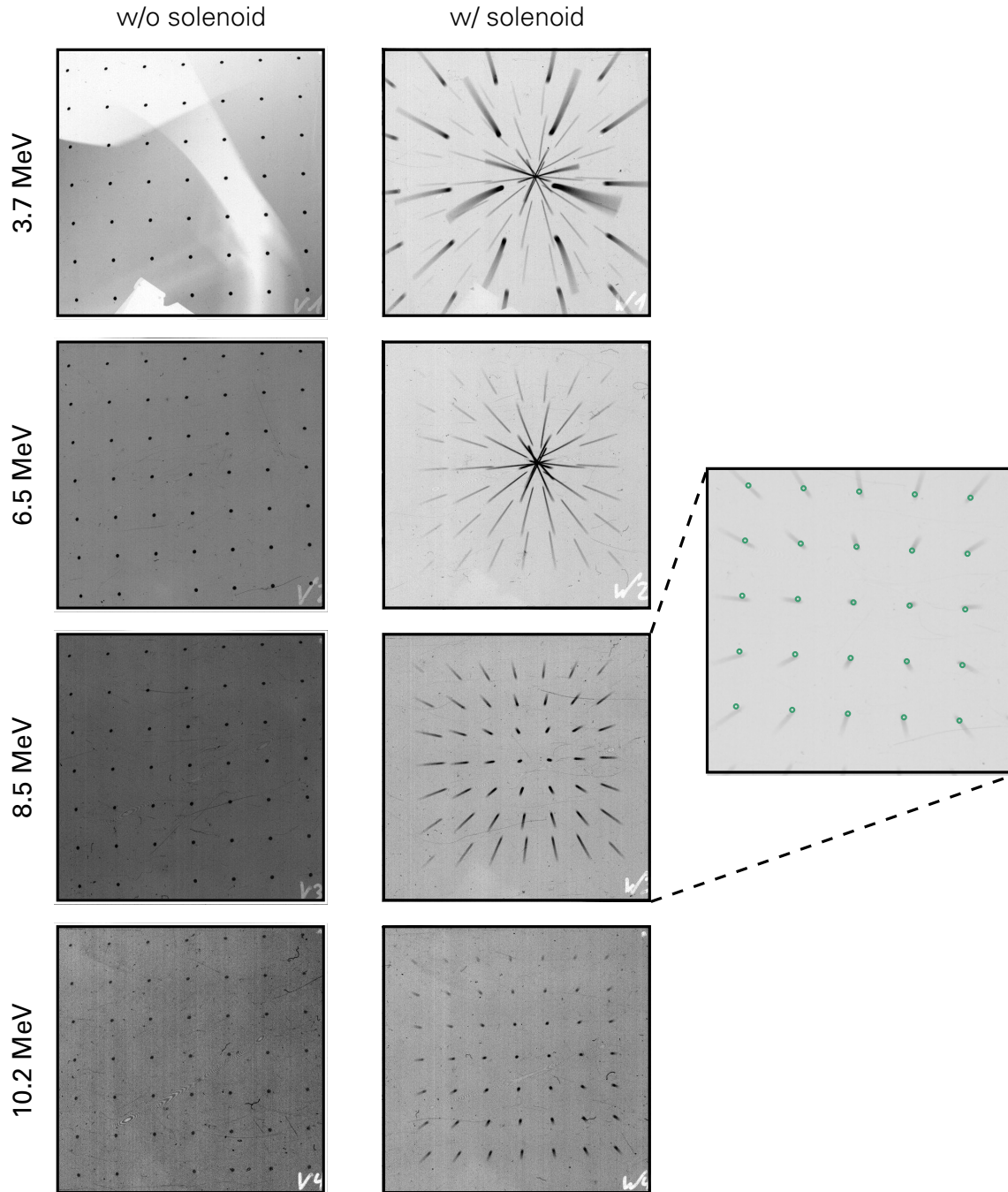


Figure 4.11: Pepper-pot measurements at Draco with (10 shots integrated) and without (15 shots integrated) solenoid field. Shown is the contrast enhanced red channel data of the used RCFs of type EBT3. The rightmost picture compares the positions of the PP apertures (green) to the traces visible on the third RCF. The Bragg peak energies (left) differ from previously presented RCF data, due to an adapted stack composition.

## 4.2 Characterization at Draco

PP measurement taken at the PHELIX laser shall serve as example.<sup>13</sup>

Figure 4.12 shows a recorded pepper-pot signature from a slightly misaligned solenoid and compares it to the simulation output for a solenoid that has been tilted by  $0.25^\circ$  upwards at its rear end. The pivot point was chosen to be on the beam axis at the z-position of the first solenoid winding, i.e. the solenoid entrance. The RCF was taken from a stack. It shows the absorbed dose of 8 MeV protons and above. Therefore, protons of 8 to 9 MeV kinetic energy composed the GPT particle source, were set to approximate a typical TNSA angular distribution and traversed the solenoid field (straight windings). The pepper-pot cannot be simulated in GPT. Instead, a python script was used to sort out particles at PP position. The hole size was increased to  $500\ \mu\text{m}$  in order to maximize the transmitted proton number and keep the simulation small. The transmitted protons were then fed back into GPT where they propagated to the position of the simulated detector screen.

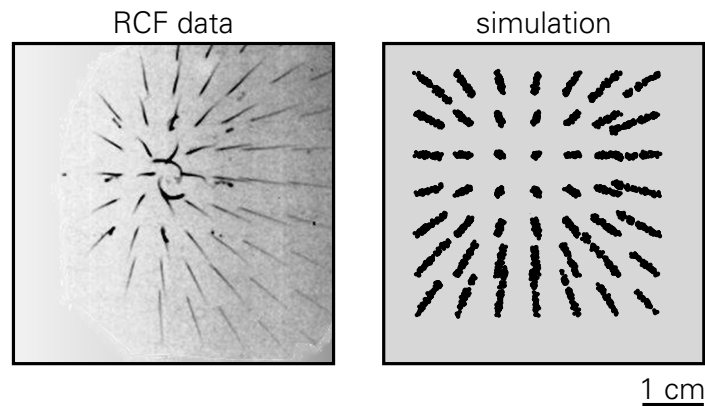


Figure 4.12: Pepper-pot RCF signature (red channel) from a misaligned solenoid in comparison to a simulated signature corresponding to  $0.25^\circ$  tilt of the solenoid (solenoid exit tilted upwards). For more details see text. Shot/simulation parameters: PP position 1080 mm to target/source, RCF/screen position 1650 mm to target/source, PHELIX,  $\approx 11\ \text{J}$  on  $10\ \mu\text{m}$  Ti target.

The simulation reproduces key features of the experimentally recorded PP signature. The (virtual) intersection point of the traces is in both cases shifted upwards and to the left. The length of the traces is longer on the right and bottom, whereas the traces on the left and top appear truncated. The resemblance is not perfect, yet the data suggests that a similar misalignment was present in the experiment. Unfortunately, the limited number of available laser shots made verification measurements unfeasible at the PHELIX facility. Nevertheless, the presented method allows to gain a rough idea about the alignment of the solenoid with respect to the beam axis and the simulation model can predict PP signatures even for complex misalignment scenarios. It is of great importance for solenoid alignment at laser systems with low repetition rate like PHELIX and considered to be applied in the future. Finally it may be noted that some misalignment scenarios can result in similar PP signatures as fig. C.5 in appendix C.4 reveals. It also depicts selected simulated PP signatures for different mis-

<sup>13</sup>Solenoid alignment is a challenging task that is especially tedious at the PHELIX laser for three reasons: First, the low repetition rate of the PHELIX laser (1 shot per 90 minutes) limits the available number of alignment shots to a few 10 per beamtime. Second, the solenoid is removed after every experiment, thus solenoid alignment has to be performed for every campaign. Third, precise remote motorization is not applicable due to weight and size limitations.

alignment severity and therefore makes quantitative predictions on solenoid misalignment possible.

### CONCLUSION

In this section the detailed characterization of the capturing solenoid at the Dresden laser acceleration source Draco has been presented and discussed. It was demonstrated that with typical efficiencies of the order of 30 % up to  $10^8$  protons of  $10 \pm 0.5$  MeV kinetic energy can be transported and focused by the solenoid, well controlled and tunable. The solenoid focal spot shows signs of astigmatism resulting from the interplay of the helical solenoid windings and the high divergence beams. Yet, the confinement of the particles to an area of few  $\text{mm}^2$  was demonstrated and doses above 200 Gy recorded. To improve on the astigmatism, conceptual changes on the solenoid winding geometry have to be the long-term goal. Meanwhile, decreasing the focal distance or reducing the incoming beam divergence can minimize the astigmatic effect of the solenoid lens. The pepper-pot measurements set an upper limit on source emittance of laser driven proton sources and measured an emittance blowup by almost a factor of 4 when the solenoid is operated. Nevertheless, the measurements show only minor deviations from the simulation predictions. The PP has been identified as valuable tool for solenoid alignment.

The technology platform developed in this thesis allows for easy adaptation. Therefore, improvements, as they are worthwhile, e.g. considering beam optical quality, can now be pursued and studied easily. Extensions of the beamline are possible, thus allowing for further studies in the field of medical beam guidance, gantry development and fundamental research. The next chapter will now deal with first hands-on application experiments for the developed and characterized solenoid.



# 5 APPLICATION STUDIES USING THE CAPTURING SOLENOID

## 5.1 THE LIGHT BEAMLINE

The previous chapters focused on the characterization of the capturing solenoid at a conventional reference source as well as at the laser accelerator Draco. It has been shown that the capturing solenoid is suitable to gain control over beam divergence in close vicinity to the laser-target interaction position. It is therefore key for a variety of application studies in the field of translational medical research. Yet, possible application scenarios are as various as the magnet is versatile. The studies performed within the framework of the LIGHT collaboration will be discussed in the following as a demonstration of named versatility.

### 5.1.1 INTRODUCTION

The LIGHT project is a German scientific collaboration pursuing the scientific goal of studying Laser Ion Generation, Handling and Transport, conjoint in the acronym **LIGHT**. The LIGHT collaboration partners<sup>1</sup> bring together expertise in the fields of high-power laser development, laser acceleration, targetry as well as conventional accelerator and high-field magnet technology.

The flagship experiment of the collaboration is the LIGHT beamline. It is located at GSI – Helmholtzzentrum für Schwerionenforschung, Darmstadt, Germany. The main purpose of the LIGHT beamline is to study and demonstrate the feasibility of combining laser-driven ion sources with conventional accelerator technology to provide tunable beams for application. Therefore, a dedicated branch of GSI’s high-power short-pulse laser PHELIX is used to drive a proton or heavy ion source at the Z6 experimental area (see appendix A). LIGHT studies magnet systems to efficiently inject the laser-driven beam into a radiofrequency (RF) accelerator cavity. The cavity is used to manipulate the ion beam phase space, with two operation modes coming to mind: First, generation of quasi-monoenergetic ion beams via phase rotation [44] and second, temporal compression for reaching ion bunch lengths below ns-level by

---

<sup>1</sup>The collaborators are GSI – Helmholtzzentrum für Schwerionenforschung, Darmstadt; Helmholtz-Zentrum Dresden – Rossendorf; the Helmholtz Institute Jena; Technische Universität Darmstadt; Technische Universität Dresden; Friedrich Schiller Universität, Jena and Johann Wolfgang Goethe Universität, Frankfurt.

over-rotation in phase space and drift [46].<sup>2</sup> In this context, the capturing solenoid (cf. right side of fig. 3.7) has been studied extensively [43, 44, 46]. In addition, permanent magnetic quadrupole magnets were examined [45].

Figure 5.1 depicts the LIGHT beamline experiment setup and shows exemplarily how the cavity acts on a proton bunch preselected by the capturing solenoid. When the injection time is tuned in a way that allows particles at nominal energy to pass without experiencing accelerating or decelerating forces, while the more energetic, leading particles that enter the cavity earlier are slowed down and the less energetic, trailing particles are accelerated, the cavity is operated as a so-called buncher. Thereby, a quasi-monoenergetic bunch can be generated from parts of the broad exponentially decaying energy spectrum of laser accelerated ions while still preserving high particle numbers. As reported in Busold et al. [44], FWHM energy spread was reduced from 18 % to well below 5 % by applying the RF cavity in addition to the capturing solenoid. Still, the particle numbers within the FWHM stay above  $10^9$  owing to the pulsed high-field magnet.

The second operation mode of the beamline explored by the LIGHT project is the so-called phase or temporal focusing. If the leading particles are decelerated below the mean bunch velocity, the central part of the bunch can overtake them while simultaneously being overtaken by the former trailing particles that have been accelerated to speeds above mean. Thereby, after a certain drift, temporally short bunches are produced that, if laterally confined, allow for the generation of very high beam intensities, as will be shown later on. The necessary drift length can be tuned by adjusting the cavity field amplitude.

More detailed explanations of the LIGHT collaboration and the beamline experiments that have been accompanied within the framework of this thesis can be found in Busold et al. [43–46]. The following sections build on the previous experiments and present exemplary results that could be achieved owing to the developed magnet and pulse generator technology. The presented results shall be viewed as a collective achievement of the LIGHT collaboration.

### 5.1.2 TOWARDS HIGHEST PROTON BEAM INTENSITIES

This section summarizes how the LIGHT beamline was used to generate intense proton bunches. A comparison of two different beam transport setups towards the second target chamber (TC2, cf. fig. 5.1) is given.

As depicted by the inset in fig. 5.1, the cavity is operated as a buncher. The RF amplitude has been tuned to generate a proton bunch over-rotated in phase space that has a temporal focus approximately 3.5 m downstream of the cavity exit. The position of the temporal focus is inside TC2, where diagnostics detect the beam and material samples can be irradiated.

To measure the temporal length of the proton bunch compressed by the LIGHT beamline, several methods have been applied in the past, including streaked optical imaging of fast scintillators [46]. Here, data obtained by a different method is presented. Measuring the time of flight (TOF) of the protons can be used to gain spectral information if the time of production and the flight distance are precisely known. Measurements with fast TOF detectors can also be used to determine the temporal length of a particle bunch as the signal incline and following decline are analyzed. This clearly requires detectors with shorter response and decay times than the bunch length to measure. As the goal of the LIGHT beamline is to temporally compress the bunches close to their duration at origin, i.e. to the ps level, exceptionally fast

---

<sup>2</sup>The cavity only provides a total potential of 1.1 MV over its three gaps limiting the particle energy gain accordingly. It is therefore not used for post-acceleration. The RF power (up to 100 kW) is provided to the cavity by the 108.4 MHz RF infrastructure of GSI's UNILAC accelerator. The design energy of the cavity is  $8 \text{ MeV u}^{-1}$ .

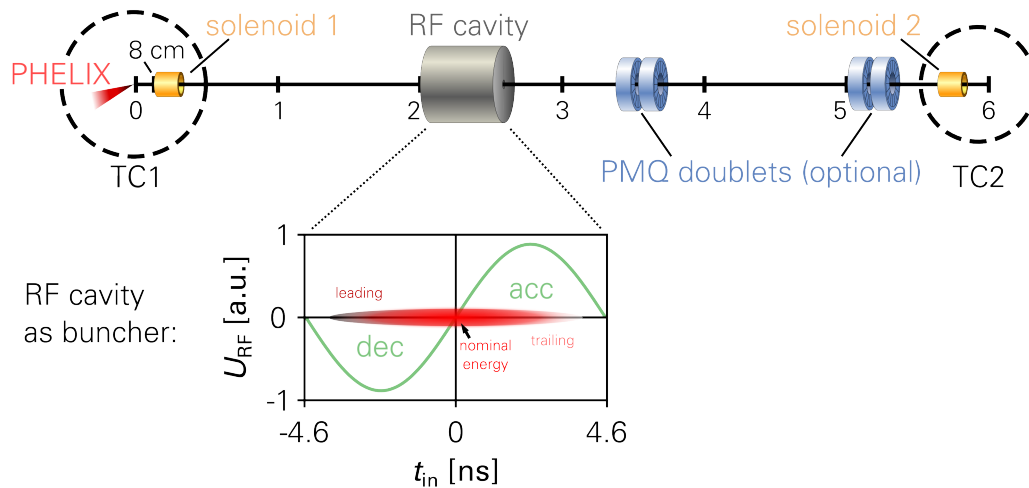


Figure 5.1: Sketch of the LIGHT beamline at GSI, Darmstadt. The PHELIX laser drives a TNSA ion source in target chamber 1 (TC1). Solenoid 1 is set to capture and focus ions of nominal energy. It provides for an effective injection into the RF cavity. The injection time  $t_{in}$  is chosen so that the cavity operates as buncher (see text and plot). The particles are transported further to a second target chamber (TC2) where they can be analyzed and applied for irradiation studies, six meters downstream of the laser-target-interaction point. The transport can be assisted by additional focusing elements, i.e. two permanent magnetic quadrupole (PMQ) doublets. A second solenoid in TC2 provides for steep final focusing.

detectors are required. Diamond detectors have been found to meet the demands of the predicted measurement. These diagnostics operate like semi-conductor particle detectors. By applying a bias voltage to the diamond, free charge carriers induced by the impinging beam can be recorded as voltage signal. The artificial diamond can be fabricated by chemical vapor deposition in very thin slabs of only few  $10\ \mu\text{m}$  thickness, thus allowing for low charge drift times in the range of few 100 ps. Diamond detectors are additionally very radiation hard ( $> 10^7$  particles/ $\text{mm}^2$ ) and routinely used at GSI's accelerators.

The TOF detector used to record the following data was developed and characterized by Diana Jahn of TU Darmstadt and manufactured by GSI's detector laboratory. It employs a  $13\ \mu\text{m}$  thick polycrystalline diamond. The detector's voltage signal can be described as convolution of the real signal (containing the temporal information) and the characteristic detector response expressed by the point spread function.<sup>3</sup> The temporal bunch length can therefore be extracted from the deconvoluted measurement signal. An iterative deconvolution algorithm was developed by Dennis Schumacher of GSI and applied to the data.

Figure 5.2 shows the measured diamond detector signal (blue) corresponding to a temporally compressed, impinging proton bunch of 7.8 MeV central energy. It also compares the measurement to the deconvolution (green) of the signal after ten thousand iterations. The reconvolution of the green curve with the detector inherent point spread function yields the orange curve that reproduces the measured data. The integral difference between reconvolution (orange) and measured signal (blue) is depicted in purple. The deconvoluted signal

<sup>3</sup>The point spread function was measured by means of exciting the detector with fs laser pulses and recording the detector response.

## 5.1 The LIGHT Beamline

(green) finally gives a temporal bunch length of  $468 \pm 104$  ps (FWHM). For comparison, a reference bunch of 7.8 MeV central energy and an energy spread of  $\pm 0.5$  MeV has a temporal length of 9 ns after traveling the distance of 6 m to TC2. Thus, by recompression in time, a 20-fold increase in proton current can be achieved at the position of the diamond detector.

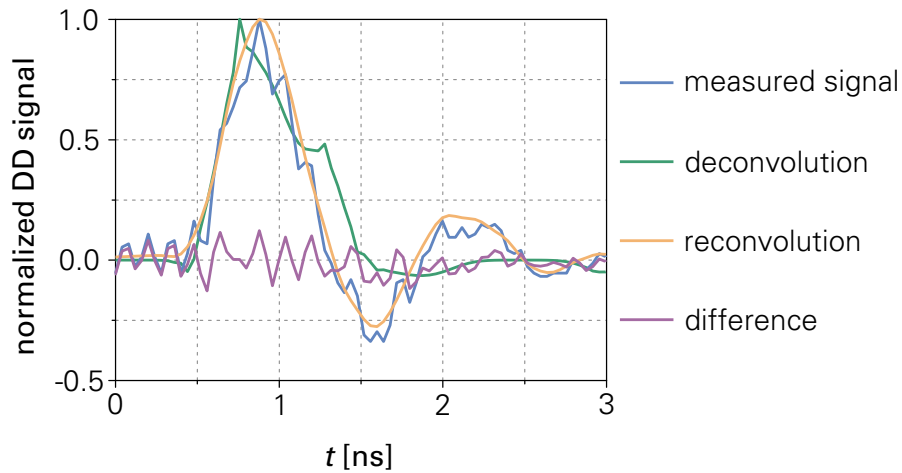


Figure 5.2: Proton TOF signal measured by means of the diamond TOF detector at conditions optimized for temporal focusing. The bunch length was extracted to be  $468 \pm 104$  ps. See text for detailed information. Shot parameters: solenoid 1 field 6.6 T, 11.3 J on 10  $\mu$ m Au target.

To generate highest intensities, in terms of proton flux, a narrow lateral confinement of the temporally compressed bunch is key. The LIGHT beamline was therefore equipped with a second pulsed high-field solenoid of identical type. It was installed in TC2 and fed by a distinct pulse generator.<sup>4</sup> The goal is to refocus the diverging beam and reduce its lateral dimension, thus maximizing the flux.

The first study was carried out using permanent magnet quadrupoles (PMQs) as depicted in fig. 5.1. The PMQs were arranged in two doublets to prevent particle loss in the 40 mm beam pipe. In a follow up experiment, the PMQs were discarded and a 100 mm beam pipe was installed.

RCF data for both experimental campaigns was analyzed for absolute proton numbers. For the nominal energy, i.e. 7.8 MeV, the analysis yields

$$N_{\text{PMQ}} = (2.9 \pm 1.5) \cdot 10^8, \quad (5.1)$$

$$N_{\text{noPMQ}} = (5.7 \pm 2.9) \cdot 10^8. \quad (5.2)$$

Considering the large error margins of the analysis method and the TNSA inherent fluctuation of particle numbers at production, the data does not allow to conclude a significantly higher transport efficiency for the setup without PMQs. On the other hand, the RCFs irradiated with the PMQ setup exhibit a less confined proton distribution within TC2. Apparently, field imperfections and quadrupole misalignment limit their efficiency and introduce velocity components that can only partially be compensated by the second solenoid. Thus, due to the improved lateral confinement, in case of transport without PMQs, a strongly enhanced proton flux (at least twofold) was obtained.

<sup>4</sup>Both PG3 and PG4 have been used consecutively in two experiment campaigns.

The proton transport solely by pulsed high-field solenoids confines the beam laterally to an area of  $30 \text{ mm}^2$ . With the particle number given by eq. (5.2) and the temporal bunch length of 468 ps, the proton current for the presented setting is determined to  $I = 195 \text{ mA}$ . Thus, the presented setup is even superior to the best shot obtained by Busold et al. [46], where the final focusing with the second solenoid was not applied. The current could be slightly increased and the lateral confinement was improved by a factor of two.

It has been proven that the LIGHT beamline poses a unique opportunity to generate high-intensity proton bunches. Owing to continuous improvement it now enables peak particle flux above  $6 \text{ mA mm}^{-2}$  for future application studies like proton radiography. The LIGHT beamline also suffers from solenoid aberrations. Hence, for such studies it might be necessary to homogenize the particle distribution by means of scatter foils in the beamline. That would decrease the proton flux slightly. The decrease is planned to be compensated by increasing the initial laser acceleration performance with improved laser optics.

### 5.1.3 TOWARDS APPLICATION OF HEAVY ION BEAMS

Many applications of intense, energetic ion beams do not solely focus on protons. In fact, for a variety of applications, heavier ions can be favorable. For example, in ion beam therapy the treatment of tumors with heavier ions like helium, oxygen or carbon can be of advantage for the radiotherapy patient [4, 6, 120]. Laser-based warm dense matter research, isochoric heating or material damage studies for the fusion sciences also rely on heavy ion beams. Like all acceleration mechanisms, TNSA favors particles with a high charge-to-mass ratio. Thus, in analogy to conventional accelerator infrastructure, the demands for efficient acceleration of heavy ions by laser-driven plasma processes are much greater. Anyhow, a rather simple method can be used to prepare a (solid) laser target for the acceleration of heavy ions.

As discussed in chapter 2, a TNSA proton source relies on the contaminant layer of hydrocarbons present on foil targets. When a target is fully cleaned of the contaminants, the ion species with the next highest charge-to-mass ratio is accelerated most efficiently. Typical cleaning procedures include laser-based methods like laser heating or ablation [121, 122], or complementary simple ohmic heating [123, 124] of the conducting target material. In this manner, even unconventional ion species can be accelerated as only the target composition limits the acceleration possibilities.

In the following, a kick-off experiment will be presented, where the unique properties of the LIGHT beamline are applied to laser-accelerated heavy ion beams. The ion species of interest was fluorine. Fluorine is the element with highest electronegativity and hence extremely reactive. Therefore, conventional accelerators usually do not operate with this ion species. Laser-driven sources, however, are not negatively affected by the highly corrosive fluorine and pose as opportunity to facilitate beam experiments with otherwise inaccessible ion species.

In analogy to Hegelich et al. [123], an ohmically heated  $13 \mu\text{m}$  tungsten (W) target coated with a  $1 \mu\text{m}$  calcium fluoride ( $\text{CaF}_2$ ) layer was used to generate laser-accelerated heavy ion beams with  $\text{F}^{7+}$  as dominant ion species ( $E_{\text{max}} \approx 5 \text{ MeV u}^{-1}$ ). At first the transport of this reference species shall be discussed:

Revisiting eq. (3.15) and generalizing it for ions of charge  $q_i$  and mass  $m_i$  one gets the following focal length formula:

$$\frac{1}{f} = \frac{q_i^2}{4\gamma^2 m_i^2 v_{i,z}^2} B_0^2 l. \quad (5.3)$$

## 5.1 The LIGHT Beamline

For non-relativistic ions, i.e.  $E_{i,\text{kin}} = p_i^2/2m_i$  with ion momentum  $p_i = m_i v_i$ , the following proportionality relations for focal length and magnetic field hold:

$$f \propto \frac{p_i^2}{q_i^2} B_0^{-2} \propto \frac{m_i E_{i,\text{kin}}}{q_i^2} B_0^{-2} \propto \frac{A_i^2 \langle E_{i,\text{kin}} \rangle}{Q_i^2} B_0^{-2} \Rightarrow B_0 \propto \frac{A_i}{Q_i} \sqrt{\frac{\langle E_{i,\text{kin}} \rangle}{f}}. \quad (5.4)$$

with atomic mass number  $A_i$ , ion charge number  $Q_i$  and kinetic energy per nucleon  $\langle E_{i,\text{kin}} \rangle$ . Thus, comparing a proton beam ( $A = 1$ ,  $Q = 1$ ) with named fluorine ions ( $A = 19$ ,  $Q = 7$ ) of identical kinetic energy per nucleon, one finds that focusing the fluorine beam at the same position as the protons requires a field increase by a factor of  $19/7 \approx 2.7$ . Usual field strengths, as described in the previous section 5.1.2, are 5 to 7.5 T for transporting 5 to 10 MeV protons through the cavity. The maximum achievable field strength at Z6, limited by the available pulse generator PG2, is 8.8 T. Hence, the transport of  $F^{7+}$  ions is limited to energies of approximately  $1.9 \text{ MeV u}^{-1}$ .

As a matter of fact, the cavity cannot be used to manipulate ion bunches with kinetic energies close to  $2 \text{ MeV u}^{-1}$ . The cavity frequency of 108.4 MHz corresponds to a cavity cycle period of  $T_c = 9.2 \text{ ns}$ , meaning that after every 9.2 ns the cavity is in the initial state again. Unfortunately, 9.2 ns is also the duration that particles of named energy need to travel from one gap to the next.<sup>5</sup> Thus, the effect of the first gap is canceled by the following. In this particular situation, the cavity cannot compress the bunch spectrally or temporally.

Towards lower energies, the next sweet spot is distinct at approximately  $1 \text{ MeV u}^{-1}$  corresponding to  $1.5 \times T_c$  (or  $3\pi$ ). It may be noted that the rapidly changing field amplitudes, experienced by the slow particles passing the gap, limit the efficiency of the cavity.

The data presented in the following fig. 5.3 was obtained at a 6 T field strength corresponding to the discussed central energy of  $1 \text{ MeV u}^{-1}$ . In spite of the decreased cavity efficiency, the cavity amplitude needed to be reduced by approximately 75 % in comparison to protons, accounting for low energy and high charge of the ions. This enabled the generation of narrow peaked heavy ion bunches. The TOF signal measured by the diamond detector in TC2 was converted to an energy spectrum and is depicted in fig. 5.3.

Figure 5.3 shows a multitude of ion bunches of narrow energy bandwidth attributed to  $F^{6+}$  and  $F^{7+}$  as tracing simulation show the strong suppression of other charge states in the given energy range. The proton signal is completely suppressed. This demonstrates that the cleaning process by means of ohmic heating is effective. The result verifies the functionality of the LIGHT heavy ion beamline.

The high number of bunches arises from the long bunch length upon cavity injection, as the following comparison exemplifies: Ions of  $1 \text{ MeV u}^{-1}$  reach the center of the cavity after approximately 164 ns, whereas  $0.8 \text{ MeV u}^{-1}$  ions take 183 ns. Thus, even for this low energy spread, a bunch of 19 ns duration, twice the cycle period, is injected into the cavity. This results in the formation of so-called satellite bunches. A peak is generated when the energy-dependent injection time for a part of the bunch matches the cavity phase ( $-90^\circ$ , cf. fig. 5.1).

Anyhow, the goal of the LIGHT beamline is to generate a single high-intensity ion bunch. Thus, the generation of multiple bunches is counterproductive. The production of multiple ion species and charge states cannot be suppressed. The generation of multiple bunches per charge state, on the other hand, can be actively stalled by two methods: First, increasing the ion energies to a degree comparable to the proton scenario enables shorter durations of the bunches transported by the high-field magnet. Second, moving the cavity closer to the

<sup>5</sup>The distance from gap center to gap center is 180 mm.

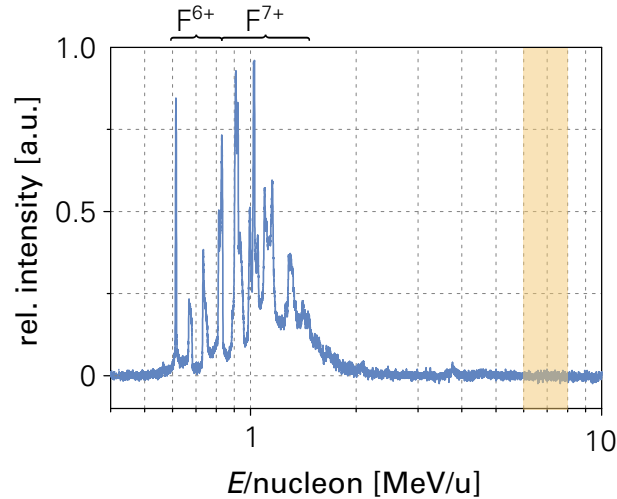


Figure 5.3: Fluorine ion spectrum after capturing solenoid and RF cavity. The spectrum was extracted from TOF data of the diamond detector at TC2. For the applied solenoid field and cavity settings, the proton signal is expected in the area marked orange. As can be seen, the proton acceleration was suppressed. The cavity generates multiple, spectrally narrow fluorine bunches due to the long incoming bunch duration and the different charge-to-mass ratios for  $F^{6+}$  and  $F^{7+}$ . Shot parameters: PHELIX, 11.5 J on  $13\ \mu\text{m}$  W +  $1\ \mu\text{m}$   $\text{CaF}_2$  target, heated to approx.  $1100^\circ\text{C}$  for 10 min,  $E_{\text{max}} \approx 5\ \text{MeV u}^{-1}$ , solenoid 1 field 6 T.

laser-target-interaction point also reduces the temporal spread. Both options are considered for future application.

According to the scaling law in eq. (5.3), the capturing solenoid is able to transport fluorine ions of the cavity design energy ( $8\ \text{MeV u}^{-1}$ , if accessible for  $F^{7+}$  in future experiments) at 17 T peak field. That is currently not reachable with the pulsed-power equipment present at the LIGHT beamline. Anyhow, it can be accomplished with the pulse generator technology developed in this thesis. For the proof-of-principle measurement at hand, it was not yet applicable since a thorough testing of the interplay of the entire pulsed power equipment on site was deemed necessary in advance to the experiment for safety reasons. Upgrading the existing pulse generator PG2 or (temporarily) replacing it by PG3 or the upcoming PG5 allows for field generation up to almost 20 T and is therefore a promising opportunity for future experiments. For the time being, qualitative and quantitative analyses of heavy ion generation will be performed. Measurements with dedicated Thomson parabola spectrometer and Faraday cup will provide spectral information and cut-off energies for the different ion species and charge states as well as absolute charge values of the laser-generated ion beams.<sup>6</sup>

#### 5.1.4 CONCLUSION

The successful generation of intense and/or mono-energetic proton and ion bunches in a well-controlled manner from a laser-driven source is a remarkable proof of concept and makes the

<sup>6</sup>It may be noted here, that an energy resolved measurement of the laser-drive fluorine beams is not possible by means of RCF stacks, since the penetration depth of the particles is only in the range of few  $10\ \mu\text{m}$ . The lateral beam profile, accumulated over all ion species, can only be registered by films without protective coating, since the coating thickness is typically  $125\ \mu\text{m}$ .

LIGHT beamline an exceptional test bed for many application experiments in the fields of fusion science [70], warm dense matter research [125–127] and diagnostics [76, 128, 129]. Laser repetition rate as well as laser and RF availability limit the applicability of the LIGHT beamline as user facility. The desirable goal for the future is therefore to enable permanent installation of the beamline with dedicated RF infrastructure and high laser availability accompanied by improved particle beam transport by advanced high-field magnets. The exceptional trinity of laser accelerator, pulsed high-field magnet and accelerator cavity, make the LIGHT beamline the first and only laser-driven systems that may compete with the sophisticated accelerator infrastructure for highest ion beam intensities like NDCX-I/II [130, 131].

## 5.2 FUNCTIONAL TEST OF A FIRST PULSED MEDICAL BEAMLINE

### 5.2.1 INTRODUCTION

In section 1.1 a visionary concept for a compact, cost-efficient system for ion beam therapy (IBT) of cancer was introduced. It combines a compact laser-driven ion source with a likewise compact beam delivery based on pulsed high-field magnets. The potential of such a system has been studied meticulously within the onCOOPtics project. The theoretical feasibility of a realistic pulsed high-field gantry system, able to shape laser-driven proton beams both spatially and spectrally, was successfully shown by Masood et al. [33] and Masood et al. [34]. Parts of the innovative concepts are to be protected by patent [132]. Up until now, however, sophisticated medical beam transport for laser-accelerated ions via high-field magnets has only been studied in simulation. The presented pioneering work, however, is a first step into the uncharted territory of experimental studies on named topic.

A functional demonstration of a novel pulsed high-field beamline is presented, consisting of the capturing solenoid and a dipole sector magnet, representing two crucial parts of a gantry system for laser-accelerated ion beams [33]. The beamline marks a fundamental step towards application of laser-accelerated beams in IBT, but also for a variety of other applications, as it allows to gain control over the divergence and energy bandwidth of the proton bunches.

As can be seen from fig. 1.1, medical beam transport requires deflecting the beam by up to 90°. For this matter, dipole magnets like the one presented here are essential. Furthermore, it will be demonstrated that dipole magnets are valuable tools to perform energy selection on laser-driven beams with broad kinetic energy distribution. Investigations on shot-to-shot fluctuations of the pulsed high-field beamline conclude the study.

### 5.2.2 EXPERIMENTAL SETUP

Upgrading the setup for solenoid characterization (cf. fig. 4.1), both pulsed high-field magnets and the diagnostic chamber were connected to the tandemron accelerator's evacuated beam pipe. The proton beam traverses the capturing solenoid first. The dipole is entered secondly by the beam and is constructed with an integrated beam pipe of 18 mm diameter. The experimental setup is depicted by fig. 5.4.

The dipole sector magnet was developed within the onCOOPtics project by the laser-radiooncology group of OncoRay – National Center for Radiation Research in Oncology, Dresden. In line with this thesis, conception, construction and functional testing of the dipole prototype have been assisted.

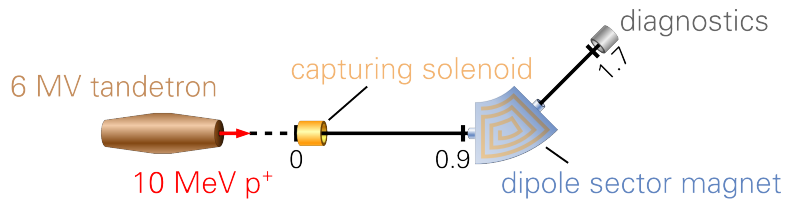


Figure 5.4: Schematic of the experimental setup of the pulsed beamline at HZDR's tandemron accelerator. Distances given in meters. The diagnostics chamber at the end of the beamline could be equipped with scintillator and radiochromic film detectors.

In accelerator physics, a dipole magnet is used to deflect charged particle beams by field generation perpendicular to their propagation direction. Ideally, the field amplitude inside the dipole magnet is constant and vanishes on the outside. In conventional (DC) dipole magnets, the field can be shaped accordingly by using cores of high magnetic permeability. Iron or other core materials typically saturate below 2 T field strength, preventing the generation of higher fields. To approximate the desired field configuration, scaled towards higher fields, complex wire geometries are required that cannot be fabricated by the winding techniques for cylindrical magnets as presented in section 3.1.4. Therefore, a novel, patented production technique has been developed for practical realization of the magnet [133].

The dipole sector magnet used in this study consists of two saddle-shaped halves formed to match the particle trajectories. The dipole was consecutively wound from stranded copper wire that was lain in a PU support structure. Thereby, the magnet was set up layer by layer. The assembled magnet consists of 80 windings in 12 layers. With a mass of only 52 kg and a volume of  $0.03 \text{ m}^3$  it is very compact and lightweight in comparison to conventional dipole magnets (several tons and cubic meters) for similar proton beam properties [134]. Figure 5.5 shows a photograph of the dipole during production and on-axis field profile. As can be seen, the magnetic field does not show a flat top. Therefore, the beam pipe was tailored according to the different curvatures of the ion beam at different positions along the dipole axis. In the central part of the dipole, the beam pipe curvature has a radius of 200 mm. The magnet is designed to deflect particles by a  $50^\circ$  angle.

The support structure has to withstand the forces during the magnetic pulse since the stranded wire has almost no structural integrity. It also provides for the necessary insulation between neighboring wires and winding layers. The dipole was successfully operated up to peak field strengths of 4.6 T at 8 kA current, sufficient for deflecting protons of 31 MeV kinetic energy. Increasing the field strength further led to a magnet failure as the support structure gave in, insulation dropped and a flashover damaged parts of the magnet. Failure analysis accompanied by comprehensive electrical and mechanical evaluation of the magnet led to a revised dipole design. Currently an optimized prototype is under construction.

Note, that the dipole is the first magnet that can be operated while cooled with (deionized) water. The water circulates around the stranded copper wire to take up the heat input of the current pulse. The prototype is therefore of highest importance for exploring the feasibility of magnet operation at high repetition rates in the range of 1 to 10 Hz matching current ultra-short pulse laser systems like Draco.<sup>7</sup>

<sup>7</sup>A collaboration study of HZDR and the Chair of Power Electronics of TU Dresden on repetition rate optimized pulse generators aims to develop a scalable prototype current driver with pulse repetition rates of 1 to 10 Hz. Such a novel system is necessary to investigate whether pulsed high-field magnets can be operated at similarly high repetition rates. An ideal topology has been found and prototype production has begun [135].

## 5.2 Functional Test of a First Pulsed Medical Beamline

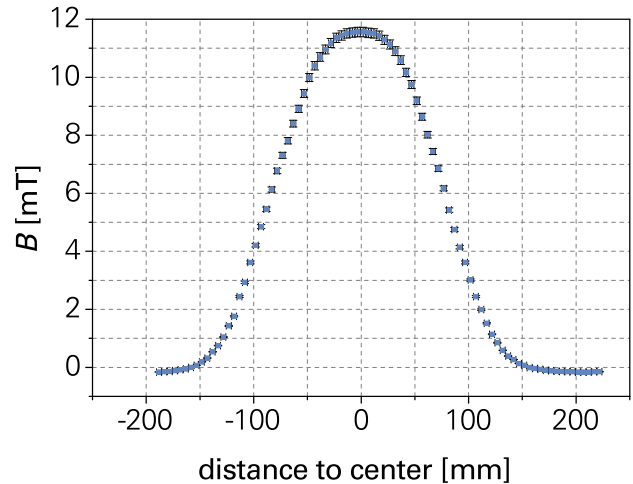
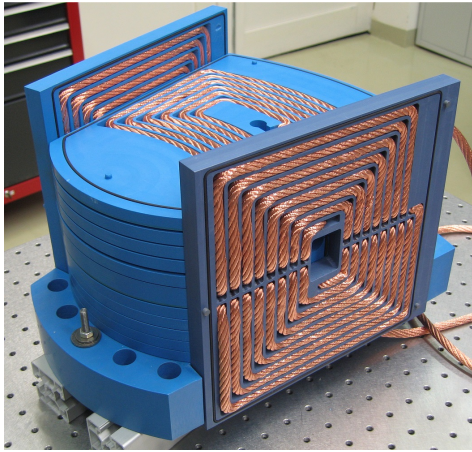


Figure 5.5: Left: Photograph of the dipole prototype during production. The saddle shaped upper half of the magnet's windings is visible, the lower half is already completely assembled. Right: On-axis field map plot obtained by hall probe measurement along the bent beam axis with respect to magnet center at 20 A DC current.

The experiment was conducted using 20 to 70  $\mu\text{s}$  bunches, rather long in comparison to the previously used  $\mu\text{s}$  bunches in section 4.1, but still temporally well shorter than both corresponding magnet pulses. Again, they were timed with respect to the maximum of the magnetic field, as can be seen from fig. 5.6.

The first experiment run was performed using PG3 to power both solenoid and dipole.<sup>8</sup> A limited number of four operation modes of the beamline resulted: solenoid only, dipole only as well as series and parallel connection of both magnets. The parallel connection was not applicable due to the specific inductance ratio of solenoid and dipole.<sup>9</sup>

### 5.2.3 RESULTS

#### BEAM TRANSPORT

The first operation mode, solenoid only, was discussed in section 4.1. There it has been demonstrated that a laterally broad ( $\approx 25$  mm) proton beam of low divergence ( $< 1^\circ$ ) can be focused by means of the capturing solenoid to a sub-mm (0.8 mm FWHM) spot size (cf. fig. 4.2(c)).

In second operation mode, dipole only, a lossless  $50^\circ$  deflection of the proton beam could be achieved (cf. fig. 5.7). The beam is laterally slightly broadened. The FWHM beam dimensions are increased by factor 1.1 vertically and 2.4 horizontally, i.e in the dipole's dispersive direction. The vertical broadening corresponds to the small, intrinsic beam divergence. The horizontal broadening arises because particles that are horizontally off-axis experience lower field strengths than on-axis particles. It might be necessary to compensate the horizontal

<sup>8</sup>During the initial experiment, PG4 was under construction and therefore not yet applicable.

<sup>9</sup>The dipole magnet has an inductance of approximately 450  $\mu\text{H}$ , thus larger than the solenoid. In parallel operation the solenoid current would therefore be higher than the dipole current. For efficient particle transport the opposite ratio was required making the parallel connection inapplicable. Series connection allows for (not yet perfect but more adequate) identical currents.

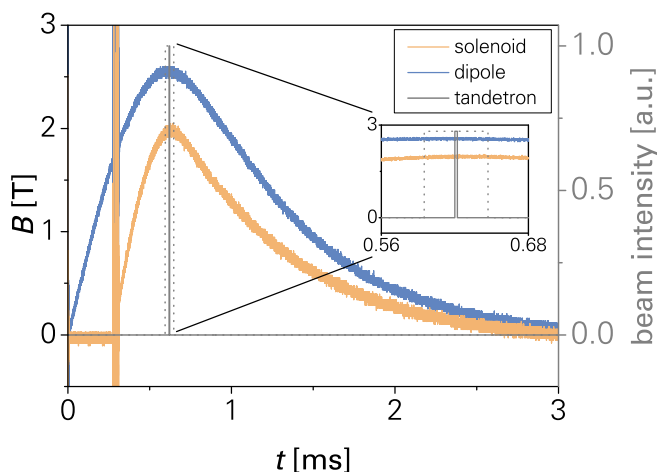


Figure 5.6: Time structure of the magnetic field pulses (calculated from Rogowski coil current measurements) in comparison to proton bunch lengths (20 to 70  $\mu\text{s}$ ) of the tandetron accelerator. The inset illustrates the constancy of the field amplitudes even for the longest chosen bunch lengths (dashed).

broadening effect in a future beam guidance system. The magnet was typically operated at 2.6 T/4.5 kA.

The third operation mode, series connection of both magnets, comes with a drawback. In series connection, the current pulse amplitude is equal in both magnets, thus making an separate adjustment impossible. Since the dipole can only transport the protons when its field is precisely at the right magnitude (only deviations of the order of 1 % can be tolerated, see below), it dictates the current for both magnets. This lead to a very short solenoid focal length, approximately half a meter. So the particles were already highly divergent when entering the dipole.<sup>10</sup> The result is loss of particles. To prevent the loss, we introduced a 25  $\mu\text{m}$  thick brass scatter foil in front of the solenoid. The selection of foil material and thickness was accompanied by SRIM [136] calculations. The chosen scatter foil represents a reasonable compromise between energy loss, particle loss, scattering and availability. The divergence of the incoming beam could be increased to a mean scatter angle of 3° according to SRIM. Thereby, the solenoid focus was slightly shifted towards the dipole and the majority of the protons could be transported. Particle loss occurred at the solenoid entrance, due to the laterally very broad scattered beam, and inside the dipole, due to beam divergence.

In a follow-up experiment, with pulse generators PG3 and PG4 available and separately tunable  $B$ -field amplitudes, the lossless proton beam transport (without scatter foil) was achieved and monitored by measuring the incoming intensity of the laterally broad proton beam and consecutively the intensity at the end of the beamline by means of RCF and scintillator.<sup>11</sup> No significant particle loss could be detected over multiple shots. As can be seen from fig. 5.7, the beamline and the magnets separately are fully operational and able to focus and deflect pulsed ion beams. Thus the basic functionality was demonstrated. In the following, measurements on energy dispersion and shot-to-shot stability of the beamline are presented.

<sup>10</sup>For practical reasons the dipole magnet could not be placed in such close vicinity to the solenoid.

<sup>11</sup>The limited amount of beamtime in the follow-up experiment made it necessary to focus on the transmission and stability (described below) study. The reproduction of previously obtained data, under extended experimental capabilities owing to the two pulse generator setup, had to be omitted.

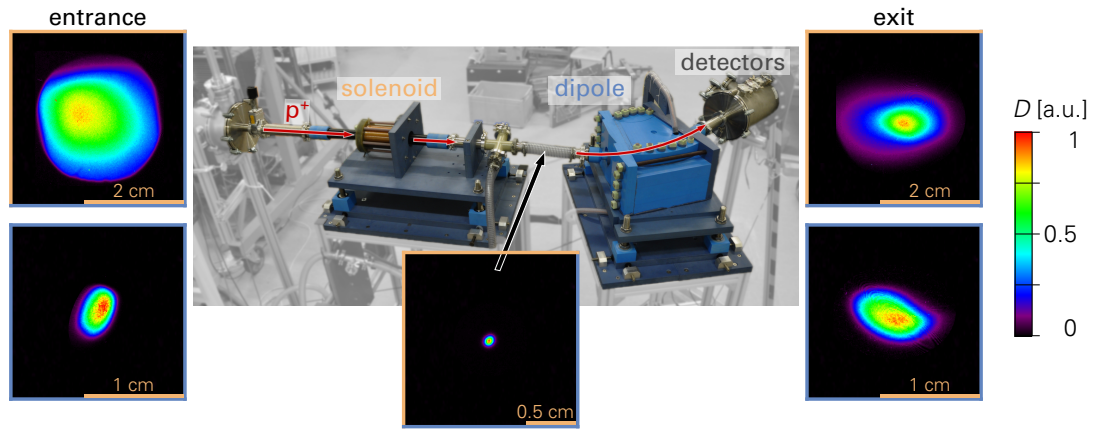


Figure 5.7: Experimental setup and typical lateral beam profiles (RCF, dose color coded) at different positions along the beamline. Blue framed images indicate that the beam parameters were chosen to fit dipole only operation, bicolored frames indicate typical beam profiles when both magnets were operated, e.g. broad incoming beam (top left) focused by solenoid (bottom middle) and then deflected by the dipole (top right). The top right picture was taken when an additional scatter foil was introduced in front of the solenoid to generate a distribution like the upper left but with increased divergence, see text for details.

## ENERGY SELECTION

Every rotational radiotherapy gantry system utilizes some sort of bending magnet to guide the beam towards the patient. In laser-driven IBT these bending magnets, like the presented dipole, additionally can serve another purpose. Whereas conventional proton accelerators provide monoenergetic particles of adjustable energy, a laser-driven proton source feeds the gantry a broad energy spectrum. Thus, an energy selection system needs to be included in the gantry.

The chromatic focusing of the solenoid can give a first rough energy selection [43]. To choose the energy more precisely, the dispersion of the dipole magnet is key. To study the capabilities for energy selection, we chose to vary the dipole field strength instead of the incoming particle energy, since the latter requires extensive accelerator adjustment. Nevertheless, the measurement allows for determination of energy selection capabilities as will be explained now.

When a proton with momentum  $p$  and elementary charge  $e$  enters a dipole magnet field  $B$  it is deflected. The bending radius  $\rho$  of the proton trajectory can be calculated in accordance to the so-called magnetic rigidity formula

$$B\rho = \frac{p}{e}. \quad (5.5)$$

Equation (5.5) shows that for a given bending radius  $\rho$  a change in  $B$  is equivalent to a corresponding change in proton beam momentum, as  $\Delta B/B = \Delta p/p$ . Figure 5.8 visualizes the relation between magnetic field and proton momentum/energy for the presented dipole setup.

In the experiment, the field strength was reduced in steps of 0.02 T from 2.6 T to roughly 2.52 T. Thereby, the deflection of the protons is decreased, as can be seen from fig. 5.9. The change in deflection was measured downstream of the dipole (inside the diagnostics

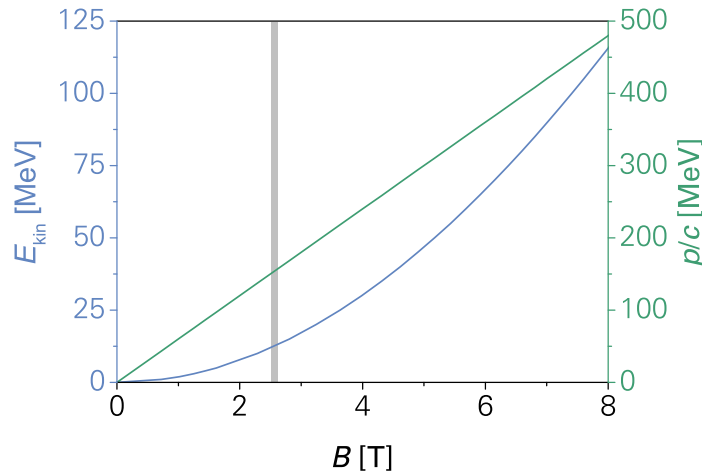


Figure 5.8: Plot of the magnetic rigidity relation between dipole field and kinetic energy  $E_{\text{kin}}$  (blue) as well as momentum  $p$  (green) for a proton beam. A bending radius of 200 mm, corresponding to the curvature of the inner part of the dipole beam pipe, was used. The gray area marks the region in which the field strength was varied to study dipole deflection.

chamber, cf. fig. 5.4) to be  $4.9 \pm 0.25$  mm and thus of an order that is well applicable for energy selection purposes. The applied change in  $B$ , of the order of 1 %, is analog to a 1 % momentum deviation. Thus with the presented configuration a dispersive separation of 10 MeV protons and  $10 \pm 0.2$  MeV protons is feasible. Scaled to clinically relevant proton energies, e.g. 200 MeV, the same holds true for  $200 \pm 3.7$  MeV. In future beam delivery systems, by applying an adjustable slit downstream of the pulsed dipole magnet, the mean transported energy as well as the energy bandwidth can be selected with high precision, enabling the generation of quasi-monoenergetic and broad energetic particle beams from laser-accelerated bunches as requested by Masood et al. [33]. The presented pulsed high-field beamline is therefore an important tool to prepare laser-accelerated ion beams for any kind of application that requires beams well defined spatially as well as in terms of energy.

### SHOT-TO-SHOT STABILITY

Finally, the shot-to-shot stability of the beamline and its components was studied. The strong forces acting on the magnet windings can lead to movement of the windings during the pulse. Especially the stranded wire of the dipole but also the rigid solenoid wires embedded in reinforcement composite materials have to be considered to experience small displacements during the pulse. Therefore it is necessary to measure the stability of the beamline over several shots. In order to do so, we installed a scintillator detector imaged by a CCD camera at different positions of the beamline and measured the beam position for 20 consecutive shots performed within few minutes. To quantify the stability, for each measured scintillation light distribution the centroids (first moments) of the scintillator's light distribution are calculated to compare their standard deviations and ranges for the different operation modes.

The incoming beam of the tandetron accelerator, as table 5.1 indicates, has a non-negligible spatial fluctuation of several  $100 \mu\text{m}$ , more pronounced in  $x$ - than in  $y$ -direction. This

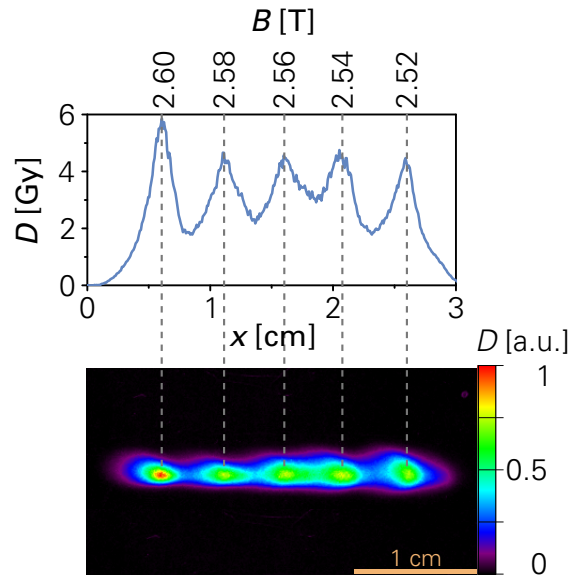


Figure 5.9: Dipole magnetic deflection illustrated by RCF (bottom, color coded absorbed dose in Gy) and corresponding dose profile (top). From left to right the field strength was gradually reduced from 2.6T in 0.02T steps. Every field reduction step is analog to raising the proton bunch energy by approximately 0.2 MeV.

fluctuation is reduced if the solenoid field is applied and the position of the focal spot is measured by the scintillator. The reduction can be explained in analogy to an optical system generating a demagnified image.

When the dipole magnet is operated individually, the spatial fluctuations are increased by a factor of 2–3. These stronger fluctuations are also present for operation of the entire transport system and can be explained by intrinsic beam fluctuations and geometry. We performed the latter two measurements downstream of the entire beamline. In contrast, the first two measurements were carried out introducing the scintillator in vicinity to the solenoid (cf. fig. 5.7). Therefore, the distance between the beam defining aperture and the detector was increased by a factor of approximately two, likewise increasing the lateral offset of the incoming beam. This, in combination with the beam induced variation of the lateral injection position into the dipole, results in mean fluctuation of approximately 0.6 mm in horizontal, i.e. dipole dispersive, direction with max deviation of up to 2 mm. The findings indicate that, with a better defined beam axis, the beamline intrinsic stability is of clinically acceptable sub-mm precision.

## 5.2.4 CONCLUSION

In this section, the full functionality of a first pulsed high-field beamline able to capture, deflect and spectrally shape proton beams with kinetic energies of up to 31 MeV has been shown. Both magnets exhibit very good pulse to pulse stability only limited by fluctuations of the incoming beam.

The pulsed high-field beamline potentially enables further practical studies towards laser-driven IBT. The presented results are first evidence that medical beam transport systems, such as gantries, can be adapted to be more compact and efficient when combining pulsed

|               | beam only | solenoid only | dipole only | beamline |
|---------------|-----------|---------------|-------------|----------|
| $\sigma(S_x)$ | 174       | 32            | 389         | 573      |
| $\sigma(S_y)$ | 110       | 42            | 216         | 53       |
| $R_x$         | 594       | 132           | 1567        | 2004     |
| $R_y$         | 331       | 174           | 652         | 200      |

Table 5.1: Comparison of beam and beamline stability measured by scintillator. For the first two setups, beam only and solenoid only, the measurement was performed in between solenoid and dipole. For the latter two setups the data was taken inside the diagnostics chamber downstream of the dipole. Shown are the standard deviations  $\sigma$  of the centroids/first moments  $S_{x/y}$  of the scintillation light distribution as well as the ranges  $R_{x/y} = \text{Max}(S_{x/y}) - \text{Min}(S_{x/y})$  of the first moments. All values in  $\mu\text{m}$ . Both magnet amplitudes tuned independently.

laser-driven sources with likewise pulsed high-field magnets. They encourage to further deepen simulation studies and promote magnet development, since capturing and deflecting protons of clinically relevant energies, i.e.  $> 200 \text{ MeV}$ , requires even higher fields than currently achievable. For the solenoid in Masood et al. [33] a maximum magnetic field of 38 T is anticipated. For the dipole, respectively, 10 T on axis field would enable the deflection of 220 MeV protons. Scalable current sources are on the way (cf. section 3.3.3) and magnet prototypes are under constant improvement. They will be employed for transport studies at clinical energies in the future as the dedicated experimental hall of the proton therapy facility of the University Hospital Carl Gustav Carus, Dresden allows to house the pulsed beamline and associated current pulse drivers. Finally, a first pulse high-field quadrupole magnet has been designed by OncoRay in collaboration with HZDR. A first prototype is currently manufactured. It will complete the set of magnets necessary to form a gantry and allow for further in-depth study on medical beam transport. In analogy to the characterization studies in sections 4.1 and 4.2, the medical beamline will also be characterized at Draco.

## 5.3 PREPARATION OF VOLUMETRIC TUMOR IRRADIATION WITH LASER-ACCELERATED PROTONS

### 5.3.1 INTRODUCTION

The Laser Particle Acceleration Division of the Institute for Radiation Physics at HZDR looks back on a history of successful radiobiological experiments. In close collaboration with OncoRay's Laser-Radiooncology Group, it was demonstrated that high dose rate laser-accelerated protons show identical radiobiological effectiveness as conventionally applied proton beams for in vitro cell samples [26, 27].<sup>12</sup>

<sup>12</sup>In addition, the onCOOPtics collaboration was able to study the response to laser-driven electrons for in vitro cell cultures as well as in vivo tumor tissue [28–31]. Laser-driven electrons are considered less interesting for future application in radiotherapy, yet, the measurements are of fundamental importance for understanding cell response at highest dose rates.

### 5.3 Preparation of Volumetric Tumor Irradiation with Laser-accelerated Protons

In continuance to the previously performed radiobiological studies, the next consequential step is to examine how intense laser-accelerated proton bunches act on a volumetric tumor in a living organism. For this specific study, scientists of OncoRay and HZDR have developed a dedicated tumor model that was successfully accredited by the responsible state authorities. The following simplified explanation of the tumor model and irradiation modalities help to assess the requirements for a successful experimental campaign.

Cultivated human cancer cells of relevant entity for proton radiotherapy (LN229, glioblastoma) are subcutaneously injected into the ears of nude mice with suppressed immune system. In 95 % of cases (tumor take rate), a tumor starts growing on the mouse ear.<sup>13</sup> After 14 to 32 days, the tumor has reached its irradiation size of approximately 3 mm in diameter. Within a one day time frame, the irradiation has to be performed otherwise the maximum tumor size is exceeded. After successful application of a prescribed proton dose to the tumor of the anesthetized mouse, the growth of the tumor is monitored and documented. Depending on the dose, different radiation induced tumor growth delays<sup>14</sup> are expected. The growth delay curves obtained at the laser acceleration source are to be compared with control group results. The over-all follow-up examination extends to 180 days.

The above explanation reveals that dose controlled irradiation experiments, involving living animals, are particularly complex and make great demands on the experimental performance. The following list sums up the requirements that need to be met to allow for a successful radiobiology campaign with laser-driven protons at Draco:

- **Proton energy:** At the day of irradiation the tumor has a diameter of approximately 3 mm. To reach the deeper parts of the tumor, an adequately high proton range is mandatory. To account for small deviations in tumor shape and size and to enable dosimetric control measurements on the front and/or back side of the mouse ear, e.g. with RCFs, a proton range of at least 5 mm in water was set as goal.<sup>15</sup> The long range in the tumor tissue make irradiation studies with laser-driven protons only possible when kinetic energies of at least 25 MeV are generated by Draco.
- **Integrated dose and irradiation time:** The goal is to irradiate the tumor with multiple laser-accelerated proton bunches until the prescribed integrated proton dose of  $D_{\text{int}} \leq 10 \text{ Gy}$  is absorbed by the tissue. The dose application has to be performed within a 10 min time frame to prevent the anesthesia from abating. For an experiment as complex as this, a maximum of two laser shots per minute can be considered realistic. This corresponds to an applied dose per shot of  $D_{\text{shot}} > 500 \text{ mGy}$ .
- **Depth dose distribution:** The radiobiological model requires that every part of the volumetric tumor absorbs the identical proton dose. Thus, in particular the so-called depth dose distribution has to be constant over the entire tumor depth (5 mm including tolerance, see above). Two methods may be applicable to generate an almost uniform depth dose distribution. Firstly, the use of protons with higher kinetic energies, i.e.  $\geq 40 \text{ MeV}$ , to allow for tumor irradiation in the nearly constant plateau region in front

<sup>13</sup>Another 8 % of the animals have to be rejected due to the formation of secondary tumors.

<sup>14</sup>The radiation induced tumor growth delay is the radiobiological end point of the study. The radiobiological end point is a representative measure to quantify a radiation effect. Other examples for radiobiological end points are the number of DNA double strand breaks or the cell survival rate. It may be noted here that in the proposed study it is not the aim to "cure" the cancer. In fact, mice showing regressive tumor growth after irradiation may be eliminated from the analysis.

<sup>15</sup>Water is the reference medium for such dosimetric or radiobiological considerations. The tumor can be considered as roughly water-equivalent in terms of proton stopping power.

of the Bragg peak. Or, secondly, the generation of a spread-out Bragg peak (SOBP), a homogeneous depth dose distribution generated by superimposing discrete Bragg peaks of different energy and intensity. For this matter, the proton spectrum has to be specifically shaped, proton energies of approximately 25 MeV are required initially.

- **Lateral dose distribution:** Equally to the depth dose distribution, the lateral dose distribution has to be uniform over a circular area of 5 mm diameter.
- **Relative dose uncertainties:** Deviations with respect to the absolute prescribed dose value or the uniformity of depth dose and lateral dose distribution should be within a  $\pm 6\%$  margin.
- **Uptime and maintenance:** The tumor model allows for shifting the mouse irradiation by one day. A realistic modality for the experiment is to plan for six days of irradiation per week and one day of laser and beamline maintenance. To irradiate the designated 70 mice, the Draco laser and the pulsed high-field beamline has to operate stably over a period of at least three weeks.

In the following sections, preparatory experiments will be discussed that allow to conclude that such a complex radiobiological campaign, despite of all critical demands, will become feasible in the future owing to the installed pulsed high-field beamline at Draco PW.

## 5.3.2 RESULTS

### PROTON TRANSPORT

Revisiting section 4.2, it becomes immediately clear that the acceleration performance of the 150 TW beam of the Draco laser is not sufficient to provide protons of 25 MeV kinetic energy. Thus, the aspired radiobiology experiments rely on the PW beam of Draco. The experimental setup depicted in fig. 4.3 and discussed in section 4.2.2 has been adopted for the presented preparatory study. It has been shown in section 2.2 that the TNSA proton source driven by Draco PW exhibits cut-off energies of up to 40 MeV. Even the conservatively given spectrum in fig. 2.2 features maximum proton energies of approximately 30 MeV, sufficiently high to provide for the required penetration depth of approximately 5 mm in tumor tissue, yet not high enough to provide for irradiation in the constant plateau region in front of the Bragg peak. Therefore, the generation of a spread-out Bragg peak (SOBP) has to be the method of choice, requiring a high number of protons at approximately 25 MeV kinetic energy.

Equation (2.2) and the data given in eq. (2.3) shall be used to derive a conservative estimate for proton numbers at the prescribed energy of 25 MeV for the proposed irradiation study. When the reference source spectrum is integrated over a 1 MeV broad energy bin around 25 MeV, one finds that

$$N_{25\pm 0.5\text{ MeV}} \approx 1.5 \cdot 10^9 \quad (5.6)$$

particles are generated at this high energy.<sup>16</sup> The following thought experiment sets this particle number in context with the proton dose that may be delivered to the tumor volume  $V_T$ : In agreement with the upper requirements on lateral and depth dose homogeneity, consider the volume that absorbs the dose cylindrical with diameter  $d = 5$  mm, height  $h = 5$  mm and

<sup>16</sup>Keep in mind that this number is strongly fluctuating when the proton spectrum is changing. For example, if the cut-off energy drops, leaving the 25 MeV particles close to the brim of the spectrum, the number can decrease by one order of magnitude.

### 5.3 Preparation of Volumetric Tumor Irradiation with Laser-accelerated Protons

water equivalent density  $\rho_T \approx 1 \text{ g cm}^{-3}$ . It follows  $V_T = \pi/4 \cdot d^2 \cdot h$ . If all  $3 \cdot 10^9$  protons deposit their mean kinetic energy of 25 MeV inside the tumor volume, for the tumor dose follows

$$D_T = \frac{25 \text{ MeV} \cdot 1.5 \cdot 10^9}{m_T} = \frac{25 \cdot 10^6 \cdot 1.6022 \cdot 10^{-19} \text{ J} \cdot 1.5 \cdot 10^9}{\rho_T V_T} \approx \frac{6 \text{ mJ}}{0.098 \text{ g}} \approx 61 \text{ Gy}, \quad (5.7)$$

with  $m_T$  being the tumor mass. Consequently, a single successfully accelerated proton bunch carries a factor of four to five more protons at nominal energy than required for a prescribed maximum dose of 10 Gy. In conclusion, if the laser acceleration performance is better or constantly on a level as presented in fig. 2.2, the number of generated protons is high enough for the proposed radiobiological study and it might even be necessary to selectively reduce the particle numbers to gain dose control. On the other hand, transport and dose formation will already reduce the proton number drastically as will be critically discussed now.

The simple method presented in the previous chapter (see fig. 4.6) allows to estimate the transport efficiency for the considered 25 MeV protons. The maximum envelop divergence of the 25 MeV protons was determined to  $17^\circ$  (half-angle) from the RCF data in fig. 2.2. Figure 4.6 predicts an acceptance angle of  $8^\circ$  for fields in the 15 T range. From eq. (4.2) for the transmission follows  $T \approx 21 \%$ . The transmission is therefore decreasing the particle number by roughly a factor of five which can be tolerated considering the high number of incoming particles and the aim for controlled dose application via multiple laser shots. The predicted dose per shot is approximately 9 Gy.

Considering the high demands on lateral dose homogeneity, the diamond-shaped focal spot may become an issue. The mouse irradiation has to take place in air and thus far away from the target chamber. Therefore, the capturing solenoid has to be operated with high focal length. As a result, cm-large, distorted focal spots as previously shown have to be anticipated for the radiobiology study. However, particle tracing simulations have shown that by using a second solenoid magnet, the particle confinement at focus position can be increased more than 10-fold. The simulation results, in terms of proton densities, are depicted in fig. 5.10 and compared to previous simulation outputs.

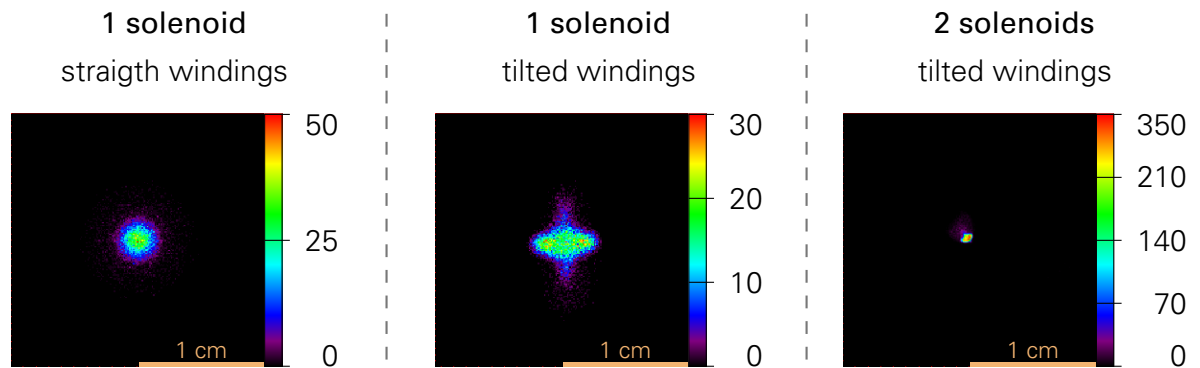


Figure 5.10: Revision of the simulation data for a single solenoid (cf. fig. 4.8) in comparison to a double solenoid beamline. The source parameters were chosen identically (10,000 protons at 10.8 MeV, divergence up to  $8^\circ$ , source to focus distance 1.6 m). The first solenoid collimates the incoming beam, the second solenoid generates a well-defined focal spot with superior proton confinement. Notice the different color scales indicating the numbers of simulated protons per pixel ( $200 \times 200$  pixels) at focus position.

The shape of the focal spot is significantly improved. The simulations show a point-like proton distribution that can be easily spread by letting it propagate and/or by applying a scatter foil for further lateral broadening and homogenization. Thus, a double solenoid beamline could be a crucial step towards the realization of said radiobiology study. Hence, to enhance the experimental capabilities for this preparatory examination, a second identical solenoid was installed on the outside of the target chamber (see fig. 4.3).

The setup distances were chosen in accordance to mimic the classical optics scenario of a bi-telecentric lens system that also posed as inspiration for the beamline upgrade. In classical optics, telecentric lens systems allow for imaging free of distortion and parallax error. The adopted concept resulted in a setting of the solenoid lenses where the image-sided focal plane of solenoid 1 and the object-sided focal plane of solenoid 2 align. The magnification of the resulting "imaging system" is the ratio of focal distances of the two lenses and for the chosen distances (see appendix D) approximately nine considering an ideal match. The ideal match can be generated by tuning the focal length  $f_2$  of solenoid 2 to fulfill  $f_1 + f_2 =$  distance between solenoids = 1034 mm. With  $f_1 \approx 99.5$  mm follows  $f_2 = 934.5$  mm. This corresponding to a focal spot formation at the in-air irradiation site 2121 mm downstream of the target and is well applicable for irradiation studies. The classical optics analog predicts an equally lower limit on focal spot size for single and double solenoid transport (cf. explanation in section 4.2.3).

Figure 5.11 shows a sketch of the considered single or double solenoid setups and depicts how protons of different energies are transported by the beamline. Comparing the upper and lower picture, a major difference of the beam transportation becomes apparent: While the single solenoid setup focuses protons of nominal energy with a certain small energy bandwidth onto the tumor, the double solenoid setup does the same but additionally focuses a different part of the broad proton spectrum at the position of the mouse ear. These particles are of significantly lower kinetic energy. They are focused by solenoid 1 in-between both magnets and then recaptured by the second solenoid. GPT simulations of the beamline setup have determined that these particles travel at approximately 76 % of the nominal momentum (not energy!). A 25 MeV proton focus is therefore overlain by a low-energy focus corresponding to protons of 14.5 MeV kinetic energy. The overlap of low- and high-energy focus may be a problem for the irradiation study, but it could also allow for an efficient generation of a SOBP by filling up the low dose region of the high-energy Bragg peak.<sup>17</sup>

For the double solenoid setup it was intended to make use of both portable pulse generators (PG3 and PG4) to allow for setting the solenoid field strengths individually and to make the beamline more flexible and eliminate geometrical constraints. The nominal energy is supposed to be collimated by solenoid 1 and then steeply focused by solenoid 2. So far, solenoid 1 was solely used to generate focal spots. To prove the successful collimation the detection method illustrated by fig. 4.4 was adapted by installing a half RCF stack directly at the exit of solenoid 1 (RCF 2) and a full stack close to the entrance of solenoid 2 (RCF 4). Figure 5.12 compares the RCF dose imprints for 18.6 MeV protons accelerated by the PW Draco beam. A lower energy than the desired 25 MeV had to be chosen due to limited laser acceleration performance on the day when the data was taken. Anyhow, the tunability of the magnet system provides for the necessary scalability. The figure shows that the lateral dimensions of the proton beam stay constant while propagating towards solenoid 2. Thus, a successful collimation is shown.

<sup>17</sup> For this, the intensity of the low-energy focus would have to be decreased to counterbalance that TNSA generates higher numbers of low-energy protons.

### 5.3 Preparation of Volumetric Tumor Irradiation with Laser-accelerated Protons

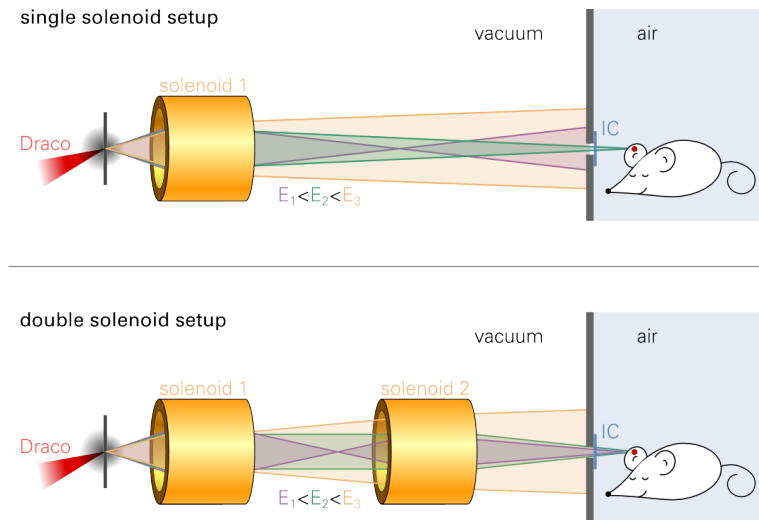


Figure 5.11: Illustration of the two studied beamline setups for the volumetric tumor irradiation experiment at Draco. The impact of the solenoid(s) on different parts of the broad proton spectrum generated by Draco is depicted. The lower picture shows that besides the nominal energy ( $E_2$ , green) also particles of lower energy ( $E_1$ , purple) can be focused at the position of the mouse ear. The irradiation site is in air and the applied dose can be monitored online by means of transmission ionization chamber (IC).

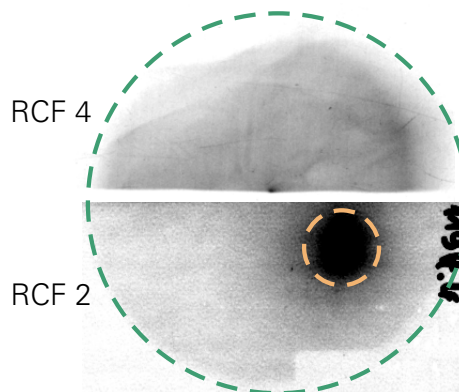


Figure 5.12: Contrast enhanced RCF data (red channel, EBT3, five integrated shots) to prove the collimation of the proton beam when injected into solenoid 2. Solenoid 1 was operated at 10.1 T maximum field strength to collimate 18.6 MeV protons. A half EBT3 stack was irradiated directly behind solenoid 1 (RCF 2) and an identical full stack in front of solenoid 2 (RCF 4). The data proves successful collimation since both RCFs show a beam of identical size ( $\approx 3$  cm, green circle). The orange circle marks dose originating from electrons contributing to the laser acceleration process. Shot parameters: Draco PW,  $\approx 17$  J on  $2 \mu\text{m}$  Ti target,  $E_{\text{max}} \approx 22$  MeV.

With field parameters as before for solenoid 1 and solenoid 2 operated at 5 T, the focal spot shape and intensity was studied next. Figure 5.13 shows the dose imprint on an RCF stack irradiated inside of the diagnostic chamber, hence, close to the actual in-air irradiation position. It compares the focal spot with a similar focus generated by operating only solenoid 1 and with a focal spot generated using a slightly decreased solenoid 1 field compensated by solenoid 2. A small misalignment of the solenoids with respect to each other allowed to separate the low- and high-energy focus to study their shapes individually.<sup>18</sup>

As can be seen from fig. 5.13, this experiment was also conducted with reduced proton energies. Still, conclusions on the effectiveness of the double solenoid setup and potential improvements can be drawn. The focal spots are in comparison to single solenoid transport only slightly smaller, yet more intense. The middle focus shows an enhancement of 43 % with respect to the proton numbers with single solenoid transport (right dose picture). The diamond shape is less pronounced but still clearly visible. The foci are more symmetric. The focal spots of the double solenoid setting and the left and middle show no severe differences, except for beam intensity due to particle loss for the left setting (still slightly diverging beam in-between magnets). Thus, even if the collimation criterion is not perfectly matched, efficient particle transport is still possible. Finally, the comparison with the previously shown simulation results in fig. 5.10 concludes that the predicted weakening of the astigmatic effect is in theory stronger than in a real world experiment. Nevertheless, when the field of solenoid 1 is increased to allow for a shallow focusing ( $f > 2$  m) before entering the second solenoid, an improved focal spot shape was recorded. Figure 5.14 shows the Bragg peak dose deposition of protons at 26 MeV kinetic energy transported in this manner. We see a well-confined more homogeneous spot that shows less of the previously explained diamond shape.

When the mean dose over a 20 mm<sup>2</sup> area, corresponding to the lateral dimensions of the irradiation field, is calculated, one finds a dose value of  $D_{\text{mean}} \approx 2$  Gy. Thus, by applying up to five shots at said beamline parameters the maximum prescribed dose of 10 Gy at a tumor depth of approximately 5 mm would be applied, in first instance neglecting the lower dosage in shallow depths as well as the lateral inhomogeneity. To provide for a superior control of the absorbed dose value, the application of lower doses per laser shot is desirable. Thus, leaving a certain margin of dose reduction for lateral and depth homogenization.

## PROTON DOSE HOMOGENIZATION

The dose homogenization procedure is based on the selective application of scatter foils and filter plates to manipulate angular and energy distribution of the protons. This allows to smoothen the generated dose distribution laterally and in depth. The following paragraphs show first results on dose homogenization. The gradually decreasing laser acceleration performance, due to a damaged optical component in the laser chain, required a temporary discontinuation of the experiments. In accordance to the experimental agenda, only data obtained with single solenoid transport is presented. The optimization process will continue after the damaged components are replaced and the laser acceleration performance is restored.

<sup>18</sup> The misalignment of a single solenoid, either a slight shift or a tilt with respect to the beam axis, leads to the generation of a dipole field that acts stronger on the low-energy particles. Their deflection is therefore more pronounced and they are separated from the main focal spot. In the presented experiments, solenoid 2 was slightly misaligned.

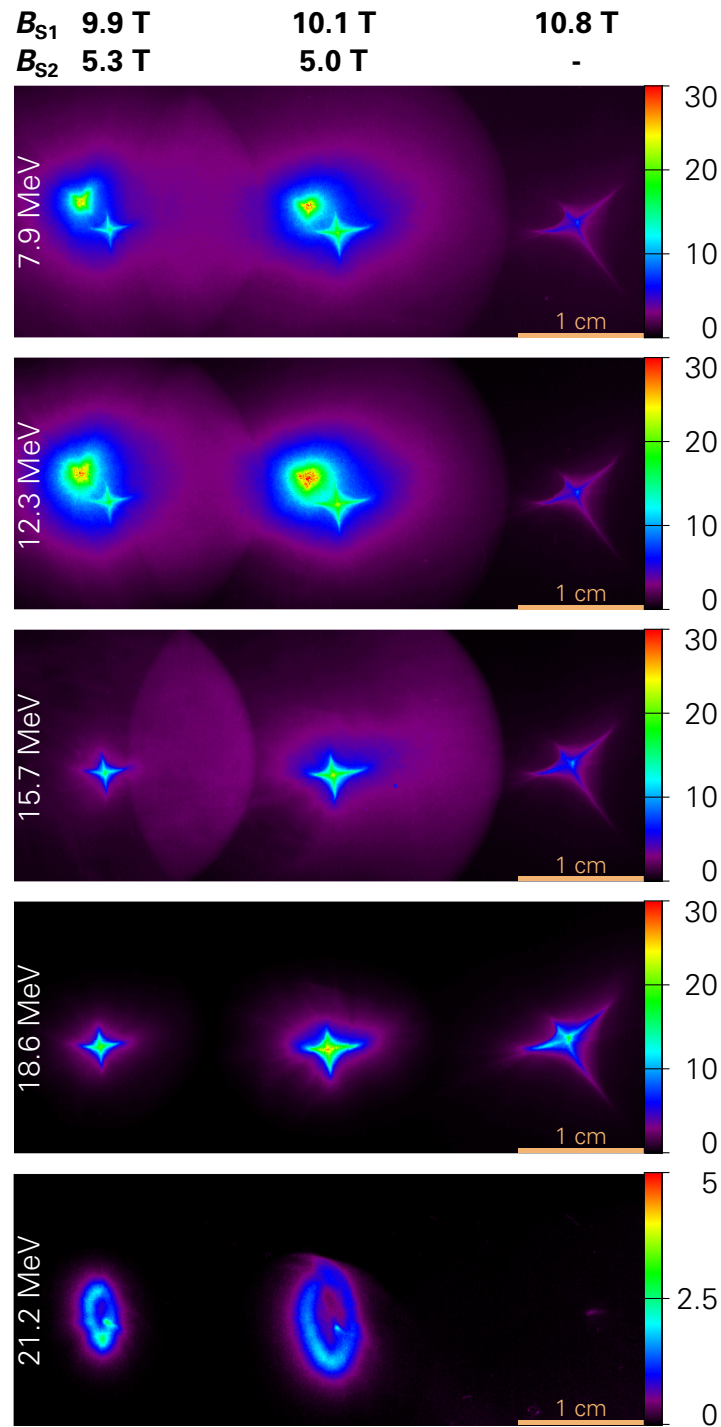


Figure 5.13: Comparison of dose distributions (color coded in Gy, different scales, beam's eye view) induced by 18.6 MeV protons focused via single (right) or double solenoid (left, middle). The middle one matches ideal collimation conditions (cf. fig. 5.12). Notice the shifted low-energy foci for double solenoid transport. The RCF size is  $2 \times 5 \text{ cm}^2$  (cf. fig. E.3 under appendix E). The given energy values correspond to the kinetic energies of protons with Bragg peak at film layer position. Shot parameters: Draco PW,  $\approx 17 \text{ J}$  on  $2 \mu\text{m}$  Ti target,  $E_{\text{max}} \approx 23 \text{ MeV}$ .

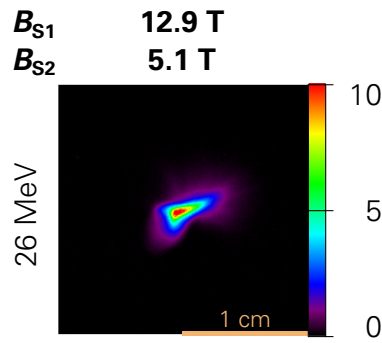


Figure 5.14: Dose picture induced by 26 MeV proton bunch accelerated by Draco PW and transported by the double solenoid beamline. The protons at nominal energy are already converging towards a focus after passing solenoid 1 and are then steeply focused by solenoid 2. Shot parameters: Draco PW,  $\approx 19.2$  J on  $2 \mu\text{m}$  Ti +  $1 \mu\text{m}$  photoresist target,  $E_{\text{max}} \approx 34$  MeV.

In fig. 5.15, the depth dose distribution (blue) in a pure RCF stack (no absorbers plates, for highest depth dose resolution) is drawn for single solenoid transport towards the in-air irradiation site 2 m downstream of the target. It has been stated above that the tumor tissue can be considered as approximately equivalent to water in terms of proton stopping power. On the other hand, the employed RCF stacks are not water-equivalent. Therefore, in fig. 5.15 and in the following plot the proton penetration depth in the RCF stack has been translated to the corresponding range in water. To do so, the depth axis has been scaled using the constant factor of 1.235. The factor has been calculated from SRIM stopping power tables for proton beams in water and RCF (polyester, mass density  $1.335 \text{ g cm}^{-3}$ ). Within the energy range of 5 to 50 MeV the error of the simple scaling method is well below 1 %.

The depth dose distribution in fig. 5.15 shows almost twofold smaller mean dose values for shallow depths in comparison to the Bragg peak region. Consequently, an irradiation without spectral modification (besides the "cut-out" by the chromatic solenoid magnet) is insufficient for the purposes of the aspired radiobiology experiment.

In addition, fig. 5.15 can be used to assess the proton beam spectrum at the in-air irradiation site after passing the  $125 \mu\text{m}$  Kapton vacuum window. For this purpose, the mean energy deposited per film layer was calculated from an assumed Gaussian spectrum with 25 MeV central energy. The best conformity with the experimental data was reached for an FWHM energy bandwidth of 3.8 MeV on condition that the spectrum was cut immediately after the central energy of 25 MeV. The resulting mean dose values are summarized by the orange bar plot in fig. 5.15. The abrupt cut was necessary to reproduce the dose drop in the experimental data. The drop can be attributed to the fact that the weakened acceleration performance only allowed for beamline operation directly on the edge of the proton energy distribution.

The small discrepancies between the measured and calculated dose distributions are only profound for low penetration depths. This can be explained by a general transport of low-energy particles when they are emitted from the source almost on axis. These particles pass the solenoid without being focused and can increase the surface dose which is in fact welcome considering the goal to generate a homogeneous dose distribution. Yet, it is not enough and special measures need to be taken to provide for the spread-out Bragg peak (SOBP) irradiation.

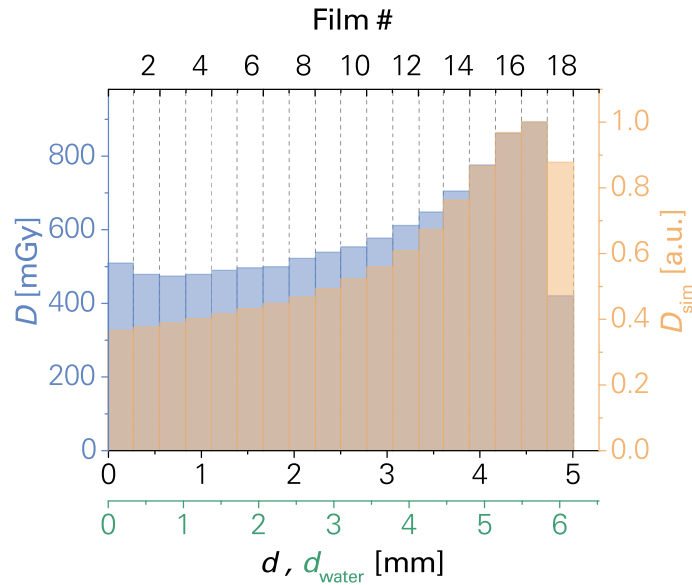


Figure 5.15: (Blue) Depth dose distribution measured via RCF stack (4 mm circular area evaluated, average of three applied laser shots): RCF at in-air irradiation site, single solenoid transport. (Orange) Calculated normalized mean dose per film layer  $D_{\text{sim}}$  for an assumed Gaussian proton beam (25 MeV central bunch energy, 3.8 MeV FWHM, sharp cut-off at 25 MeV). Shot parameters: Draco PW,  $\approx 21$  J on 2  $\mu\text{m}$  Ti + 1  $\mu\text{m}$  photoresist target,  $E_{\text{max}} \approx 25$  MeV, solenoid 1 field 12.9 T.

In conventional accelerators, rotating modulator wheels are typically used to produce the SOBP [4]. They can only be applied for quasi-continuous beams, hence, are not suited for short laser-accelerated proton bunches. Therefore, the colleagues of OncoRay developed a so-called ridge filter prototype to be used for the radiobiological study. A ridge filter is a structured scatterer in which parts of the proton beam lose more energy than others (due to higher material thickness to pass), changing the spectral distribution to provide SOBP dose distributions. For a preliminary measurement at limited particle energy, the filter was installed in front of the RCF stack that mimics the tumor tissue. The depth and assorted lateral dose distributions are presented in fig. 5.16.

The ridge filter, as can be seen, significantly improves the homogeneity of the depth dose distribution. The relative dose variation up to film #14, corresponding to a depth of approximately 4.8 mm in water, stays within the set boundary of  $\pm 6\%$ . Thus, excluding the reduced penetration depth in comparison to fig. 5.15, the ridge filter already provides an acceptable SOBP dose distribution for tumor irradiation experiments. The scattering properties of the filter and the previously mentioned Kapton window in the transition area of the beamline gives a certain amount of lateral dose homogenization. Without further ado, the lateral dose distributions exhibit relative deviations of  $\pm 13$  to 25%. The aspired  $\pm 6\%$  constraint only holds for parts of the order of 1 mm. Yet, the demonstrated depth homogenization is the more critical parameter to reach, since the lateral homogenization can be tailored by introducing additional scattering material. In consequence, the RCF wheels have been equipped with interchangeable scatter foils of different thicknesses, e.g. Kapton 25 to 125  $\mu\text{m}$ , and will be applied for added lateral homogenization in future experiments. The data in fig. 5.16 can

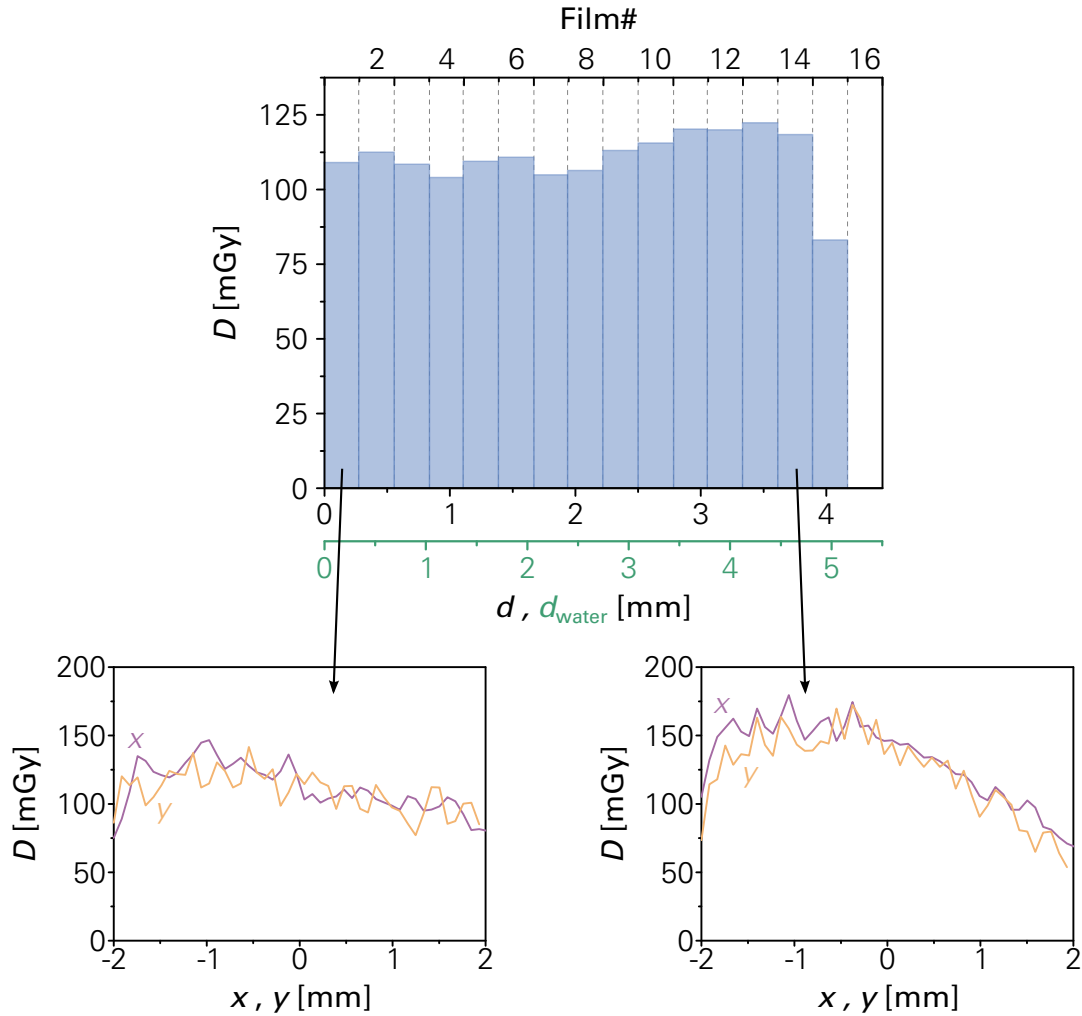


Figure 5.16: (Upper plot) Depth dose distribution measured via RCF stack (4 mm circular area evaluated, average of three applied laser shots): RCF at in-air irradiation site, single solenoid transport, ridge filter in front of RCF. For films #1 and #14, lateral dose profiles (lower plots) are shown. Shot parameters: Draco PW,  $\approx 21$  J on  $2 \mu\text{m}$  Ti +  $1 \mu\text{m}$  photoresist target,  $E_{\text{max}} < 25$  MeV, solenoid 1 field 12.9 T.

therefore be seen as highly promising as it proves that the generation of a SOBP can also be performed at a pulsed, laser-based accelerator.

It shall not be withheld that the decreasing acceleration performance was further limiting the penetration depth as well as the providable dose (compare fig. 5.15 and fig. 5.16). The mean SOBP dose values applicable per single laser shot were of the order of 100 mGy. As a result, a total of 100 laser shots would be required to accumulate the prescribed total dose of 10 Gy. At the conservatively predicted rate of two shots per minute, a single tumor irradiation would take up to 50 min. This is in violation to the radiobiological tumor model and therefore intolerable, as it would severely prolong the time under anesthesia for the mice. Thus, a fivefold dose increase has to be achieved in future experimental campaigns before the radiobiology study can be performed. Considering the improved performance of the two solenoid transport setup in combination with a return to the initially presented laser acceleration performance after laser maintenance (or beyond by enabling full PW shots), the presented results bear good prospects for the feasibility of volumetric tumor irradiation studies at Draco.

#### 5.3.3 CONCLUSION

To conclude this section, the previously stated requirements for a successful in vivo tumor irradiation and whether they are already met or can be met in the near future will be discussed:

- **Proton energy:** It was shown that the PW beam of Draco, even at slightly reduced peak power of 600 TW, is able to generate protons of sufficiently high kinetic energy, i.e.  $E_{\text{kin}} \geq 25 \text{ MeV}$ , and number.
- **Integrated dose and irradiation time:** The number of particles generated by Draco can be sufficiently high and the efficient particle transport via the single or double solenoid setup allows to provide a dose of few Gy in a single shot. Yet, when the acceleration performance drops to cut-off energies below 30 MeV, the dose per shot is decreased to the critical level of  $D_{\text{shot}} < 500 \text{ mGy}$ .
- **Depth dose distribution:** The spread-out Bragg peak generation over a 4.8 mm depth has been successfully demonstrated. SOBP generation over the full 5 mm penetration depth was deemed feasible as long as the laser-driven source generates the necessary particle energies. A modular ridge filter currently under investigation will allow for fine tuning the depth dose homogenization in future campaigns.
- **Lateral dose distribution:** Ridge filter and Kapton window already provide a certain amount of homogenization. The installed scatter foils will allow for precise adjustment of the lateral dose homogeneity.
- **Relative dose uncertainties:** Deviations with respect to the uniformity of depth dose and lateral dose distribution are already in the clinically relevant range, i.e.  $\pm 6 \%$  margin, yet only over a smaller volume of approximately 1 mm diameter and 4.8 mm depth. Regarding the absolute prescribed dose values no final conclusion can be drawn from the preliminary data set obtained so far. It would require a large scale sham irradiation campaign which goes beyond the scope of this thesis. Yet, the previously demonstrated dose-controlled irradiation studies on in vitro tumor cells by Zeil et al. [27] prove

that relative dose uncertainty of below 10 % are feasible with the proposed irradiation scheme and thus bear good prospects.

- **Uptime and maintenance:** As pointed out multiple times, the laser acceleration performance was not stable over the course of several experiment weeks and dropped significantly at the end of the campaign. Necessary proton energies could not be reached then. The laser is currently undergoing maintenance, damaged components are being replaced. With Draco operating at its design peak power of 1 PW, the chances are still high, that sufficiently energetic protons can be generated in high-enough numbers to allow for dose homogenization while still maintaining the necessary dose per shot and thus successful irradiation experiments. Nevertheless, a continuous operation over six days a week for at least three weeks is a venture into uncharted terrain for a laser system like Draco under such strict conditions.

In summary, the requirements for a successful irradiation campaign that studies the radiobiological effectiveness of laser-driven proton beams on in vivo tumors could only be met separately and/or partially. Nevertheless, for the developed technology platform and the built up high-field beamline the results prove that efficient beam shaping and transport for the aspired irradiation study is in fact feasible. The beam transport system based on the capturing solenoid opens up the possibility to irradiate volumetric tumors in the specifically developed mouse model, as it allows to provide a sufficiently high number of protons at the prescribed energy in a controlled and stable way. The performance of the beam delivery was only restricted due to the deteriorating laser acceleration performance during the commissioning phase of Draco PW that put an end to the practical optimization and proof-of-principle study. As the laser maintenance goes on, the beam transport and dose delivery is being investigated in detail by combining the developed GPT model with sophisticated simulations on scattering and spectral modulation using GEANT4 [137]. These simulations will provide a set of optimized beamline parameters for superior dose homogeneity and transport efficiency. The next step after successful restoration of the laser acceleration performance would then be to verify these parameters experimentally. Before a full-scale irradiation experiment can really be considered, it has to be demonstrated that all requirements can be met to full extent and at the same time. Furthermore, a "dry run" has been recommended and should be performed to train the operational procedures for the highly complex experiment and monitor long-term laser stability. The section shall be concluded by the notion that the installed beamline is of exceptional importance for the feasibility of the experiment. Neither the solenoid astigmatism nor the limited repetition rate are show-stoppers. The development of high rep-rate PW-class lasers over the last years in combination with the presented pulsed power technology sets us on the brink of enabling a novel type of radiobiological experiment that is of highest importance for the laser acceleration community.



## 6 SUMMARY AND OUTLOOK

Within the framework of this thesis, a diverse set of three pulsed high-field solenoids has been developed. The capturing solenoid is constructed to collect and transport highly divergent laser-accelerated ion beams. It is the magnet most extensively studied in this work. The split-pair solenoid is a miniature Helmholtz-like coil with optical access to the high-field region via transversal bores. It has been used in proof-of-principle experiments at the LULI2000 laser facility to magnetize laser-driven plasmas. In this manner, complex astrophysical processes like the formation of accretion columns can be explored in a scaled laboratory experiment. Finally, the 40-T-solenoid widens the range of possible applications as well as the explorable magnetic field region. It has not yet been commissioned for experimentation. The developed technology is supposed to be used for investigating the interactions between a several 10 T strong magnetic field at position of the laser target and the laser-driven particle source. It will be of great scientific interest to study how the external field influences e.g. sheath formation and particle transport.

All three magnets employ compact housing techniques tailored to fit their intended use. Thus, they are exceptionally small and easy to install, operate and motorize. Adapted to match the electrical properties of the high-field magnets, three current pulse drivers have been developed. Pulse generators PG3 and PG4 are assembled and in routine operation. They successfully delivered several thousand current pulses to the solenoids. Pulse generator PG5 is currently under construction. It employs thyristor semi-conductor switches, offering unlimited scalability towards higher current pulse energies and in consequence magnetic field. The scalability has been proven in high-field laboratories around the world.

The detailed experimental studies of this thesis focus on beam transport by means of the capturing solenoid. The magnet has been thoroughly characterized at conventional and laser-based acceleration sources. It has been shown that the solenoid is able to generate submillimeter focal spots from a parallel incoming proton beam. The large divergence of a laser-driven TNSA source translates to a distorted focal spot shape and reveals a solenoid aberration that was later identified as astigmatism. The focal spot sizes range from millimeter to centimeter depending on the focal distance and source divergence. The astigmatism is caused by a quadrupole-like field component originating from the winding pitch of the wire-wound magnet. The strength of this perturbing field component was estimated to  $0.5 \text{ T m}^{-1}$  acting over the entire solenoid length. The astigmatic focus limits the lateral confinement of the transported particles. A new solenoid design with decreased winding pitch was suggested that could improve the magnet performance for applications relying on

well-defined, intense and circular focal spots. The characterization studies were concluded by pepper-pot measurements that allow to assess the emittance blow-up introduced by the capturing solenoid. The pepper-pot method was demonstrated to be a helpful tool to assist the solenoid alignment procedure.

A detailed simulation model of the capturing solenoid has been developed using the General Particle Tracer software. The model can be used to precisely predict beam transport characteristics like focal length, transport efficiency and focal spot shape and size, for the capturing solenoid or a beamline consisting of multiple pulsed high-field magnets. The model can be easily tailored to fit novel experiment conditions.

Ultimately, the capturing solenoid had to prove its utility in three diverse application experiments. The developed versatile technology platform can couple laser-driven beams into conventional accelerator structures. Following the agenda of the LIGHT collaboration to gradually increase particle flux and expand the experimental capabilities (cf. Busold et al. [43–46]), the beam transport has been improved, a second solenoid for steep final focusing was installed and the functionality of the beamline for utilizing heavier ion beams verified. Proton bunches, efficiently captured, temporally compressed and finally laterally well confined by means of two solenoids and an accelerator cavity allowed to generate an unmatched peak proton flux of  $6 \text{ mA mm}^{-2}$ .

In combination with a collaboratively developed dipole sector magnet prototype, first practical studies on medical beam transport for laser-driven protons have been carried out. The experimental research performed at a 6 MV tandetron accelerator complements the previous theoretical studies by Masood et al. [33] and Masood et al. [34] and enables systematic verification of the simulation predictions. The principle functionality of the coupled magnet system, including lossless transport and beam deflection ( $50^\circ$ ) by the dipole magnet, was shown. The beamline offers precise energy selection via dipole dispersion and is in its current form suited to transport proton bunches with up to 31 MeV kinetic energy. Improved magnet prototypes as well as a first quadrupole will extend the experimental capabilities in the future. The fabrication process is ongoing. After completion a thorough characterization of the medical beamline at a clinical proton accelerator and at a laser acceleration source is scheduled.

A beamline, built up at the Desden laser acceleration source Draco and composed of two capturing solenoids, was investigated in the context of novel radiobiological research. It is supposed to enable radiobiological effectiveness studies that use laser-accelerated proton beams to deliver a prescribed dose value to a volumetric tumor on a mouse ear. The high dose rate irradiation has to be explored in order to verify the usability of laser-driven ion sources for the frequently proposed vision of a laser-driven ion beam therapy of tumor diseases. It has been explored, whether a large scale irradiation campaign can become possible in the near future. Owing to the enhanced laser acceleration performance of the upgraded Draco laser facility, the principle demands were met by the laser-driven source, as demonstrated during the commissioning experiments on the novel petawatt-class laser. The double solenoid transport allows for a more efficient transport and better confined beams at focus position. This keeps particle numbers high and allows to study dose homogenization demanded by the radiobiological model. The experiments had to be discontinued due to a decreasing laser acceleration performance. Yet, the taken data is a promising demonstration of first steps necessary to generate a homogeneous dose distribution inside of a volumetric cell structure.

The presented first feasibility study on volumetric in vivo tumor irradiation with laser-driven protons shows that the built up beamline at Draco PW is fully operational, features high

transport efficiencies and, owing to the flexible double solenoid setup, opens up a wide range of possible operation scenarios for optimizing transport conditions. On the other hand, it also shows how complex it will be to maintain stable laser acceleration performance over the course of several experiment weeks.

In summary, the developed magnet technology is in every presented study the key element for taming the source and preparing the generated particles for utilization. It enables to study potential applications practically and to prove or disprove their feasibility and is thus the missing link between proposing an application and investigating it. The ambitious and visionary concept of a laser-based ion beam therapy (IBT) facility in particular, can now be studied hands-on owing to the performed groundwork. In this context, I am convinced that this thesis takes the laser acceleration community one step further along the translational research track. The thesis is now concluded by a proposition for a focused continuation of the presented research.

A great collaborative success of a multidisciplinary team is described in Tillner et al. [138]. The researchers have developed a dedicated image-guided photon radiation therapy machine for small animal studies. The inspiring work resulted in a flexible, non-profit academic research platform that enables a variety of systematic preclinical trials. Such a system, operating with ion instead of photon beams, would be a remarkable scientific breakthrough, as it provides for gaining deeper insights into the radiobiological properties of particle beams. Yet, complexity, cost and size of such a system make a realization very unlikely. As result, preclinical research has to be performed solely at the few large-scale ion or proton therapy facilities that are already used to capacity. On the other hand, the synergetic effects between a laser-driven pulsed source and likewise pulsed magnets make a small animal irradiation platform worth considering. As an intermediate step towards the long-term goal of laser-driven IBT, a similar concept could be facilitated when a petawatt-class laser is combined with a compact beam delivery system based on pulsed high-field magnets. The development process of such a system would significantly promote the scientific and technological innovation process, as the prospect of the unique multidisciplinary research platform is a strong driving force. If such a system could be realized, it would allow to simultaneously perform studies on reliable proton production, beam transport, field formation, dose delivery, treatment planning and radiobiology. All together, yet in a scaled approach that lowers the demands on proton energy and magnetic field amplitude. In a strong multidisciplinary research collaborations like onCOOPtics, a focused continuation of the presented work would lead to the completion of the feasibility study on volumetric tumor irradiation and subsequently to said irradiation. The successful completion of this key experiment for the laser acceleration community would pave the way and the proposed, remarkable laser-based high-field irradiation system for small animals could become reality in the not so distant future.



# APPENDIX A

## LASER SYSTEMS

The following table gives a comparison of main parameters of the laser systems that were used for experiments during this thesis. For the PHELIX laser the short pulse beam options of the two experimental areas, the PHELIX laser bay and the so-called Z6 area, are shown. It may not be presented, but PHELIX can also provide long pulses comparable to the NANO2000 beam of the LULI facility in the laser bay target area.

| Center/<br>Institute        | Helmholtz-Zentrum<br>Dresden – Rossendorf,<br>Dresden, Germany |                          | GSI Helmholtzzentrum für<br>Schwerionenforschung,<br>Darmstadt, Germany |                                  | École Polytechnique,<br>Palaiseau, France |                                     |
|-----------------------------|--|--------------------------|---|----------------------------------|---|-------------------------------------|
| Laser<br>Facility           | Draco  |                          | PHELIX  |                                  | LULI2000                                  |                                     |
| Beam<br>Option              | Draco TW   | Draco PW                 | PHELIX @ Z6   | PHELIX @<br>Laser Bay            | PICO2000                                  | NANO2000                            |
| Laser<br>Medium             | Ti:Sa  |                          | Nd:Glass  |                                  | Nd:Glass                                  |                                     |
| Central<br>Wavelength       | 800 nm   |                          | 1053 nm   |                                  | 1053 nm                                   |                                     |
| Pulse<br>Energy             | 4.5 J  | 30 J                     | 50 J  | 200 J                            | 200 J* (10 to<br>25 J, $2\omega$ )        | 800 J (350 to<br>450 J, $2\omega$ ) |
| Temporal<br>Pulse<br>Length | $\approx 30$ fs  |                          | 0.5 to 20 ps (650 fs)   |                                  | 1 to 30 ps<br>(1 ps)                      | 0.5 to 15 ns<br>(1.5 ns)            |
| Peak Power                  | 150 TW   | 1 PW<br>(600 TW)         | 100 TW<br>(60 TW)   | 400 TW                           | 200 TW<br>(20 TW)                         | $\approx 1$ TW<br>(0.3 TW)          |
| Repetition<br>Rate          | 10 Hz  | 1 Hz                     | $1/90$ min  | $1/90$ min                       | $1/90$ min                                | $1/90$ min                          |
| Intensity on<br>Target      | $10^{21} \frac{W}{cm^2}$                                       | $10^{22} \frac{W}{cm^2}$ | $>10^{19} \frac{W}{cm^2}$   | $2 \cdot 10^{21} \frac{W}{cm^2}$ | $10^{18} \frac{W}{cm^2}$                  | $10^{14} \frac{W}{cm^2}$            |

Table A.1: Typical parameters of the laser systems used throughout this thesis. Values in brackets show other than nominal parameters used in the presented experiments. \*Due to radiation safety restrictions the maximum energy focused on target is usually limited to 50 J.



## APPENDIX B

# DERIVATION OF THE SOLENOID FIELD

To derive the axisymmetric field of a solenoid magnet, we conveniently use cylinder coordinates (CC)  $r, \varphi, z$ . Rotational symmetry results in the vanishing of derivatives with respect to  $\varphi$ :  $\frac{\partial}{\partial \varphi} \dots = 0$ .

Àmpere's law

$$\text{rot} \vec{B} = \nabla \vec{B} = \mu_0 \vec{j} + \mu_0 \varepsilon \frac{\partial \vec{E}}{\partial t} \quad (\text{B.1})$$

is reduced to

$$\text{rot} \vec{B} = 0. \quad (\text{B.2})$$

for static fields. The magnetic field  $\vec{B}$  can be expressed by the magnetic scalar potential  $\psi(r, z)$ . Then follows  $\vec{B} = -\nabla \psi$ . With Gauss's law  $\nabla \cdot \vec{B} = 0$  we get for the scalar potential  $\psi$  the Laplace equation

$$\nabla^2 \psi(r, z) = \Delta \psi(r, z) \stackrel{\text{CC}}{=} \frac{1}{r} \frac{\partial}{\partial r} \left( r \frac{\partial \psi}{\partial r} \right) + \frac{\partial^2 \psi}{\partial z^2} = 0 \quad (\text{B.3})$$

The axial symmetry of the solenoid magnet requires that the radial component of the magnetic field vanishes at  $r = 0$ , i.e. on-axis, thus  $B_r(r=0) = 0$ . In addition, the potential needs to be finite and continuous along the  $z$ -axis. Equation (B.3) can therefore be solved by means of the following power series

$$\psi(r, z) = \sum_{n=0}^{\infty} \psi_{2n}(z) r^{2n} = \psi_0 + \psi_2 r^2 + \psi_4 r^4 + \dots, \quad (\text{B.4})$$

with  $\psi_0 = \psi(0, z)$  being the potential along the  $z$ -axis. The magnetic potential  $\psi(r, z)$  is an even function with respect to  $r$  due to the named symmetry requirements. Substitution of eq. (B.4) in eq. (B.3) and performing the differentiations yields

$$0 = \sum_{n=1}^{\infty} 2n^2 \psi_{2n} r^{2n-2} + \sum_{n=0}^{\infty} \psi_{2n}'' r^{2n} \quad (\text{B.5})$$

where the prime denotes the partial derivative with respect to  $z$ . It is now possible to recursively calculate the coefficients  $\psi_{2n}$  according to

$$(2n+2)^2 \psi_{2n+2} + \psi_{2n}'' = 0. \quad (\text{B.6})$$

Consequently the magnetic potential can be expressed as

$$\psi(r, z) = \psi(0, z) - \frac{1}{4} \frac{\partial^2 \psi(0, z)}{\partial z^2} r^2 + \frac{1}{64} \frac{\partial^4 \psi(0, z)}{\partial z^4} r^4 - \dots \quad (\text{B.7})$$

$$= \sum_{n=0}^{\infty} \frac{(-1)^n}{(n!)^2} \frac{\partial^{2n} \psi(0, z)}{\partial z^{2n}} \left(\frac{r}{2}\right)^{2n}. \quad (\text{B.8})$$

In conclusion, the axial ( $B_z$ ) and radial ( $B_r$ ) components of the magnetic field of a solenoid can be derived from eq. (B.8) and  $\vec{B} = -\nabla\psi$ . With  $B_z(0, z) = B(z) = -\frac{\psi(0, z)}{\partial z}$  it follows

$$B_z(r, z) = -\frac{\partial\psi(r, z)}{\partial z} \quad (\text{B.9})$$

$$= B(z) - \frac{r^2}{4} B''(z) + \dots \quad (\text{B.10})$$

$$= \sum_{n=0}^{\infty} \frac{(-1)^n}{(n!)^2} \frac{\partial^{2n} B(z)}{\partial z^{2n}} \left(\frac{r}{2}\right)^{2n} \quad (\text{B.11})$$

and

$$B_r(r, z) = -\frac{\partial\psi(r, z)}{\partial r} \quad (\text{B.12})$$

$$= -\frac{r}{2} B'(z) + \frac{r^3}{16} B'''(z) + \dots \quad (\text{B.13})$$

$$= \sum_{n=1}^{\infty} \frac{(-1)^n}{n!(n-1)!} \frac{\partial^{2n-1} B(z)}{\partial z^{2n-1}} \left(\frac{r}{2}\right)^{2n-1}. \quad (\text{B.14})$$

## APPENDIX C

# PARTICLE BEAM DIAGNOSTICS

### C.1 RADIOCHROMIC FILMS

Radiochromic films, or RCFs as they are usually referred to, are self-developing films sensitive to ionizing radiation. They allow for simple qualitative and quantitative two-dimensional dose evaluation and are an indispensable detector for radiotherapeutic dosimetry and quality assurance [139–141].

An RCF consists of at least one transparent polyester coating foil carrying the radiation-sensitive detector material. When radiation impinges on the film and energy is deposited in the active layer, polymerization processes lead to a darkening of the RCF. The optical density (OD) of the irradiated film is a function of the absorbed dose (cf. fig. C.1) and can be digitized by means of conventional flatbed scanners [142]. The dose response has to be calibrated for every type of film and scanner. A reference irradiation at a conventional accelerator source with prescribed doses<sup>1</sup> is therefore inevitable. The calibration process is typically complex enough to be treated in Bachelor or Master theses.

RCFs can spatially resolve beam modulations in the range of few 10  $\mu\text{m}$ . The different available film types allow for a variety of dose ranges. The films used in the presented experiments, namely Gafchromic EBT and HD films of different types and batches, can be used to measure dose values up to a few 10 Gy (EBT) and up to 1000 Gy (HD) [143]. Depending on the color channel that is analyzed, calibration towards even higher absorbed doses can be established. The standard color channel for dosimetric evaluation is the red channel of the RGB image created by the scanner. Green and blue channel (in this particular order) allow for increasing the detector dynamic range [144].

Finally, applying the planar detectors in a stacked configuration can be used to gain not only a lateral but also the depth dose distribution of an unknown incoming beam. RCF stacks, if necessary with inlaid metal foils for additional stopping, allow for comprehensive characterization of a laser driven ion source including rough absolute particle numbers and energy spectrum, angular divergence distribution as well as beam modulations [145]. The stacked films typically allow for energy resolution up to 1 MeV. Due their flexibility in application, easy handling and dose rate independence, RCFs have become the reference (offline) detector in the field of laser ion acceleration.

---

<sup>1</sup>More precisely, the RCF optical density is typically calibrated against the absorbed dose to water, a reference standard in radiobiology, dosimetry and clinical radiotherapy.

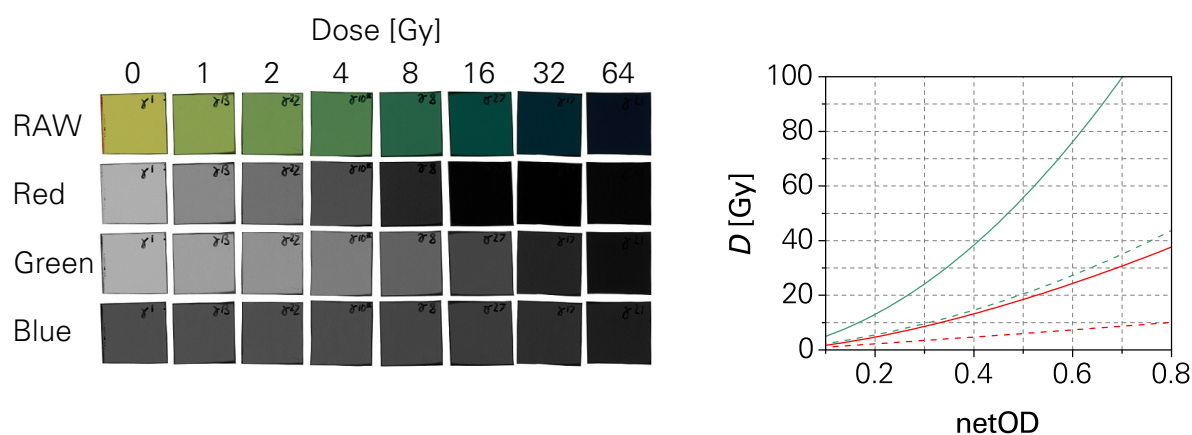


Figure C.1: Left: Scanned EBT3 films of different absorbed dose values taken from a calibration data set obtained at an X-ray tube. The raw data was split up to show the low dynamic range of the red channel, the high dynamic range of the blue channel at very low sensitivity (only marginal color change in the presented dose range) and the intermediate performance of the green channel. Right: Determined dose response curves for red and green channel (plot colors respectively) and two scanner settings (dashed: standard, solid:  $\gamma = 1$ ). The net optical density is the optical density of the irradiated film subtracted by the OD of an unirradiated film. The curves are defined by the formula  $D = a \cdot \text{netOD} + b \cdot (\text{netOD})^c$ , with parameters  $(a, b, c)$ : solid red (3.4704, 49.3804, 1.5595); solid green (34.7769, 154.5126, 2.0109); dashed red (-10, 22.7976, 1.0497); dashed green (19.1821, 44.8192, 2.0415).

## C.2 SCINTILLATORS

Scintillators are materials that emit luminescence when excited by radiation. The luminescence or scintillation light can be detected by means of photomultiplier tubes, photodiodes, cameras or even the naked eye. The light output is a function of the absorbed dose. Decay times ranging from 700 ps (fast organic scintillators, fast component of BaF<sub>2</sub>) to several 100 ns (inorganic scintillators) and even shorter rise times of the scintillation light, favor time-of-flight (TOF) application and optical gating. In contrast to RCFs, scintillators are reusable detectors.<sup>2</sup> Furthermore, scintillators, coupled with electronic readout, give instantaneous on-shot feedback thus significantly increasing the data acquisition rate. Therefore, scintillators, most commonly plastic scintillators, gained popularity especially in labs operating high rep-rate laser accelerators. Stacked configurations or combinations of scintillator screen and pixelated absorber plate allow for angularly resolved measurement of laser-accelerated proton spectra and beam profiling [23, 25, 146].

In this work, a configuration based on blocks of organic scintillator materials was applied. The scintillation light distribution generated in the transparent scintillator block, was imaged

<sup>2</sup>However, scintillators can suffer from radiation damage decreasing the light output. Thus, a scintillator's lifetime is limited by the absorbed dose. Depending on the application scenario and the scintillator type deterioration might occur at kGy dose level.

by digital cameras. Light attenuation and scattering effects can be neglected in the transparent scintillator medium. Therefore, the camera data represents a projection of the three-dimensional light distribution onto a plain. Two observation directions have been chosen: Backside imaging for beam profile determination and transverse imaging for ion beam range and depth dose estimation. The setup is depicted by fig. C.2. In situations with intense background light sources, e.g. in close vicinity to the laser target, color filters matching the scintillation spectrum can attenuate surrounding light while preserving scintillation light intensity. Therefore, the emission of the scintillator should not strongly overlap with the surrounding light spectrum. The red-emitting scintillator BC-430 (580 nm wavelength of maximum emission) of Saint-Gobain Crystals has proven to be well suited for the application at the Draco laser. The concept of camera imaged scintillator blocks can be extended to tomographic reconstruction of the three-dimensional dose distribution. Thereby, single-shot three-dimensional dose assessment becomes possible [24].

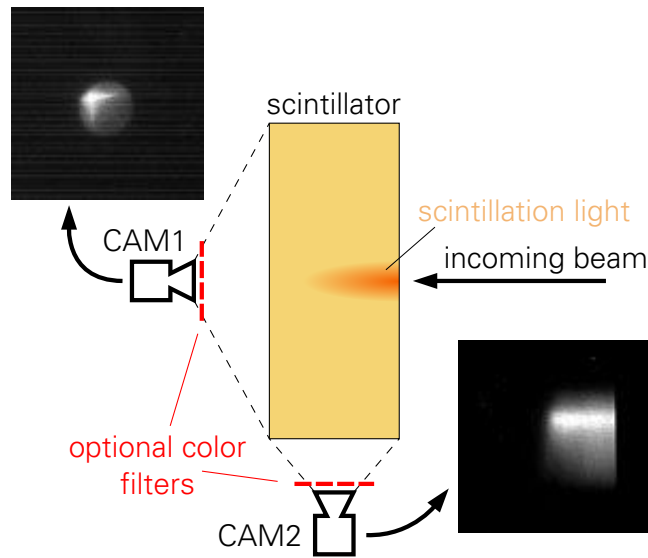


Figure C.2: Illustration of a beam diagnostic setup using scintillator block images for lateral (left) and depth (right) profiling. The scintillation light distribution is imaged by cameras.

### C.3 THOMSON PARABOLA SPECTROMETER

A Thomson parabola spectrometer (TPS) is an online detector for measuring relative particle beam spectra resolved by ion species and charge state. It is therefore exceptionally useful to monitor broad-energetic laser-accelerated multi-species beams. A small fraction of the beam passes a pinhole aperture of few 100  $\mu\text{m}$  size and enters a region of the TPS where magnetic and electric fields, aligned perpendicular to the beam axis (cf. left side of fig. C.3), deflect the particles. The force acting on the particles is the Lorentz force

$$\vec{F}_L = q \left( \vec{E} + \vec{v} \times \vec{B} \right). \quad (\text{C.1})$$

$\vec{B}$  and  $\vec{E}$  are generated by means of permanent magnet and high-voltage (HV) plate capacitor. Downstream, the particles impinge on a detector and are electronically registered. The

### C.4 The Pepper-Pot Method

traces, that a multi-species broad-energetic beam leaves on the detector, are of parabolic shape and follow the well-known parabola equation

$$y = \left(\frac{q}{m}\right)^{-1} \cdot \frac{E}{B^2(0.5s_F + s_FD)} x^2, \quad (\text{C.2})$$

where  $x$  and  $y$  denote the deflection perpendicular to the ion propagation direction,  $\frac{q}{m}$  the charge-to-mass ratio,  $B$  and  $E$  the magnetic and electric field of (in this case identical) length  $s_F$  and  $D$  the drift length downstream of the field area before the particles impinge on the detector. Equation (C.2) shows that for a given TPS geometry and fixed field strengths a parabola trace is defined by the charge-to-mass ratio ( $0 < \frac{q}{m} \left[\frac{e}{u}\right] \leq 1$ ) of the positive ions. Therefore, ion species with identical charge-to-mass ratio cannot be distinguished. For every individual trace it holds that the closer the traces reach towards the origin, the higher the particle kinetic energy. The origin  $(x, y) = (0, 0)$  corresponds to the position of the pinhole and can be visible in laser acceleration experiments due to background  $\gamma$ -rays passing the field region without deflection.

Figure C.3 shows the concept and example traces of laser-accelerated ions measured by a TPS. The trace with the lowest deflection in  $y$ -direction corresponds to particles with highest  $\frac{q}{m}$ , in a TNSA scenario typically  $\frac{q}{m} = 1$ , i.e. protons.

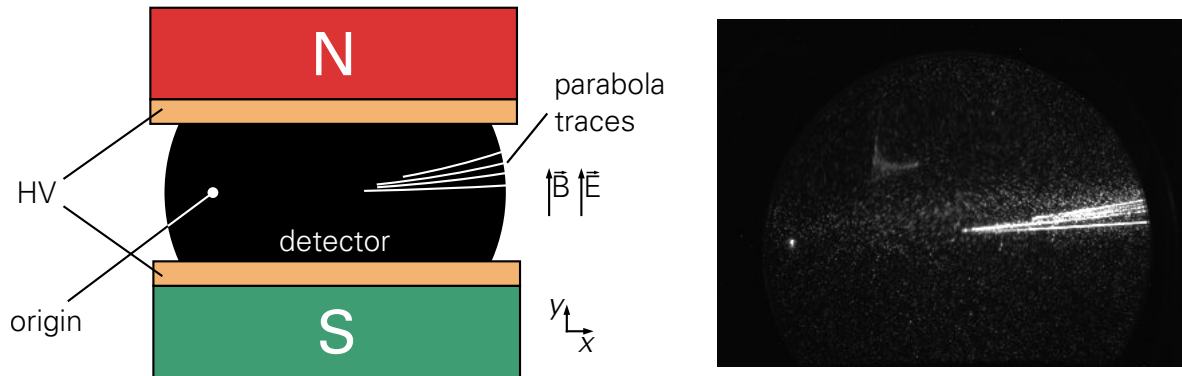


Figure C.3: Left: Illustration of the particle deflection in a Thomson parabola spectrometer (TPS) for positively charged ions traveling into the drawing plane. The origin represents the position of the TPS pinhole; the lowest trace represents the proton signal. Right: Exemplary TPS raw signal.

The TPS used at the Draco PW laser acceleration source employs a micro-channel plate as detector, features gap field strengths of up to 940 mT and is typically operated with plate voltages of  $\pm 15$  kV to  $\pm 20$  kV. Its lower detection limit for protons is at 9 MeV, the upper limit at approximately 100 MeV.

## C.4 THE PEPPER-POT METHOD

The pepper-pot (PP) method is commonly used in accelerator physics to measure the transverse phase space distribution of particle beams and allows to determine the transverse beam emittance. The PP is an absorber plate with a two-dimensional array of small open apertures that resemble the holes in a pepper-pot thus explaining its name. The PP divides

the incoming beam in sample beamlets that hit a viewing screen or similar particle detector downstream. The resulting "spots" on the detector have different shapes, sizes and brightness levels. Using this data set obtained in a single-shot measurement, a variety of information can be extracted (cf. Humphries [147]):

1. Integration of the detector signal associated with a single aperture gives the relative current density of the beam at aperture position. Analyzing the entire hole pattern yields a two-dimensional current density profile.
2. The displacement of the signal spot centroid, with respect to the corresponding aperture, gives information on beam pointing in the PP plane. It is possible to assess whether the beam is converging, diverging or parallel.
3. Averaging over the  $y$ -direction, i.e. an aperture column, the relative distribution of  $x' = dx/dz$  at  $(x, y)$  can be determined as well as average horizontal divergence angle and emittance  $\epsilon_x$ . Analog procedure for  $y$ -direction.
4. The analysis of the entire spot pattern allows for estimating the complete four-dimensional trace-space distribution  $(x, x', y, y')$  and thereby the hyperemittance  $\epsilon_4 = \epsilon_x \epsilon_y$ .

In conventional accelerator physics, the PP is typically used in monoenergetic beams. Therefore, a single screen is sufficient to measure the distribution of the beamlets. In laser-driven ion acceleration, however, the incoming beam has a broad energy spectrum and energy dependent angular distribution. This complicates the analysis of the PP measurement severely. Therefore, the application of stacked RCFs was introduced to enable energy resolved measurements. Similar methods as used in RCF spectroscopy [145], permit the analysis of the PP data analog to the conventional approach, by binning the broad energetic beamlets in accordance to the energy bands detected by the active layers of the RCFs.

The two pepper-pot plates that have been applied experimentally during this study have a regular aperture pattern oriented in  $x$ - and  $y$ -direction with 5 mm hole spacing. The PP employed at the Draco laser acceleration source has apertures of 100  $\mu\text{m}$  diameter. The PP used at PHELIX, respectively, has a 300  $\mu\text{m}$  hole diameter. Emittance measurements of the laser-driven source as well as potential emittance blow-up due to the solenoid can be measured by applying the PP method as depicted in fig. C.4. Keep in mind, that for a radially symmetric charged particle beam, entering an ideal solenoid from a field free region, the emittance is conserved.

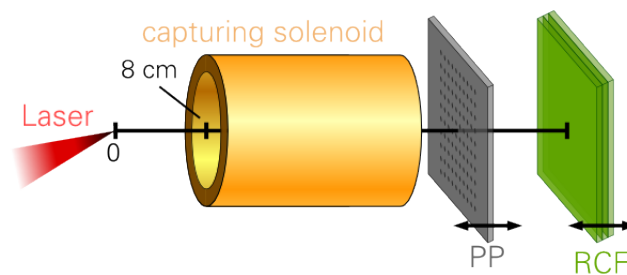


Figure C.4: Sketch of a typical setup for pepper-pot (PP) measurements at a laser accelerator. The beamlets are detected via stacked radiochromic film detectors. Distances between PP and solenoid or PP and RCF were adjusted to fit the experimental conditions and geometrical constraints.

#### C.4 The Pepper-Pot Method

Figure C.5 shows simulated PP signatures for a typical laser acceleration scenario (see caption for details). The signature of a well-aligned solenoid magnet (reference) is compared to several cases of misalignment. Although the signatures can be hard to distinguish, the method helps to assist and speed-up solenoid alignment procedures.

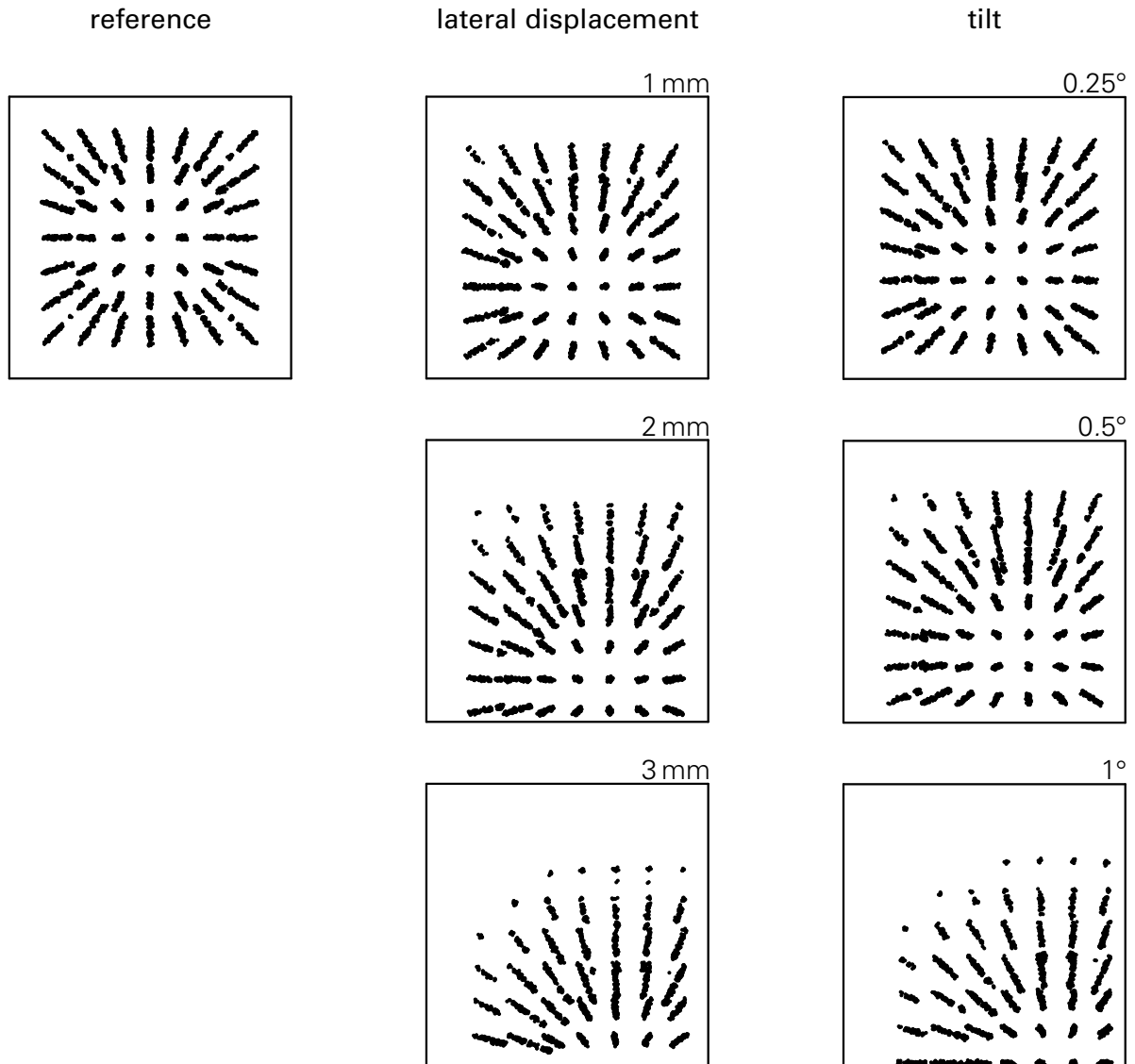


Figure C.5: Simulated PP signatures from misaligned capturing solenoids in comparison to the reference scenario of ideal alignment. Lateral displacement: solenoid shifted to the right (beam's eye view). Tilt: solenoid rear tilted downwards (beam's eye view); pivot point on beam axis at solenoid entrance. Signatures for opposite misalignment scenarios follow from symmetry considerations. Simulation parameters: PP aperture size  $500\ \mu\text{m}$ , PP position 1080 mm to source, RCF/screen position 1650 mm to source.

## APPENDIX D

# DISTANCES AT THE DRACO BEAMLINE

|                        | single solenoid | double solenoid | description   |
|------------------------|-----------------|-----------------|---|
| target                 | 0               | 0               | -   |
| RCF 1                  | 30              | 24.5            | RCF wheel in front of solenoid 1, for source characterization |
| solenoid 1             | 85              | 77.5            | first winding of solenoid 1                                   |
| RCF 2                  | 322             | 329.5           | RCF directly behind solenoid 1                                |
| RCF 3                  | 515             | -               | RCF wheel downstream of solenoid 1, inside target chamber     |
| RCF 4                  | 712             | 779.5           | RCF wheel downstream of solenoid 1, inside target chamber     |
| scintillator 1         | 527             | 529.5           | online scintillation detector, inside target chamber          |
| solenoid 2             | -               | 1111.5          | first winding of solenoid 2                                   |
| RCF 5 & scintillator 2 | 1597            | 1806.5          | RCF/scintillator inside diagnostics chamber                   |
| in-air diagnostics     | -               | 1960 to 2230    | area where in-air diagnostics can be freely placed            |
| TPS                    | 2022            | 2313.5          | entrance of TPS chamber                                       |

Table D.1: Distances (in mm) of important beam guidance and diagnostic elements (cf. fig. 4.3), with respect to the laser target, for single and double solenoid setup.



# APPENDIX E

## RAW DATA

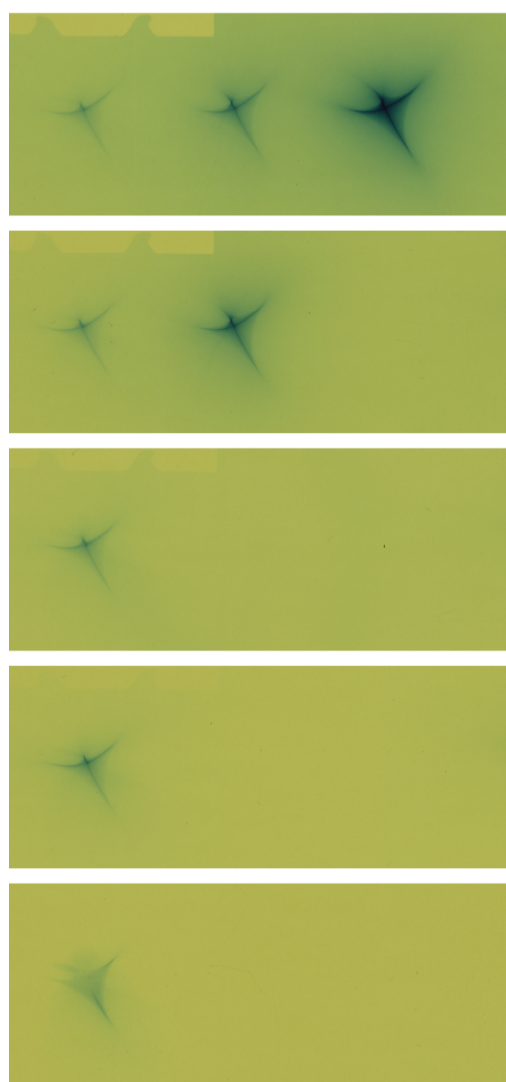


Figure E.1: RAW data corresponding to fig. 4.7.

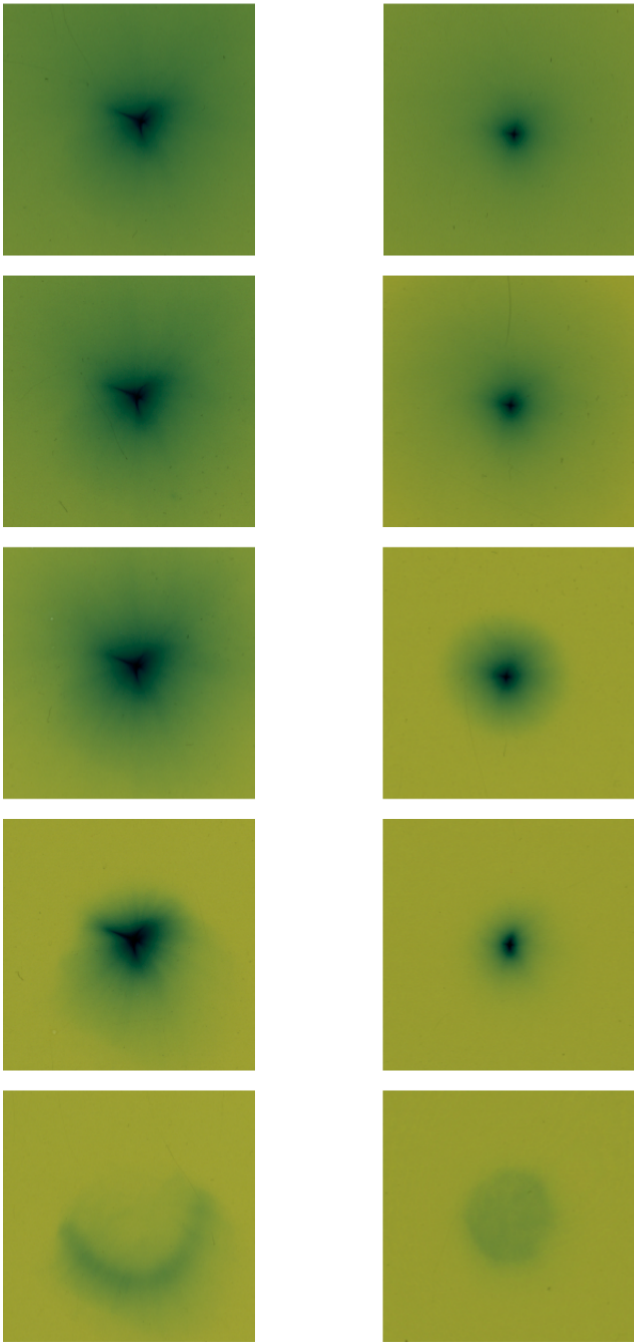


Figure E.2: RAW data corresponding to fig. 4.10.

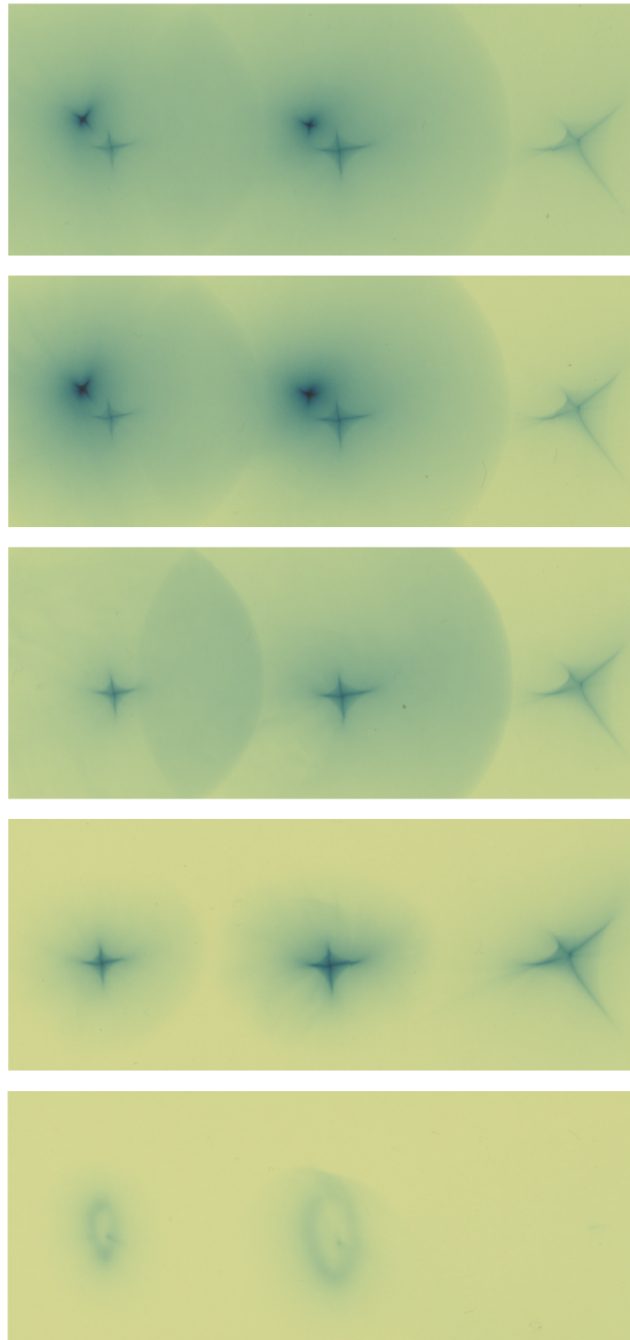


Figure E.3: RAW data corresponding to fig. 5.13.



## REFERENCES

- [1] M Planck. *The new science. 3 complete works: Where is science going? The universe in the light of modern physics; The philosophy of physics*. Meridian Books, 1959. 328 pp. (cit. on p. 9).
- [2] M Baumann, SM Bentzen, W Doerr, MC Joiner, M Saunders, IF Tannock, and HD Thames. „The translational research chain: is it delivering the goods?“ In: *International Journal of Radiation Oncology\*Biophysics* 49.2 (2001), pp. 345–351. DOI: 10.1016/s0360-3016(00)01483-8 (cit. on pp. 9, 10).
- [3] SF Keevil. „Physics and medicine: a historical perspective“. In: *The Lancet* 379.9825 (2012), pp. 1517–1524. DOI: 10.1016/s0140-6736(11)60282-1 (cit. on p. 9).
- [4] CMC Ma and T Lomax, eds. *Proton and Carbon Ion Therapy*. Taylor & Francis Inc, 2012. 256 pp. ISBN: 1439816077 (cit. on pp. 10, 83, 102).
- [5] AR Smith. „Proton therapy“. In: *Physics in Medicine and Biology* 51.13 (2006), R491–R504. DOI: 10.1088/0031-9155/51/13/r26 (cit. on p. 10).
- [6] O Jäkel, CP Karger, and J Debus. „The future of heavy ion radiotherapy“. In: *Medical Physics* 35.12 (2008), pp. 5653–5663. DOI: 10.1118/1.3002307 (cit. on pp. 10, 83).
- [7] URL: <https://www.ptcog.ch/index.php/facilities-in-operation> (cit. on p. 10).
- [8] M Goitein and M Jermann. „The Relative Costs of Proton and X-ray Radiation Therapy“. In: *Clinical Oncology* 15.1 (2003), S37–S50. DOI: 10.1053/clon.2002.0174 (cit. on p. 10).
- [9] H Suit, S Goldberg, A Niemierko, A Trofimov, J Adams, H Paganetti, GTY Chen, T Bortfeld, S Rosenthal, J Loeffler, and T Delaney. „Proton Beams to Replace Photon Beams in Radical Dose Treatments“. In: *Acta Oncologica* 42.8 (2003), pp. 800–808. DOI: 10.1080/02841860310017676 (cit. on p. 10).
- [10] J Lundkvist, M Ekman, SR Ericsson, B Jönsson, and B Glimelius. „Cost-effectiveness of proton radiation in the treatment of childhood medulloblastoma“. In: *Cancer* 103.4 (2005), pp. 793–801. DOI: 10.1002/cncr.20844 (cit. on p. 10).

## References

- [11] RJ Schulz, AR Smith, and CG Orton. „Proton therapy is too expensive for the minimal potential improvements in outcome claimed“. In: *Medical Physics* 34.4 (2007), pp. 1135–1138.  
DOI: 10.1118/1.2717380 (cit. on p. 10).
- [12] RL Maughan, FV den Heuvel, and CG Orton. „Within the next 10-15 years protons will likely replace photons as the most common type of radiation for curative radiotherapy“. In: *Medical Physics* 35.10 (2008), pp. 4285–4288.  
DOI: 10.1118/1.2955553 (cit. on p. 10).
- [13] K Zeil, SD Kraft, S Bock, M Bussmann, TE Cowan, T Kluge, J Metzkes, T Richter, R Sauerbrey, and U Schramm. „The scaling of proton energies in ultrashort pulse laser plasma acceleration“. In: *New Journal of Physics* 12.4 (2010), p. 045015.  
DOI: 10.1088/1367-2630/12/4/045015 (cit. on pp. 11, 17).
- [14] K Zeil, J Metzkes, T Kluge, M Bussmann, T Cowan, S Kraft, R Sauerbrey, and U Schramm. „Direct observation of prompt pre-thermal laser ion sheath acceleration“. In: *Nature Communications* 3 (2012), p. 874.  
DOI: 10.1038/ncomms1883 (cit. on pp. 11, 17, 20).
- [15] RA Snavely, MH Key, SP Hatchett, TE Cowan, M Roth, TW Phillips, MA Stoyer, EA Henry, TC Sangster, MS Singh, SC Wilks, A MacKinnon, A Offenberger, DM Pennington, K Yasuike, AB Langdon, BF Lasinski, J Johnson, MD Perry, and EM Campbell. „Intense High-Energy Proton Beams from Petawatt-Laser Irradiation of Solids“. In: *Physical Review Letters* 85.14 (2000), pp. 2945–2948.  
DOI: 10.1103/physrevlett.85.2945 (cit. on pp. 11, 15, 17).
- [16] M Siebold, F Roeser, M Loeser, D Albach, and U Schramm. „PEneLOPE: a high peak-power diode-pumped laser system for laser-plasma experiments“. In: *High-Power, High-Energy, and High-Intensity Laser Technology; and Research Using Extreme Light: Entering New Frontiers with Petawatt-Class Lasers*. Ed. by J Hein, G Korn, and LO Silva. SPIE, 2013.  
DOI: 10.1117/12.2017522 (cit. on p. 11).
- [17] M Hornung, H Liebetrau, A Seidel, S Keppler, A Kessler, J Körner, M Hellwing, F Schorcht, D Klöpfel, AK Arunachalam, GA Becker, A Sävert, J Polz, J Hein, and MC Kaluza. „The all-diode-pumped laser system POLARIS – an experimentalist’s tool generating ultra-high contrast pulses with high energy“. In: *High Power Laser Science and Engineering* 2 (2014).  
DOI: 10.1017/hpl.2014.26 (cit. on p. 11).
- [18] M Hornung, H Liebetrau, S Keppler, A Kessler, M Hellwing, F Schorcht, GA Becker, M Reuter, J Polz, J Körner, J Hein, and MC Kaluza. „54 J pulses with 18 nm bandwidth from a diode-pumped chirped-pulse amplification laser system“. In: *Optics Letters* 41.22 (2016), p. 5413.  
DOI: 10.1364/ol.41.005413 (cit. on p. 11).
- [19] K Zeil, J Metzkes, T Kluge, M Bussmann, TE Cowan, SD Kraft, R Sauerbrey, B Schmidt, M Zier, and U Schramm. „Robust energy enhancement of ultrashort pulse laser accelerated protons from reduced mass targets“. In: *Plasma Physics and Controlled Fusion* 56.8 (2014), p. 084004.  
DOI: 10.1088/0741-3335/56/8/084004 (cit. on p. 11).

- [20] J Metzkes, T Kluge, K Zeil, M Bussmann, SD Kraft, TE Cowan, and U Schramm. „Experimental observation of transverse modulations in laser-driven proton beams“. In: *New Journal of Physics* 16.2 (2014), p. 023008. DOI: 10.1088/1367-2630/16/2/023008 (cit. on p. 11).
- [21] J Metzkes, K Zeil, SD Kraft, M Rehwald, TE Cowan, and U Schramm. „Reflective optical probing of laser-driven plasmas at the rear surface of solid targets“. In: *Plasma Physics and Controlled Fusion* 58.3 (2016), p. 034012. DOI: 10.1088/0741-3335/58/3/034012 (cit. on p. 11).
- [22] C Richter, L Karsch, Y Dammene, SD Kraft, J Metzkes, U Schramm, M Schürer, M Sobiella, A Weber, K Zeil, and J Pawelke. „A dosimetric system for quantitative cell irradiation experiments with laser-accelerated protons“. In: *Physics in Medicine and Biology* 56.6 (2011), pp. 1529–1543. DOI: 10.1088/0031-9155/56/6/002 (cit. on pp. 11, 64).
- [23] J Metzkes, L Karsch, SD Kraft, J Pawelke, C Richter, M Schürer, M Sobiella, N Stiller, K Zeil, and U Schramm. „A scintillator-based online detector for the angularly resolved measurement of laser-accelerated proton spectra“. In: *Review of Scientific Instruments* 83.12 (2012), p. 123301. DOI: 10.1063/1.4768672 (cit. on pp. 11, 116).
- [24] F Kroll, J Pawelke, and L Karsch. „Preliminary investigations on the determination of three-dimensional dose distributions using scintillator blocks and optical tomography“. In: *Medical Physics* 40.8 (2013), p. 082104. DOI: 10.1118/1.4813898 (cit. on pp. 11, 117).
- [25] J Metzkes, K Zeil, SD Kraft, L Karsch, M Sobiella, M Rehwald, L Obst, HP Schlenvoigt, and U Schramm. „An online, energy-resolving beam profile detector for laser-driven proton beams“. In: *Review of Scientific Instruments* 87.8 (2016), p. 083310. DOI: 10.1063/1.4961576 (cit. on pp. 11, 116).
- [26] SD Kraft, C Richter, K Zeil, M Baumann, E Beyreuther, S Bock, M Bussmann, TE Cowan, Y Dammene, W Enghardt, U Helbig, L Karsch, T Kluge, L Laschinsky, E Lessmann, J Metzkes, D Naumburger, R Sauerbrey, M Schürer, M Sobiella, J Woithe, U Schramm, and J Pawelke. „Dose-dependent biological damage of tumour cells by laser-accelerated proton beams“. In: *New Journal of Physics* 12.8 (2010), p. 085003. DOI: 10.1088/1367-2630/12/8/085003 (cit. on pp. 11, 18, 93).
- [27] K Zeil, M Baumann, E Beyreuther, T Burris-Mog, TE Cowan, W Enghardt, L Karsch, SD Kraft, L Laschinsky, J Metzkes, D Naumburger, M Oppelt, C Richter, R Sauerbrey, M Schürer, U Schramm, and J Pawelke. „Dose-controlled irradiation of cancer cells with laser-accelerated proton pulses“. In: *Applied Physics B* 110.4 (2012), pp. 437–444. DOI: 10.1007/s00340-012-5275-3 (cit. on pp. 11, 18, 93, 104).
- [28] E Beyreuther, W Enghardt, M Kaluza, L Karsch, L Laschinsky, E Lessmann, M Nicolai, J Pawelke, C Richter, R Sauerbrey, HP Schlenvoigt, and M Baumann. „Establishment of technical prerequisites for cell irradiation experiments with laser-accelerated electrons“. In: *Medical Physics* 37.4 (2010), pp. 1392–1400. DOI: 10.1118/1.3301598 (cit. on pp. 11, 93).

## References

- [29] L Laschinsky, M Baumann, E Beyreuther, W Enghardt, M Kaluza, L Karsch, E Lessmann, D Naumburger, M Nicolai, C Richter, R Sauergrey, HP Schlenvoigt, and J Pawelke. „Radiobiological Effectiveness of Laser Accelerated Electrons in Comparison to Electron Beams from a Conventional Linear Accelerator“. In: *Journal of Radiation Research* 53.3 (2012), pp. 395–403.  
DOI: 10.1269/jrr.11080 (cit. on pp. 11, 93).
- [30] K Brüchner, E Beyreuther, M Baumann, M Krause, M Oppelt, and J Pawelke. „Establishment of a small animal tumour model for in vivo studies with low energy laser accelerated particles“. In: *Radiation Oncology* 9.1 (2014), p. 57.  
DOI: 10.1186/1748-717x-9-57 (cit. on pp. 11, 93).
- [31] M Oppelt, M Baumann, R Bergmann, E Beyreuther, K Brüchner, J Hartmann, L Karsch, M Krause, L Laschinsky, E Leßmann, M Nicolai, M Reuter, C Richter, A Sävert, M Schnell, M Schürer, J Woithe, M Kaluza, and J Pawelke. „Comparison study of in vivo dose response to laser-driven versus conventional electron beam“. In: *Radiation and Environmental Biophysics* 54.2 (2015), pp. 155–166.  
DOI: 10.1007/s00411-014-0582-1 (cit. on pp. 11, 93).
- [32] E Beyreuther, K Brüchner, M Krause, M Schmidt, R Szabo, and J Pawelke. „An optimized small animal tumour model for experimentation with low energy protons“. In: *PLOS ONE* 12.5 (2017). Ed. by R Amendola, e0177428.  
DOI: 10.1371/journal.pone.0177428 (cit. on p. 11).
- [33] U Masood, M Bussmann, TE Cowan, W Enghardt, L Karsch, F Kroll, U Schramm, and J Pawelke. „A compact solution for ion beam therapy with laser accelerated protons“. In: *Applied Physics B* 117.1 (2014), pp. 41–52.  
DOI: 10.1007/s00340-014-5796-z (cit. on pp. 11, 12, 41, 58, 86, 91, 93, 108).
- [34] U Masood, TE Cowan, W Enghardt, KM Hofmann, L Karsch, F Kroll, U Schramm, JJ Wilkens, and J Pawelke. „A light-weight compact proton gantry design with a novel dose delivery system for broad-energetic laser-accelerated beams“. In: *Physics in Medicine & Biology* 62.13 (2017), pp. 5531–5555.  
DOI: 10.1088/1361-6560/aa7124 (cit. on pp. 11, 86, 108).
- [35] URL: <https://www.klinikum.uni-heidelberg.de/First-heavy-ion-gantry.112987.0.html?&L=1> (cit. on p. 11).
- [36] URL: <http://pronovasolutions.com/technology/> (cit. on p. 12).
- [37] Y Iwata, T Fujimoto, S Matsuba, T Fujita, S Sato, T Furukawa, Y Hara, K Mizushima, Y Saraya, R Tansho, N Saotome, T Shirai, and K Noda. „Beam commissioning of a superconducting rotating-gantry for carbon-ion radiotherapy“. In: *Nuclear Instruments and Methods in Physics Research Section A: Accelerators, Spectrometers, Detectors and Associated Equipment* 834 (2016), pp. 71–80.  
DOI: 10.1016/j.nima.2016.07.050 (cit. on p. 12).
- [38] U Linz and J Alonso. „Laser-driven ion accelerators for tumor therapy revisited“. In: *Physical Review Accelerators and Beams* 19.12 (2016).  
DOI: 10.1103/physrevaccelbeams.19.124802 (cit. on p. 12).

- [39] K Harres, I Alber, A Tauschwitz, V Bagnoud, H Daido, M Günther, F Nürnberg, A Otten, M Schollmeier, J Schütrumpf, M Tampo, and M Roth. „Beam collimation and transport of quasineutral laser-accelerated protons by a solenoid field“. In: *Physics of Plasmas* 17.2 (2010), p. 023107.  
DOI: 10.1063/1.3299391 (cit. on p. 13).
- [40] KJ Harres. „Strahltransport laserbeschleunigter Ionen“. PhD thesis. Technische Universität, Darmstadt, 2010 (cit. on p. 13).
- [41] T Burris-Mog, K Harres, F Nürnberg, S Busold, M Bussmann, O Deppert, G Hoffmeister, M Joost, M Sobiella, A Tauschwitz, B Zielbauer, V Bagnoud, T Herrmannsdoerfer, M Roth, and TE Cowan. „Laser accelerated protons captured and transported by a pulse power solenoid“. In: *Physical Review Special Topics - Accelerators and Beams* 14.12 (2011), p. 121301.  
DOI: 10.1103/physrevstab.14.121301 (cit. on pp. 13, 39).
- [42] TJ Burris-Mog. „Capture and Transport of Laser Accelerated Protons by Pulsed Magnetic Fields: Advancements Toward Laser-Based Proton Therapy“. PhD thesis. University of Nevada, Reno, 2012 (cit. on pp. 13, 39, 51).
- [43] S Busold, D Schumacher, O Deppert, C Brabetz, S Frydrych, F Kroll, M Joost, H Al-Omari, A Blažević, B Zielbauer, I Hofmann, V Bagnoud, TE Cowan, and M Roth. „Focusing and transport of high-intensity multi-MeV proton bunches from a compact laser-driven source“. In: *Physical Review Special Topics - Accelerators and Beams* 16.10 (2013).  
DOI: 10.1103/physrevstab.16.101302 (cit. on pp. 13, 39, 65, 67, 80, 90, 108).
- [44] S Busold, D Schumacher, O Deppert, C Brabetz, F Kroll, A Blažević, V Bagnoud, and M Roth. „Commissioning of a compact laser-based proton beam line for high intensity bunches around 10 MeV“. In: *Physical Review Special Topics - Accelerators and Beams* 17.3 (2014).  
DOI: 10.1103/physrevstab.17.031302 (cit. on pp. 13, 30, 39, 79, 80, 108).
- [45] S Busold, A Almomani, V Bagnoud, W Barth, S Bedacht, A Blažević, O Boine-Frankenheim, C Brabetz, T Burris-Mog, T Cowan, O Deppert, M Droba, H Eickhoff, U Eisenbarth, K Harres, G Hoffmeister, I Hofmann, O Jaeckel, R Jaeger, M Joost, S Kraft, F Kroll, M Kaluza, O Kester, Z Lecz, T Merz, F Nürnberg, H Al-Omari, A Orzhekhovskaya, G Paulus, J Polz, U Ratzinger, M Roth, G Schaumann, P Schmidt, U Schramm, G Schreiber, D Schumacher, T Stoehlker, A Tauschwitz, W Vinzenz, F Wagner, S Yarmyshev, and B Zielbauer. „Shaping laser accelerated ions for future applications – The LIGHT collaboration“. In: *Nuclear Instruments and Methods in Physics Research Section A: Accelerators, Spectrometers, Detectors and Associated Equipment* 740 (2014), pp. 94–98.  
DOI: 10.1016/j.nima.2013.10.025 (cit. on pp. 13, 39, 80, 108).
- [46] S Busold, D Schumacher, C Brabetz, D Jahn, F Kroll, O Deppert, U Schramm, TE Cowan, A Blažević, V Bagnoud, and M Roth. „Towards highest peak intensities for ultra-short MeV-range ion bunches“. In: *Scientific Reports* 5.1 (2015).  
DOI: 10.1038/srep12459 (cit. on pp. 13, 80, 83, 108).
- [47] S Busold. „Construction and characterization of a laser-driven proton beamline at GSI“. PhD thesis. Technische Universität, Darmstadt, 2014 (cit. on pp. 13, 20, 39).

## References

- [48] SC Wilks, AB Langdon, TE Cowan, M Roth, M Singh, S Hatchett, MH Key, D Pennington, A MacKinnon, and RA Snavely. „Energetic proton generation in ultra-intense laser–solid interactions“. In: *Physics of Plasmas* 8.2 (2001), pp. 542–549. DOI: 10.1063/1.1333697 (cit. on pp. 15, 17, 30).
- [49] M Borghesi. „Laser-driven ion acceleration: State of the art and emerging mechanisms“. In: *Nuclear Instruments and Methods in Physics Research Section A: Accelerators, Spectrometers, Detectors and Associated Equipment* 740 (2014), pp. 6–9. DOI: 10.1016/j.nima.2013.11.098 (cit. on p. 15).
- [50] P Gibbon. *Short Pulse Laser Interactions with Matter*. IMPERIAL COLLEGE PRESS, 2005. 328 pp. ISBN: 1860941354 (cit. on p. 15).
- [51] P Mulser and D Bauer. *High Power Laser-Matter Interaction*. Springer-Verlag GmbH, 2010. 160 pp. ISBN: 3540506691 (cit. on p. 15).
- [52] A Macchi. *A Superintense Laser-Plasma Interaction Theory Primer*. Springer Netherlands, 2013. 114 pp. ISBN: 9789400761254 (cit. on p. 15).
- [53] P Mora. „Laser driven ion acceleration“. In: *AIP Conference Proceedings*. AIP, 2007. DOI: 10.1063/1.2756774 (cit. on p. 15).
- [54] C Perego, A Zani, D Batani, and M Passoni. „Extensive comparison among Target Normal Sheath Acceleration theoretical models“. In: *Nuclear Instruments and Methods in Physics Research Section A: Accelerators, Spectrometers, Detectors and Associated Equipment* 653.1 (2011), pp. 89–93. DOI: 10.1016/j.nima.2011.01.100 (cit. on p. 15).
- [55] H Daido, M Nishiuchi, and AS Pirozhkov. „Review of laser-driven ion sources and their applications“. In: *Reports on Progress in Physics* 75.5 (2012), p. 056401. DOI: 10.1088/0034-4885/75/5/056401 (cit. on pp. 15, 21).
- [56] TE Cowan, J Fuchs, H Ruhl, A Kemp, P Audebert, M Roth, R Stephens, I Barton, A Blazevic, E Brambrink, J Cobble, J Fernández, JC Gauthier, M Geissel, M Hegelich, J Kaae, S Karsch, GPL Sage, S Letzring, M Manclossi, S Meyroneinc, A Newkirk, H Pépin, and N Renard-LeGalloudec. „Ultralow Emittance, Multi-MeV Proton Beams from a Laser Virtual-Cathode Plasma Accelerator“. In: *Physical Review Letters* 92.20 (2004). DOI: 10.1103/physrevlett.92.204801 (cit. on pp. 17, 74).
- [57] F Wagner, O Deppert, C Brabetz, P Fiala, A Kleinschmidt, P Poth, V Schanz, A Tebartz, B Zielbauer, M Roth, T Stöhlker, and V Bagnoud. „Maximum Proton Energy above 85 MeV from the Relativistic Interaction of Laser Pulses with Micrometer ThickCH2Targets“. In: *Physical Review Letters* 116.20 (2016). DOI: 10.1103/physrevlett.116.205002 (cit. on p. 17).
- [58] U Schramm, M Bussmann, A Irman, M Siebold, K Zeil, D Albach, C Bernert, S Bock, F Brack, J Branco, J Couperus, T Cowan, A Debus, C Eisenmann, M Garten, R Gebhardt, S Grams, U Helbig, A Huebl, T Kluge, A Köhler, J Krämer, S Kraft, F Kroll, M Kuntzsch, U Lehnert, M Loeser, J Metzkes, P Michel, L Obst, R Pausch, M Rehwald, R Sauerbrey, H Schlenvoigt, K Steiniger, and O Zarini. „First results with the novel petawatt laser acceleration facility in Dresden“. In: *Journal of Physics: Conference Series* 874 (2017), p. 012028. DOI: 10.1088/1742-6596/874/1/012028 (cit. on p. 17).

- [59] P Mora. „Plasma Expansion into a Vacuum“. In: *Physical Review Letters* 90.18 (2003). DOI: 10.1103/physrevlett.90.185002 (cit. on p. 17).
- [60] P Mora. „Thin-foil expansion into a vacuum“. In: *Physical Review E* 72.5 (2005). DOI: 10.1103/physreve.72.056401 (cit. on p. 17).
- [61] J Fuchs, P Antici, E d’Humières, E Lefebvre, M Borghesi, E Brambrink, CA Cecchetti, M Kaluza, V Malka, M Manclossi, S Meyroneinc, P Mora, J Schreiber, T Toncian, H Pépin, and P Audebert. „Laser-driven proton scaling laws and new paths towards energy increase“. In: *Nature Physics* 2.1 (2005), pp. 48–54. DOI: 10.1038/nphys199 (cit. on p. 17).
- [62] L Robson, PT Simpson, RJ Clarke, KWD Ledingham, F Lindau, O Lundh, T McCanny, P Mora, D Neely, CG Wahlström, M Zepf, and P McKenna. „Scaling of proton acceleration driven by petawatt-laser–plasma interactions“. In: *Nature Physics* 3.1 (2006), pp. 58–62. DOI: 10.1038/nphys476 (cit. on p. 17).
- [63] URL: <https://eli-laser.eu/> (cit. on p. 17).
- [64] URL: <https://www.cala-laser.de/> (cit. on p. 17).
- [65] J Zou, CL Blanc, D Papadopoulos, G Chériaux, P Georges, G Mennerat, F Druon, L Lecherbourg, A Pellegrina, P Ramirez, F Giamb Bruno, A Fréneaux, F Leconte, D Badarau, J Boudenne, D Fournet, T Valloton, J Paillard, J Veray, M Pina, P Monot, J Chambaret, P Martin, F Mathieu, P Audebert, and F Amiranoff. „Design and current progress of the Apollon 10 PW project“. In: *High Power Laser Science and Engineering* 3 (2015). DOI: 10.1017/hpl.2014.41 (cit. on p. 17).
- [66] T Kluge, T Cowan, A Debus, U Schramm, K Zeil, and M Bussmann. „Electron Temperature Scaling in Laser Interaction with Solids“. In: *Physical Review Letters* 107.20 (2011). DOI: 10.1103/physrevlett.107.205003 (cit. on p. 18).
- [67] A Yogo, K Sato, M Nishikino, T Maeda, H Sakaki, T Hori, K Ogura, M Nishiuchi, T Teshima, H Nishimura, K Kondo, PR Bolton, and S Kawanishi. „Measurement of DNA Double-Strand Break Yield in Human Cancer Cells by High-Current, Short-Duration Bunches of Laser-Accelerated Protons“. In: *Japanese Journal of Applied Physics* 50.10 (2011), p. 106401. DOI: 10.1143/jjap.50.106401 (cit. on p. 18).
- [68] J Bin, K Allinger, W Assmann, G Dollinger, GA Drexler, AA Friedl, D Habs, P Hinz, R Hoerlein, N Humble, S Karsch, K Khrennikov, D Kiefer, F Krausz, W Ma, D Michalski, M Molls, S Raith, S Reinhardt, B Röper, TE Schmid, T Tajima, J Wenz, O Zlobinskaya, J Schreiber, and JJ Wilkens. „A laser-driven nanosecond proton source for radiobiological studies“. In: *Applied Physics Letters* 101.24 (2012), p. 243701. DOI: 10.1063/1.4769372 (cit. on p. 18).
- [69] S Raschke, S Spickermann, T Toncian, M Swantusch, J Boeker, U Giesen, G Iliakis, O Willi, and F Boege. „Ultra-short laser-accelerated proton pulses have similar DNA-damaging effectiveness but produce less immediate nitroxidative stress than conventional proton beams“. In: *Scientific Reports* 6.1 (2016). DOI: 10.1038/srep32441 (cit. on p. 18).

## References

- [70] M Roth, TE Cowan, MH Key, SP Hatchett, C Brown, W Fountain, J Johnson, DM Pennington, RA Snavely, SC Wilks, K Yasuike, H Ruhl, F Pegoraro, SV Bulanov, EM Campbell, MD Perry, and H Powell. „Fast Ignition by Intense Laser-Accelerated Proton Beams“. In: *Physical Review Letters* 86.3 (2001), pp. 436–439.  
DOI: 10.1103/physrevlett.86.436 (cit. on pp. 21, 86).
- [71] W Bang, BJ Albright, PA Bradley, EL Vold, JC Boettger, and JC Fernández. „Uniform heating of materials into the warm dense matter regime with laser-driven quasimonoenergetic ion beams“. In: *Physical Review E* 92.6 (2015).  
DOI: 10.1103/physreve.92.063101 (cit. on p. 21).
- [72] M Borghesi, A Schiavi, DH Campbell, MG Haines, O Willi, AJ MacKinnon, LA Gizzi, M Galimberti, RJ Clarke, and H Ruhl. „Proton imaging: a diagnostic for inertial confinement fusion/fast ignitor studies“. In: *Plasma Physics and Controlled Fusion* 43.12A (2001), A267–A276.  
DOI: 10.1088/0741-3335/43/12a/320 (cit. on p. 21).
- [73] L Volpe, D Batani, B Vauzour, P Nicolai, JJ Santos, C Regan, A Morace, F Dorchies, C Fourment, S Hulin, F Perez, S Baton, K Lancaster, M Galimberti, R Heathcote, M Tolley, C Spindloe, P Koester, L Labate, LA Gizzi, C Benedetti, A Sgattoni, M Richetta, J Pasley, F Beg, S Chawla, DP Higginson, and AG MacPhee. „Proton radiography of laser-driven imploding target in cylindrical geometry“. In: *Physics of Plasmas* 18.1 (2011), p. 012704.  
DOI: 10.1063/1.3530596 (cit. on p. 21).
- [74] S Fritzler, V Malka, G Grillon, JP Rousseau, F Burgy, E Lefebvre, E d’Humières, P McKenna, and KWD Ledingham. „Proton beams generated with high-intensity lasers: Applications to medical isotope production“. In: *Applied Physics Letters* 83.15 (2003), pp. 3039–3041.  
DOI: 10.1063/1.1616661 (cit. on p. 21).
- [75] KL Lancaster, S Karsch, H Habara, FN Beg, EL Clark, R Freeman, MH Key, JA King, R Kodama, K Krushelnick, KWD Ledingham, P McKenna, CD Murphy, PA Norreys, R Stephens, C Stöeckl, Y Toyama, MS Wei, and M Zepf. „Characterization of  $7\text{Li}(p,n)7\text{Be}$  neutron yields from laser produced ion beams for fast neutron radiography“. In: *Physics of Plasmas* 11.7 (2004), pp. 3404–3408.  
DOI: 10.1063/1.1756911 (cit. on p. 21).
- [76] M Roth, D Jung, K Falk, N Guler, O Deppert, M Devlin, A Favalli, J Fernandez, D Gautier, M Geissel, R Haight, CE Hamilton, BM Hegelich, RP Johnson, F Merrill, G Schaumann, K Schoenberg, M Schollmeier, T Shimada, T Taddeucci, JL Tybo, F Wagner, SA Wender, CH Wilde, and GA Wurden. „Bright Laser-Driven Neutron Source Based on the Relativistic Transparency of Solids“. In: *Physical Review Letters* 110.4 (2013).  
DOI: 10.1103/physrevlett.110.044802 (cit. on pp. 21, 86).
- [77] M Bird and Z Gan. „Low resolution NMR magnets in the 23 to 35 T range at the NHMFL“. In: *IEEE Transactions on Applied Superconductivity* 12.1 (2002), pp. 447–451.  
DOI: 10.1109/tasc.2002.1018440 (cit. on p. 23).

- [78] J Schwartz, T Effio, X Liu, Q Le, A Mbaruku, H Schneider-Muntau, T Shen, H Song, U Trociewitz, X Wang, and H Weijers. „High Field Superconducting Solenoids Via High Temperature Superconductors“. In: *IEEE Transactions on Applied Superconductivity* 18.2 (2008), pp. 70–81.  
DOI: 10.1109/tasc.2008.921363 (cit. on p. 23).
- [79] F Herlach and M von Ortenberg. „Pulsed magnets for strong and ultrastrong fields“. In: *IEEE Transactions on Magnetics* 32.4 (1996), pp. 2438–2443.  
DOI: 10.1109/20.511366 (cit. on p. 24).
- [80] CM Fowler. „Megagauss Physics“. In: *Science* 180.4083 (1973), pp. 261–267.  
DOI: 10.1126/science.180.4083.261 (cit. on p. 24).
- [81] S Zherlitsyn, B Wustmann, T Herrmannsdörfer, and J Wosnitza. „Magnet-Technology Development at the Dresden High Magnetic Field Laboratory“. In: *Journal of Low Temperature Physics* 170.5-6 (2012), pp. 447–451.  
DOI: 10.1007/s10909-012-0764-7 (cit. on p. 24).
- [82] J Sims, D Rickel, C Swenson, J Schillig, G Ellis, and C Ammerman. „Assembly, Commissioning and Operation of the NHMFL 100 Tesla Multi-Pulse Magnet System“. In: *IEEE Transactions on Applied Superconductivity* 18.2 (2008), pp. 587–591.  
DOI: 10.1109/tasc.2008.922541 (cit. on p. 24).
- [83] H Busch. „Berechnung der Bahn von Kathodenstrahlen im axialsymmetrischen elektromagnetischen Felde“. In: *Annalen der Physik* 386.25 (1926), pp. 974–993.  
DOI: 10.1002/andp.19263862507 (cit. on p. 24).
- [84] M Reiser. *Theory and Design of Charged Particle Beams*. Wiley-VCH, 2008. ISBN: 9780471306160 (cit. on pp. 24, 30, 45).
- [85] V Kumar. „Understanding the focusing of charged particle beams in a solenoid magnetic field“. In: *American Journal of Physics* 77.8 (2009), pp. 737–741.  
DOI: 10.1119/1.3129242 (cit. on pp. 24, 27).
- [86] URL: <http://www.pulsar.nl/gpt/> (cit. on pp. 28, 61).
- [87] E Fourkal, JS Li, M Ding, T Tajima, and CM Ma. „Particle selection for laser-accelerated proton therapy feasibility study“. In: *Medical Physics* 30.7 (2003), pp. 1660–1670.  
DOI: 10.1118/1.1586268 (cit. on p. 28).
- [88] J Metzkes, T Cowan, L Karsch, S Kraft, J Pawelke, C Richter, T Richter, K Zeil, and U Schramm. „Preparation of laser-accelerated proton beams for radiobiological applications“. In: *Nuclear Instruments and Methods in Physics Research Section A: Accelerators, Spectrometers, Detectors and Associated Equipment* 653.1 (2011), pp. 172–175.  
DOI: 10.1016/j.nima.2010.12.065 (cit. on p. 28).
- [89] G Cirrone, G Cuttone, F Romano, F Schillaci, V Scuderi, A Amato, G Candiano, M Costa, G Gallo, G Larosa, G Korn, R Leanza, R Manna, M Maggiore, V Marchese, D Margarone, G Milluzzo, G Petringa, and A Tramontana. „Design and Status of the ELIMED Beam Line for Laser-Driven Ion Beams“. In: *Applied Sciences* 5.3 (2015), pp. 427–445.  
DOI: 10.3390/app5030427 (cit. on p. 28).

## References

- [90] T Eichner, F Grüner, S Becker, M Fuchs, D Habs, R Weingartner, U Schramm, H Backe, P Kunz, and W Lauth. „Miniature magnetic devices for laser-based, table-top free-electron lasers“. In: *Physical Review Special Topics - Accelerators and Beams* 10.8 (2007).  
DOI: 10.1103/physrevstab.10.082401 (cit. on p. 30).
- [91] M Schollmeier, S Becker, M Geißel, KA Flippo, A Blažević, SA Gaillard, DC Gautier, F Grüner, K Harres, M Kimmel, F Nürnberg, P Rambo, U Schramm, J Schreiber, J Schüttrumpf, J Schwarz, NA Tahir, B Atherton, D Habs, BM Hegelich, and M Roth. „Controlled Transport and Focusing of Laser-Accelerated Protons with Miniature Magnetic Devices“. In: *Physical Review Letters* 101.5 (2008).  
DOI: 10.1103/physrevlett.101.055004 (cit. on p. 30).
- [92] F Schillaci, L Pommarel, F Romano, G Cuttone, M Costa, D Giove, M Maggiore, A Russo, V Scuderi, V Malka, B Vauzour, A Flacco, and G Cirrone. „Characterization of the ELIMED Permanent Magnets Quadrupole system prototype with laser-driven proton beams“. In: *Journal of Instrumentation* 11.07 (2016), T07005–T07005.  
DOI: 10.1088/1748-0221/11/07/t07005 (cit. on p. 30).
- [93] I Hofmann. „Performance of solenoids versus quadrupoles in focusing and energy selection of laser accelerated protons“. In: *Physical Review Special Topics - Accelerators and Beams* 16.4 (2013).  
DOI: 10.1103/physrevstab.16.041302 (cit. on p. 30).
- [94] HB Luna, XK Maruyama, NJ Colella, JS Hobbs, RS Hornady, B Kulke, and JV Palomar. „Bremsstrahlung radiation effects in rare earth permanent magnets“. In: *Nuclear Instruments and Methods in Physics Research Section A: Accelerators, Spectrometers, Detectors and Associated Equipment* 285.1-2 (1989), pp. 349–354.  
DOI: 10.1016/0168-9002(89)90478-6 (cit. on p. 31).
- [95] J Alderman, P Job, R Martin, C Simmons, and G Owen. „Measurement of radiation-induced demagnetization of Nd–Fe–B permanent magnets“. In: *Nuclear Instruments and Methods in Physics Research Section A: Accelerators, Spectrometers, Detectors and Associated Equipment* 481.1-3 (2002), pp. 9–28.  
DOI: 10.1016/s0168-9002(01)01329-8 (cit. on p. 31).
- [96] T Toncian, M Borghesi, J Fuchs, E d’Humieres, P Antici, P Audebert, E Brambrink, CA Cecchetti, A Pipahl, L Romagnani, and O Willi. „Ultrafast Laser-Driven Microlens to Focus and Energy-Select Mega-Electron Volt Protons“. In: *Science* 312.5772 (2006), pp. 410–413.  
DOI: 10.1126/science.1124412 (cit. on p. 31).
- [97] PA Ni, SM Lund, C McGuffey, N Alexander, B Aurand, JJ Barnard, FN Beg, C Bellei, FM Bieniosek, C Brabetz, RH Cohen, J Kim, P Neumayer, M Roth, and BG Logan. „Initial experimental evidence of self-collimation of target-normal-sheath-accelerated proton beam in a stack of conducting foils“. In: *Physics of Plasmas* 20.8 (2013), p. 083111.  
DOI: 10.1063/1.4818147 (cit. on p. 31).
- [98] S Kar, H Ahmed, R Prasad, M Cerchez, S Brauckmann, B Aurand, G Cantono, P Hadjisolomou, CLS Lewis, A Macchi, G Nersisyan, APL Robinson, AM Schroer, M Swantusch, M Zepf, O Willi, and M Borghesi. „Guided post-acceleration of laser-driven ions by a miniature modular structure“. In: *Nature Communications* 7 (2016), p. 10792.  
DOI: 10.1038/ncomms10792 (cit. on p. 31).

- [99] KFF Law, M Bailly-Grandvaux, A Morace, S Sakata, K Matsuo, S Kojima, S Lee, X Vaisseau, Y Arikawa, A Yogo, K Kondo, Z Zhang, C Bellei, JJ Santos, S Fujioka, and H Azechi. „Direct measurement of kilo-tesla level magnetic field generated with laser-driven capacitor-coil target by proton deflectometry“. In: *Applied Physics Letters* 108.9 (2016), p. 091104.  
DOI: 10.1063/1.4943078 (cit. on p. 31).
- [100] S Karsch, J Osterhoff, A Popp, TP Rowlands-Rees, Z Major, M Fuchs, B Marx, R Hörlein, K Schmid, L Veisz, S Becker, U Schramm, B Hidding, G Pretzler, D Habs, F Grüner, F Krausz, and SM Hooker. „GeV-scale electron acceleration in a gas-filled capillary discharge waveguide“. In: *New Journal of Physics* 9.11 (2007), pp. 415–415.  
DOI: 10.1088/1367-2630/9/11/415 (cit. on p. 31).
- [101] J van Tilborg, S Steinke, C Geddes, N Matlis, B Shaw, A Gonsalves, J Huijts, K Nakamura, J Daniels, C Schroeder, C Benedetti, E Esarey, S Bulanov, N Bobrova, P Satorov, and W Leemans. „Active Plasma Lensing for Relativistic Laser-Plasma-Accelerated Electron Beams“. In: *Physical Review Letters* 115.18 (2015).  
DOI: 10.1103/physrevlett.115.184802 (cit. on p. 31).
- [102] J Pozimski and M Aslaninejad. „Gabor lenses for capture and energy selection of laser driven ion beams in cancer treatment“. In: *Laser and Particle Beams* 31.04 (2013), pp. 723–733.  
DOI: 10.1017/s0263034613000761 (cit. on p. 31).
- [103] H Wheeler. „Simple Inductance Formulas for Radio Coils“. In: *Proceedings of the IRE* 16.10 (1928), pp. 1398–1400.  
DOI: 10.1109/jrproc.1928.221309 (cit. on p. 33).
- [104] FW Grover. *Inductance Calculations: Working Formulas and Tables*. DOVER PUBN INC, 2009. 286 pp. ISBN: 0486474402 (cit. on pp. 33, 41).
- [105] R Kratz and P Wyder. *Principles of Pulsed Magnet Design (Engineering Materials)*. Springer, 2013. ISBN: 9783662049693 (cit. on pp. 34, 35).
- [106] (Cit. on p. 35).
- [107] URL: <http://www.orcad.com/products/orcad-pspice-designer/overview> (cit. on p. 35).
- [108] T Peng and C Gu. „Stress calculation in pulsed magnet with distributed windings“. In: *2005 International Conference on Electrical Machines and Systems*. IEEE, 2005.  
DOI: 10.1109/icems.2005.202917 (cit. on p. 43).
- [109] Y Huang, P Frings, and E Hennes. „Mechanical properties of Zylon/epoxy composite“. In: *Composites Part B: Engineering* 33.2 (2002), pp. 109–115.  
DOI: 10.1016/s1359-8368(01)00064-6 (cit. on p. 43).
- [110] B Albertazzi, J Béard, A Ciardi, T Vinci, J Albrecht, J Billette, T Burris-Mog, SN Chen, DD Silva, S Dittrich, T Herrmannsdörfer, B Hirardin, F Kroll, M Nakatsutsumi, S Nitsche, C Riconda, L Romagnagni, HP Schlenvoigt, S Simond, E Veuillot, TE Cowan, O Portugall, H Pépin, and J Fuchs. „Production of large volume, strongly magnetized laser-produced plasmas by use of pulsed external magnetic fields“. In: *Review of Scientific Instruments* 84.4 (2013), p. 043505.  
DOI: 10.1063/1.4795551 (cit. on pp. 46, 54).

## References

- [111] B Albertazzi, A Ciardi, M Nakatsutsumi, T Vinci, J Beard, R Bonito, J Billette, M Borghesi, Z Burkley, SN Chen, TE Cowan, T Herrmannsdorfer, DP Higginson, F Kroll, SA Pikuz, K Naughton, L Romagnani, C Riconda, G Revet, R Riquier, HP Schlenvoigt, IY Skobelev, AY Faenov, A Soloviev, M Huarte-Espinosa, A Frank, O Portugall, H Pepin, and J Fuchs. „Laboratory formation of a scaled protostellar jet by coaligned poloidal magnetic field“. In: *Science* 346.6207 (2014), pp. 325–328.  
DOI: 10.1126/science.1259694 (cit. on pp. 46, 54).
- [112] B Warner. *Cataclysmic Variable Stars*. CAMBRIDGE UNIV PR, 2003. 596 pp. ISBN: 052154209X (cit. on p. 47).
- [113] É Falize, B Loupiau, A Ravasio, CD Gregory, A Dizière, M Koenig, C Michaut, C Cavet, P Barroso, JP Leidinge, X Ribeyre, J Breil, H Takabe, Y Sakawa, Y Kuramitsu, T Morita, NC Woolsey, W Nazarov, and S Pikuz. „The scalability of the accretion column in magnetic cataclysmic variables: the POLAR project“. In: *Astrophysics and Space Science* 336.1 (2011), pp. 81–85.  
DOI: 10.1007/s10509-011-0655-4 (cit. on p. 47).
- [114] C Busschaert, É Falize, B Loupiau, C Michaut, A Ravasio, A Pelka, R Yurchak, and M Koenig. „POLAR project: a numerical study to optimize the target design“. In: *New Journal of Physics* 15.3 (2013), p. 035020.  
DOI: 10.1088/1367-2630/15/3/035020 (cit. on p. 47).
- [115] JE Cross, G Gregori, JM Foster, P Graham, JM Bonnet-Bidaud, C Busschaert, N Charpentier, CN Danson, HW Doyle, RP Drake, J Fyrth, ET Gumbrell, M Koenig, C Krauland, CC Kuranz, B Loupiau, C Michaut, M Mouchet, S Patankar, J Skidmore, C Spindloe, ER Tubman, N Woolsey, R Yurchak, and É Falize. „Laboratory analogue of a supersonic accretion column in a binary star system“. In: *Nature Communications* 7 (2016), ncomms11899.  
DOI: 10.1038/ncomms11899 (cit. on p. 47).
- [116] M Sonoda, M Takano, J Miyahara, and H Kato. „Computed radiography utilizing scanning laser stimulated luminescence.“ In: *Radiology* 148.3 (1983), pp. 833–838.  
DOI: 10.1148/radiology.148.3.6878707 (cit. on p. 48).
- [117] E Brambrink, S Baton, M Koenig, R Yurchak, N Bidaut, B Albertazzi, JE Cross, G Gregori, A Rigby, E Falize, A Pelka, F Kroll, S Pikuz, Y Sakawa, N Ozaki, C Kuranz, M Manuel, C Li, P Tzeferacos, and D Lamb. „Short-pulse laser-driven x-ray radiography“. In: *High Power Laser Science and Engineering* 4 (2016).  
DOI: 10.1017/hpl.2016.31 (cit. on p. 48).
- [118] URL: <http://www.infineon.com/cms/en/product/power/high-power-thyristor-diode/thyristor-diode-presspack/thyristor-presspack/T1503N75TOH/productType.html?productType=db3a304444fe2ffa0144fe307d310001> (cit. on p. 56).
- [119] RF Egerton. *Physical Principles of Electron Microscopy: An Introduction to Tem, Sem, and Aem*. SPRINGER VERLAG GMBH, 2011. 202 pp. ISBN: 0387258000 (cit. on pp. 69, 71).
- [120] O Jäkel, AR Smith, and CG Orton. „The more important heavy charged particle radiotherapy of the future is more likely to be with heavy ions rather than protons“. In: *Medical Physics* 40.9 (2013), p. 090601.  
DOI: 10.1118/1.4798945 (cit. on p. 83).

- [121] SM Pfoth, O Jäckel, A Sachtleben, J Polz, W Ziegler, HP Schlenvoigt, KU Amthor, MC Kaluza, KWD Ledingham, R Sauerbrey, P Gibbon, APL Robinson, and H Schwoerer. „Spectral shaping of laser generated proton beams“. In: *New Journal of Physics* 10.3 (2008), p. 033034.  
DOI: 10.1088/1367-2630/10/3/033034 (cit. on p. 83).
- [122] G Hoffmeister, C Bellei, K Harres, D Ivanov, D Kraus, A Pelka, B Rethfeld, G Schumann, and M Roth. „Influence of fs-laser desorption on target normal sheath accelerated ions“. In: *Physical Review Special Topics - Accelerators and Beams* 16.4 (2013).  
DOI: 10.1103/physrevstab.16.041304 (cit. on p. 83).
- [123] M Hegelich, S Karsch, G Pretzler, D Habs, K Witte, W Guenther, M Allen, A Blazevic, J Fuchs, JC Gauthier, M Geissel, P Audebert, T Cowan, and M Roth. „MeV Ion Jets from Short-Pulse-Laser Interaction with Thin Foils“. In: *Physical Review Letters* 89.8 (2002).  
DOI: 10.1103/physrevlett.89.085002 (cit. on p. 83).
- [124] BM Hegelich, BJ Albright, J Cobble, K Flippo, S Letzring, M Paffett, H Ruhl, J Schreiber, RK Schulze, and JC Fernández. „Laser acceleration of quasi-monoenergetic MeV ion beams“. In: *Nature* 439.7075 (2006), pp. 441–444.  
DOI: 10.1038/nature04400 (cit. on p. 83).
- [125] P Patel, A Mackinnon, M Key, T Cowan, M Foord, M Allen, D Price, H Ruhl, P Springer, and R Stephens. „Isochoric Heating of Solid-Density Matter with an Ultrafast Proton Beam“. In: *Physical Review Letters* 91.12 (2003).  
DOI: 10.1103/physrevlett.91.125004 (cit. on p. 86).
- [126] GM Dyer, AC Bernstein, BI Cho, J Osterholz, W Grigsby, A Dalton, R Shepherd, Y Ping, H Chen, K Widmann, and T Ditmire. „Equation-of-State Measurement of Dense Plasmas Heated With Fast Protons“. In: *Physical Review Letters* 101.1 (2008).  
DOI: 10.1103/physrevlett.101.015002 (cit. on p. 86).
- [127] A Pelka, G Gregori, DO Gericke, J Vorberger, SH Glenzer, MM Günther, K Harres, R Heathcote, AL Kritcher, NL Kugland, B Li, M Makita, J Mithen, D Neely, C Niemann, A Otten, D Riley, G Schaumann, M Schollmeier, A Tauschwitz, and M Roth. „Ultrafast Melting of Carbon Induced by Intense Proton Beams“. In: *Physical Review Letters* 105.26 (2010).  
DOI: 10.1103/physrevlett.105.265701 (cit. on p. 86).
- [128] S Karsch, S Düsterer, H Schwoerer, F Ewald, D Habs, M Hegelich, G Pretzler, A Pukhov, K Witte, and R Sauerbrey. „High-Intensity Laser Induced Ion Acceleration from Heavy-Water Droplets“. In: *Physical Review Letters* 91.1 (2003).  
DOI: 10.1103/physrevlett.91.015001 (cit. on p. 86).
- [129] AJ Mackinnon, PK Patel, RP Town, MJ Edwards, T Phillips, SC Lerner, DW Price, D Hicks, MH Key, S Hatchett, SC Wilks, M Borghesi, L Romagnani, S Kar, T Toncian, G Pretzler, O Willi, M Koenig, E Martinolli, S Lepape, A Benuzzi-Mounaix, P Audebert, JC Gauthier, J King, R Snavely, RR Freeman, and T Boehlly. „Proton radiography as an electromagnetic field and density perturbation diagnostic (invited)“. In: *Review of Scientific Instruments* 75.10 (2004), pp. 3531–3536.  
DOI: 10.1063/1.1788893 (cit. on p. 86).

## References

- [130] B Logan, F Bieniosek, C Celata, J Coleman, W Greenway, E Henestroza, J Kwan, E Lee, M Leitner, P Roy, P Seidl, JL Vay, W Waldron, S Yu, J Barnard, R Cohen, A Friedman, D Grote, MK Covo, A Molvik, S Lund, W Meier, W Sharp, R Davidson, P Efthimion, E Gilson, L Grisham, I Kaganovich, H Qin, A Sefkow, E Startsev, D Welch, and C Olson. „Recent US advances in ion-beam-driven high energy density physics and heavy ion fusion“. In: *Nuclear Instruments and Methods in Physics Research Section A: Accelerators, Spectrometers, Detectors and Associated Equipment* 577.1-2 (2007), pp. 1–7.  
DOI: 10.1016/j.nima.2007.02.070 (cit. on p. 86).
- [131] J Barnard, R More, M Terry, A Friedman, E Henestroza, A Koniges, J Kwan, A Ng, P Ni, W Liu, B Logan, E Startsev, and A Yuen. „NDCX-II target experiments and simulations“. In: *Nuclear Instruments and Methods in Physics Research Section A: Accelerators, Spectrometers, Detectors and Associated Equipment* 733 (2014), pp. 45–50.  
DOI: 10.1016/j.nima.2013.05.096 (cit. on p. 86).
- [132] U Masood, L Karsch, J Pawelke, and F Kroll. *Einrichtung zum Abrastern mit aufgeweiteten Teilchenstrahlen*. Patent App. No. DE 10 2016 225 798.6. 2017 (cit. on p. 86).
- [133] M Schürer, L Karsch, J Pawelke, J Zschetzsche, and F Kroll. *Elektromagnet zur Führung von Teilchenstrahlen zur Strahlentherapie*. Patent No. DE 10 2015 200 213 A1. 2016 (cit. on p. 87).
- [134] A Gabard, M Negrazus, V Vrankovic, and D George. „Magnetic Measurements and Commissioning of the Fast Ramped 90° Bending Magnet in the PROSCAN Gantry 2 Project at PSI“. In: *IEEE Transactions on Applied Superconductivity* 20.3 (2010), pp. 794–797.  
DOI: 10.1109/tasc.2010.2040916 (cit. on p. 87).
- [135] S Wettengel. „Untersuchung und Vergleich von Topologien zur Erzeugung hoher gepulster Magnetfelder für eine medizinische Anwendung“. MA thesis. Technische Universität Dresden, 2014 (cit. on p. 87).
- [136] JF Ziegler. *SRIM - The Stopping and Range of Ions in Matter*. URL: <http://www.srim.org> (cit. on p. 89).
- [137] S Agostinelli et al. „Geant4—a simulation toolkit“. In: *Nuclear Instruments and Methods in Physics Research Section A: Accelerators, Spectrometers, Detectors and Associated Equipment* 506.3 (2003), pp. 250–303.  
DOI: 10.1016/s0168-9002(03)01368-8 (cit. on p. 105).
- [138] F Tillner, P Thute, S Löck, A Dietrich, A Fursov, R Haase, M Lukas, B Rimarzig, M Sobiella, M Krause, M Baumann, R Büttof, and W Enghardt. „Precise image-guided irradiation of small animals: a flexible non-profit platform“. In: *Physics in Medicine and Biology* 61.8 (2016), pp. 3084–3108.  
DOI: 10.1088/0031-9155/61/8/3084 (cit. on p. 109).
- [139] MJ Butson, PK Yu, T Cheung, and P Metcalfe. „Radiochromic film for medical radiation dosimetry“. In: *Materials Science and Engineering: R: Reports* 41.3-5 (2003), pp. 61–120.  
DOI: 10.1016/s0927-796x(03)00034-2 (cit. on p. 115).
- [140] CG Soares. „Radiochromic film dosimetry“. In: *Radiation Measurements* 41 (2006), S100–S116.  
DOI: 10.1016/j.radmeas.2007.01.007 (cit. on p. 115).

- [141] SM Vatnitsky, RWM Schulte, R Galindo, HJ Meinass, and DW Miller. „Radiochromic film dosimetry for verification of dose distributions delivered with proton-beam radio-surgery“. In: *Physics in Medicine and Biology* 42.10 (1997), pp. 1887–1898. DOI: 10.1088/0031-9155/42/10/003 (cit. on p. 115).
- [142] S Devic, J Seuntjens, E Sham, EB Podgorsak, CR Schmidlein, AS Kirov, and CG Soares. „Precise radiochromic film dosimetry using a flat-bed document scanner“. In: *Medical Physics* 32.7Part1 (2005), pp. 2245–2253. DOI: 10.1118/1.1929253 (cit. on p. 115).
- [143] URL: <http://www.gafchromic.com/gafchromic-film/radiotherapy-films/index.asp> (cit. on p. 115).
- [144] N Hayashi, Y Watanabe, R Malmin, and H Kato. „Evaluation of triple channel correction acquisition method for radiochromic film dosimetry“. In: *Journal of Radiation Research* 53.6 (2012), pp. 930–935. DOI: 10.1093/jrr/rrs030 (cit. on p. 115).
- [145] F Nürnberg, M Schollmeier, E Brambrink, A Blažević, DC Carroll, K Flippo, DC Gaudier, M Geißel, K Harres, BM Hegelich, O Lundh, K Markey, P McKenna, D Neely, J Schreiber, and M Roth. „Radiochromic film imaging spectroscopy of laser-accelerated proton beams“. In: *Review of Scientific Instruments* 80.3 (2009), p. 033301. DOI: 10.1063/1.3086424 (cit. on pp. 115, 119).
- [146] JS Green, M Borghesi, CM Brenner, DC Carroll, NP Dover, PS Foster, P Gallegos, S Green, D Kirby, KJ Kirkby, P McKenna, MJ Merchant, Z Najmudin, CAJ Palmer, D Parker, R Prasad, KE Quinn, PP Rajeev, MP Read, L Romagnani, J Schreiber, MJV Streeter, O Tresca, CG Wahlström, M Zepf, and D Neely. „Scintillator-based ion beam profiler for diagnosing laser-accelerated ion beams“. In: *Laser Acceleration of Electrons, Protons, and Ions; and Medical Applications of Laser-Generated Secondary Sources of Radiation and Particles*. Ed. by KWD Ledingham, WP Leemans, E Esarey, SM Hooker, K Spohr, and P McKenna. SPIE, 2011. DOI: 10.1117/12.888967 (cit. on p. 116).
- [147] S Humphries. *Charged Particle Beams*. Wiley, 1990. ISBN: 9780471600145 (cit. on p. 119).



# DANKSAGUNG

An dieser Stelle möchte ich ganz unförmlich aber umso herzlicher allen Personen Danke sagen, die zum Gelingen dieser Arbeit beigetragen haben. An erster Stelle den beiden Direktoren des Instituts für Strahlenphysik des HZDR, Tom Cowan und Ulrich Schramm. Unser dynamisches Professorenduo ermöglichte mir, mich wissenschaftlich zu entfalten, unfassbar viel zu lernen, im In- und Ausland zu experimentieren und meine Arbeit an den entlegensten Fleckchen dieser Erde zu präsentieren. Dafür und für die Begutachtung und Betreuung meiner Arbeit über die letzten Jahre hinweg danke ich euch!

An zweiter Stelle möchte ich dem kompletten Ionenteam danken. Dabei zunächst den eingeschworenen Eingeborenen aus Raum 106, den Ur-Gesteinen, dem Establishment, dem Core-Team: Captain Karl Zeil, Josefine Metzkes und Stephan Kraft – die Dresdner Dreifaltigkeit der Laser-Ionenbeschleunigung. Vielen Dank dafür, dass ihr euren Erfahrungsschatz mit dem Rest des Teams teilt und bei gemeinsamen Experimenten genauso eifrig seid, wie beim Korrekturlesen dieser Arbeit. Danke auch an meinen emsigen Zimmergenossen und Frühaufsteher HP Schlenvoigt, der es immer schaffte vor mir auf Arbeit zu sein. Natürlich gebührt auch dem jungen Blut der Arbeitsgruppe ein gehöriges Stück Dankbarkeit, all denjenigen, die (noch) vollkommen unverbraucht und ohne ein einziges graues Haar durchs Labor wuseln – Lotti Obst, Martin Rehwald, Tim Ziegler, Lennart Gaus und ganz besonders Florian Brack. Flo, ohne deinen unermüdlichen Einsatz bei den laufenden Experimenten hätte ich wohl nie die Zeit gefunden meine Arbeit zu schreiben. Von dir war ich niemals *Disappointed!*

Zwei Grundpfeiler für das Gelingen dieser Arbeit in technischer Hinsicht waren Manfred Sobbiella und Robert Schönert. Eure Arbeit bei Konzeption, Konstruktion, Auf- und Zusammenbau von Spulen und Pulsgeneratoren ist unersetzlich. Danke, dass ich jederzeit auf euch bauen konnte. Ebenfalls danke ich dem Rest des Werkstatt-Teams, Matthias, Mathias, Marco und Rolf sowie Liane Heinrich, Heiko Gude und Maik Görler für eure Hilfs- und Einsatzbereitschaft.

Ein herzliches Dankeschön gebührt auch allen Beteiligten der onCOOPtics-Kollaboration, darunter Jörg Pawelke, Leo Karsch, Michael Schürer und Elke Beyreuther, für die stets hervorragende Zusammenarbeit bei den Strahlführungsexperimenten am Tandem, bei der gemeinsamen Magnetentwicklung und bei der Vorbereitung der Mausbestrahlungskampagne. Of course I would also like to thank Umar Masood. I had a great time working with you, buddy!

Sergei Zherlitsyn und Thomas Herrmannsdörfer danke ich für die zahlreichen Diskussionen zum Thema Magnetentwicklung und ihre uneingeschränkte Hilfsbereitschaft. Selbst wenn mal wieder ein Magnet in allerhöchster Eile gefertigt werden musste, bleibt ihr und eure

eifrigen Mannen an der Wickelmaschine cool. Martin Joost und Steffen Dittrich danke ich zudem für die Unterstützung zu Beginn der Pulsgeneratorentwicklung; Lars Lindenmüller und Stefan Wettengel für die ausgezeichnete Zusammenarbeit und dafür, dass sie mir bei (für den Physiker) komplexen elektrotechnischen Fragen immer mit Rat und Tat zur Seite standen. Auch Shavkat Akhmadaliev hat unserem Team mehr als einmal unter die Arme gegriffen. Dafür danke, Shavkat! Ein Riesenlob geht auch an die beiden Spulen-Ingenieure mit denen ich während meiner Zeit als Doktorand zusammenarbeiten durfte, Bernd Wustmann und Stefan Findeisen sowie die gesamte Zentralabteilung-Forschungstechnik inklusive Zentralwerkstatt.

Weiterhin gebührt großer Dank den Teams von Beschleuniger- und Laseroperatoren, Technikern und Ingenieuren rund um Tandem, PHELIX, LULI und ganz besonders Stefan Bock, Uwe Helbig und René Gebhardt für ihren unermüdlichen Einsatz den störrischen „Drachen“ zu bändigen.

Merci, to my french colleagues in the teams of Julien Fuchs and Michel Koenig, especially to Bruno Albertazzi and all the other great people I met during experiments at LULI.

Ich danke allen Mitgliedern der LIGHT-Kollaboration um Prof. Markus Roth, ganz besonders Diana Jahn, Dennis Schumacher, Olli Deppert, Christian Brabetz, Abel Blažević und den drei Simons: Busold, Frydrych und Weih. Zusammen haben wir so viele Experimente gemeistert und unsere Nerven immer wieder auf die Probe gestellt. Egal ob Abel mal wieder ein undichtes „Isolierstück“ einbauen lassen will, in der Nachtschicht gegen 3 Uhr morgens Bandsägearbeiten zu erledigen sind, Cavitylecks unter (gefühlte) 50 Lagen Blei gefunden und beseitigt werden müssen oder Last-Minute-Reparaturaufträge für den Pulser hereinflattern, während man eigentlich schon auf dem Weg nach Darmstadt ist – alles Worscht, für euch setz' ich mich gerne in den Zug oder Mietwagen (Kofferraum natürlich voller Ersatzteile) und diese gut gelaunt zur GSI. May *The Wild Horde* keep on riding!

Die moderne Physik ist voller Akronyme und Abkürzungen, doch neben TNSA, RPA, HIBEF, LIGHT und Co. sind mir während meiner Promotion besonders WDAWKT und das BHP ans Herz gewachsen! Danke an die besten Kollegen, Freunde, Boulder-Buddies, LEGO- und GoT-Fans die man sich wünschen kann! Danke an Klaus Steiniger, Sebastian „Mo“ Molatta, Roland Wuchrer, Thomas „Toto“ Buchheim, Lotti Obst, Axel Hübl, Florian Brack, Nick Hartley, Jurjen Couperus, Rengin Cabadağ, Josefine Metzkes, Raphael Ng, Fabian Röser, Axel Jochmann, Alex Köhler, Marco Garten, Martin Rehwald, Melanie Rödel, Malte Zacharias, Jakob Krämer und Karsten Rost aka Horst.

Last but not least möchte ich meinen Eltern, Großeltern, Schwiegereltern in Spe, der Lieblingstante und meinem Schatz Viki danken. Ihr wart immer da und habt mir den Rücken gestärkt und freigehalten. Vielen, vielen Dank an die beste Familie die man sich wünschen kann!

Diese Arbeit beginnt mit einem Zitat, nun soll sie auch mit einem Zitat Enden – ein Zitat welches den Leser dieses Büchleins (ich hoffe die Lektüre ist nicht allzu dröge) mit einem Augenzwinkern dazu anspornen soll, nicht nach hinten zur Danksagung zu blättern, sondern weiterzulesen:

"A mind needs books as a sword needs a whetstone, if it is to keep its edge."  
Tyrion Lannister

## Erklärungen

Hiermit versichere ich, dass ich die vorliegende Arbeit ohne unzulässige Hilfe Dritter und ohne Benutzung anderer als der angegebenen Hilfsmittel angefertigt habe; die aus fremden Quellen direkt oder indirekt übernommenen Gedanken sind als solche kenntlich gemacht. Die Arbeit wurde bisher weder im Inland noch im Ausland in gleicher oder ähnlicher Form einer anderen Prüfungsbehörde vorgelegt.

Die Dissertation wurde unter der wissenschaftlichen Betreuung von Prof. Dr. Ulrich Schramm am Helmholtz-Zentrum Dresden – Rossendorf angefertigt.

Die Promotionsordnung der Fakultät Mathematik und Naturwissenschaften an der Technischen Universität Dresden vom Februar 2011 mit letzten Änderungen vom Juni 2014 erkenne ich an.

Dresden, Dezember 2017

Florian Kroll







Bautzner Landstr. 400  
01328 Dresden, Germany  
Tel. +49 351 260-2745  
Fax +49 351 260-12745  
florian.kroll@hzdr.de  
<http://www.hzdr.de>